Title
Electrospun Nanofiber Metal Oxides for Reactive Sorption and Catalysis

Permalink
https://escholarship.org/uc/item/6hf3w4bc

Author
Alshafei, Faisal

Publication Date
2018

Peer reviewed|Thesis/dissertation

UNIVERSITY OF CALIFORNIA

Los Angeles

Electrospun Nanofiber Metal Oxides

for Reactive Sorption and Catalysis

A thesis submitted in partial satisfaction

of the requirements for the degree of Master of Science

in Chemical Engineering

by

Faisal H. Alshafei

2018

ABSTRACT OF THE THESIS

Electrospun Nanofiber Metal Oxides

for Reactive Sorption and Catalysis

by

Faisal H. Alshafei

Master of Science in Chemical Engineering

University of California, Los Angeles, 2018

Professor Dante A. Simonetti, Chair

Electrospun metal oxides is a new class of materials that have demonstrated auspicious potential and have been used in a wide range of applications. In this work, various smooth, continuous, and defect-controlled metal-polymer nanofibers were synthesized via electrospinning with diameters ranging from approximately 50 to 600 nm, and subsequently thermally treated to decompose the polymer (PVP or PEO) and form highly porous, fibrous metal (Cu-, Ni-, Mg-, and Ca-) oxide nanostructures. In the first part of this thesis, parameters that influence the electrospinning process were systematically investigated for PVP-Cu(NO$_3$)$_2$ systems. Both solution properties (polymer/metal concentration, polymer molecular weight, and solvent identity) and processing conditions (applied voltage, tip-of-needle to collector distance, extrusion rate, and humidity) were varied to probe the effect of these electrospinning factors on fiber quality prior to thermal

treatment. The data collected demonstrated that factors that do not directly and strongly influence viscosity, conductivity and solvent evaporation (e.g., applied voltage, extrusion rate, and tip-of-needle to collecting plate distance) do not have substantial effects on fiber diameter and morphology. Subsequent thermal treatment of the electrospun nanofibers and choice of metal, however, were found to markedly impact the morphology of the formed fiber oxides (e.g., string-like structures or segmented particles).

In the second part of this thesis, electrospun fiber metal oxide materials were tested in two main applications (high temperature CO_2 removal and low-temperature H_2S removal) and their performance was compared to materials prepared via traditional synthesis routes (e.g., sol-gel, co-precipitation, hydrothermal treatment, etc.) In the first application, CaO-based materials were tested as potential sorbents in sorption enhanced steam methane reforming (SE-SMR) to capture CO_2 and shift the reaction towards producing more hydrogen. The electrospun CaO-nanofibers, when reacted with CO_2, achieved complete conversion to $CaCO_3$ and had an initial CO_2 sorption capacity of $0.79 g_{CO2}/g_{sorbent}$ at 873 K and 923 K (highest of all materials tested), as the macro-porosity imparted by the electrospinning process improved the CO_2 diffusion through the $CaCO_3$ product layers. Furthermore, when these electrospun sorbents were added to a commercial catalyst and tested in SE-SMR conditions, they had three to four times longer breakthrough times than CaO sorbents derived from natural sources (e.g., CaO-marble). To further improve the stability of CaO-based sorbents, chemical doping of Ca-supports with Mg, Al, Y, La, Zn, Er, Ga, Li, Nd, In, and Co was combined with electrospinning to yield mixed oxide materials with high sorption capacities ($\sim$0.4-0.7 $g_{CO2}/g_{sorbent}$) and improved durability (up to 17 cycles). It was demonstrated that metals that have high Tammann

iii

temperatures were effective at reducing sintering and CaO particle agglomeration by acting as spacers, thus, retaining the sorbent's initial sorption capacity upon repeated cycling.

In the second application, CuO nanofibers with varying diameters (~70-650 nm) were prepared from two polymers (PEO and PVP) and reacted with H_2S at ambient conditions to form CuS. The results from this study demonstrated that the sulfur removal capacity of CuO materials, whether prepared via electrospinning, hydrothermal treatment, sol-gel or co-precipitation, was strongly dependent on crystallite size (a linear relationship was established between CuO removal capacity and crystallite size and held true for all CuO materials with crystallites between 5-26 nm) and CuO purity (i.e., presence of residual carbon on the surface of the oxide). Indeed, properties such as surface area, pore volume and morphology (e.g., flowerlike, fiber-like, belt-like, etc.) were found to have an insignificant impact on removal capacity. This work offers fundamental insights into the design of multifunctional and highly porous metal oxide nanofibers for sorptive and catalytic applications.

The thesis of Faisal H. Alshafei is approved.

Philippe Sautet

Yunfeng Lu

Dante A. Simonetti, Committee Chair

University of California, Los Angeles

2018

Table of Contents

List of Figures

List of Tables

Acknowledgements

Firstly, I would like to acknowledge and thank my thesis supervisor, Prof. Dante Simonetti, for his invaluable teachings and unconditional support during my time at UCLA. His patience and guidance were crucial in helping me bring this thesis to fruition. In the same respect, I would like to thank my thesis committee members: Prof. Philippe Sautet and Prof. Yunfeng Lu for their generous time and for advising me on this project. I also would like to thank my fellow labmates and peers. I will always cherish the memories we had together. Additionally, I would like to thank and acknowledge the following individuals who worked with me on this project: Luke Minardi, Sara Azzam, Derrick Rosales, Richa Ghosh (undergraduate), Zubin Mishra (undergraduate), Steven Drooz (undergraduate), Dr. Sergey Prikhodko (associate adjunct professor, Materials Science and Engineering Department at UCLA), Dr. Tirso Lopez-Ausens (post-doc), and Dr. Gen Chen (post-doc).

Secondly, I would like to acknowledge everyone who played a role in my success, in all my previous destinations. Specifically, I would like thank Dr. Abraham Clearfield (TAMU) for taking a chance on me as a freshman at Texas A&M University and allowing me to work in his lab. I did so many things wrong in his lab, but he never gave up on me. I also would like to thank and acknowledge my previous research advisors/mentors: Dr. Iraj Ershaghi, Dr. Theodore Tsotsis, and Dr. Sohel Shaikh.

Finally, I would like to express special thanks to my family and friends.

Chapter 1 | Introduction

1.1 Background

Nanotechnology is a broad field that has gained accrued attention and evolved dramatically over the last couple of decades. Indeed, today, nanoparticles and nanostructured materials represent an active area of research and discovery, epitomizing a techno-economic force with full expansion. On a fundamental level, nanoparticles are particles that are between 1 and 100 (or more broadly 1000) nanometers (nm) in size. As an example, to get a comparative size of this small dimension, a human hair has a diameter of approximately 80,000 nm.[1] Nanotechnology, as a term, corresponds to the scientific methods which exploit unique material properties at nanometer dimensions to perform tasks that are not possible using the same materials in their bulk, macroscopic form.[1] Indeed, the ability to understand, control, and manipulate materials at the level of individual atoms and molecules is what this field is all about.

What makes nanotechnology such a fascinating field and an area that is of great interest to the scientific community is that nanomaterials often manifest special characteristics and have unique mechanical, optical, magnetic, and/or chemical properties, which are different than the bulk material[2] (because at the atomic level, gravity forces take a backseat to electrostatic forces and quantum effects).[1,3] These unique and sometimes unexpected properties that arise at the atomic level allow for the development of more efficient and robust materials (e.g., more effective medicines, extremely active catalysts, improved storage devices, etc.).[4–6] Because of the wide assortment of potential applications for nanomaterials, research involving them have encompassed numerous disciplines, including, molecular engineering, medicine, construction, biology,

chemistry, physics, polymer science, mechanical engineering, catalysis, food technology, environmental health, energy, and cosmetics.[7–14]

Nanofibers is a type of nanomaterial that has been widely researched. Various techniques have been exploited for the fabrication of nanofibers including mechanical drawing,[15] template synthesis,[16,17] phase separation,[18] and electrospinning.[19,20] Electrospinning, which as an electrostatic fabrication technique, has been widely recognized as a simple, easy-to-use, and an efficient method for the synthesis of nanofibrous structures.[21–23] Electrospinning produces fine and robust materials with specialized features and exceptional properties such as, high surface areas, superior mechanical strengths, flexible surface functionalities, and tunable porosities.[24–26] It's precisely these outstanding properties and functionalities that make electrospun materials applicable to many important applications today. Some notable applications were electrospun materials have been successfully used include tissue engineering, biosensors, filtration, drug delivery, enzyme immobilization, fuel cells, energy storage cells, protective clothing, optical electronics, healthcare, defense and security, environmental engineering, and catalysis.[27–38] This thesis reports in depth on this synthesis technique and the utilization of electrospun metal oxides for the fabrication of highly active materials, for use in sorption and catalysis applications.

1.2 Thesis Overview

This thesis describes the author's work in two major areas of research in electrospinning: the first deals with the fundamental, experimental science of electrospinning metal oxide nanofibers (chapters 3-4). Specifically, this part deals with investigating and understanding the effect of electrospinning solution and processing parameters on metal-polymer fiber properties (e.g., dimension and morphology); the latter focuses on the utilization of electrospun metal oxide

materials in sorption and catalysis applications and comparing the performance of these nanostructures to traditional (i.e., powder or quasi-spherical) materials (chapters 5-7).

Chapter 2 presents a literature review covering the overall electrospinning process (historical background, key fiber properties, and electrospinning parameters/variables). Chapter 3 deals with the synthesis of copper-polymer nanofibers as well as copper oxide nanofibers and describes the effect of electrospinning solution and processing conditions on metal-polymer fiber dimension and morphology. Chapter 4 showcases other metal oxides that were electrospun using polyvinylpyroolidone (PVP) and various metal nitrates (nickel, magnesium and calcium). Chapter 5 deals with the utilization of electrospun calcium oxide-based materials as sorbents in sorption enhanced steam methane reforming and compares the performance of electrospun materials to other materials prepared via different synthesis techniques (e.g., hydrothermal treatment, thermal decomposition, etc.). Chapter 6 expands on chapter 5 by surveying 11 dopants (Mg, Al, Y, La, Zn, Er, Ga, Li, Nd, In, and Co) that were incorporated into the fibrous CaO structure, to enahce stability and durability in high temperature CO_2 removal applications. Chapter 7 deals with CuO materials that were prepared via electrospinning, sol-gel, co-precipitation, hydrolysis, and hydrothermal treatment and then reacted with H_2S at room temperature, to investigate the sorbent properties (surface area, pore volume, pore diameter, morphology, etc.) that influence the removal capacity of CuO-materials. Chapter 8 offers a brief conclusion.

Chapter 2 | Literature Review

2.1 Historical Background and Popularity

Although the term "electrospinning" was first used in 1994—very recently, indeed—the fundamental concept of electrospinning dates back to the early 1900s.[21,29] In 1902, John Cooley invented an apparatus which electrically dispersed fluids.[39] Thereafter, from 1934 to 1944, Anton Formhals published several patents, in which an experimental setup was described, which relied on an electrostatic force to produce polymer filaments.[21,40–43] For example, in the first patent by Formhals in 1934, cellulose acetate and acetone were introduced into an electric field, resulting in the formation of polymer filaments between two electrodes with opposite polarities.[40] In 1952, Vonnegut and Neubauer developed an apparatus which was able to produce a stream of highly electrified droplets with small diameters.[21] Later, in 1955, Drozin examined the dispersion of several liquids under high electric potentials, using a glass tube with a fine capillary.[21,44] He concluded that certain liquids under appropriate conditions form highly dispersed aerosols, with uniform sizes. These were some of the earliest reports on electrospinning.

Several inventions and scientific reports continued to be filed or written on this topic in the 1960s and 1970s,[29] however, despite these discoveries, electrospinning did not gain real popularity, momentum, or true scientific attention until the late 1900s and early 2000s (**Figure 1**)—most likely due to a surging interest in the field of nanotechnology during that time. The interest in electrospinning has only grown since those early days, as this method's ability to consistently produce fibers in the submicron and nano-range that is otherwise difficult to achieve by using other mechanical fiber spinning fabrication techniques became realized. Indeed, electrospinning is the only method of choice for large scale preparation of nanofibers, as it offers

easy handling and processing, consumes relatively small amounts of solution and raw materials, fabricates reproduceable materials, and is easily scaled up.[21,29,33]
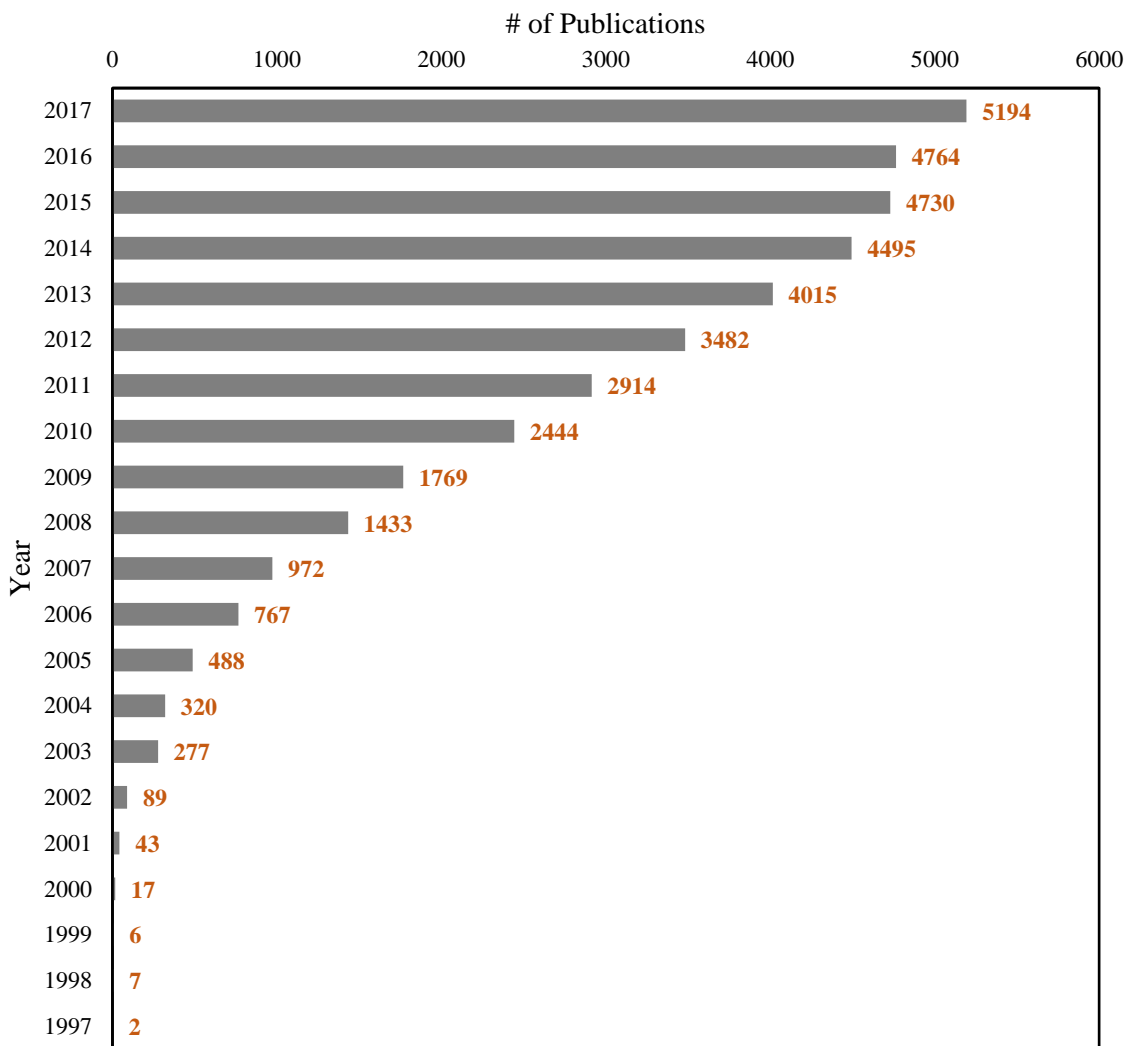
Figure 1. Comparison of the annual number of scientific publications involving the term "electrospinning" covering the period from 1997 until 2017.

A survey of open publications—including, but not limited to, books, reviews, patents, journal articles, reports, and conference proceedings—related to electrospinning in the past 20 years (from 1997 until 2017) is given in **Figure 1**. These literature data were obtained based on a SciFinder search system. The data clearly demonstrates that electrospinning has attracted increased

attention recently, especially in the last decade. It's worth mentioning, though, that the majority of research involving electrospinning in the last fifteen years has mainly dealt with the application of these materials as opposed to understanding the fundamentals of the electrospinning process. That said, oddly enough, even though this process has existed in the literature for a quite a bit of time now and has been used in several applications and rather successfully, its understanding is still fairly limited.

2.2 Working Principle and Instrumentation

Figure 2 illustrates the working principle of electrospinning and offers a schematic diagram of a typical experimental apparatus used to perform electrospinning experiments. As shown in **Figure 2**, typically, there are three main components to an electrospinning apparatus: a high voltage supplier, a metal collector (either stationary, which is ideal for the formation of randomly-oriented fibers, or a rapidly rotating wheel/drum (not shown in scheme), which is ideal for the formation of aligned fibers), and a capillary tube or a needle with a small diameter. Other modifications, particularly different collector designs, can be and in fact have been added to the basic electrospinning apparatus by other researchers[45] in order to overcome certain limitations involving the typical electrospinning scheme or to enhance the quality of the formed fibers.

On a very fundamental level, the electrospinning technique operates on the principle of electrostatic interactions. Simply put, the solution that is being electrospun (often comprises of a natural or synthetic polymer and a solvent) has a surface tension that must be overcome in order for the solution to electrospin and form fibers. By applying a high voltage power supply at the spinneret (needle), the solution in the syringe becomes charged. As a result, the polymeric liquid droplet at the tip of the needle comes under the action of two electrostatic forces: Coulombic forces, which are applied by an external electric field (power supply), and mutual electrostatic

repulsion forces, which exist between the surface charges of the fluid.[28] On the opposite side of the spinneret lies the oppositely charged collector (often a rotating drum or a stationary collecting plate) (~10-35 cm). During the supply of a high voltage (~10-40 kV) and due to electrostatic interactions, the solution emerges out of the needle and the liquid droplet elongates by overcoming its own surface tension and charges towards the collector. Indeed, the intensity of the electric field applied must be high enough in order for the electrostatic forces to overcome the fluid's surface tension. As the solution emerges and the liquid droplet elongates to travel to the collector, it forms a cone-like structure referred to as a "Taylor Cone". The droplet/jet, therefore, elongates by first forming this cone and then spins, following first a linear trajectory, but at some critical distance (bending instability), whip out in a chaotic fashion in a helical path. As the jet travels, the solvent undergoes extreme instabilities and elongation,[46] which allows the jet to become long and thin. Meanwhile, in this process, the solvent evaporates, allowing for polymeric nanofibers to form.
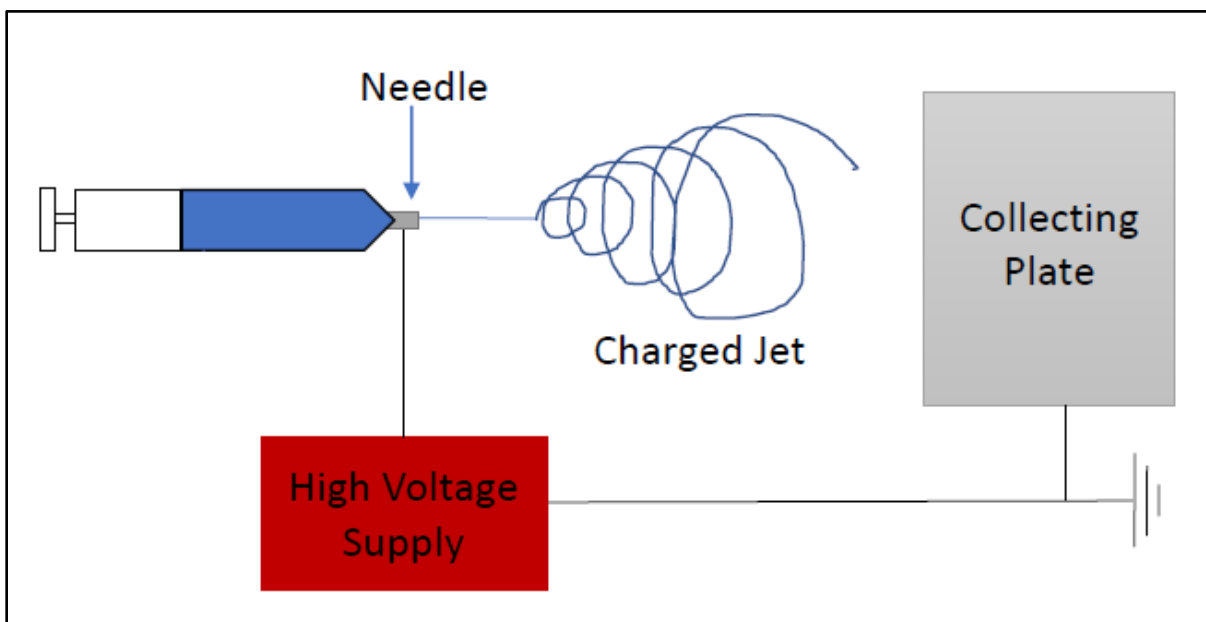
Figure 2. Schematic diagram showing the formation of nanofibers by electrospinning.

Although many researchers have used the single-needle scheme shown in **Figure 2** and described in the previous paragraph to form nanofibers, the low fluid throughput of this scheme has limited its industrial use. And, as such, to meet the high liquid throughput requirements required by industry, multi-jet schemes or needless processes have been developed and as a matter of fact have been successfully implemented.[47,48] Those complex designs, however, will not be discussed in this work.

2.3 Properties of Electrospun Nanofibers

As mentioned previously, nanofibers fabricated via electrospinning exhibit unique properties that are often not seen in other one-dimensional structures such as, nanowires, nanorods, and nano-ribbons. Some of these key properties and features that distinguish electrospun nanofibers (or are of paramount importance to describing electrospun materials) are described in this section.

2.3.1 Fiber Dimension and Morphology

Fiber diameter is likely the most important nanofiber property, as often times this property controls which application the fibers can be used in. The diameter of an electrospun fiber is dependent on practically (and collectively) all the electrospinning parameters and conditions affecting the process (e.g., viscosity, conductivity, surface tension, voltage, distance between the capillary and collector, flowrate, and ambient conditions).[28] However, of these parameters, polymer concentration or more broadly solution concentration is perhaps the most crucial parameter influencing the diameter of the formed fibers. An increase in solution concentration generally results in the formation of fibers with thicker and larger diameters. In fact, by critically increasing a solution concentration, fibers in the micron range can be formed. Demir et al.[49] studied

the effect of polymer concentration (and thus, viscosity) and the authors reported a power law relationship (cubical) between polymer concentration and polyurethane fiber diameter. It has also been shown that increasing the solution concentration results in the formation of fibers with wider distributions due to the presence of secondary jets (i.e., jet splitting).[50] Zong et al.[51] studied the effect of solution conductivity, another important electrospinning parameter, on fiber diameter and found that they were inversely related (i.e., solutions with higher conductivities resulted in fibers with smaller diameters). Parameters such as, polymer molecular weight, voltage, flowrate, distance, humidity, and solution temperature were also found to impact the diameter of the formed fibers in various ways, depending on the identity of the polymer/solvent system used and their interaction with each other.[52–57] These parameters and their influence on fiber diameter will be discussed in greater depth in subsequent sections.

In addition to fiber diameter, the presence of beads, a structural defect, in electrospun materials is an important property affecting fiber morphology and is considered a commonly encountered problem in electrospinning.[50,56,58] This structural defect occurs due to operating the electrospinning setup under un-optimal conditions. There are various processing variables which have been reported in the literature to be responsible for the occurrence of beading. For instance, when the applied voltage is increased beyond a certain point, the jet velocity is drastically increased and the solution withdrawn from the tip of the needle is removed at a much higher speed and force. As such, the volume of the droplet at the tip of the needle becomes smaller resulting in the formation of a Taylor cone that oscillates, which in turn results in the formation of beaded fibers.[28] Solution concentration has also been shown to greatly affect bead formation. Specifically, highly concentrated solutions have been shown to produce more uniform nanofibers with fewer structural defects.[59] It's also been shown in the prior art that the shape of the bead can be altered from

9

spherical to spindle-like by increasing the viscosity of the electrospun solution (by increasing the polymer molecular weight or polymer concentration, for example).[60] In addition to viscosity, a solution's surface tension is another property that influences the morphology and size of electrospun nanofibers (as well as their structural defects). For instance, it's been reported that the addition of ethanol to poly(vinyl alcohol) (PVA) and polyethylene oxide (PEO) affected the solutions surface tension, which in turn led to the formation of less beaded fibers for PEO but more for PVA. The reason being is that ethanol is considered a solvent for PEO, but not for PVA.[28,61]

2.3.2 Fiber Surface Structure

Electrospun nanofibers are generally smooth and cylindrical in shape; however, certain processing parameters can result in the formation of fibers with different surface structures. For instance, by operating the electrospinning apparatus at a high electric potential or by electrospinning a solution with a low polymer concentration, fibers with rougher surface structures are formed.[62] Additionally, although electrospun nanofibers generally have circular cross sections, other structures can also be synthesized such as, ribbon-like structures. Ribbon-like structures form when polymers with high molecular weights or solutions with high polymer concentrations (i.e., high viscosity) are used.[63,64] Specifically, these structures form as a result of the formation of wet fibers as opposed to dry fibers. When wet fibers reach the collector, they get flattened out upon impact as a result of the collapse of the outer skin of the fiber, thus, yielding ribbon-like structures.[28]

2.3.3 Fiber Porosity

The neat thing about electrospinning is that it allows for the synthesis of fibers with varied and tunable porosities. When dealing with electrospun materials, two types of pores exist: pores within each fiber, which can form by controlling the humidity inside the electrospinning chamber

(discussed in detail in subsequent sections),[65] and pores between the fibers. When compared to mesoporous materials (e.g., molecular sieves), the BET surface area of electrospun fibers is generally lower, but the sizes of the pores present in electrospun fibrous structures are relatively larger (i.e., macro-pores) and they are fully interconnected, forming a three-dimensional network.[66] Indeed, understanding the fibrous structure pore size and porosity is essential to controlling and enhancing a membrane's performance, for example, and/or for applying electrospun materials in certain fields, such as, biomedical applications.

2.4 Electrospinning Parameters

Although the electrospinning process appears simple, a number of processing variables ought to be properly regulated, as evidenced from the previous sections, in order to effectively and efficiently use this technique to generate smooth, bead-less fibers. As a matter of fact, a major challenge with the electrospinning process lies in the optimization of these parameters to achieve fibers with desirable properties (e.g., morphology, size (width), porosity, surface area, and topography). The main variables that impact the quality of the formed fibers include: polymer concentration and molecular weight (i.e., solution viscosity), solution conductivity (i.e., metal concentration), nature of solvent, applied voltage, solution flow-rate, distance between the capillary and collector, and humidity. These parameters and variables will be discussed in this section, in light of the prior art.

2.4.1 Polymer Concentration, Polymer Molecular Weight, and Solution Viscosity

Because the process of electrospinning is based on the principle of uniaxial stretching of a charged polymer jet,[21,67] the choice of polymer (identity, molecular weight, and concentration) is of a paramount importance to forming defect-free nanofibers. Indeed, the concentration of a

polymer in an electrospinning solution has a direct effect on both the viscosity as well as the surface tension of the liquid, which in combination decide the electrospinnibility of a solution (i.e., whether a solution will electrospin or electrospray).[21,68] In general, low polymer concentrations (below a critical value required for electrospinning) result in the formation of fragmented charged jets (instead of a continuous jet). A fragmented jet does not form fibers but rather electrosprays, thus, forming discrete droplets as opposed to nanofibers. Increasing the polymer concentration improves the viscosity of a solution which in turn increases and improves the chain entanglements between the polymer chains. Increased chain entanglements lead to the formation of continuous jets, and thus, nanofibers. At the lower end of this acceptable concentration (i.e., viscosity) range, fibers with structural defects form. As the viscosity is increased, these defects tend to reduce in size and quantity until they disappear. At some critical value, increasing the polymer concentration (viscosity) further results in a solution that is too viscous to properly electrospin. At this limit, the viscosity becomes so high that it disrupts the flow of the polymer through the capillary (e.g., tube and/or needle).[69] It's important to note, though, that each polymer and solvent system has unique values for these critical viscosity values, which not only depend on the identity of the solvent and concentration of the polymer, but also on the other electrospinning parameters (e.g., voltage, distance, etc.).

Deitzel et al.[70] studied the electrospinning of PEO solutions and reported that the optimal range for PEO fiber formation was between 4 and 10% wt/v. The authors reported that below this range a combination of fibers and droplets formed due to high surface tension and low viscosity. When viscosity was optimal, nanofibers that were regular and cylindrical formed, with only a few junctions and bundles. Junctions and bundles form due to inadequate drying/evaporation. Doshi and Reneker[71] also investigated the effect of viscosity; they observed that when the viscosity of

their PEO solutions were between 800 and 4000 cp, fibers formed. However, below 800 cp, dispersed droplets formed and above 4000 cp, no fibers formed. At those conditions (high viscosity), it was difficult to form fibers since clogging occurred. Similar results were observed involving a myriad of polymer and solvent systems by other authors as well.[21,72]

2.4.2 Metal Concentration and Solution Conductivity

Conductivity is another important solution parameter because conductivity corresponds to the charge carrying capacity of an electrospinning solution. Essentially, the charge carrying capacity of an electrospinning solution is higher when a solution has higher conductivity. This higher conductivity means that the solution is subjected to a greater tensile force when its exposed to an external applied voltage. In general, it has been observed that an increase in solution conductivity translates to fibers with thinner diameters. Zong et al.[51] studied the effect of adding different salts (KH_2PO_4, NaH_2PO_4, and $NaCl$) to a 30 wt% poly(D,L-lactide) (PDLA) solution and found that adding 1% wt/v of salt resulted in the synthesis of fibers with significantly smaller diameters for all three metals tested. The size of the ions in solution where also found to have an impact on the diameter of the formed fibers, with ions with smaller radii producing thinner fibers due to them having higher charge densities. Son et al.[73] investigated the effect of adding poly(allylamine hydrochloride) (PAH) and poly(acrylic acid) (PAA) on the conductivity of PEO aqueous solutions. The authors concluded that adding PAH and PAA increased the conductivity of the solutions, which resulted in the formation of thinner fibers.

2.4.3 Solvent

The selection of a solvent is another critical parameter as the choice of solvent indirectly influences properties such as, surface tension, conductivity and viscosity. When considering a solvent, the three most important properties to consider are the solubility of the polymer in the

13

solvent, the solvent's boiling point., and the solvent's surface tension. The solvent's dielectric constant and dipole moment are also two properties that should be considered. In electrospinning, solvents with low boiling points are generally preferred as these solvents evaporate quicker during the electrospinning process, thus, forming dry fibers as opposed to wet, fused fibers or droplets. However, it important to note that solvents with extremely low boiling points are also to be avoided as these solvents tend to evaporate at the tip of the needle, thus, clogging the needle. The surface tension of the solvent also ought to be acceptable as solutions with high surface tensions tend not to electrospin easily, and even when they do electrospin, they generally form beaded fibers. They also require more extreme electrospinning conditions (e.g., higher voltages).

Some of the most common solvents used in the electrospinning literature (with their key intrinsic properties in parenthesis), include: dichloromethane (DCM; low dielectric constant and high surface tension), methanol (high dielectric constant and low surface tension), ethanol (low surface tension and high viscosity), water (low intrinsic viscosity), dimethylformamide (DMF; high conductivity and high dipole moment), tetrahydrofuran (THF; high dipole moment and good conductivity), and chloroform (high viscosity).[61,74–78] Jarusuwannaopoom et al.[78] studied eighteen different solvents and found that of the eighteen, DMF, THF, ethyl acetate, 1,2-dichloroethane, and methylethylketone (MEK) were optimal for electrospinning polystyrene fibers. These solvents were found to be suitable for electrospinning because they had excellent conductivity, viscosity, and surface tension; high dipole moment; and an acceptable boiling point. Fong at el.[61] investigated a solvent mixture of ethanol and water to produce PEO fibers. The authors found that increasing the ratio of ethanol to water while maintaining all other parameters constant (e.g., polymer concentration, distance, voltage, distance, etc.) resulted in the formation of fibers with larger diameters and lesser (or no) beads. The authors attributed these observations to the fact that ethanol

14

has a lower boiling point than water, and therefore evaporated faster, and also lower surface tension, which resulted in the formation of defect-free or defect-controlled fibers.

2.4.4 Applied Voltage

Aside from the three solution parameters described previously (polymer concentration (or viscosity), metal concentration (or conductivity), and solvent selection), there are processing conditions that also must be in an acceptable range in order for electrospinning to occur. One of the most critical processing parameters in electrospinning is applied voltage. Each polymer-solvent system has a unique critical applied voltage value, which is required to cause a polymer droplet to become conical in shape (i.e., form a Taylor cone). If an external voltage below this value is applied on an electrospinning solution, no fibers form. Any increase in voltage beyond this critical value, however, leads to the ejection of a polymer jet, which results in the formation of fibers. Each polymer-solvent system has an optimal electric field range. When within this range, smooth, defect-free fibers form. When outside this range, however, fibers with beaded morphologies or rough structures are generally formed.

Interestingly, despite being a key processing condition in electrospinning, the effect of voltage on fiber diameter and morphology is not fully understood and there seems to be conflicting reports on the effect of voltage, where some groups have reported increased diameters with increased applied voltages whereas other groups have reported decreased diameters with increased applied voltages. Mazoochi et al.[56] reported on the diameter of polysulfone nanofibers as a function of voltage applied. The authors showed that increasing the voltage led to an increase in fiber diameter, which was followed by a decrease in the diameter as the voltage continued to increase. Moreover, Zhang et al. [79] reported that increased voltage led to the synthesis of thicker PVA fibers when 6-8 % PVA aqueous solutions were electrospun. In both of these cases, the increase in

nanofiber diameter was attributed to a decrease in travel time of the polymeric jets due to the higher applied voltages. A study by Wu et al.,[80] however, showed that fiber diameter decreased with increased voltage. This was explained by the fact that at elevated applied voltage values, the polymer jet was subjected to greater stretching forces, which in turn led to thinner fibers. The results in the literature seem to demonstrate the complexity of the effect of applied voltage on fiber diameter and morphology, showing that its indirectly dependent on other properties as well (e.g., polymer identity and concentration, solvent identity, distance, and flowrate).

2.4.5 Flowrate (Extrusion Rate)

The flowrate at a which a polymer is pumped and passed through a needle influences, to varying degrees, the nanofiber diameter, porosity, and geometry. Beachley and Wen[55] reported that within a certain range, solution extrusion rate generally does not have a significant impact on the diameter and morphology of most electrospun materials. Ideally, a balance between the rate at which a solution is pumped/dispensed and the rate at which a solution is drawn from a needle (due to the applied voltage) ought to be present.[81] When the flowrate is too high, periodic dripping of the solution will occur and thicker fibers, with wider distributions, will form. Zargham et al.[54] studied the effect of flowrate of Nylon 6 in formic acid on fiber diameter and reported that increasing the feed-rate led to the formation of thicker fibers. Megelski et al.[82] also demonstrated that increasing flowrate results in an increase in diameter as well as in pore size of polystyrene nanofibers. As the flowrate of an electrospinning solution is increased, more polymer becomes available at the tip of the needle. That results in larger volumes of polymer being spun, which in turn results in the formation of thicker jets. Simply put, thicker jets form thicker nanofibers. Moreover, flattened ribbon-like nanofibers can form at extremely high flowrates because at high flowrates, fibers do not have adequate time to completely dry by the time they reach the collector,

16

thus, they form wet fibers.[82] As mentioned previously, wet fibers are more likely to collapse upon impact, thus, forming ribbon-like structures.

2.4.6 Distance Between the Capillary and Collector

The distance between the capillary (needle) and a collector influences the size, distribution and morphology of the formed nanofibers, as it effects the jet's path and travelling time. The effect of distance, however, is probably the least pronounced processing condition on fiber diameter of all the other processing variables discussed in this section. Generally, an optimum distance between the capillary and collector is required to form smooth, bead-free nanofibers and to prevent electrospraying. But, when changes in distance are applied within the optimum distance, small to no changes in diameter are generally observed (depending on the polymer-solvent system used and the other electrospinning processing conditions). Doshi and Reneker[71] studied the effect of distance between the capillary and collector. They reported that a decrease in nanofiber diameter was observed when distance was increased. They also reported that beyond a certain distance, the fiber jet became too small or unstable. Megelski et al.[82] studied this parameter as well; they noted no significant changes in fiber diameter with respect to distance, albeit they observed bead formation when the distance between the capillary and collector was decreased. At short distances, a few authors also observed and collected fused fibers. Fused fibers form due to insufficient evaporation. Ghelich et al.,[83] for example, observed fused fibers when they electrospun composite nanofibers.

2.4.7 Humidity

The electrospinning process and the physical characteristic of the formed fibers are strongly influenced by ambient conditions, especially humidity. Humidity, in effect, controls the rate of solvent evaporation; therefore, it effects the diameter, morphology and porosity of

electrospun polymer nanofibers. The effect of humidity on fiber diameter could be positive, resulting in thinner fibers, or negative, resulting in thicker fibers, depending on the very interaction between the solution and the surrounding water vapor. Polymers that could absorb water vapor from the atmosphere (i.e., water soluble) tend to form thinner fibers as their viscosities decrease upon absorbing water vapor, whereas polymers that are water insoluble tend to form thicker fibers, as water vapor precipitates on their surfaces, thus, inhibiting the solvent evaporation process. Kim et al.[84] reported that at higher relative humidity levels, thicker polystyrene fibers were synthesized. Polystyrene is a polymer that is water insoluble. Htike et al.[85], on the other hand, demonstrated the opposite effect of humidity on fiber diameter. Specifically, by using PVA as a water-soluble polymer, they showed that increasing humidity resulted in the formation of thinner fibers.

A less commonly reported observation associated with operating the electrospinning apparatus at low humidity levels has to do with the formation of broken fibers. Nezarati et al.[65] hypothesized, after studying poly(ethylene glycol) (PEG) and polycaprolactone (PCL) fibers, that fiber breakage occurs at low humidity levels as a result of the presence of excessive electrostatic charges. At higher relative humidity levels, some of these electrostatic charges are discharged from the jet to the surrounding water vapor molecules. But, at low relative humidity levels, most of these charges remain in the jet. Therefore, the force generated due to the repulsion experienced by the charges causes the fibers to break.

2.5 Summary

The electrospinning technique has certainly come a long way since it was first used in the early 20th century. Since that time, significant improvements have been made to the electrospinning apparatus (i.e., design) to efficiently produce numerous fibers with desirable and varying

properties. Fiber properties such as fiber diameter, morphology, surface structure, and porosity can be controlled by carefully regulating the electrospinning processing conditions. However, this is where the real challenge lies: in understanding how these processing parameters interact with each other and how they impact the properties of the formed fibers for various polymer and solvent systems. This chapter shed light on the complex nature of the electrospinning process and showed how the electrospinning processing parameters (e.g., polymer concentration and molecular weight (viscosity), metal concentration (conductivity), solvent properties (surface tension, boiling point, dipole moment, etc.), applied voltage, flowrate, distance between the capillary and collector, and humidity) are closely interrelated. It's interesting how a slight change in one parameter or one property can affect the thinning of a jet and thus the quality of the formed fibers.

Although the influences of numerous solution properties (e.g., viscosity, conductivity, etc.) and processing conditions (e.g., voltage, flowrate, distance, etc.) on fiber morphology have been investigated experimentally by various groups, as rather exemplified in this chapter, the effect of these parameters on fiber diameter and morphology have not been studied systematically. This is particularly true for solutions comprising of metals (metal nitrates, metal acetates, etc.) and polymers, where there is no comprehensive work that addresses the effects of electrospinning variables on metal-containing fibrous structures. As such, the next chapter will deal with investigating these electrospinning parameters for such metal-polymer systems.

Chapter 3 | Targeted Morphology of Copper Oxide Nanofibers

3.1 Introduction

The field of nanotechnology has paralleled the rise in demand for energy as global consumptions continue to surge. The interest in this field stems from the belief that nanotechnology has the potential to ameliorate energy efficiency across multiple industries through novel and innovative solutions, prompting researchers to extensively research and systematically investigate the unique properties of nanomaterials,[70,72] especially those that are prepared from earth-abundant and inexpensive metals.[86] The behavior of materials in the nanoscale is believed to offer insight into the control and design of objects on the atomic scale. Although nanotechnology has a lofty potential, it remains a new area of research that is not completely understood. The synthesis of nanostructures that offer superior properties and catalytic performances is a major challenge across multiple disciplines.

Nanofibers is a type of nanomaterial that has been widely researched. Various techniques have been exploited for the fabrication of nanofibers including mechanical drawing,[15] template synthesis,[16,17] phase separation,[18] and electrospinning.[19,20] Electrospinning, which is an electrostatic fabrication technique for the synthesis of long continuous fibers, has received heightened interest due to its potential for application in various fields, including catalysis,[31] sorption,[87] and separation processes.[22] Unlike other techniques that are used for generating one-dimensional nanostructures, electrospinning is a relatively simple, easy to use, and cost-effective method, which is based on uniaxial stretching.[70,50] When compared with mechanical drawing, electrospinning is more suitable for producing fibers with ultra-thin diameters because the elongation process is due to an external applied electric field. Recently, electrospinning has been

extended to produce nanofibers made of ceramics, composite materials, and oxides.[88] In fact, a variety of metal oxides have been fabricated using this technique and have shown potential in different engineering domains. The addition of metal particles into the polymer produces nanofibers that are multifunctional and have enhanced properties.[89,90] Quasi-cylindrical materials produced from electrospinning may be tuned to have high surface area-to-volume ratios, superior mechanical properties, interconnected porous networks, and tunable porosities,[72,50,91,37] thus, out-performing quasi-spherical particles or powders. Although several polymer/metal combinations have been successfully formed via electrospinning,[70,66,23] limited information exists regarding the impact of synthesis conditions on metal-polymer nanofiber morphology.

Previous research has shown that the properties of fibers formed via electrospinning are determined by synergetic effects of the solution variables, electrostatic forces applied on the solution jet, as well as electrospinning operational conditions.[61,76] A comprehensive work that addresses the effect of the electrospinning parameters and variables on metal-containing fiber structures, however, is still lacking. Diezel et al.[70] examined fiber formation of polyethylene glycol (PEO) via electrospinning by changing the concentration of the polymer and the voltage applied; however, many critical parameters such as, polymer molecular weight, solvent properties, extrusion rate, distance between tip-of-needle and collecting plate, and relative humidity were not investigated in that work and the effects of metal precursor addition were not tested. Similarly, previous work by Casper et al. focused only on the effects of molecular weight and atmospheric conditions for polystyrene fibers,[92] and Khalil and Hashaikeh probed only the effect of metal precursor concentration within electrospinning solutions.[25]

The work presented herein aims to elucidate the effects of several electrospinning parameters for nanofibers comprised of copper and polyvinyl pyrolindone (PVP). PVP was used

as a polymer source because it is an important amorphous polymer, which has low toxicity, excellent solubility in most organic solvents, capability to interact with a wide range of hydrophilic materials, and high biocompatibility.[93] Additionally, PVP is considered an excellent steric stabilizer or capping agent for various metal nanoparticles.[94] Copper nitrate was used as a metal source because nitrates tend to dissolve easily in ethanol, which is the preferred electrospinning solvent.[21] Ethanol plays a vital role in local polarization during the electrospinning process and has low surface tension, which encourages the formation of smooth, defect-free, and continuous nanofibers.[23] Copper was selected as the metal source because of its broad application in catalysis, energy storage, gas and liquid sensors, and optoelectronic devices.[95,96]

The principal factors that affect the electrospinning process, which have been systematically examined in this study, can be divided into two categories: (1) polymer/metal solution parameters (polymer molecular weight, polymer/metal concentration, solvent(s) properties). These three parameters were found to intrinsically impact the viscosity, boiling point, density, surface tension, dipole moment, and conductivity of the electrospinning solution. (2) processing conditions (applied voltage, distance between tip-of-needle and collecting plate, extrusion flowrate, and relative humidity). These parameters were found to mostly affect the travel time and the overall forces applied on and experienced by the travelling jet. To elucidate compositional, morphological, and structural information about the formed solids, the electrospun nanofibers were characterized using thermogravimetric analysis (TGA), X-ray diffraction (XRD), scanning electron microscopy (SEM), energy dispersive X-ray spectroscopy (EDS), transmission electron microscopy (TEM), and high resolution TEM (HRTEM). It was found that significant changes in fiber diameter, size distribution, and morphology accompany changes in these parameters. By optimizing and regulating the electrospinning parameters (particularly,

22

polymer/metal concentration, solvent identity, and humidity), smooth, continuous, ultrafine and defect-free nanofibers were synthesized.

3.2 Experimental Methods

3.2.1 Materials and Electrospinning Synthesis

Polyvinylpyrrolidone (M.W. 1,300,000, 360,000, and 40, 000; Sigma-Aldrich), copper (II) nitrate trihydrate (Sigma Aldrich, 99%), N,N-Dimethylformamide (DMF; Sigma-Aldrich, anhydrous, 99.8%), ethyl alcohol (Sigma-Aldrich, 100%), and 1-propanol (Alfa Aesar, 99+%) were purchased and used without subsequent purification.

Polymer solutions were prepared by dissolving PVP (0.7-1.9 g) in solvent (methanol, ethanol, 1-propanol, DI water, or N,N-Dimethylformamide; 23 cm^3). The polymer solution was then vortexed (Fisher Scientific Digital Vortex Mixer) at 3000 rpm for 1 h until the polymer was completely dissolved. The solution was left to settle for 10 minutes, transferred to a beaker, and stirred for 0.5 h. The metal containing solution was prepared by dissolving copper (II) nitrate (0-1.3 g) in 10 cm^3 of DI water and stirring the solution for 0.5 h. The copper containing solution was then added dropwise to the polymer containing solution. The solution was stirred for 0.25 h, and then vortexed for 0.5 h at 3000 rpm.

The electrospinning solution was placed in a 10 mL syringe (BD 10 mL syringe with Luer Lok^{TM} tip) with a hypodermic needle (Monoject^{TM} Standard 30G x ¾"). The distance between the tip of the needle and a stainless-steel collecting plate covered with aluminum foil was between 14-22 inches. A Gamma High Voltage Research ES75 power supply was used to apply voltage (25-45 kV) while the polymer solution was extruded through the needle at a rate controlled by a syringe pump (0.25-2.0 cm^3 h^{-1}; Kent Scientific Genie Plus). Dry air was circulated inside a 3 m^3 chamber

at 0.1-5 cm^3 min^{-1} to control the relative humidity (20-60 ± 1%). All electrospinning was carried out at ambient temperature (294 K) and pressure (101 kPa). The collected fibers were thermally treated under air at 823 K for 4 h at a ramping rate of 2 K min^{-1}. To investigate the effect of parameters on the morphology of the electrospun fibers, the parameters mentioned in Section 3.1 were systematically varied. **Table 1** lists the ranges for the parameters probed in this study.

3.2.2 Characterization

The viscosity and conductivity of the electrospinning solutions were measured using CANNON-FENSKE viscometers (size: 50, 100 and 200) and an Oakton conductivity meter (CON 6). The synthesized nanofibers were characterized using a variety of techniques. Powder X-ray diffraction patterns were obtained on an X-ray diffractometer (JEOL JDX-3530 and Philips X-Pert) using Cu Kα radiation of 1.5410 Å to identify the CuO phases and average crystallite sizes. Thermogravimetric analysis was conducted on a Perkin Elmer TGA system. Alumina crucibles were used to hold the sample. Gas flow rates were set to 200 standard cm^3 min^{-1}. Heating occurred under air or argon (Matheson UHP Argon; 99.999% purity) at a ramping rate of 10 K min^{-1}. Scanning electron microscopy and energy dispersive X-ray spectrometry (SEM/EDS; NOVA 230 Nano SEM) were used to determine the morphology and elemental composition of the nanofibers. Both Low Vacuum Detector (LVD) and Everhart-Thornley Detector (ETD) detectors were used. The mean diameter and size distribution of the fibers were calculated from the SEM micrographs using ImageJ software (n = 250; where, n is the number of fibers that were measured and averaged). The FEI Titan 80-300 kV S/TEM was used to carry out the transmission electron microscopy (TEM) analysis. The TEM/HRTEM sample was prepared by drop casting an ethanolic dispersion of CuO nanofibers onto a carbon-coated Cu-grid.

Table 1. Experiment list and operating conditions for the electrospinning parameter study.

Effect of Electrospinning Parameters		Unit	Ranges Tested					
			#1	#2	#3	#4	#5	#6
Solution Properties:	Polymer Molecular Weight	g/mol	1,300,000	360,000	40,000	-	-	-
	Polymer Concentration	g/cm^3	0.021	0.027	0.033	0.039	0.045	0.058
	Metal Nitrate to Polymer Weight Ratio	wt %	0	25	50	75	100	-
	Solvent (Polymer Solvent)	-	Methanol	Ethanol	1-Propanol	Water	DMF	-
	Binary Solvent (Ethanol:Water Ratio)	vol %	100:0	70:30	50:50	30:70	0:100	-
	Ternary Solvent (Ethanol:Water:DMF Ratio)	vol %	70:0:30	70:15:15	70:22.5:7.5	50:0:50	50:25:25	-
Processing Conditions:	Applied Voltage	kV	25	30	35	40	45	-
	Distance between Tip-of-Needle and Collector	inches	14	16	18	20	22	-
	Extrusion Rate	cm^3/h	0.25	0.50	1.00	1.50	2.00	-
	Relative Humidity	%	20.0	30.0	40.0	50.0	60.0	-

3.3 Results and Discussion

3.3.1 Electrospinning of PVP-Cu(NO$_3$)$_2$ Fibers and Requirements for CuO Formation

A standard solution comprising of 1.3 g of PVP (MW=1,300,000), 1.3 g of copper nitrate trihydrate, 23 cm^3 of ethanol and 10 cm^3 of DI water was prepared following the method described in section 3.2.1. The standard solution was electrospun at: 30 kV (voltage), 1.0 cm^3 h^{-1} (extrusion rate), 18 inches (distance between tip-of-needle and collecting plate), and 20 % (relative humidity). These conditions were selected to be in the middle of our experimental capabilities. Electrospinning the standard solution at these parameters yielded PVP-Cu(NO$_3$)$_2$ nanofibers that were long, smooth, and defect-free, which were subsequently characterized.

XRD was used to identify the crystalline phases of the PVP-Cu(NO$_3$) nanofibers synthesized under the conditions described in the previous paragraph. **Figure 3** shows the XRD patterns of the PVP-Cu(NO$_3$)$_2$ nanofibers before and after thermal treatment at 823 K. Well defined diffraction peaks are absent from the pattern of the PVP-Cu(NO$_3$) nanofibers before thermal treatment (**Figure 3 (a)**) which indicates that these materials consist of amorphous polymer phases and Cu species that are either ionic or crystalline, with crystallites sizes too small to diffract X-rays. The XRD pattern of the nanofibers after thermal treatment (**Figure 3 (b)**) shows peaks at 2θ = 32.5 °, 35.6 °, 38.8 °, 48.8 °, 53.4 °, 58.1 °, 61.5 °, 65.9 °, and 68.1 °, which are consistent with the (110), (002), (200), (-202), (020), (202), (113), (311), and (220) planes of a single-phase monoclinic CuO, respectively.[97] The average crystal domain size of the CuO nanofibers calculated using Scherrer's equation based on the 35.6 °, 38.8 °, 48.8 °, 68.1 ° peaks are 55.4, 80.1, 73.5, and 65.8 nm, respectively. The mean values of a = 4.688 Å, b = 3.419 Å, c = 5.099 Å, β = 99.8 °, and α = γ = 89.7 ° are in good accord with the reported values (a = 4.6837 Å, b = 3.4226 Å, c = 5.1288 Å, β = 99.54 °, and α = γ = 90 °).[98]
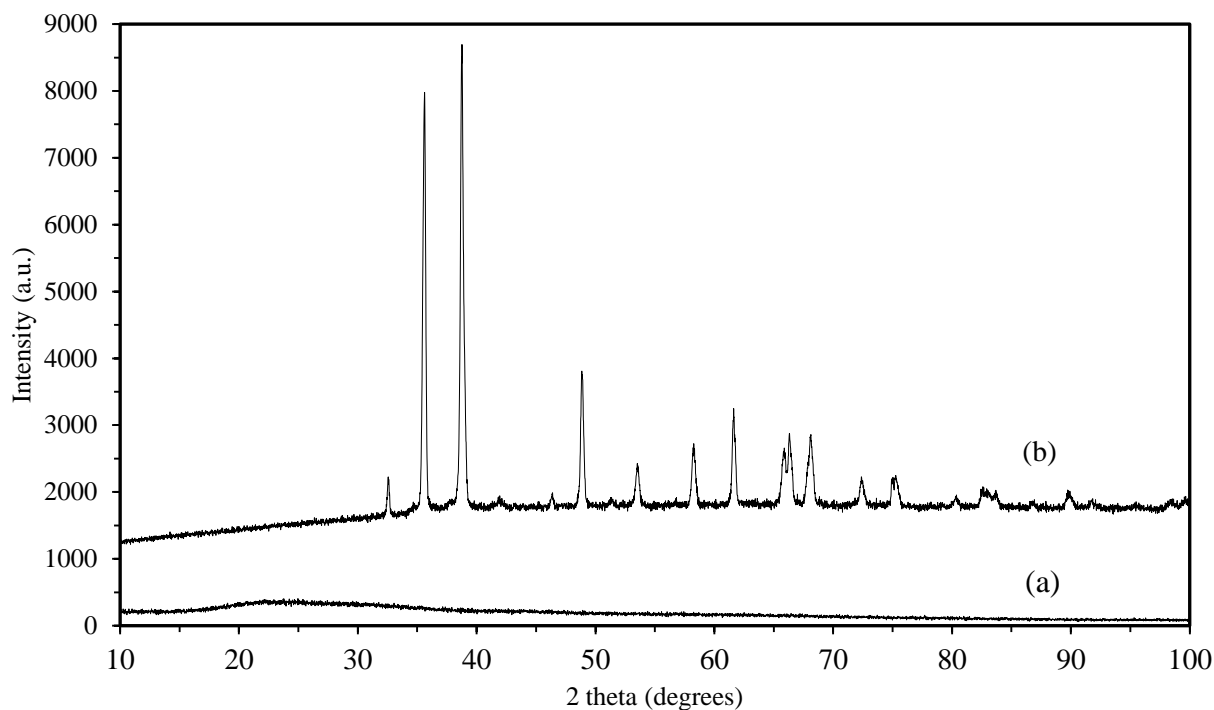
Figure 3. XRD patterns of (a) PVP-Cu(NO$_3$)$_2$ and (b) thermally treated CuO nanofibers at 823 K.

The XRD data indicate that thermal treatment in air is required for the formation of phase pure, monoclinic CuO from non-crystalline copper species that exist in PVP-Cu(NO$_3$)$_2$ nanofibers. No reaction of the copper (II) nitrate precursor occurs during the electrospinning process (as also supported by other characterization techniques discussed subsequently). The crystal sizes of the CuO nanofibers synthesized in this work via electrospinning were compared against other synthesis techniques reported in the literature. Prakash et al.[99] synthesized and characterized copper oxide nano-powders using a copper nitrate trihydrate precursor (similar to the precursor used in this work). The authors reported average crystal domain sizes of 70.47, 74.36, and 90.17 nm based on the following peaks 35.7°, 38.8°, 48.9°, respectively. Furthermore, Wongpisutpaisan et al.[100] synthesized copper oxide nanoparticles by a sonochemical process using a copper nitrate precursor, and the authors reported a CuO crystal domain size of approximately 80 nm at a reaction

time of 30 minutes. Compared to these fabrication techniques, electrospinning produces copper oxide particles and crystallites that are smaller in size.

SEM and EDS of the nanofibers were used to probe the effect of thermal treatment on nanofiber morphology (at the micron scale) and elemental composition. **Figure 4** shows the SEM image (5,000 and 20,000 times magnification) of the PVP-Cu(NO$_3$)$_2$ nanofibers before and after thermal treatment. **Figure 4 (a, b)** shows that the PVP-Cu(NO$_3$)$_2$ nanofibers consist of uniform, continuous cylinders that are free of micron-scale surface defects and have diameters of 261 ± 63 nm and lengths of up to several hundred micrometers. The SEM images of the thermally treated nanofibers (**Figure 4 (c, d)**) indicate a distinct change in morphology. Thermal treatment causes a transition in morphology from smooth, continuous cylindrical fibers to a network of fibers that appear to consist of segments. The reason for this morphological change is that at the initial stage of thermal treatment, the PVP molecules act as a template. As the fibers undergo thermal treatment, the PVP molecules escape along with the nitrate residuals leaving behind CuO nanoparticles, which tend to agglomerate due to Van der Waals forces.
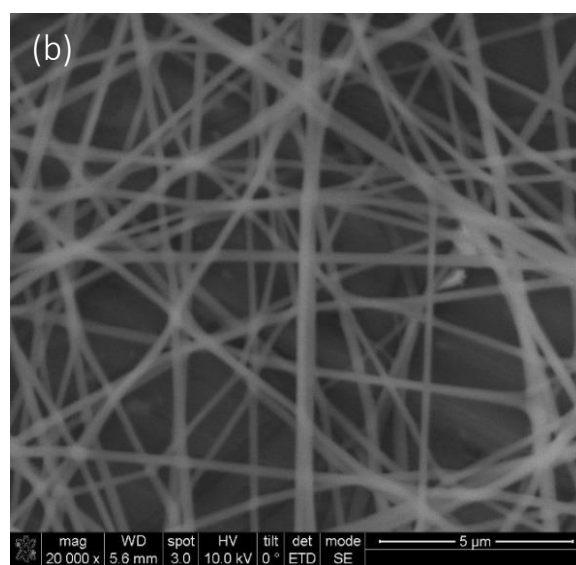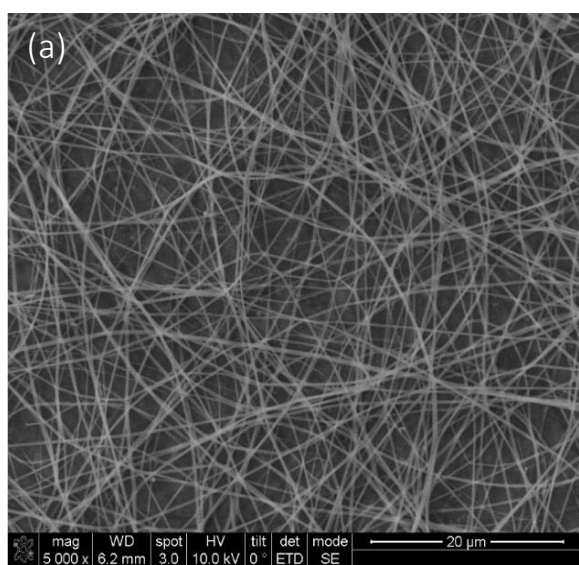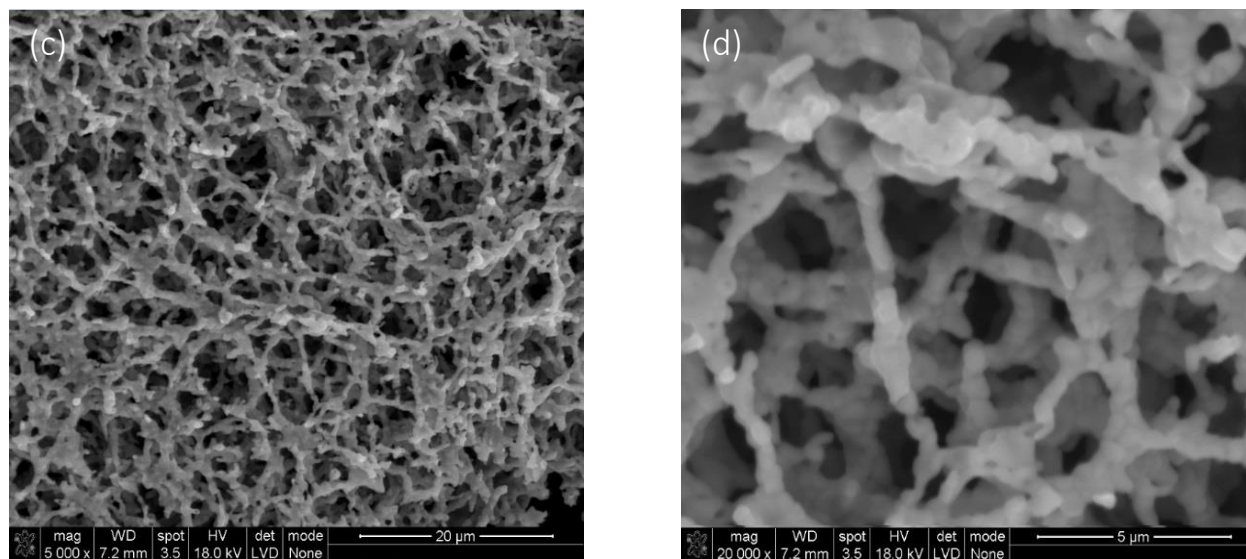
Figure 4. (a, b) SEM images of PVP-Cu(NO$_3$)$_2$ nanofibers and (c, d) CuO nanofibers after thermal treatment at 823 K.

Figure 5 shows the EDS spectrum of the thermally treated fibers. The Cu to O atomic ratio in the CuO nanofibers was 35.57 to 36.31%, respectively, which is close to 1:1, indicating the presence of pure copper (II) oxide. The C content in the EDS data was from the carbon tape used in the SEM analysis (**Figure 5**). The SEM and EDS data prove that the change in morphology upon thermal treatment is due to the removal of the PVP matrix and crystallization of CuO which causes a compositional transition from a polymeric-based nanofiber to a CuO nanofiber.
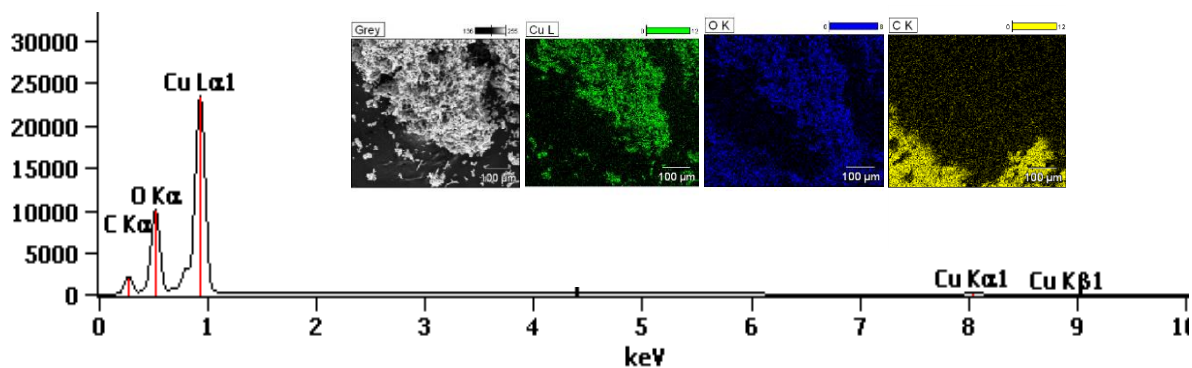
Figure 5. EDS spectra of CuO nanofibers after thermal treatment at 823 K.

TEM and HRTEM analysis were carried out to investigate the individual CuO grains of the nanofibers. **Figure 6 (a, b)** shows the TEM micrograph of an individual CuO nanofiber at different magnifications (0.2 µm and 100 nm scales). The CuO nanoparticles that comprise the nanofibers appear as multi-layered, agglomerated particles, with irregular shapes. The CuO fibers have widths of approximately 300-400 nm. The growth direction for the CuO nanofibers were determined from HRTEM as shown in **Figure 6**. The lattice images shown in **Figure 6 (c, d)** confirm the presence of CuO as highly crystalline grains. **Figure 6 (c)** shows the lattice spacing along the (200) plane for a CuO structure (indicated by white arrows) to be 2.33 Å, which is consistent with the d-spacing obtained from the XRD data (2.319 Å) for the same plane.
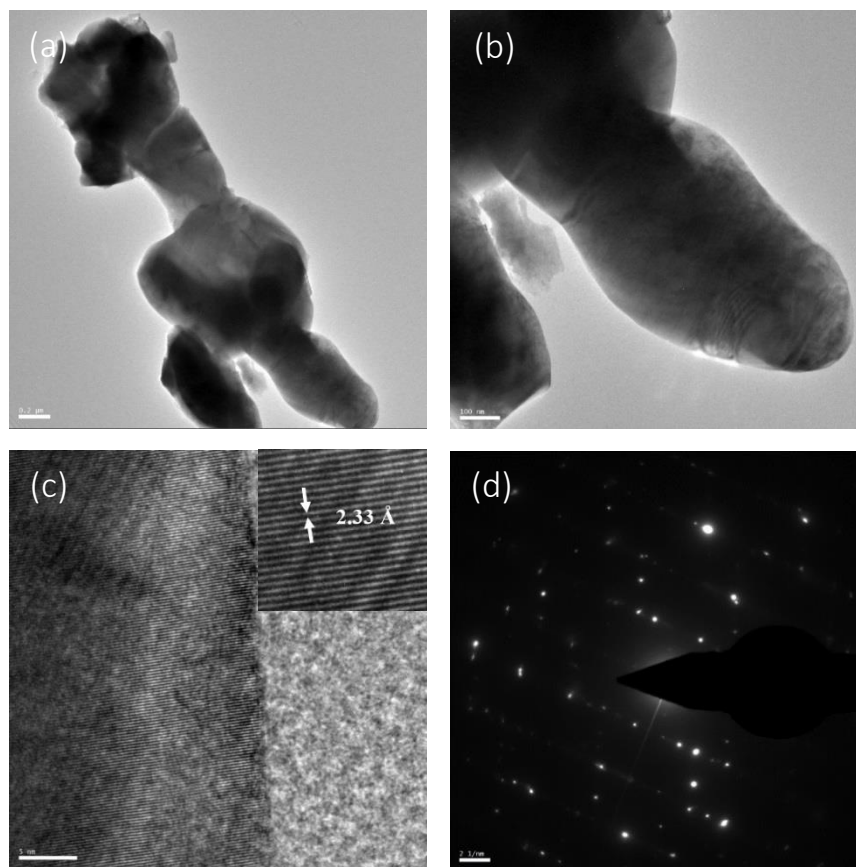
Figure 6. (a, b) TEM and (c, d) HRTEM of CuO nanofibers after thermal treatment at 823 K.

TGA experiments were conducted to quantify the extent of PVP removal during thermal treatment, and **Figure 7** shows the TGA curves of pure PVP and PVP-Cu(NO$_3$)$_2$ nanofibers. All nanofibers were decomposed under air and/or argon at a heating rate of 10 K min^{-1}. Nanofibers synthesized using only PVP decomposed under argon in two steps with a total weight loss of approximately 96%. Weight loss of 16% occurred from ambient temperature to 623 K and was followed by a 78% weight loss between 623 and 763 K. The first weight loss step can be attributed to the loss of volatile solvents, and the second weight loss can be attributed to the thermal decomposition and degradation of the PVP chains. It is clear from the TGA curve that the PVP matrix is removed at temperatures higher than 773 K and, thus, supports the conclusion of PVP removal from PVP-Cu(NO$_3$)$_2$ nanofibers during thermal treatment at 823 K.
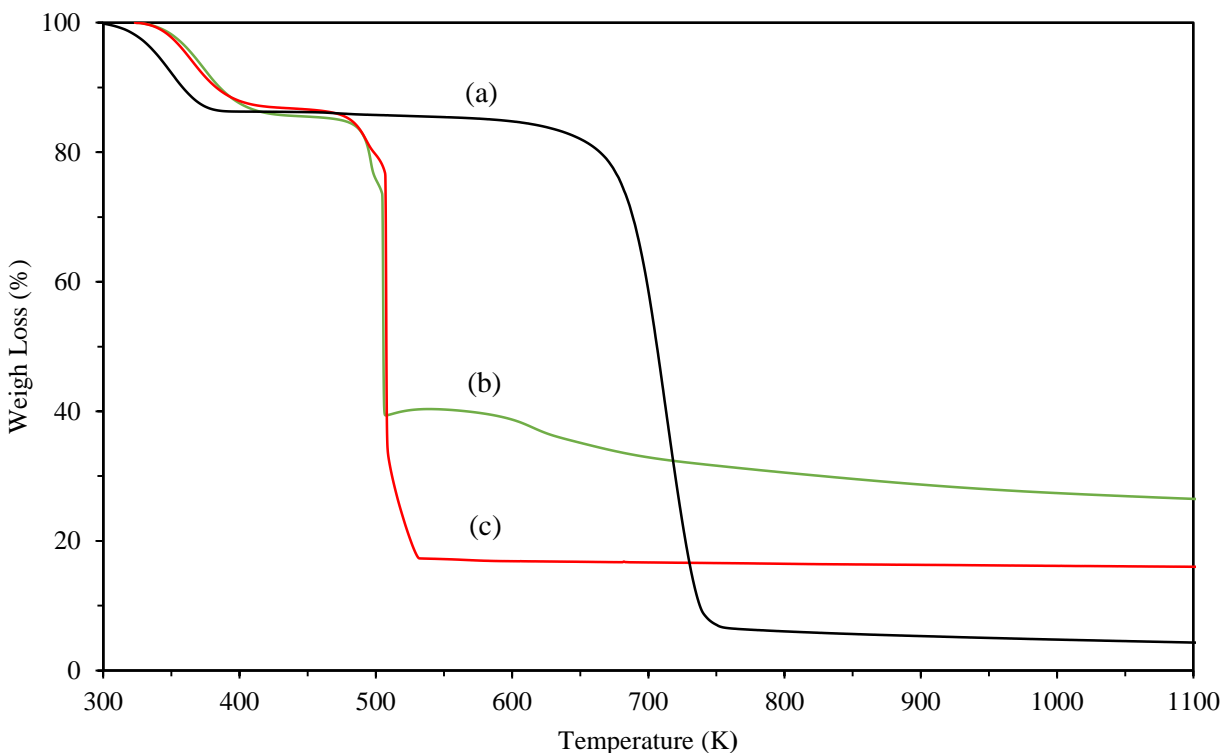
Figure 7. Thermogravimetric analysis (TGA) curves of (a) pure PVP nanofibers run under argon (black), (b) PVP-Cu(NO$_3$)$_2$ nanofibers run under argon (green), and (c) PVP-Cu(NO$_3$)$_2$ nanofibers run under air (red).

Figure 7 also shows the decomposition of the PVP-Cu(NO$_3$)$_2$ nanofibers under air and argon. More weight loss was observed under air, and this can be attributed to the increased extent of PVP and copper nitrate decomposition in the presence of oxygen. Also, it is possible that copper (I) oxide formed under argon during the decomposition of the nitrate group due to the lack of oxygen, thus, also explaining the weight loss differences observed under air and argon. As the TGA data shows, the decomposition of PVP occurs at lower temperatures in the PVP-Cu(NO$_3$)$_2$ fibers (~475 K) than the pure PVP fibers (~640 K) indicating the effect of copper nitrate, which weakens the bonds within the PVP chains, and the impact of the nitrate anions, which act as an oxidant to combust PVP. The degradation profiles of the PVP-Cu(NO$_3$)$_2$ nanofibers also exhibited a two-stage weight loss process, with a total weight loss of 73% and 84% in argon and air, respectively. The total weight loss in air is consistent with the complete conversion of Cu(NO$_3$)$_2$ to CuO. Thus, the first stage mass loss can be attributed to the loss of volatile solvents, and the second can be attributed to the decomposition of PVP and copper nitrate and formation of CuO. These TGA results are in agreement with the results from the other characterization techniques described in this section. Each of these techniques provide quantitative evidence of the removal of the majority of PVP, decomposition of copper nitrate, and formation of CuO during thermal treatment of PVP-Cu(NO$_3$)$_2$ nanofibers in air at 823K.

3.3.2 Tuning Nanofiber Morphology by Changing Synthesis Conditions

Due to the flexibility and adaptability of electrospinning, the materials that can be synthesized using this method and the applications in which they can be applied to are wide in scope. In fact, the electrospinning process can be modified to yield fibers with different properties (e.g., dimensions, structures, morphology, porosity, etc.). Therefore, understanding how the fibers change, specifically, on a morphological-level with respect to these electrospinning parameters, is

critical. Synthesizing defect-free, ultrafine fibers requires the process parameters to be within a specified and an optimized range. If the synthesis and spinning parameters are outside this range, even slightly, one of two things occur: (1) highly-defective fibers are formed, which may contain different types, shapes, and sizes of structural defects, or (2) no electrospinning happens and instead electrospraying takes place, which results in the formation of single droplets rather than continuous fibers. Section 3.3.1 described the successful synthesis and detailed characterization of PVP-Cu(NO$_3$)$_2$ and CuO-based nanofibers. To understand the effects of changing process parameters on the dimensionality and morphology of these nanofibers, PVP-Cu(NO$_3$)$_2$ nanofibers were synthesized at various conditions (**Table 1**), and the results of these studies are reported and discussed in the following sections.

As shown in chapter 2, the properties of the polymer-metal solution (e.g., viscosity, conductivity, dielectric constant, and surface tension) play a pivotal role in the electrospinning process and the resultant fiber diameter and fiber morphology for polymer only systems. These properties were controlled by changing the viscosity of the solutions (polymer identity and molecular weight, polymer concentration in solution, and solvent matrix), and/or the conductivity of the solutions (metal precursor identity and concentration). In this work, these solution parameters were systematically varied to examine their effects on metal-polymer nanofibers.

As in the case of solution properties, the electrospinning processing conditions can also influence the morphology of fibers for polymer systems because they affect the overall forces applied on and experienced by the jet. As shown in the literature review, the strength (or magnitude) of these effects is dependent on the electrospinning solution being examined and the specific value of the processing parameter. The processing conditions studied in this work were:

voltage supplied, extrusion rate, distance between the tip-of-needle and collecting plate, and humidity.

3.3.2.1 Altering Solution Viscosity via Polymer Molecular Weight and Concentration

One of the key factors that influences the properties of the synthesized nanofibers is the molecular weight of the polymer. As discussed in chapter 2, the molecular weight of a polymer is one indicator of the extent of chain entanglements present in the electrospinning solution, which ultimately influences viscosity. Changes in viscosity have been shown to strongly affect the morphology of electrospun fibers for various polymer systems.[101,102]

In this work, three molecular weights of PVP (1,300,000; 360,000; and 40,000) were used to probe the effect of polymer molecular weight on PVP-$Cu(NO_3)_2$ nanofibers diameter and morphology. In these experiments, three electrospinning solutions were prepared using 1.3 g of PVP at each molecular weight. The other electrospinning parameters were the same as those described in section 3.3.1. **Table 2** shows the viscosity measurements at room temperature (298 K) for PVP MW=1,300,000 (56.23 cP), MW=360,000 (44.79 cP) and MW=40,000 (6.23 cP), indicating the effect of molecular weight on viscosity. The conductivity of the three solutions is also shown in **Table 2**. Despite showing a strong influence on viscosity, changes in molecular weight did not have a significant impact on conductivity as the recorded conductivity values were 16.66 mS cm^{-1} for PVP MW=1,300,000, 1 6.32 mS cm^{-1} for PVP MW=360,000, and 15.96 mS cm^{-1} for PVP MW=40,000.

Table 2. Solution properties (viscosity and conductivity), fiber properties (SEM images, average diameter, standard deviation and morphology), and structural defects (type and average diameter) of PVP-Cu(NO$_3$)$_2$ fibers prepared using three molecular weights of PVP. Each electrospinning solution was prepared using 1.3 g of each polymer, 1.3 g of copper nitrate, 23 cm^3 of ethanol, and 10 cm^3 of DI water. Electrospinning was operated at 30 kV, 1.0 cm^3 hr^{-1}, 18 inches, and 20% relative humidity.
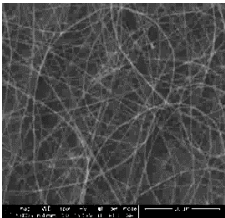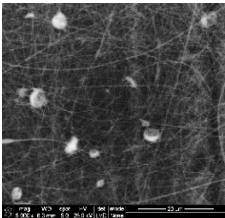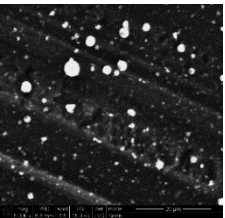
		PVP Molecular Weight (g/mol)		
		1,300,000	360,000	40,000
Solution Properties:	Dynamic Viscosity (cP)	56.23	44.79	6.23
	Conductivity (mS/cm)	16.66	16.32	15.96
Fiber Appearance:	SEM			
	Average Diameter (nm)	261.33	168.04	-
	1 Standard Deviation (nm)	63.01	38.08	-
	Morphology	cylindrical	cylindrical	discrete droplets
Structural Defects:	Type of Defect	no defects	spherical beads	-
	Diameter of Beads (µm)	-	3.9	-

Table 2 shows the SEM micrographs, average diameter as well as standard deviation of the PVP-Cu(NO$_3$)$_2$ nanofibers. The average diameter and standard deviation of the formed fibers were measured using ImageJ software (n=250). The trend observed from the SEM micrographs revealed that molecular weight had an instrumental effect on fiber diameter (average and standard deviation) as well as on bead formation. Specifically, when the molecular weight of the polymer was reduced (thus, viscosity), the nanofibers average diameter decreased. The PVP (MW=1,300,000) solution resulted in the formation of fibers that had an average diameter and standard deviation of 277 ± 79 nm whereas the PVP (MW=360,000) solution resulted in the formation of fibers that were 168 ± 38 nm (**Table 2**). The lower molecular weight solution, PVP (MW=40,000), did not form any fibers, however, as this solution's viscosity (6.23 cP) was too low to electrospin. The results in this study confirm the role of polymer chain entanglements on electrospinning even for solutions containing high metal concentrations. Reducing these entanglements by means of reducing the molecular weight (and thus viscosity) is necessary for obtaining ultrathin fibers. However, by significantly reducing the molecular weight of the polymer, the chain entanglements are not able to maintain a continuous jet and as a result discrete droplets form. **Figure 8** shows the diameter distribution of the three materials formed. When the molecular weight of PVP was reduced from 1,300,000 to 360,000 it was observed that the diameter distribution of the fibers was lowered.
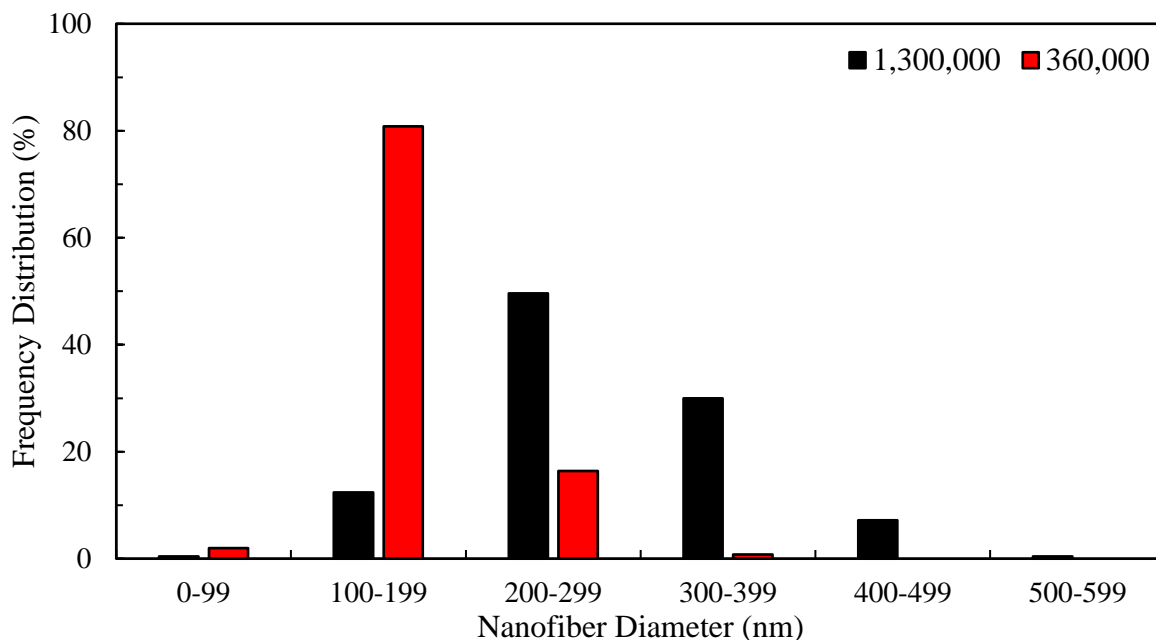
Figure 8. Diameter distribution of PVP-Cu(NO$_3$)$_2$ nanofibers at different PVP (M.W.=1,300,000 and 360,000) molecular weights. PVP (M.W.= 40,000) did not form any fibers (not shown). Each electrospinning solution was prepared by mixing 1.3 g of each polymer, 1.3 g of copper nitrate, 23 cm^3 of ethanol, and 10 cm^3 of DI water. Electrospinning was conducted at 30 kV, 1 cm^3 hr^{-1}, 18 inches, and 20% relative humidity.

In this work, one by-product of altering the molecular weight of the polymer that was observed in the synthesized fibers under SEM was structural defects. In this set of experiments, structural defects with diameters in the micro-range (1-4 µm) formed when the molecular weight of PVP was lowered from 1,300,000 to 360,000 (**Table 2**). Specifically, the solution that contained PVP (MW=360,0000) had both spindle-like and spherical defects. Structural defects of that magnitude may deleteriously impact the reactivity and/or performance of the formed fibers in certain applications, and thus, avoiding their formation may be critical for the fibers to work.

Just like in the case of polymeric fibers, the data here suggests that metal-polymer fibers are also prone to the formation of structural defects. When the polymer's viscosity is reduced by means of reducing its molecular weight, fewer chain entanglements are present in the solution,

thus, allowing surface tension to influence the electrospinning jet. Therefore, when working with lower molecular weight polymers, higher concentrations of the polymer are generally required to increase viscosity and stabilize the electrically charged jet. Basically, increasing the concentration of the polymer compensates for the low molecular weight by increasing the number of polymer chain entanglements.

Although the choice of molecular weight was shown to significantly influence viscosity and thus fiber diameter and morphology, concentration is another way to change a solution's viscosity and spinnibility. To examine the effect of PVP (MW=1,300,000) concentration on the morphology of PVP-Cu(NO$_3$)$_2$ nanofibers, six different masses of PVP (0.7, 0.9, 1.1, 1.3, 1.5, and 1.9 g) were added to the electrospinning solution to yield solutions with the following polymer concentrations: 0.212, 0.0273, 0.0333, 0.0394, 0.0455, and 0.0576 g cm^{-3}, respectively. Additionally, appropriate masses of copper nitrate were added to each solution to so that the PVP to copper nitrate weight ratio remained at 1:1 in all the electrospinning solutions. The other electrospinning parameters were the same as those described in section 3.3.1.

Figure 9 shows the measured dynamic viscosity values of the six solutions. The trend observed in **Figure 9** reveals that viscosity increases exponentially as a function of PVP (MW=1,300,000) concentration (y = $9.488e^{44.56x}$ with a coefficient of determination (R^2) = 0.996, where "y" is viscosity (cP) and "x" is PVP concentration (g cm^{-3})). Gomes et al.[103] investigated the synthesis of polyacrylonitrile (PAN) at different processing conditions and reported a similar exponential trend for viscosity as a function of polymer concentration for PAN (1-8 %) in DMF. In addition to the viscosity changes, increasing the PVP concentration in the electrospinning solution resulted in changes in conductivity (because the metal concentration in this section was also varied to maintain a weight ratio of 1:1 between the polymer and copper nitrate). When plotted

(not shown), conductivity increased linearly as a function of PVP concentration, with a coefficient of determination equal to 0.995. The conductivity values measured experimentally for the six solutions were: 11.21 mS cm^{-1} (0.012 g cm^{-3}), 12.32 mS cm^{-1} (0.0273 g cm^{-3}), 14.49 mS cm^{-1} (0.0333 g cm^{-3}), 16.66 mS cm^{-1} (0.0394 g cm^{-3}), 18.00 mS cm^{-1} (0.0455 g cm^{-3}), and 22.10 mS cm^{-1} (0.0576 g cm^{-3}) (**Table 3**).
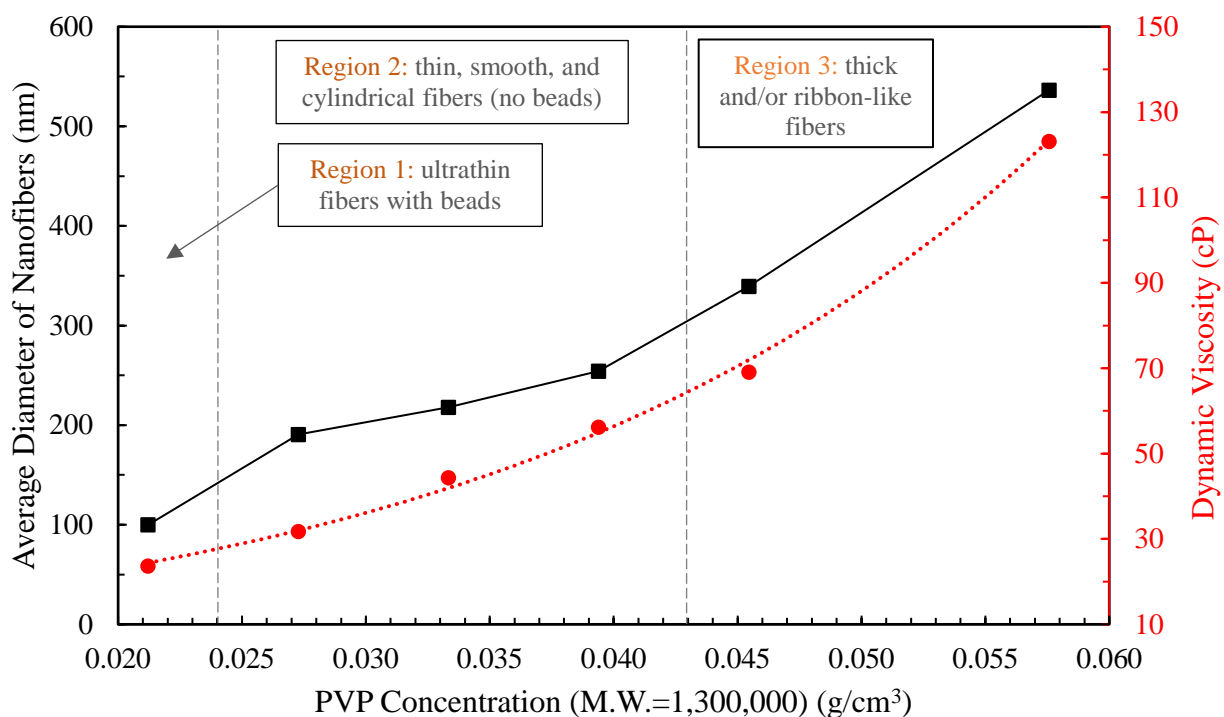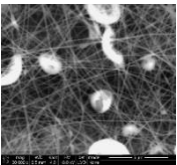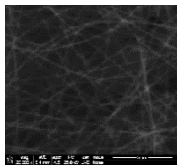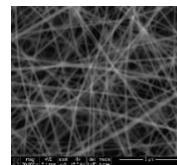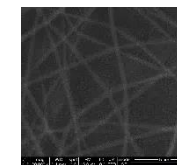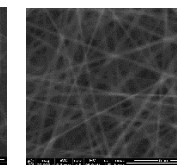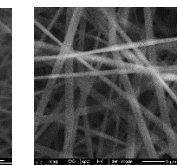
Figure 9. Dynamic viscosity of the electrospinning solutions (fitted using an exponential curve) and average diameter of PVP-Cu(NO$_3$)$_2$ nanofibers at five concentrations of PVP (MW=1,300,000). Each electrospinning solution was prepared using an appropriate amount of PVP and copper nitrate to maintain a polymer to copper nitrate weight ratio of 1:1, 23 cm^3 of ethanol, and 10 cm^3 of DI water. Electrospinning was conducted at 30 kV, 1.0 cm^3 hr^{-1}, 18 inches, and 20% relative humidity.

Table 3 shows the SEM images, average diameters and standard deviations of the synthesized PVP-Cu(NO$_3$)$_2$ nanofibers. The data obtained reveals a strong correlation between PVP (MW=1,300,000) concentration and average nanofiber diameter (**Figure 9**). When the PVP

concentration was 0.0212 g cm^{-3}, the PVP-Cu(NO$_3$)$_2$ nanofibers had an average diameter of 99 nm (**Table 3**). Indeed, the electrospinning of this solution (0.0212 g cm^{-3}) resulted in the formation of ultrathin nanofibers because of the relatively low viscosity of the solution (23.7 cP). Increasing the polymer concentration increases the viscosity by increasing the polymer chain entanglements.[104,105] Therefore, when the PVP concentration was increased from 0.0212 to 0.0273 g cm^{-3}, the viscosity increased accordingly from 23.70 to 31.75 cP, yielding fibers that were 190 nm (**Table 3**). This trend was observed for all six concentrations that were tested, as shown in **Figure 9**, and agrees with the literature.[58]

Based on the SEM micrographs shown in **Table 3**, **Figure 9** can divided into three distinct regions: region 1 (0.0212 g cm^{-3}), region 2 (0.0273, 0.0333, and 0.0394 g cm^{-3}) and region 3 (0.0455 and 0.0576 g cm^{-3}). Region 1 comprised of PVP-Cu(NO$_3$)$_2$ fibers that were ultrathin, but contained structural defects in the form of spherical or spindle-like beads. The nanofibers in this region were formed from a solution that had a low viscosity (23.7 cP) (**Table 3**). It's been reported in the electrospinning literature (for polymer only nanofibers) that when viscosity is marginally increased above the critical value necessary for electrospinning, structurally defective fibers tend to form.[106,107] These defects form because of capillary instability, which is caused by the reduction in the overall electrical charges experienced by the jet (due to low viscosity).[50] This reduction in electric charge causes the liquid jet to effectively separate, forming droplets. When these droplets dry and solidify, they form beads. As viscosity increases, a gradual change occurs to the shape of these structural defects as they start to change from spherical to spindle-like until they completely disappear and smooth fibers are obtained.[108]

Table 3. Solution properties (viscosity and conductivity), fiber properties (SEM micrographs, average diameter, standard deviation and morphology), and structural defects (type and average diameter) of PVP-Cu(NO$_3$)$_2$ fibers prepared using different PVP (MW=1,300,000) concentrations. Each electrospinning solution was prepared using an appropriate amount of PVP and copper nitrate to maintain a metal nitrate to PVP weight ratio of 1:1, 23 cm^3 of ethanol, and 10 cm^3 of DI water. Electrospinning was conducted at 30 kV, 1.0 cm^3 hr^{-1}, 18 inches, and 20% relative humidity.

		PVP Concentration (MW=1,300,000) (g/cm^3)					
		0.0212	0.0273	0.0333	0.0394	0.0455	0.0576
Solution Properties:	Dynamic Viscosity (cP)	23.7	31.75	44.35	56.23	69.06	123.17
	Conductivity (mS/cm)	11.21	12.32	14.49	16.66	18.00	22.10
Fiber Appearance:	SEM						
	Average Diameter (nm)	99.86	190.50	217.88	254.22	339.44	536.47
	1 Standard Deviation (nm)	25.02	79.99	56.75	55.14	80.55	128.63
	Morphology	cylindrical	cylindrical	cylindrical	cylindrical	cylindrical and ribbon-like	ribbon-like
Structural Defects:	Type of Defect	spherical beads	no defects	no defects	no defects	no defects	no defects
	Diameter of Beads (µm)	3.8	-	-	-	-	-

Region 2 in **Figure 9** comprised of PVP-Cu(NO$_3$)$_2$ fibers that were continuous, cylindrical, smooth, and free of surface defects. The fibers in this range were electrospun from solutions that had viscosities that are significantly above the critical viscosity value necessary for electrospinning PVP and copper nitrate with water and ethanol as co-solvents. Because the viscosity was adequate, enough chain entanglements of the polymer were present in the solution. Increasing the PVP concentration in this region (region 2) from 0.0273 to 0.0333 to 0.0394 g cm^{-3} resulted in increasing the viscosity from 12.32 to 14.49 to 16.66 cP, respectively (**Figure 9**). As the viscosity increased, thicker fibers formed as increasing the polymer concentration improved the intermolecular interactions between the polymer molecules and increased the solution's resistance to stretching.

Region 3 comprised of fibers that not only had large diameters, but also ribbon-like structures (**Figure 9**). The fibers in this region were prepared from solutions that contained high PVP concentrations (0.0455 and 0.0576 g cm^{-3}) and as such, high viscosities (69.06 and 123.17 cP) (**Table 3**). Ribbon-like structures occur because at high polymer concentrations, the skin of the fibers solidify before all solvent molecules diffuse through. As the evaporation process proceeds, the skin of the fibers form hollow tubes, which later collapse forming ribbon-like structures (instead of circular cross section tubes).[50] The results in **Figure 9** demonstrate the importance of maintaining an optimal polymer concentration (region 2) to allow the electrospinning solvent ample time to evaporate to form smooth and cylindrical metal-polymer fibers, with minimal defects.

In addition to its influence on diameter size, polymer concentration affects the standard deviation and distribution of the formed nanofibers. Diameter distribution is a key and a real challenge in the synthesis of nanofibers via electrospinning because electrospun nanofibers are

rarely uniform.[21] Synthesizing fibers with a wide distribution could considerably limit the application and use of these fibers, especially in fields like filtration, where a narrow distribution is required. Therefore, the effect of viscosity (by means of varying the polymer concentration) on diameter distribution is reported. **Figure 10** shows the diameter distribution of all the PVP-Cu(NO$_3$)$_2$ nanofibers that were electrospun. The results show that in order to obtain a narrow fiber diameter distribution, lower polymer concentrations (viscosity) are required.
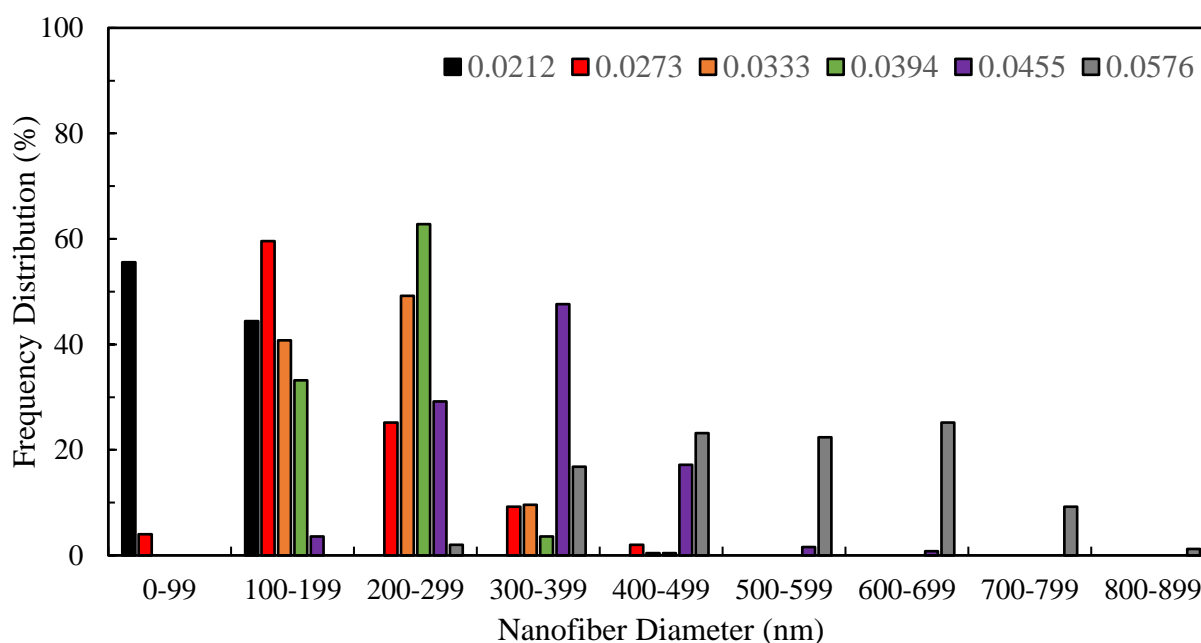
Figure 10. Diameter distribution of PVP-Cu(NO$_3$)$_2$ nanofibers at six different PVP (MW=1,300,000) concentrations. Each solution was prepared using an appropriate amount of PVP and copper nitrate to maintain a polymer to metal nitrate weight ratio of 1:1, 23 cm^3 of ethanol, and 10 cm^3 of DI water. Electrospinning was conducted at 30 kV, 1 cm3 hr^{-1}, 18 inches, and 20% relative humidity.

3.3.2.2 Controlling Solution Conductivity via Metal Concentration

The previous section demonstrated that PVP-Cu(NO$_3$)$_2$ nanofibers properties (e.g., diameter and morphology) were sensitive to the viscosity of the electrospinning solution. Both polymer molecular weight and polymer concentration were found to strongly influence metal-

polymer fiber diameter and morphology. In this section, the effect of conductivity (or simply, metal concentration) is investigated by changing the weight ratio of copper nitrate to PVP. Of all the electrospinning parameters that were reported in the literature, the effect of metal to polymer ratio (or simply, metal concentration) was the least researched. This is due to the fact that the synthesis of metal-polymer fibers or metal oxide fibers is a relatively new area of research in electrospinning.

To probe the metal concentration effect on fiber diameter and morphology, five solutions were prepared in which 1.3 g (0.0394 g cm^{-3}) of PVP (MW=1,300,000) was added while the weight ratio of metal nitrate to PVP was changed: 0% (0 g), 25% (0.325 g), 50% (0.65 g), 75% (0.975 g), and 100% (1.3 g). In this work, more emphasis was placed on the lower metal loadings (since the prior art shows that lower metal concentrations correspond to thinner and rougher fibers).[25] Thin and rough fibers are generally desired especially in catalysis-based applications where rough fibers are believed to be more reactive. As in the previous section, electrospinning was conducted under the conditions described in section 3.3.1. In this section, the PVP-Cu(NO$_3$)$_2$ nanofibers were collected for 12 h before they were thermally treated at 823 K for 4 h to form CuO nanofibers.

Table 4 lists the viscosity and conductivity measurements of the five solutions. The results shown in **Table 4** indicate that adding copper nitrate to a PVP-containing solution does not significantly alter viscosity, as the viscosity of the 0% and 100% solutions were 52.76 to 56.23 cP, respectively (**Table 4**). However, as **Figure 11** shows, conductivity increased steadily as a function of metal concentration, as adding more metal effectively increased the number of ions present in the electrospinning solution. The solution that contained PVP only (0%), for instance, had a conductivity of 0.023 mS cm^{-1} while the solution with 100% metal nitrate to PVP ratio had a conductivity of 16.66 mS cm^{-1}.

Table 4. Solution properties (viscosity and conductivity) and fiber properties (SEM micrographs, average diameter, standard deviation, and morphology) of PVP-Cu(NO$_3$)$_2$ nanofibers and CuO fibers prepared using different copper nitrate to PVP (MW=1,300,000) weight ratios. Each electrospinning solution was prepared using 1.3 g of PVP, an appropriate amount copper nitrate to yield the desired metal nitrate to PVP ratio, 23 cm^3 of ethanol, and 10 cm^3 of DI water. Electrospinning was conducted at 30 kV, 1.0 cm^3 hr^{-1}, 18 inches, and 20% relative humidity. CuO fibers formed after the PVP-Cu(NO$_3$)$_2$ fibers were subjected to thermal treatment in air at 823 K and 101 kPa for 4 h.
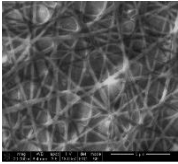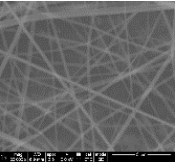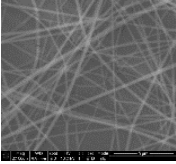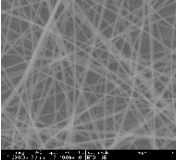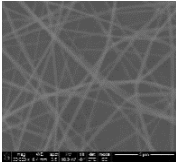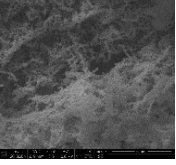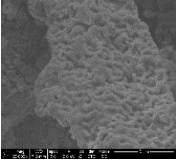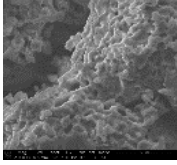
		Copper Nitrate to PVP (MW=1,300,000) Weight Ratio (%)				
		0%	25%	50%	75%	100%
Solution Properties:	Dynamic Viscosity (cP)	52.76	-	-	-	56.23
	Conductivity (mS/cm)	0.023	4.79	9.13	12.70	16.66
PVP-Cu(NO$_3$)$_2$ Fiber Appearance:	SEM					
	Average Diameter (nm)	288.61	168.55	175.32	199.9	261.33
	1 Standard Deviation (nm)	66.49	47.29	56.88	57.11	63.01
	Morphology	fused fibers	cylindrical	cylindrical	cylindrical	cylindrical
CuO Fiber Appearance:	SEM	polymer decomposes				
	Average Diameter (nm)	-	142.64	257.37	394.73	433.43
	1 Standard Deviation (nm)	-	40.18	61.85	128.43	172.76
	Morphology	-	segmented	segmented	segmented	segmented

Figure 11 shows the average diameter of PVP-Cu(NO$_3$)$_2$ and CuO nanofibers. The reported average diameters, standard deviations, and distributions were found using ImageJ software (n=250). **Table 4** shows the SEM images (20,000 times magnification) of the nanofibers before and after thermal treatment. When no metal was added to the electrospinning solution (0%), the PVP-Cu(NO$_3$)$_2$ fibers had a fused (i.e., crosslinked) structure, with an average diameter of 288 ± 66 nm. Crosslinking occurred due to inadequate drying of the fibers during the electrospinning process. The low conductivity (0.023 mS cm^{-1}) of the electrospinning solution is responsible for the inadequate drying, and thus, the crosslinked structure (**Table 4**). When the metal concentration is increased by increasing the copper nitrate to PVP ratio from 0 to 25%, the conductivity increased from 0.023 to 4.79 mS cm^{-1}, respectively (**Table 4**). This increase in conductivity caused the average diameter to drop from 288 ± 66 nm (0%) to 168 ± 47 nm (25%) (**Table 4**). Fundamentally, conductivity is related to the number of charges carried by an electrospinning jet.[109,110] Since electrospinning requires the charges on the surface of the jet to repulse to start the stretching process of the solution, having more charges (by increasing the number of copper and nitrate ions present in the solution) increases the stretching of the jet, which results in thinner fibers. These findings agree with the work of Qiu et al.[111] in which they synthesized nickel and zinc oxide nanofibers at two metal concentrations and observed a decrease in diameter size when the metal nitrate concentration was lowered.

Interestingly, in this work, as the metal content was increased from 25 to 50 to 75%, the average fiber diameter increased from 168 ± 47 nm to 175 ± 56 nm to 199 ± 57 nm, respectively, instead of decreasing (**Figure 11**). It's likely that this moderate increase in PVP-Cu(NO$_3$)$_2$ diameter going from 25 to 50 to 75% (copper nitrate to PVP ratio) was due to the competition between viscosity, which slightly increases with metal concentration and encourages the formation

of thicker fibers, and conductivity, which increases with metal concentration and encourages the formation of thinner fibers. **Figure 11** also shows that increasing the copper nitrate to PVP ratio from 3:4 to 1:1 resulted in a significant increase in fiber diameter (261 ± 63 nm). It's likely that at low copper nitrate to PVP ratios (below 75%), the copper nitrate ions deposit mostly on the surface and within the structure of the nanofiber. At these low concentrations, there is no significant crowding effect or lateral interactions between the metal ions, and as such, the fiber diameters do not significantly change. However, when the metal nitrate to PVP ratio is 100% (or greater), the interactions increase, and the fiber structure becomes considerably packed and this results in the formation of thicker fibers.
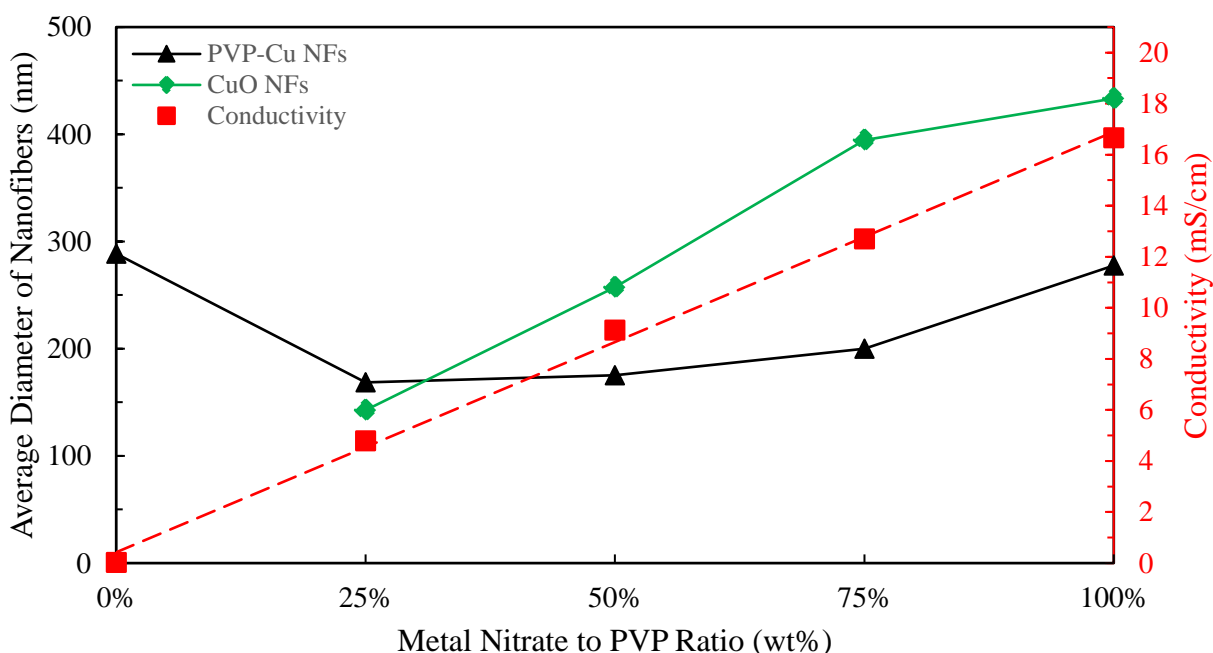
Figure 11. Conductivity of electrospinning solutions (fitted using a linear line) and average diameter of PVP-Cu(NO$_3$)$_2$ and CuO nanofibers (before and after thermal treatment at 823 K and 101 kPa for 4 h) at five copper nitrate to PVP (MW=1,300,000) weight ratios. Each electrospinning solution was prepared using 1.3 g of PVP, an appropriate amount copper nitrate to yield the desired metal nitrate to PVP ratio, 23 cm^3 of ethanol, and 10 cm^3 of DI water. Electrospinning was conducted at 30 kV, 1.0 cm^3 hr^{-1}, 18 inches, and 20% relative humidity.

Figure 12 shows the diameter distribution of the five PVP-Cu(NO$_3$)$_2$ fibers discussed in this section. It was found that increasing the metal concentration from 25% to 100% resulted in a slight increase in the PVP-Cu(NO$_3$)$_2$ diameter distribution, which is caused by viscosity. Increasing the metal concentration results in the formation of slightly more viscous solutions and bigger polymer-metal droplets at the tip of the needle. When a more viscous solution is electrospun, the droplet forms a jet that has a greater width (diameter) to start with. Since all solutions were subjected to similar forces (e.g., identical electrospinning conditions), the smaller droplets (and thus jets) resulted in the formation of thinner fibers with the narrower distributions.
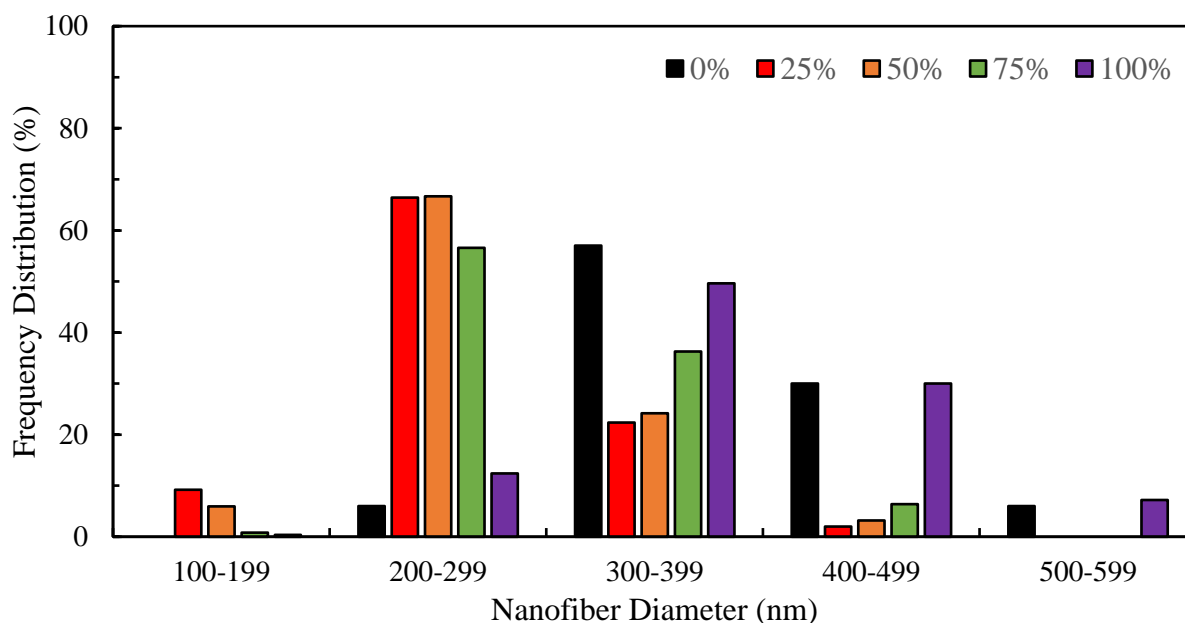
Figure 12. Diameter distribution of PVP-Cu(NO$_3$)$_2$ nanofibers (before thermal treatment) prepared using different copper nitrate to PVP weight ratios (0, 25, 50, 75, 100 %). Each electrospinning solution was prepared using 1.3 g of PVP, an appropriate amount copper nitrate to yield the desired metal nitrate to PVP ratio, 23 cm^3 of ethanol, and 10 cm^3 of DI water. Electrospinning was conducted at 30 kV, 1.0 cm^3 hr^{-1}, 18 inches, and 20% relative humidity.

Even though the effect of metal nitrate to PVP on nanofiber diameter was modest prior to thermal treatment, as shown in **Figure 11**, the fibers after thermal treatment in air at 823 K and

101 kPa for 4 h showed inordinate sensitivity to this electrospinning synthesis parameter. In fact, the CuO fiber diameter increased almost linearly between 25 to 75% (metal nitrate to PVP weight ratio), changing from 142 ± 40 to 394 ± 128 nm, respectively (**Table 4**). Also, the gap between the nanofiber diameter before and after thermal treatment was found to be larger at the higher metal nitrate to PVP ratios than at the lower ones, reaching 433 nm (after thermal treatment) compared to 261 nm (before thermal treatment) at the 100% case compared to 142 nm (after thermal treatment) and 168 nm (before thermal treatment) at 25%. **Table 4** shows the SEM images of CuO fibers after thermal treatment. The SEM images reveal that the CuO fibers appear as short and segmented particles. The PVP fibers that contained no metal (0%) burnt off completely when thermally treated under air at 823 K.

Figure 13 shows the diameter distribution of the CuO fibers. The results demonstrate the importance of lowering the metal nitrate concentration in the electrospinning solution. By lowering the copper nitrate concentration, the formed CuO fibers in this work not only had smaller average diameters, but also smaller distributions. On the other hand, CuO fibers prepared from solutions that contained higher copper nitrate concentrations suffered from particle agglomeration (because the fibrous structures were more overpacked and also because CuO particles tend to agglomerate when thermally treated at elevated temperatures).[112] Moreover, it was found in this work that the thermal treatment of a thick layer of PVP-Cu(NO$_3$)$_2$ nanofibers (after 12 hours of electrospinning as shown in **Table 4**) as opposed to a thin layer (after 1 hour of electrospinning as shown in **Figure 4 (b)**) for the same electrospinning solution (1:1 copper nitrate to PVP ratio) encouraged the formation of agglomerated CuO particles, which affected the nanofibers morphology (overall void space and macro-porosity).

49
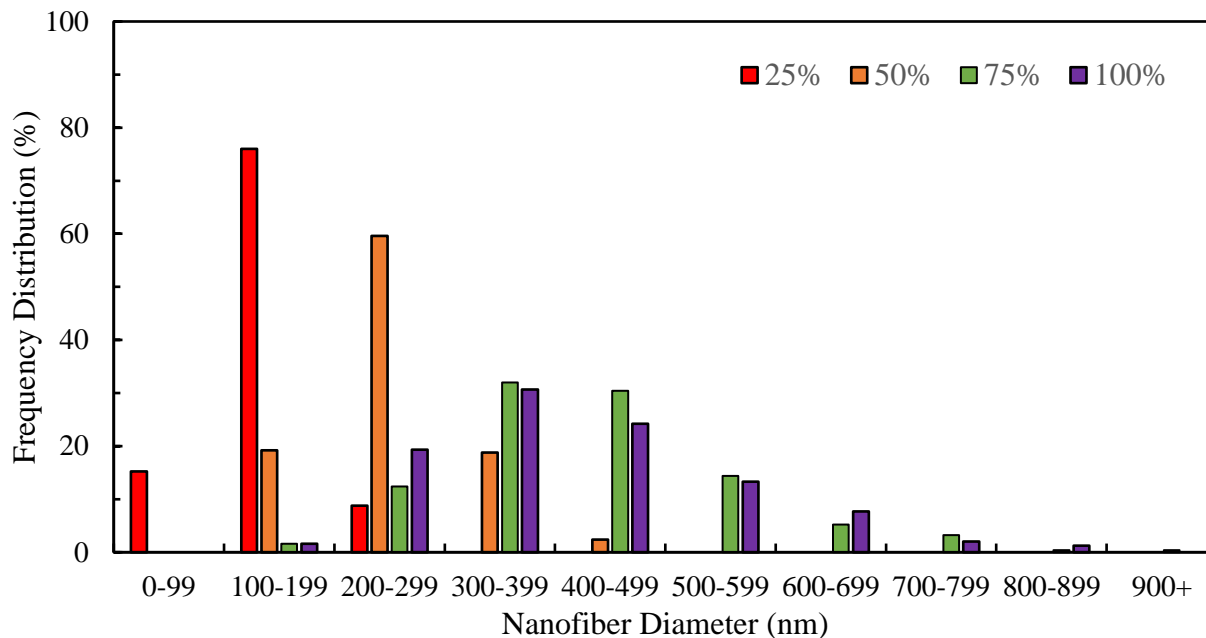
Figure 13. Diameter distribution of CuO fibers prepared using different copper nitrate to PVP weight ratios (25, 50, 75, 100%). The fibers were thermally treated in air at 823 K and 101 kPa for 4 h. Each electrospinning solution was prepared using 1.3 g of PVP, an appropriate amount copper nitrate to yield the desired metal nitrate to PVP ratio, 23 cm^3 of ethanol, and 10 cm^3 of DI water. Electrospinning was conducted at 30 kV, 1.0 cm^3 hr^{-1}, 18 inches, and 20% relative humidity.

3.3.2.3 Influence of Solvent Properties and Composition

3.3.2.3.1 Single Polymer Solvent System

As shown in chapter 2, the choice of solvent is critical for the transformation of the electrospinning solution to solid fibers.[109] An amalgam of solvents have been used and reported in the literature for electrospinning nanofibers; they include formic acid, dimethyl formamide (DMF), chloroform, water, methanol, dichloromethane, tetrahydrofuran, and acetic acid.[113,74] When it comes to PVP-based fibers, ethanol has been the most commonly used solvent due to its properties (e.g., low boiling temperature, low surface tension, high dielectric constant, and low viscosity).

To investigate the effect of solvent choice on morphology, five solutions were prepared using three alcohols (methanol, ethanol, and 1-propanol), water, and DMF. These solvents acted as single polymer solvents (23 cm^3) while DI water remained as the Cu(NO$_3$)$_2$ solvent (10 cm^3).

All other electrospinning parameters remained the same as discussed in section 3.3.1. In addition to the above listed solvents, 1-butanol and acetone were both tested as possible polymer/metal solvents for PVP and copper nitrate; however, these two solvents did not completely dissolve in PVP and $Cu(NO_3)_2$ at room temperature (~298 K) even after 24 h of stirring. Therefore, they were not electrospun. Methanol, ethanol and 1-propanol were specifically selected in this work because of their properties (shown in **Table 5**) and because they all contain the same functional group (-OH), and as such, comparisons can be made regarding the interactions between the solvent and PVP/$Cu(NO_3)_2$. **Table 5** lists key solvent properties. The data shows that the three alcohols have roughly similar dipole moment and surface tension values; however, their boiling temperatures, densities, and dielectric constants differ. Water has a considerably high dielectric constant (80.1) when compared to the other solvents while DMF has a high dipole moment (3.82 D).

Table 5. Key properties (boiling temperature, surface tension, dielectric constant, density, viscosity, and dipole moment) of the solvents used in the fabrication of PVP-$Cu(NO_3)_2$ nanofibers.

Solvents	Boiling Temperature (K)	Surface Tension (mN/m)	Dielectric Constant at 293 K	Density (g/cm^3)	Viscosity at 300 K (cP)	Dipole Moment (D)
Methanol	337.85	22.6	32.6	0.792	0.56	1.69
Ethanol	351.55	22.2	24.3	0.789	1.10	1.66
1-Propanol	370.15	23.7	20.1	0.803	1.96	1.68
Water	373.15	72.8	80.1	0.998	0.89	1.87
N,N-Dimethylformamide	426.15	37.1	36.7	0.944	0.96	3.82

Table 6 shows the average fiber diameter and standard deviation of PVP-$Cu(NO_3)_2$ fibers. Methanol, ethanol, and 1-propanol resulted in the formation of fibers that were 78 ± 23 nm, 261 ± 63 nm, and 363 ± 151 nm, respectively. The trend exhibited by the three alcohols suggest that the diameter of the PVP-$Cu(NO_3)_2$ fibers was affected by dielectric constant and viscosity. Methanol

had the highest dielectric constant (32.6) and lowest viscosity (0.56 cP), and consequently, it had the thinnest nanofibers. Of the three alcohols, 1-propanol had the highest viscosity (1.96 cP) and lowest dielectric constant (20.1), as shown in **Table 5**, and as such it had the thickest fibers. The fibers that were formed using 1-propanol also had a fused structure (**Table 6**). As mentioned previously, crosslinking or fusing of fibers at the touching points occurs due to incomplete evaporation of the solvent. From **Table 5**, it can be rationalized that crosslinking occurred because 1-propanol had the highest boiling temperature (370.15 K) of the three alcohol solvents. Ethanol and methanol, for instance, had boiling temperatures of 351.55 K and 337.85 K, respectively. By looking at the data obtained for the three alcohols (methanol, ethanol and 1-propanol) in **Table 6**, it becomes clear that boiling temperature, dielectric constant, and viscosity are the three main properties that influence the PVP-Cu(NO$_3$)$_2$ morphology and average diameter.
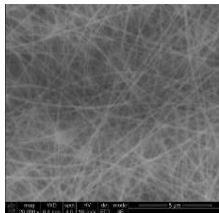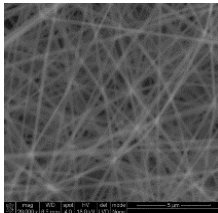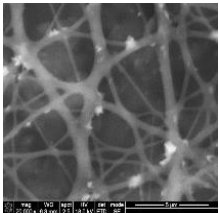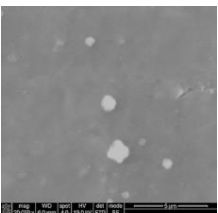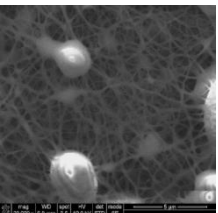
Even though the results in **Table 6** for the three alcohols indicate the effect of boiling temperature, dielectric constant, and viscosity, on fiber diameter and morphology, the data for water and DMF seem to suggest that density (which affects the kinematic viscosity of a solution) and surface tension also play a role in the suitability of a solvent for electrospinning. When water was tested as a polymer solvent, no fibers were formed. Instead, discrete droplets were collected on the aluminum foil, as shown in **Table 6**. Water, when compared to the other solvents, has a considerably high boiling temperature (373.15 K). Indeed, the high boiling temperature of water and its low volatility are the two main reasons why no fibers formed when water was used as a solvent. Water also has high surface tension (72.8 mN m^{-1}), the highest of all the solvents tested (**Table 5**). As discussed in chapter 2, when a solution is electrospun, the solution must first overcome its own surface tension.[75] The surface tension of a fluid favors the formation of sphere-like shapes that have smaller surface areas per unit volume.[50] Therefore, solutions that have high

surface tensions such as, water, essentially resist the jet formation process. Because of these reasons (high boiling temperature, low volatility, and high surface tension), water in this work did not electrospin at the conditions tested.

DMF, on the other hand, formed crosslinked and beaded fibers that had an average diameter of 82 ± 29 nm (**Table 6**). As a matter of fact, DMF was shown in this work to be a promising solvent for the formation of ultrathin fibers. DMF has a dielectric constant and viscosity of 36.7 and 0.96 cP, respectively, which are close to those of methanol (32.6 and 0.56 cP) (**Table 5**). As mentioned previously, solvents that have high dielectric constants and low viscosities tend to form thinner fibers. The main differences between the fibers formed from methanol and DMF as seen from the SEM images in **Table 6** lies in morphology. Since DMF has a high boiling temperature, DMF did not adequately dissolve prior to reaching the collecting plate, thus, forming fused fibers. Furthermore, DMF has a higher surface tension than methanol, ethanol and 1-propanol (but less than water) (**Table 5**). As mentioned previously, solutions that have high surface tension tend to either not electrospin or form fibers with defects.

Figure 14 shows the diameter distributions of PVP-Cu(NO$_3$)$_2$ nanofibers, and it shows that the usage of methanol or ethanol results in the formation of fibers with a narrow distribution. The results in this section show the complexity of the electrospinning process and the involvement of many factors (e.g., solubility, dielectric constant, surface tension, boiling temperature, and viscosity) in the selection of a solvent. Because each solvent has a unique set of properties—some that are suitable for the electrospinning process while others might be deleterious, often, to optimize the effect of solvent on fiber diameter and morphology, more than one solvent is used. This approach of using co-solvents is discussed in the next two sections.

Table 6. Solution properties (density and conductivity), fiber properties (SEM micrographs, average diameter, standard deviation, and morphology), and structural defects (type and diameter) of PVP-Cu(NO$_3$)$_2$ fibers prepared using different polymer solvents. Each electrospinning solution was prepared using 1.3 g of PVP, 1.3 g of copper nitrate, 23 cm^3 of solvent, and 10 cm^3 of DI water. Electrospinning was operated at 30 kV, 1.0 cm^3 hr^{-1}, 18 inches, and 20% relative humidity.

		Identity of Polymer Solvent				
		Methanol	Ethanol	1-Propanol	Water	DMF
Solution Properties:	Density (g/cm^3)	0.906	0.911	0.929	1.021	1.003
	Conductivity (mS/cm)	29.70	16.66	12.19	65.90	16.85
Fiber Appearance:	SEM					
	Average Diameter (nm)	78.31	261.33	363.45	-	82.89
	1 Standard Deviation (nm)	23.46	63.01	151.08	-	29.84
	Morphology	smooth, cylindrical	smooth, cylindrical	crosslinked	discrete droplets	crosslinked
Structural Defects:	Type of Defect	no defects	no defects	no defects	-	spherical beads
	Diameter of Beads (µm)	-	-	-	-	3.1

54

Figure 14. Diameter distribution of PVP-Cu(NO$_3$)$_2$ nanofibers synthesized using different polymer solvents (methanol, ethanol, 1-propanol, and DMF). Water (not shown) did not form any fibers. Each electrospinning solution was prepared using 1.3 g of PVP, 1.3 g of copper nitrate, 23 cm^3 of polymer solvent, and 10 cm^3 of DI water. Electrospinning was conducted at 30 kV, 1.0 cm^3 hr^{-1}, 18 inches, and 20% relative humidity.
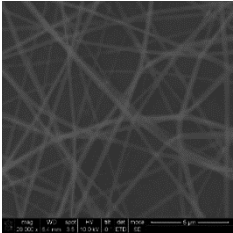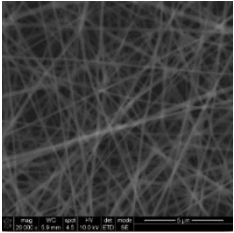
3.3.2.3.2 A Binary Solvent System (Ethanol and Water)

In the previous section, five solvents (methanol, ethanol, 1-propanol, water and DMF) were examined as possible solvents for PVP while the copper nitrate solvent (water) remained unchanged. Those results demonstrated the suitability of ethanol and water when used as co-solvents for the electrospinning of PVP-Cu(NO$_3$)$_2$ fibers. In this section, instead of having a polymer solvent (23 cm^3) and a metal solvent (10 cm^3) as two separate solvents, one binary solvent system of a total volume of 33 cm^3 was used. To investigate the effect of a binary solvent system comprising of ethanol and water on the morphology of PVP-Cu(NO$_3$)$_2$, the ethanol to water volumetric ratio in the electrospinning solution was varied (100:0, 70:30, 50:50, 30:70, and 0:100). All other electrospinning parameters remained the same as described in section 3.3.1.

Table 7 shows the SEM images of the PVP-Cu(NO$_3$)$_2$ nanofibers synthesized at the five volumetric ratios listed previously. When the ethanol to water ratio was 100:0 (pure ethanol solution of 33 cm^3), the solution gelled when the metal containing solution was added to the polymer solution. As such, this solution was not electrospun. The solutions that contained 30:70 and 100:0 ethanol to water volumetric ratios also did not electrospin. The reason these two solutions failed to electrospin was because they comprised of mostly water, which in the previous section was shown to have high surface tension. Indeed, the results demonstrate that water is an inadequate electrospinning solvent for the synthesis of PVP-Cu(NO$_3$)$_2$ nanofibers at these experimental conditions (solution parameters and processing conditions). The two solutions that electrospun and formed fibers were the ones that comprised of 70:30 and 50:50 ethanol to water volumetric ratio. The 50:50 solution resulted in the formation of thinner fibers (70 ± 21 nm) (**Table 7**). The 70:30 solution, on the other hand, formed fibers with diameters of 261 ± 63 nm (**Table 7**).

The results indicate that water encourages the formation of thinner PVP-Cu(NO$_3$)$_2$ fibers (when a small amount of it is added as a part of a binary solvent system) because of its high dielectric constant (80.1) and low viscosity (0.89 cP) (**Table 5**). When added in small volumetric ratios to ethanol, water effectively increases the dielectric constant of the solution and lowers the viscosity of the solution, resulting in the fabrication of ultrathin fibers. The trend observed in this work for a co-solvent comprising of water and ethanol agrees with the findings of Fong et al.,[61] who reported that increasing the ethanol to water ratio formed smoother and larger poly(ethylene oxide) fibers.

Table 7. SEM images, average diameter and standard deviation of PVP-Cu(NO$_3$)$_2$ nanofibers synthesized at different volumetric ratios of ethanol to water. Each electrospinning solution was prepared using 1.3 g of PVP, 1.3 g of copper nitrate, and 33 cm^3 of ethanol and water in the appropriate volumetric ratio. Electrospinning was conducted at 30 kV, 1.0 cm^3 hr^{-1}, 18 inches, and 20% relative humidity.
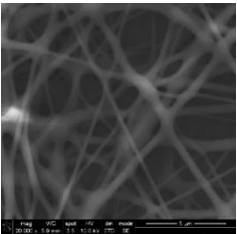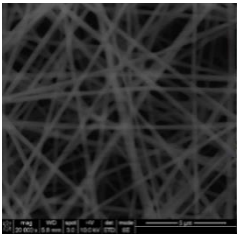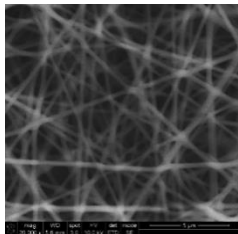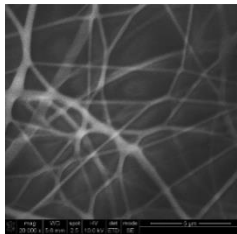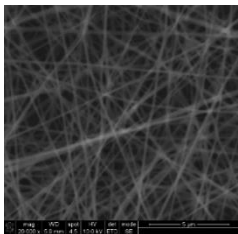
| Ethanol : Water | Volumetric Ratios of a Binary Solvent System (Ethanol and Water) | | | | |
	100:0	70:30	50:50	30:70	0:100
SEM	solution gels			no fibers	no fibers
Average Diameter (nm)	-	261.33	70.32	-	-
1 Standard Deviation (nm)	-	63.01	21.66	-	-

3.3.2.3.3 A Ternary Solvent System (Ethanol, Water, and DMF)

A ternary solvent system of a total volume of 33 cm^3 is investigated in this section. DMF has been shown in this work to form very thin, yet fused fibers. Since ethanol and water were proven to yield smooth and defect-free fibers when they were added as a binary solvent system, they were combined in this section with DMF in different volumetric ratios to test their ability to form ultrathin PVP-Cu(NO$_3$)$_2$ fibers. Five solutions were prepared with the following ethanol to water to DMF volumetric ratios: (70:0:30, 70:15:15, 70:22.5:7.5, 50:0:50, and 50:25:25). In all these electrospinning solutions, ethanol made up the volumetric majority of the ternary solvent system. All other electrospinning parameters remained the same as described in section 3.3.1.

Table 8 shows the SEM images and average diameters of the PVP-Cu(NO$_3$)$_2$ nanofibers. Solutions that contained only ethanol and DMF (70:0:30, 50:0:50) resulted in the formation of crosslinked and relatively thick fibers, as the average diameter of the fibers prepared from these electrospinning solutions were 338 ± 126 and 259 ± 104 nm, respectively. The high boiling temperature (426.15 K), density (0.944 g cm^{-3}), and surface tension (37.1 mN m^{-1}) of DMF affected the evaporation rate of the co-solvents, resulting in fused fibers (**Table 5**). On the other hand, the solutions that contained ethanol, water and DMF (70:15:15, 70:22.5:7.5, 50:25:25; ethanol to water to DMF volumetric ratio) resulted in the formation of mostly smooth and defect-free PVP-Cu(NO$_3$)$_2$ nanofibers. As shown in **Table 8**, the solution that contained 50:25:25 (ethanol to water to DMF ratio) had the thinnest PVP-Cu(NO$_3$)$_2$ fibers of the five solutions tested (108 ± 31 nm). The results in this section indicate that DMF when combined with ethanol and water results in the fabrication of thin yet crosslinked nanofibers. Although most of the electrospinning literature has focused on the synthesis and application of smooth, thin, defect-controlled, and cylindrically-shaped nanofibers, thin and crosslinked fibers are preferred in many biomedical applications due to their enhanced thermostability and mechanical properties.[114]

58

Table 8. SEM images, average diameter and standard deviation of PVP-Cu(NO$_3$)$_2$ nanofibers at different volumetric ratios of ethanol to water to DMF. Each electrospinning solution was prepared using 1.3 g of PVP, 1.3 g of copper nitrate, and 33 cm^3 of ethanol, water, and DMF in the appropriate volumetric ratio. Electrospinning was conducted at 30 kV, 1.0 cm^3 hr^{-1}, 18 inches, and 20% relative humidity.

Ethanol : Water : DMF	Volumetric Ratios of a Ternary Solvent System (Ethanol, Water, and DMF)				
	70:0:30	70:15:15	70:22.5:7.5	50:0:50	50:25:25
SEM					
Average Diameter (nm)	338.29	233.72	207.18	259.06	108.74
1 Standard Deviation (nm)	126.48	58.12	50.62	104.23	31.92
Morphology	fused	smooth, cylindrical	cylindrical and fused	fused	smooth, cylindrical

3.3.2.4 Effects of Applied Voltage

Sections 3.3.2.1-3.3.2.3 demonstrated that polymer molecular weight, polymer concentration, metal concentration, and solvent choice substantially affected the intrinsic electrospinning solution properties (e.g., viscosity, dielectric constant, surface tension, conductivity, boiling temperature, dipole moment, and density), which influenced the morphology of the synthesized PVP-Cu(NO$_3$)$_2$ nanofibers. The electrospinning processing conditions (voltage supplied, extrusion rate, distance between the tip-of-needle and collecting plate, and humidity) were also systematically varied in this work, to explore their effect on nanofiber diameter and morphology. One of the most critical elements in the electrospinning process is the application of voltage on a droplet to form a Taylor cone. The voltage value that allows for the formation of a Taylor cone is referred to as critical voltage and this value varies from one solution to another.[115]

In this work, an electrospinning solution was prepared as described in section 3.3.1. The solution was electrospun at varying voltages (25, 30, 35, 40, and 45 kV), to investigate the influence of the voltage supplied and resultant electric field on the diameter and morphology of PVP-Cu(NO$_3$)$_2$ fibers. **Figure 15** shows the average diameter of the PVP-Cu(NO$_3$)$_2$ nanofibers, which was calculated using ImageJ software (n=250). The results indicate that fiber diameter is mildly affected by this electrospinning parameter. When the applied voltage on the PVP and copper nitrate solution was higher than the critical voltage (found experimentally to be 21 kV at the current electrospinning conditions), the applied electric field caused the solution to stretch. As seen from **Figure 15**, between 25 and 40 kV there was a linear relationship, with a coefficient of determination equal to 0.999, between the applied voltage and the average diameter of the PVP-Cu(NO$_3$)$_2$ nanofibers. Specifically, as the applied voltage increased from 25 to 40 kV, the fiber diameter increased from 294 ± 55 nm to 359 ± 115 nm, respectively (**Table 9**). When the applied

voltage was 45 kV, the diameter remained roughly the same as the diameter of the fibers that formed at 40 kV (**Table 9**). It can be rationalized that between 25 and 40 kV, the high voltage led to accelerating the travel velocity of the electrospinning jet towards the collector (especially given the fact that the distance between the tip-of -needle and collecting plate in this study is long when compared to the literature), thus, reducing the overall travel and stretching time experienced by the jet, which led to the formation of fibers with larger diameters. Several authors observed and reported similar trends as the ones observed here, but for different polymers. Mazoochi et al. [56] reported on the diameter of polysulfone nanofibers as a function of voltage applied. The authors showed that increasing the voltage led to an increase in fiber diameter, which was followed by a decrease in diameter as the voltage continued to increase.
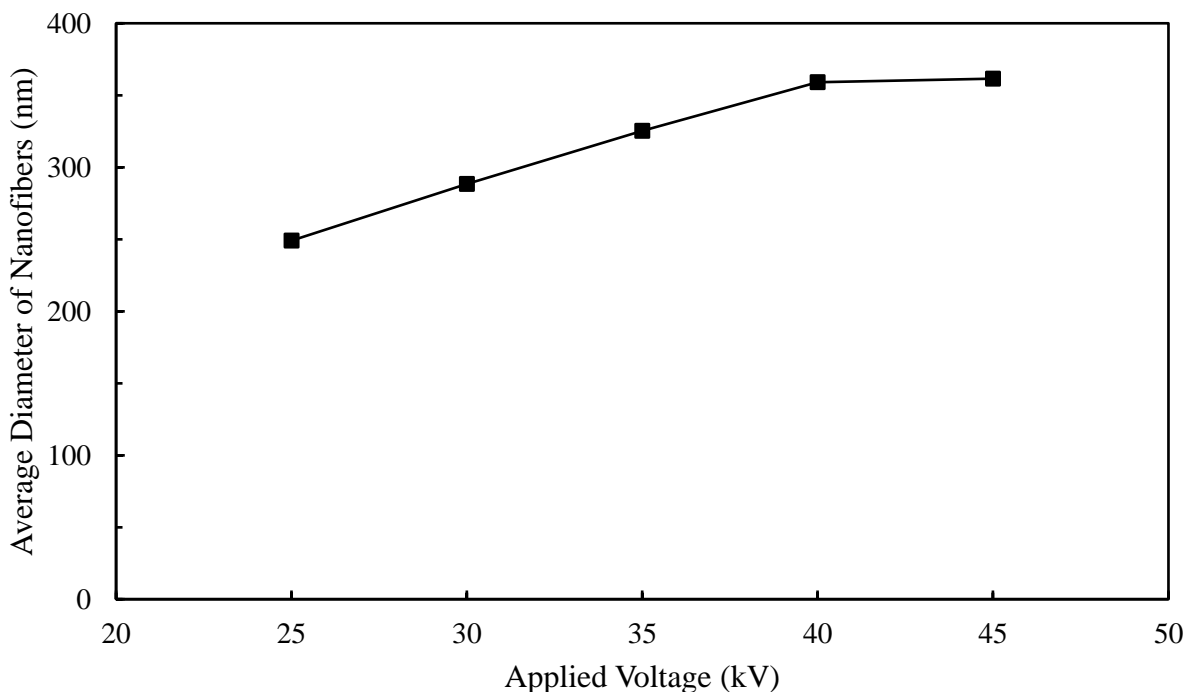
Figure 15. Average diameter of PVP-Cu(NO$_3$)$_2$ nanofibers at five applied voltages (25, 30, 35, 40, and 45 kV). Each electrospinning solution was prepared using 1.3 g of PVP, 1.3 g of copper nitrate, 23 cm^3 of ethanol, and 10 cm^3 of DI water. Electrospinning was conducted at 1.0 cm^3 hr^{-1}, 18 inches, and 20% relative humidity.

Table 9. Fiber properties (SEM micrographs, average diameter, standard deviation and morphology) and structural defects (type and diameter) of PVP-Cu(NO$_3$)$_2$ fibers prepared at different applied voltages. Each electrospinning solution was prepared using 1.3 g of PVP, 1.3 g of copper nitrate, 23 cm^3 of ethanol, and 10 cm^3 of DI water. Electrospinning was conducted at 1.0 cm^3 hr^{-1}, 18 inches, and 20% relative humidity.
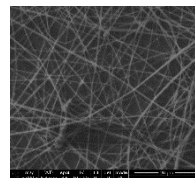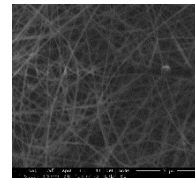
		Applied Voltage (kV)				
		25	30	35	40	45
Fiber Appearance:	SEM					
	Average Diameter (nm)	249.03	288.29	325.23	359.02	361.53
	1 Standard Deviation (nm)	55.4	83.01	103.6	115.09	112.57
	Morphology	smooth, cylindrical	smooth, cylindrical	smooth, cylindrical	smooth, cylindrical	smooth, cylindrical
Structural Defects:	Type of Defect	no defects	no defects	spindle-like	spindle-like	spherical and spindle-like
	Diameter of Beads (µm)	-	-	1.1	1.6	3.4 and 0.7

Figure 16 shows the distribution of the PVP-Cu(NO$_3$)$_2$ nanofibers. The results show that increasing the voltage increased the distribution of the formed fibers. For instance, the PVP-copper nitrate solution that was electrospun at 25 kV had 16.8% of it fibers between 100-199 nm, 68% between 200-299 nm, 14% between 300-399 nm, and 1.2% between 400-499 nm. On the other hand, the solution electrospun at 45 kV had a much wider distribution: 2.8% of its fibers were between 100-199 nm, 28.8% between 200-299 nm, 36.8% between 300-399 nm, 17.6% between 400-499 nm, 12% between 500-599 nm, 1.2% between 600-699 nm, and 0.8% between 700-799 nm (**Figure 16**). The increase in distribution could potentially be caused by the formation of more secondary jets at higher voltages, which invariably lead to wider fiber distributions.
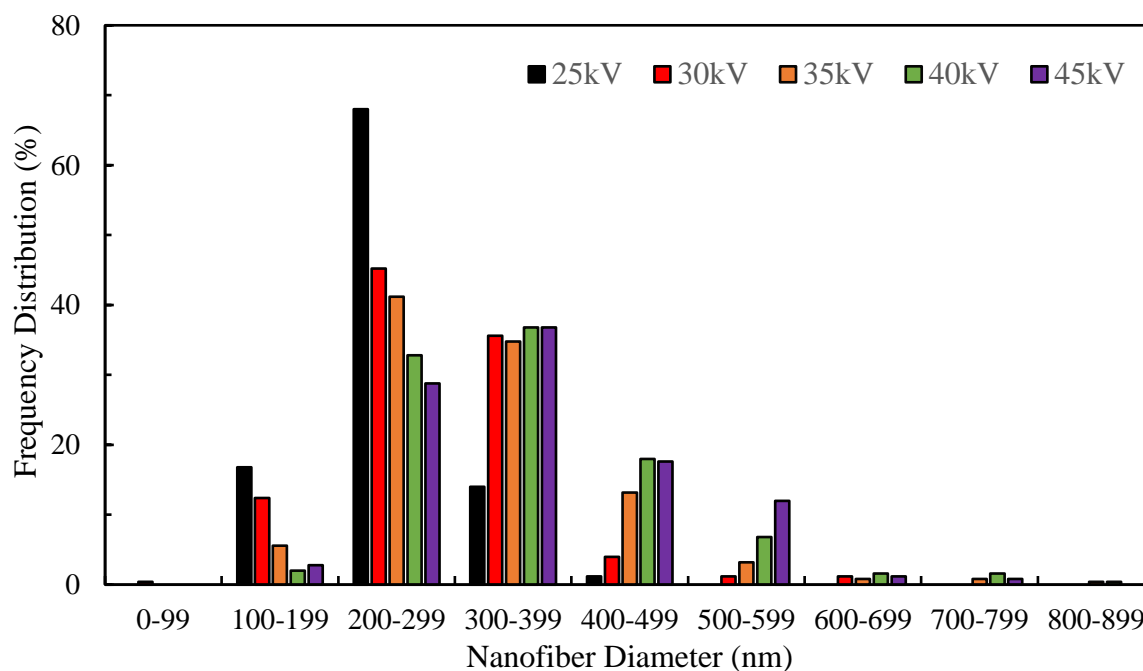
Figure 16. Diameter size distribution of PVP-Cu(NO$_3$)$_2$ nanofibers prepared at different applied voltages (25, 30, 35, 40, and 45 kV). Each electrospinning solution was prepared using 1.3 g of PVP, 1.3 g of copper nitrate, 23 cm^3 of ethanol, and 10 cm^3 of DI water. Electrospinning was conducted at 1.0 cm^3 hr^{-1}, 18 inches, and 20% relative humidity.

Table 9 shows the SEM images of the collected PVP-Cu(NO$_3$)$_2$ nanofibers and describes the structural defects that were present in those fibers. The results indicate that the fibers that were formed under more extreme conditions (i.e., higher voltages) had more spindle-like and/or spherical defects. The sizes of these defects increased, too, as a function of increased voltage. Several authors have reported that the increase in size and density of structural defects is the result of increased instabilities in the jet.[61,28] Therefore, it could be rationalized that by increasing the applied voltage on the PVP and copper nitrate electrospinning solution, the jet was indirectly subjected to more instabilities, which resulted in the formation of more pronounced defects.

3.3.2.5 Effects of Distance Between the Tip-of-Needle and Collecting Plate

The distance between the tip-of-needle and collecting plate is another parameter that has been reported to influence the electrospinning process and the quality of the synthesized nanofibers.[53] To examine the effect of distance on the morphology of PVP-Cu(NO$_3$)$_2$ nanofibers, the standard solution (from section 3.3.1) was run at different distances (14, 16, 18, 20, and 22 inches). Most publications on electrospinning report the ideal operating distance for forming smooth, bead-free and continuous nanofibers to be between 10 to 15 cm (3.94 to 5.91 inches).[116,117] However, we have carried our tests at longer distances, specifically, from 14 to 22 inches. The reason for that is that the standard solution used in this work consists of approximately 30% water and 70% ethanol (by volume) and has a low polymer concentration. Water was used as a co-solvent to form thinner fibers. However, water requires more time to evaporate as a result of its high boiling temperature. Because of this, distance and applied voltage were higher in this work.

Figure 17 shows that the average diameter of the synthesized fibers decreases with increasing distance. For example, at 16 and 22 inches, the average diameters were found (using ImageJ software, n=250) to be 283 ± 77 nm and 192 ± 47 nm, respectively. Interestingly, in this

work, when the distance was increased from 14 to 16 inches, the fiber diameter was unaffected by this change (**Table 10**). This could be attributed to the fact that at these short distances, the polymer jet experiences a high electric field (due to the high voltage) that the distance effect is essentially negated. Although there was no significant effect observed on the average diameter when the distance was increased from 14 to 16 inches, a closer look at the SEM images in **Table 10** reveals that far more structural defects were present in the fibrous structure at 14 inches than at 16. The spindle-like structural defects that formed at that these short distances were probably due to inadequate evaporation and increased instabilities experienced by the jet. The results in this section are in agreement with the work of several authors who have observed beads and structural defects at low distances for different polymeric systems.[72,27] **Table 10** shows that when the distance is set to 22 inches, structural defects in the form of beads (1.3 µm in size) were also present. These beads formed because the electrospinning jet experiences a weakened field strength at this distance, which affects its stability.
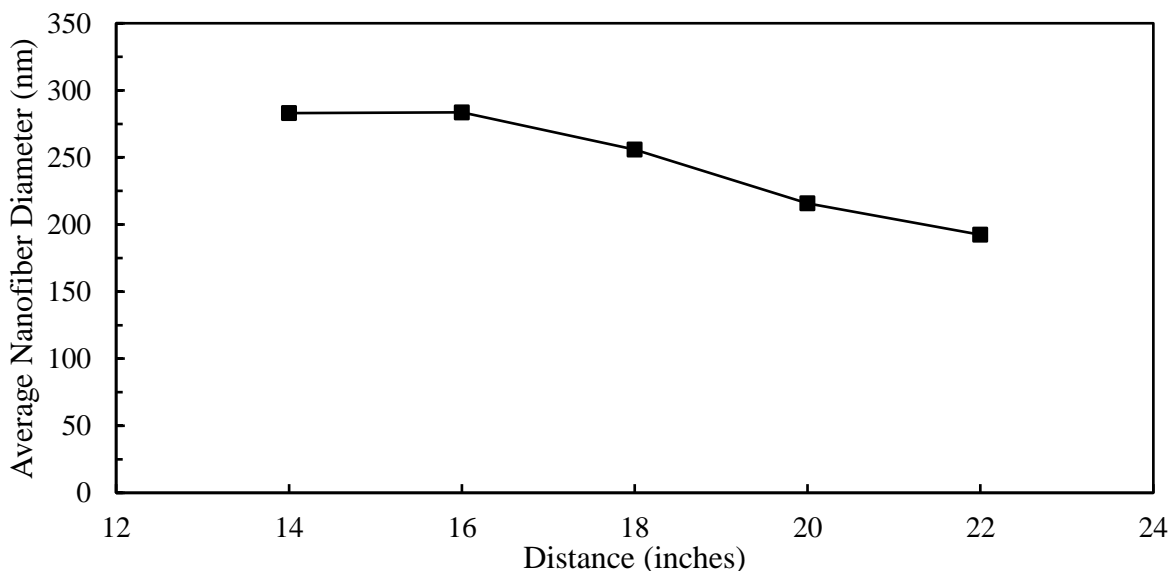
Figure 17. Average diameter of PVP-Cu(NO$_3$)$_2$ nanofibers at different tip-of-needle to collecting plate distances. Each electrospinning solution was prepared using 1.3 g of PVP, 1.3 g of copper nitrate, 23 cm^3 of ethanol, and 10 cm^3 of DI water. Electrospinning was conducted at 30 kV, 1.0 cm^3 hr^{-1}, and 20% relative humidity.

Table 10. Fiber properties (SEM micrographs, average diameter, standard deviation and morphology) and structural defects (type and diameter) of PVP-Cu(NO$_3$)$_2$ fibers at different tip-of -needle to collecting plate distances. Each electrospinning solution was prepared using 1.3 g of PVP, 1.3 g of copper nitrate, 23 cm^3 of ethanol, and 10 cm^3 of DI water. Electrospinning was conducted at 30 kV, 1.0 cm^3 hr^{-1}, and 20% relative humidity.
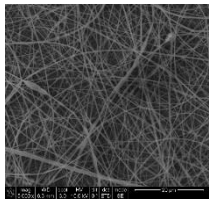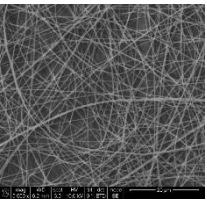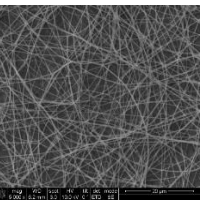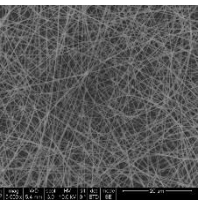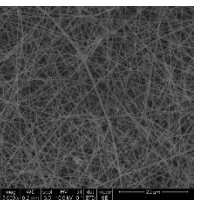
	Tip-of -Needle to Collecting Plate Distance (inches)				
	14	16	18	20	22
SEM					
Average Diameter (nm)	283.10	283.59	261.33	215.82	192.35
1 Standard Deviation (nm)	106.43	77.00	63.01	57.17	47.79
Morphology	smooth, cylindrical	smooth, cylindrical	smooth, cylindrical	smooth, cylindrical	smooth, cylindrical
Type of Defect	spindle-like	no defects	no defects	no defects	spherical
Diameter of Beads (µm)	0.9	-	-	-	1.2

Figure 18 shows the diameter distribution of the PVP-Cu(NO$_3$)$_2$ nanofibers. The results indicate that the distance between the tip of the needle and collector does not influence the distribution of the formed fibers. Indeed, this section proves that properties such as fiber diameter and morphology are only slightly affected by changes in distance.
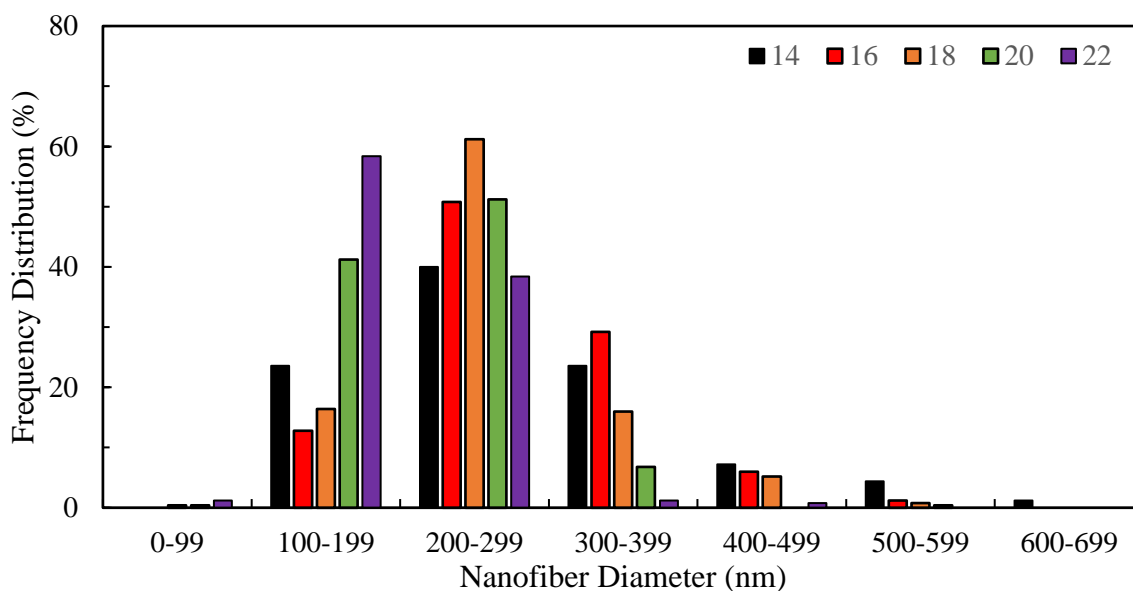
Figure 18. Diameter size distribution of PVP-Cu(NO$_3$)$_2$ nanofibers prepared at different tip-of - needle to collecting plate distances (14, 16, 18, 20, and 22 inches). Each electrospinning solution was prepared using 1.3 g of PVP, 1.3 g of copper nitrate, 23 cm^3 of ethanol, and 10 cm^3 of DI water. Electrospinning was conducted at 30 kV, 1.0 cm^3 hr^{-1}, and 20% relative humidity.

3.3.2.6 Effects of Extrusion Flowrate

The flowrate at which the electrospinning solution is extruded through a capillary has been reported to influence the diameter and morphology of polymer nanofibers.[54,82] To investigate the effect of flowrate on the diameter and morphology of PVP-Cu(NO$_3$)$_2$ nanofibers, the flowrate of the standard solution (described in section 3.3.1) was tested at 0.25, 0.50, 1.00, 1.50, and 2.00 cm^3 h^{-1}. All other electrospinning parameters were held constant. It is important to note that in these experiments when the extrusion flowrate was above 1.0 cm^3 h^{-1}, dripping was observed.

Figure 19 shows the average diameter of the PVP-Cu(NO$_3$)$_2$ fibers synthesized at different flowrates. The results demonstrate that the effect of extrusion flowrate was almost absent at 0.25, 0.50 and 1.00 cm^3 h^{-1}. At 0.25, 0.5 and 1.0 cm^3 h^{-1}, the average diameter and standard deviation of the PVP-Cu(NO$_3$)$_2$ nanofibers calculated using ImageJ software (n=250) were 256 ± 65, 258 ± 74, and 261 ± 63 nm, respectively. As the flowrate was increased from 1.00 to 1.50 to 2.00 cm^3 h^{-1}, the fiber diameter increased more significantly going from 279 ± 84 to 314 ± 78 to 372 ± 128 nm, respectively. At the higher flowrates, fibers with larger diameters were formed because more electrospinning solution was available at the tip of the needle. When more solution is available at the capillary, the electrospinning jet starts with a larger radius, which ultimately results in the formation thicker fibers.[24] **Table 11** shows the SEM images of the formed fibers, which reveal that all (except one) of the synthesized nanofibers were smooth, continuous and defect free. The only exception was the sample that was electrospun at the highest flowrate (2.0 cm^3 h^{-1}).
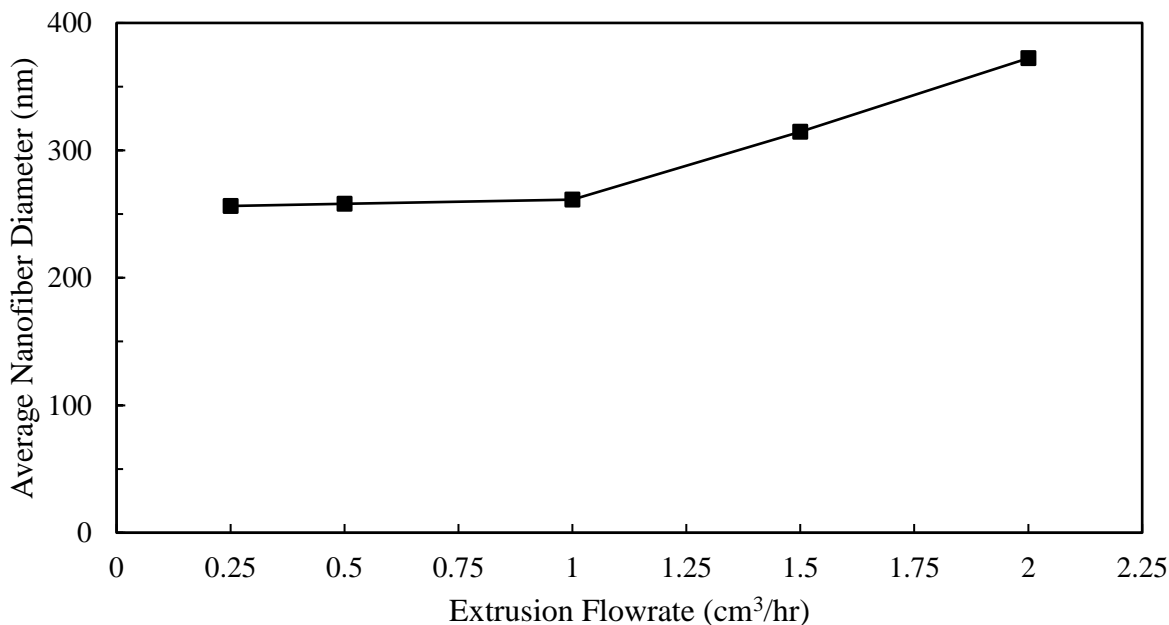
Figure 19. Average diameter of PVP-Cu(NO$_3$)$_2$ nanofibers at five extrusion flowrates (0.25, 0.5, 1.0, 1.5, 2.0 cm^3 h^{-1}). Each electrospinning solution was prepared using 1.3 g of PVP, 1.3 g of copper nitrate, 23 cm^3 of ethanol, and 10 cm^3 of DI water. Electrospinning was conducted at 30 kV, 18 inches, and 20% relative humidity.

Table 11. Fiber properties (SEM micrographs, average diameter, standard deviation and morphology) and structural defects (type and diameter) of PVP-Cu(NO$_3$)$_2$ nanofibers prepared at different extrusion rates. Each electrospinning solution was prepared using 1.3 g of PVP, 1.3 g of copper nitrate, 23 cm^3 of ethanol, and 10 cm^3 of DI water. Electrospinning was conducted at 30 kV, 18 inches, and 20% relative humidity.
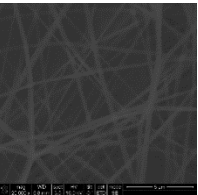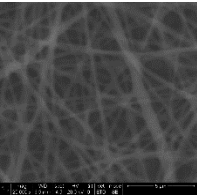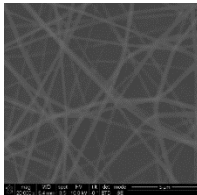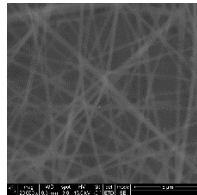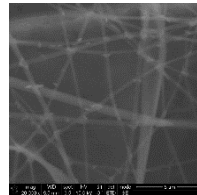
		Extrusion Rate (cm^3/h)				
		0.25	0.50	1.0	1.5	2.0
Fiber Appearance:	SEM					
	Average Diameter (nm)	256.37	258.12	261.33	314.71	372.30
	1 Standard Deviation (nm)	65.91	74.32	63.01	78.08	128.74
	Morphology	smooth, cylindrical	smooth, cylindrical	smooth, cylindrical	smooth, cylindrical	non-smooth, cylindrical
Structural Defects:	Type of Defect	no defects	no defects	no defects	no defects	no defects
	Diameter of Beads (µm)	-	-	-	-	-

Figure 20 shows the diameter distribution of PVP-Cu(NO$_3$)$_2$ nanofibers at different flowrates. The results show that when the flowrates were increased from 0.25 to 1.5 cm^3 h^{-1}, no significant changes were present in the distribution of the fibers (**Figure 20**). The distribution, however, did slightly increase when the flowrate was increased to 2.0 cm^3 h^{-1} (because more solution was available at the tip of the needle, which most likely increased the likelihood of jet splitting). The results in this section encapsulate the effect of extrusion flowrate on the morphology of PVP-Cu(NO$_3$)$_2$ nanofibers. Extrusion rate was found to have a weak to moderate effect on the diameter and morphology of PVP-Cu(NO$_3$)$_2$ nanofibers.
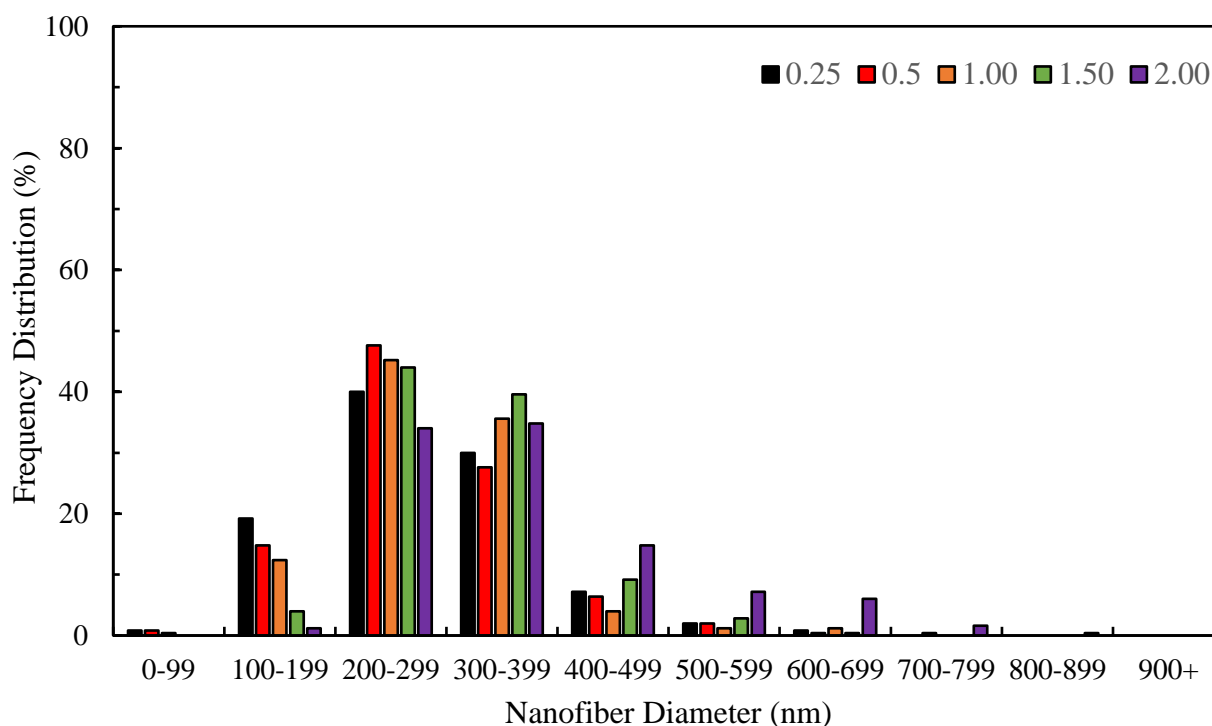
Figure 20. Diameter size distribution of PVP-Cu(NO$_3$)$_2$ nanofibers prepared at different extrusion flowrates (0.25, 0.5, 1.0, 1.5, and 2.0 cm^3 h^{-1}). Each electrospinning solution was prepared using 1.3 g of PVP, 1.3 g of copper nitrate, 23 cm^3 of ethanol, and 10 cm^3 of DI water. Electrospinning was conducted at 30 kV, 18 inches, and 20% relative humidity.

3.3.2.7 Effects of Relative Humidity

Interactions between the surrounding atmosphere (in the form of relative humidity) and the electrospinning jet have been reported to influence the morphology and properties (e.g., mechanical strength) of the synthesized nanofibers.[118,57] Yet, relative humidity, as an electrospinning parameter, remains an area that is has not been thoroughly researched. In this section, the standard PVP and copper nitrate solution was electrospun at different relative humidity levels (20, 30, 40, 50 and 60%). All other parameters were the same as those described in section 3.3.1.

Figure 21 shows the average diameter of PVP-Cu$(NO_3)_2$ nanofibers, which were measured using ImageJ software (n=250), as a function of relative humidity. The data shows that when relative humidity was increased from 20 to 50%, the average fiber diameter decreased from 271 ± 81 nm to 63 ± 21 nm, respectively (**Table 12**). Indeed, **Figure 21** demonstrates a strong correlation between relative humidity (between 20 and 50%) and fiber diameter. The diameter of PVP-Cu(NO3)$_2$ nanofibers was sensitive to the relative humidity in the electrospinning chamber due the absorption of water on the surface of the jet/fiber.[52] These water vapor molecules interfered with the solidification process of the charged jet (effectively hampering it), which led to inadequate drying, which invariably influenced the fiber morphology. **Figure 22** shows the distribution of the PVP-Cu$(NO_3)_2$ fibers at different relative humidity levels; the figure shows that, in general, increasing humidity decreases the diameter distribution of the fibers. Interestingly, as humidity was further increased from 50 to 60%, the fiber diameter as well as distribution increased rather than continue on a decreasing trajectory (**Figure 21**). This might be due to the presence of structural defects, which became abundant and significant in terms of density and size (3.7 µm) at 60% relative humidity (**Table 12**).
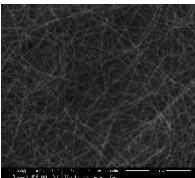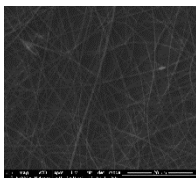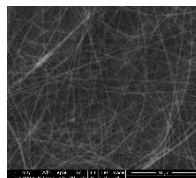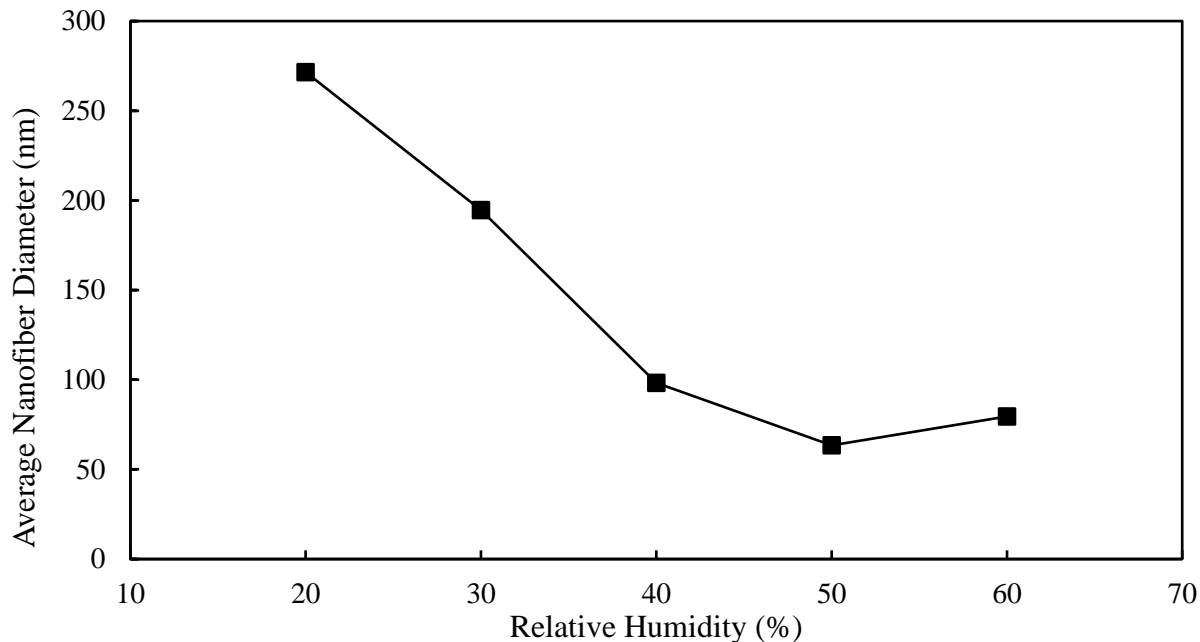
Figure 21. Average diameter of PVP-Cu(NO$_3$)$_2$ nanofibers at five relative humidity levels (20, 30, 40, 50, and 60 %). Each electrospinning solution was prepared using 1.3 g of PVP, 1.3 g of copper nitrate, 23 cm^3 of ethanol, and 10 cm^3 of DI water. Electrospinning was conducted at 30 kV, 18 inches, and 1.0 cm^3 hr^{-1}.
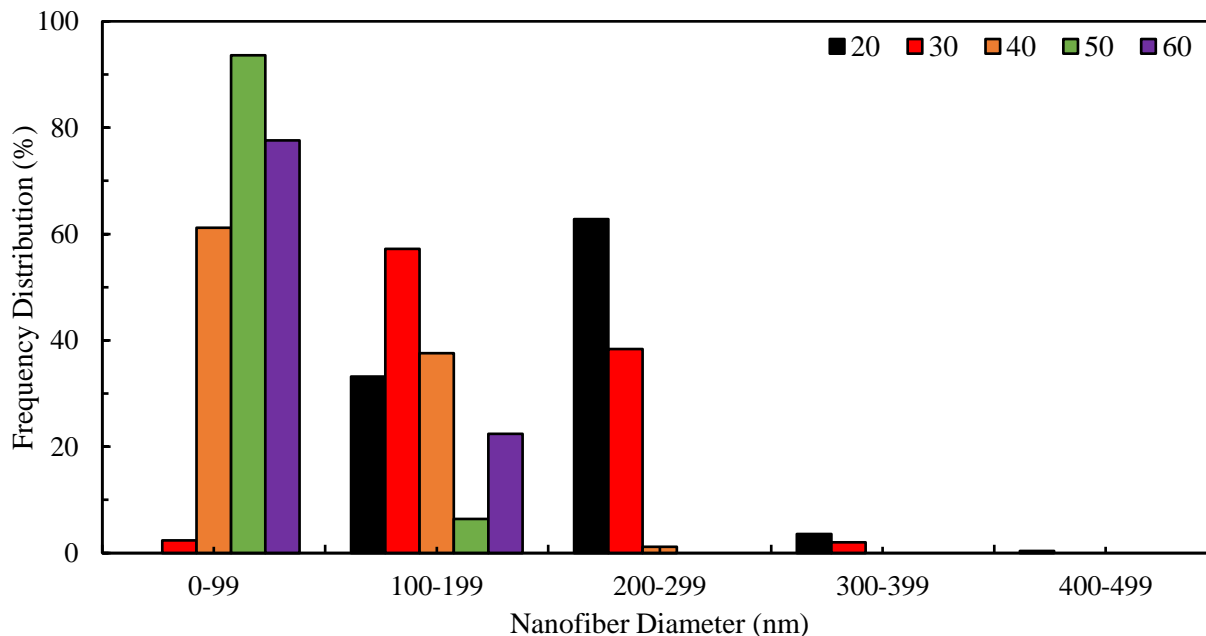
Figure 22. Diameter size distribution of PVP-Cu(NO$_3$)$_2$ nanofibers prepared at different relative humidity levels (20, 30, 40, 50, and 60%). Each electrospinning solution was prepared using 1.3 g of PVP, 1.3 g of copper nitrate, 23 cm^3 of ethanol, and 10 cm^3 of DI water. Electrospinning was conducted at 30 kV, 18 inches, and 1.0 cm^3 hr^{-1}.

Table 12. Fiber properties (SEM micrographs, average diameter, standard deviation and morphology) and structural defects (type and diameter) of PVP-Cu(NO$_3$)$_2$ nanofibers prepared at different relative humidity levels. Each electrospinning solution was prepared using 1.3 g of PVP, 1.3 g of copper nitrate, 23 cm^3 of ethanol, and 10 cm^3 of DI water. Electrospinning was conducted at 30 kV, 18 inches, and 1.0 cm^3 hr^{-1}.
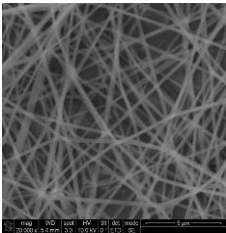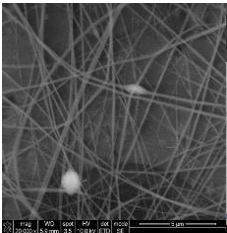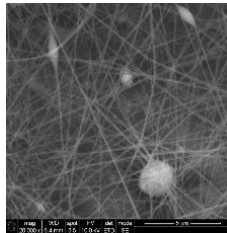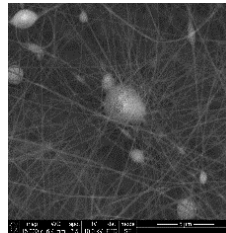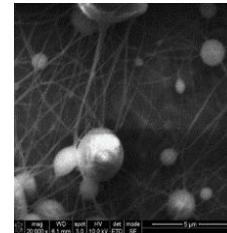
		Relative Humidity (%)				
		20	30	40	50	60
Fiber Appearance:	SEM					
	Average Diameter (nm)	261.33	194.58	98.31	63.40	79.50
	1 Standard Deviation (nm)	63.01	48.71	36.17	21.49	30.43
	Morphology	smooth, cylindrical	smooth, cylindrical	smooth, cylindrical	smooth, cylindrical	smooth, cylindrical
Structural Defects:	Type of Defect	no defects	spindle-like and spherical	spindle-like and spherical	spindle-like and spherical	spherical
	Diameter of Beads (µm)	-	1.2	2.4	2.9	3.7

73

Table 12 shows the SEM images of the PVP-Cu(NO₃)₂ nanofibers. At 20% relative humidity, smooth, continuous and defect-free nanofibers were formed. As the relative humidity was increased, however, the SEM images show that although the diameter of the spun fibers decreased (up until 50% relative humidity), the fibers formed had numerous and sizable defects. More defects formed as the humidity was increased from 30 to 40 to 50 to 60%. The structural defects that formed at these humidity levels were spindle-like and spherical in shape, and their density and sizes increased with increasing humidity. For instance, at 30% humidity, spindle like structures with diameters of 0.4 µm and spherical beads with diameters of 1.2 µm infiltrated the fibrous structure (**Table 12**). When the humidity was 60%, however, there were no spindle-like defects but the spherical defects were 3.7 µm in diameter (on average) and they covered almost entirely the fiber structure.

The results in this section show that in the case of PVP-Cu(NO₃)₂ fibers (prepared from PVP, copper nitrate, ethanol and water) humidity encouraged the absorption of water into the electrospinning jet, which decreased the diameter of the synthesized fibers. Nazarati et al.[65] investigated the effects of humidity on poly(carbonate urethane) (PCU) fibers. The authors reported an increase in fiber diameter with increased relative humidity (5 − 75%), which disagrees with the results in this section. The contradiction in the effect of humidity on morphology between our work and theirs can be explained by looking at the properties of the polymer and solvent selected in each work. PVP, which was used in this work, is more soluble in water than PCU. When water in-soluble polymers like PCU are used in electrospinning, the water vapor present in the air is not absorbed by the polymer jet (like in the case of PVP)—instead it precipitates. The precipitation of water molecules on the jet as it undergoes the stretching process hinders the elongation of the metal-polymer jet and evaporation of the solvent, which leads to the formation

of fibers with larger diameters. The results in this section prove that polymer hydrophobicity and solvent miscibility are good predictors of whether humidity will have a positive or a negative effect on the synthesized fiber diameter. Given these results, humidity can be used as a tool for regulating the morphology of polymer-metal nanofibers.

3.4 Summary

Electrospinning was shown in this chapter to be an easy and effective technique for the fabrication of continuous, smooth and defect-controlled or defect-free metal-polymer fibers (specifically, PVP-Cu(NO$_3$)$_2$ nanofibers). Thermal treatment of the synthesized PVP-Cu(NO$_3$)$_2$ fibers was shown to alter the morphology of the spun fibers from smooth and continuous to a connected network of segmented and agglomerated CuO nanoparticles.

In this chapter, parameters that effect viscosity, conductivity, dielectric constant, surface tension, boiling temperature, and density were altered by changing the solution properties (polymer molecular weight, polymer/metal concentration, and solvent identity). The experimental results demonstrated that the morphology and bulk properties of PVP-Cu(NO$_3$)$_2$ fibers were governed mainly by the choice of electrospinning material (polymer, metal and solvent(s)). Molecular weight and polymer concentration were found to strongly impact the viscosity of the PVP-copper nitrate solution (thus, fiber morphology), forming fibers with diameters as thin as 100 nm and as large as 540 nm. Metal concentration was found to greatly affect the conductivity of the spun solution. Although metal concentration did not greatly affect the morphology of PVP-Cu(NO$_3$)$_2$ fibers (prior to thermal treatment), particularly at the low metal to polymer weight ratios, the thermally-treated CuO fibers, however, showed great sensitivity towards this parameter. The investigation of solvent choice showed that ultra-thin, defect-free nanofibers can be fabricated with the right choice of solvent or by combining solvents in different volumetric ratios. A good

electrospinning solvent for the fabrication metal-polymer nanofibers is one that is able to dissolve the polymer as well as the metal precursor and has a high dielectric constant, low boiling temperature, low surface tension, and an acceptable viscosity. Methanol and water (78.31 nm), DMF and water (82.89 nm) and ethanol and water (70.32 nm) were found to be promising binary solvent systems for the synthesis of ultrafine PVP-Cu(NO$_3$)$_2$ fibers.

The electrospinning processing conditions (voltage supplied, extrusion rate, distance between the tip-of-needle and collecting plate, and humidity) were also systematically varied to explore their effects on nanofiber morphology. Our results demonstrate that factors which do not directly and strongly influence the evaporation of solvents (voltage, extrusion rate, and tip-of-needle and collecting plate distance) do not have substantial effects on fiber diameter and morphology. However, relative humidity was found to greatly impact the PVP-Cu(NO$_3$)$_2$ fibers diameter and morphology.

Although many challenges exist in the electrospinning process, this work has demonstrated that the properties of the synthesized fibers (fiber diameter and morphology) can be precisely controlled and regulated by controlling the parameters that influence electrospinning. This work offers insight into better controlling the electrospinning process for the customization of ultrathin polymer-metal fibers with specified morphologies, for various applications.

Chapter 4 | Synthesis of NiO, MgO and CaO Fibers

4.1 Introduction

In the previous chapter, it was shown that highly porous CuO materials can be synthesized by electrospinning PVP, copper nitrate, water, and ethanol and then thermally treating the PVP-$Cu(NO_3)_2$ fibers in air. In order to investigate the effects of electrospinning parameters on metal-polymer fiber diameter and morphology, copper nitrate was selected as a model metal precursor and was electrospun to form PVP-$Cu(NO_3)_2$ fibers. In this chapter, three metal precursors are used (nickel nitrate, magnesium nitrate, and calcium nitrate) to form nickel oxide (NiO), magnesium oxide (MgO) and calcium oxide (CaO) and to probe the effect of metal choice on the morphology of the thermally treated fibers.

4.2 Materials and Electrospinning Synthesis

4.2.1 Materials

Polyvinylpyrrolidone (M.W. 1,300,000; Sigma-Aldrich), nickel nitrate hexahydrate (Sigma-Aldrich, 99.999%), calcium nitrate hydrate (Sigma-Aldrich, 99.997%), magnesium nitrate hexahydrate (Sigma-Aldrich, 99.999%), and ethyl alcohol (Sigma-Aldrich, 100%) were purchased and used without subsequent purification.

4.2.2 Synthesis of NiO Nanofibers

A polymer solution was prepared by dissolving 1.0 g of PVP in 23 cm^3 of ethanol. The polymer solution was then vortexed (Fisher Scientific Digital Vortex Mixer) at 3000 rpm for 0.5 h until the polymer was completely dissolved. The solution was left to settle for 10 minutes, transferred to a beaker, and stirred for 0.5 h. The metal containing solution was prepared by

dissolving 1 g of nickel nitrate in 10 cm^3 of DI water and stirring the solution for 0.5 h. The nickel containing solution was then added dropwise to the polymer containing solution. The solution was stirred for 0.25 h, and then vortexed for 0.5 h at 3000 rpm.

The electrospinning solution was placed in a 10 mL syringe (BD 10 mL syringe with Luer Lok^{TM} tip) with a hypodermic needle (Monoject^{TM} Standard 30G x ¾"). The distance between the tip of the needle and a stainless-steel collecting plate covered with aluminum foil was between 16 inches. A Gamma High Voltage Research ES75 power supply was used to apply voltage 30 kV while the polymer solution was extruded through the needle at a rate controlled by a syringe pump (1.0 cm^3 h^{-1}; Kent Scientific Genie Plus). Dry air was circulated inside a 3 m^3 chamber at 5 cm^3 min^{-1} to control the relative humidity (20 ± 2%). All electrospinning was carried out at ambient temperature (294 K) and pressure (101 kPa). The collected fibers were thermally treated under air at 873 K for 2 h at a ramping rate of 2 K min^{-1}.

4.2.3 Synthesis of MgO Nanofibers

A polymer solution was prepared by dissolving 1.5 g of PVP in 23 cm^3 of ethanol. The polymer solution was then vortexed (Fisher Scientific Digital Vortex Mixer) at 3000 rpm for 0.5 h until the polymer was completely dissolved. The solution was left to settle for 10 minutes, transferred to a beaker, and stirred for 0.5 h. The metal containing solution was prepared by dissolving 1 g of magnesium nitrate in 10 cm^3 of DI water and stirring the solution for 0.5 h. The magnesium containing solution was then added dropwise to the polymer containing solution. The solution was stirred for 0.25 h, and then vortexed for 0.5 h at 3000 rpm.

The electrospinning solution was placed in a 10 mL syringe (BD 10 mL syringe with Luer Lok^{TM} tip) with a hypodermic needle (Monoject^{TM} Standard 30G x ¾"). The distance between the tip of the needle and a stainless-steel collecting plate covered with aluminum foil was between 16

inches. A Gamma High Voltage Research ES75 power supply was used to apply voltage 30 kV while the polymer solution was extruded through the needle at a rate controlled by a syringe pump (0.75 cm^3 h^{-1}; Kent Scientific Genie Plus). Dry air was circulated inside a 3 m^3 chamber at 3 cm^3 min^{-1} to control the relative humidity (20 ± 2%). All electrospinning was carried out at ambient temperature (294 K) and pressure (101 kPa). The collected fibers were thermally treated under air at 823 K for 4 h at a ramping rate of 1 K min^{-1}.

4.2.4 Synthesis of CaO Nanofibers

A polymer solution was prepared by dissolving 1.3 g of PVP in 23 cm^3 of ethanol. The polymer solution was then vortexed (Fisher Scientific Digital Vortex Mixer) at 3000 rpm for 0.5 h until the polymer was completely dissolved. The solution was left to settle for 10 minutes, transferred to a beaker, and stirred for 0.5 h. The metal containing solution was prepared by dissolving 0.975 g of calcium nitrate in 10 cm^3 of DI water and stirring the solution for 0.5 h. The calcium containing solution was then added dropwise to the polymer containing solution. The solution was stirred for 0.25 h, and then vortexed for 0.5 h at 3000 rpm.

The electrospinning solution was placed in a 10 mL syringe (BD 10 mL syringe with Luer Lok^{TM} tip) with a hypodermic needle (Monoject^{TM} Standard 30G x ¾"). The distance between the tip of the needle and a stainless-steel collecting plate covered with aluminum foil was between 16 inches. A Gamma High Voltage Research ES75 power supply was used to apply voltage 30 kV while the polymer solution was extruded through the needle at a rate controlled by a syringe pump (1.0 cm^3 h^{-1}; Kent Scientific Genie Plus). Dry air was circulated inside a 3 m^3 chamber at 5 cm^3 min^{-1} to control the relative humidity (20 ± 1%). All electrospinning was carried out at ambient temperature (294 K) and pressure (101 kPa). The collected fibers were thermally treated under air at 823 K for 2 h at a ramping rate of 2 K min^{-1}.

4.2.5 Characterization

Scanning electron microscopy (SEM/; NOVA 230 Nano SEM) was used to determine the morphology of the as-synthesized nanofibers and thermally treated fibers. An Everhart-Thornley Detector (ETD) detector was used.

4.3 Results and Discussion

Figure 23 shows the SEM images of the nickel-, magnesium-, and calcium-based nanofibers before and after thermal treatment. The results indicate that the as-synthesized nanofibers (PVP-Ni$(NO_3)_2$, PVP-Mg$(NO_3)_2$, and PVP-Ca$(NO_3)_2$) had similar properties as those of PVP-Cu$(NO_3)_2$ nanofibers (discussed in the previous chapter). All three metal-polymer fibers were smooth and free from surface defects. The PVP-Mg$(NO_3)_2$ nanofiber sample had somewhat of a different morphology than the other two samples, as the PVP-Mg$(NO_3)_2$ nanofibers were crosslinked (**Figure 24**). That was the only major difference evident from the SEM images. After undergoing thermal treatment, the as-synthesized metal-polymer fibers were transformed to metal oxides. As **Figure 23** shows, just in the case of PVP-Cu$(NO_3)_2$ nanofibers, thermal treatment of the as-synthesized fibers resulted in a dramatic change in the morphology of the material. Despite initially looking the same, the three fibers exhibited a significant departure from their smooth, continuous, and cylindrical morphology upon thermal treatment and they all formed porous oxide nanostructures (NiO, MgO and CaO), with different shapes, sizes, and roughness. These results demonstrate the effect of metal choice after thermal treatment on fiber morphology and structure.
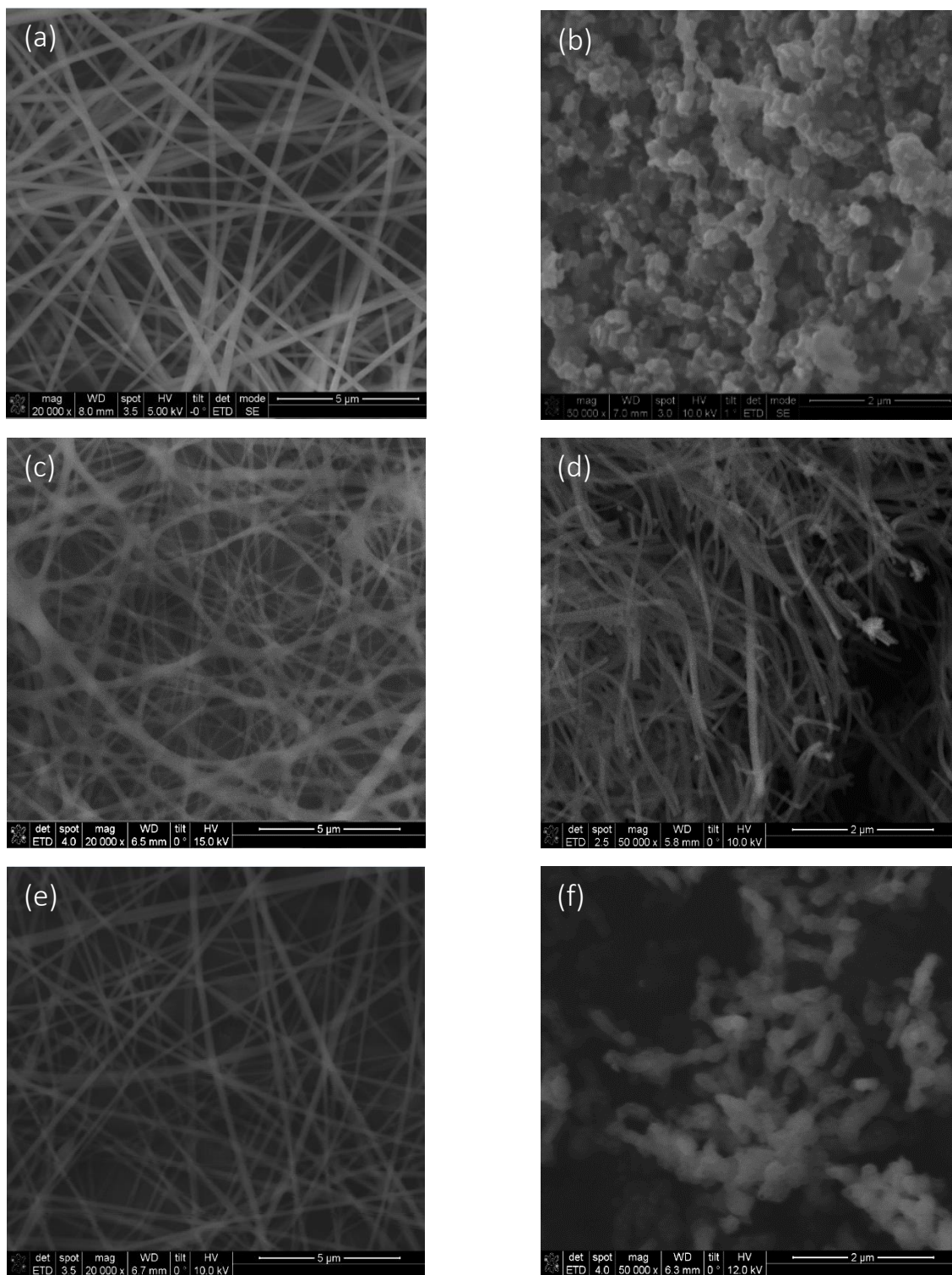
Figure 23. SEM images of (a) PVP-Ni(NO$_3$)$_2$, (b) NiO, (c) PVP-Mg(NO$_3$)$_2$, (d) MgO, (e) PVP-Ca(NO$_3$)$_2$, and (f) CaO nanofibers.

4.4 Summary

PVP-Ni(NO$_3$)$_2$, PVP-Mg(NO$_3$)$_2$, and PVP-Ca(NO$_3$)$_2$ nanofibers were synthesized via electrospinning and characterized using SEM. These three samples were later thermally treated to form NiO, MgO and CaO nanofibers. The results in this section show that even though electrospinning results in the fabrication of nanofibers that are smooth, continuous and cylindrical, thermal treatment transforms these nanofibers to highly porous, interconnected metal oxide nanoparticles with varying shapes and sizes. Indeed, the morphology of thermally treated electrospun materials (metal oxide nanofibers) is greatly influenced by the choice of metal.

Chapter 5 | Application I: Sorption Enhanced Steam Methane Reforming

5.1 Introduction

The increased reliance on fossil fuels to meet energy needs has led to increased CO_2 emissions into the atmosphere.[119,120] Mitigating the impact of CO_2 on the environment by reducing its emissions from various industrial processes and large combustion sources is a vital scientific goal.[121,122] While much research has been done on post process carbon capture and sequestration (CCS), sorption enhanced processes that trap carbon at the point of generation (i.e., as it is formed in chemical reactions) are also attractive options to mitigate CO_2 emissions. These processes have the additional advantages (compared to traditional CCS) of improved thermodynamics that often lead to lower energy consumption in addition to carbon emission mitigation.[123] One prominent example of simultaneous CO_2 capture with chemical reaction is the use of the gas-solid reaction between CO_2 and CaO for hydrogen production[124] via sorption enhanced steam methane reforming (SE-SMR).[123,125,126] In SE-SMR, the combination of CO_2 sorption with methane reforming reactions shifts the reaction equilibrium toward H_2 production (**Figure 24**), ultimately leading to greater than 90% conversion with H_2 selectivity greater than 85%. The combination of reaction and adsorption steps in a single reactor reduces the complexity of the reforming plant by eliminating the need for water-gas shift reactors and pressure swing adsorption downstream of the reforming reactor.[123] Furthermore, SE-SMR has the potential to operate at much lower temperatures and pressures (723-873 K and 101–304 kPa) than conventional methane reforming (1123-1173 K and 1520–2533 kPa). This simpler reactor configuration has the potential to significantly reduce heat and power requirements of reforming (i.e., lower compression costs and

lower consumption of natural gas to heat the reactor) while also sequestering the CO_2 byproduct, leading to a "Green Reforming" process.
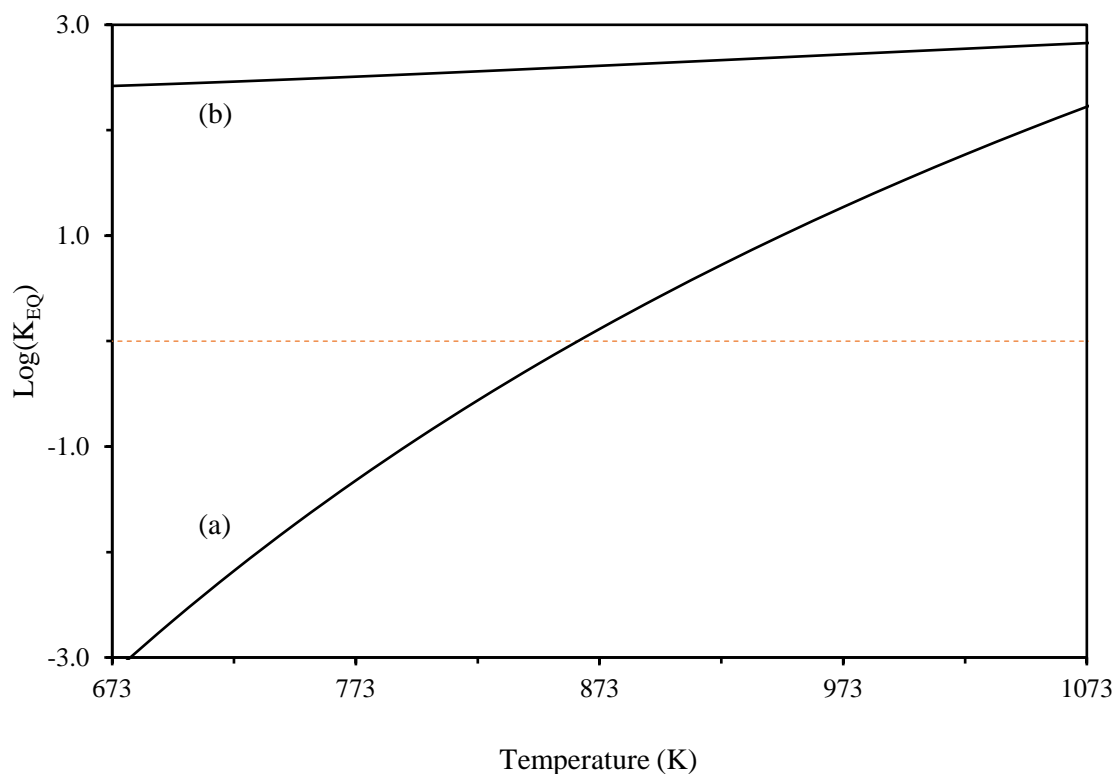
Figure 24. Chemical reaction equilibrium constants for reaction (a) $CH_{4 (g)} + 2 H_2O_{(g)} \leftrightarrow CO_{2 (g)} + 4 H_{2 (g)}$ and (b) $CH_{4 (g)} + 2 H_2O_{(g)} + CaO_{(s)} \leftrightarrow 4 H_{2 (g)} + CaCO_{3 (s)}$ at various temperatures. Steam methane reforming becomes thermodynamically favorable at $T > 873$ K. The coupling of methane reforming with CaO carbonation is thermodynamically favorable across a wide range of T.

CaO-based materials are the predominant sorbents used in SE-SMR because of their high adsorption capacity (0.79 g_{CO2}/g_{CaO}), adequate reversibility (CaO + CO_2 ↔ $CaCO_3$; K_{eq} = 87 at 923 K), fast carbonation-calcination kinetics ($E_{carbonation}$ = 20 kJ mol^{-1}; $E_{calcination}$ = 104 kJ mol^{-1}),[127] and low material cost.[128–130] Unfortunately, CaO sorbents (usually derived from natural CaO compounds such as limestone and dolomite) suffer from low conversions (54% after 60 minutes of reaction of limestone with 10% CO_2 at 923 K)[131] due to the formation of $CaCO_3$ product layers

that cover CaO surfaces and fill material pores, thereby inhibiting diffusion of CO_2 to reaction interfaces surfaces.[132] In addition, CaO-based sorbent capacities significantly decrease over multiple cycles (60% loss in initial capacity for limestone after 10 cycles)[133] due to sintering or agglomeration of the CaO particles.[134] Indeed, highly active, efficient, and inexpensive adsorbents are critical to the widespread implementation of SE-SMR technology.[135]

Current research efforts to improve the utilization and durability of CaO-based sorbents include (i) the synthesis of calcium-based sorbents from organic and inorganic precursors (instead of naturally derived CaO sources),[136] (ii) doping CaO with various metals,[137,138] and (iii) post treating the sorbents in an attempt to increase their lifespan.[139] The objective of this work is to develop high-capacity and high-stability CaO-based sorbents by synthesizing materials with controlled crystallite sizes, large intra-particle void volumes, optimal pore structures and chemical compositions, and varied morphologies. Thermal decomposition, hydrothermal dissolution-recrystallization, and electrospinning were employed to control the morphological properties of the sorbents. To elucidate the structure-activity relationship of the CaO sorbents, physico-chemical properties were determined using X-ray diffraction (XRD), N_2-physiosorption measurements, scanning electron microscopy (SEM), energy dispersive X-ray spectroscopy (EDS), and transmission electron microscopy (TEM). This characterization data was combined with reaction kinetics experiments (via thermogravimetric analysis (TGA) and steam methane reforming) to demonstrate that increases in surface area and porosity and decreases in particle agglomerate size and crystallite size lead to increases in effective diffusivities and surface reaction rate constants which, in turn, leads to improved capacity. In particular, this work demonstrates that (i) stoichiometric CO_2 capacity can be achieved using interconnected, highly porous networks of CaO-based nanofibers that consist of small CaO crystallites, and (ii) the initial high capacity of

electrospun CaO-based materials can be maintained over multiple cycles of carbonation and calcination by rationally incorporating a metal (e.g., Al) into the CaO structure to form $Ca_{12}Al_{14}O_{33}$ phases, which act as a spacer, thus, effectively separating the sorbent particles to prevent them from sintering or aggregating, which in turn prevents the porous fibrous structure from collapsing.

5.2 Experimental Methods

5.2.1 Materials and Synthesis

5.2.1.1 Materials

Polyvinylpyrrolidone (PVP) (M.W. 1,300,000, Sigma-Aldrich), calcium nitrate tetrahydrate (Sigma Aldrich, ≥99.0%), calcium acetate hydrate (Alfra Aesar, 99.9965%), calcium oxide from marble (Millipore Sigma), aluminum nitrate nanohydrate (Sigma Aldrich, 99.997%), poly(ethylene glycol)-*block*-poly(propylene glycol)-*block*-poly(ethylene glycol) (P123; Sigma Aldrich, M_n ~ 5,800), and ethyl alcohol (Sigma-Aldrich, 100%) were purchased and used without subsequent purification. The calcium oxide sample from marble is denoted as CaO-marble.

5.2.1.2 CaO-Based Nanofibers Synthesis via Electrospinning

A polymer solution was prepared by dissolving 1.3 g of PVP in 23 cm^3 of ethanol. The solution was then vortexed (Fisher Scientific Digital Vortex Mixer) at 2900 rpm for 1 h until the PVP was completely dissolved. The polymer solution was left to settle for 5-10 mins, transferred to a beaker, and stirred for 15 mins. The metal containing solution was prepared by dissolving 0.98 g of calcium nitrate and an appropriate amount of aluminum nitrate (for the Al-doped materials) in 10 cm^3 of DI water and stirring the solution for 0.5 h. The Al:Ca atomic ratio, for the three Al-doped samples, was 3:10, 1:10 and 1:20. The calcium-containing solution was then added dropwise to the polymer-containing solution. The solution was stirred for 0.25 h, and then vortexed for 0.5 h at 2900 rpm.

The electrospinning solution was placed in a 10 mL syringe (BD 10 mL syringe with Luer Lok^{TM} tip) with a hypodermic needle (Monoject^{TM} Standard 30G x ¾"). The distance between the tip of the needle and a stainless-steel collecting plate, which was covered with aluminum foil, was 16 inches. A Gamma High Voltage Research ES75 power supply was used to apply 30 kV on the polymer jet while the polymer solution was extruded through the needle at a rate controlled by a syringe pump (1.0 cm^3 h^{-1}; Kent Scientific Genie Plus). Dry air was circulated inside a 3 m^3 chamber at 6 cm^3 min^{-1} to control the relative humidity at 19.5 $\pm$ 2%. All electrospinning was carried out at ambient conditions: temperature (294 $\pm$ 3 K) and pressure (101 kPa). The collected fibers were thermally treated in air at 923 K for 8 h at a ramping rate of 5 K min^{-1} to remove the majority of PVP and form calcium oxide. A second thermal treatment was performed on the Al-doped nanofibers to yield a mayenite structure (Ca$_{12}$Al$_{14}$O$_{33}$),[140,141] a stable calcium-aluminate framework, and CaO. Specifically, the Al-doped fibers were treated in air at 923 K for 5 h at ramping rate of 5 K min^{-1} and then at 1173 K for 2 h at ramping rate of 2 K min^{-1}. In this work, the non-doped electrospun CaO sorbent is denoted as CaO-nanofibers whereas the Al-doped CaO sorbents are denoted as 3Al-10Ca-O-nanofibers, 1Al-10Ca-O-nanofibers, and 1Al-20Ca-O-nanofibers, where the numbers before the Ca and Al correspond to the atomic ratio of Al to Ca in the synthesis procedure.

5.2.1.3 Thermal Syntheses of CaO from Calcium Acetate and Calcium Nitrate

Calcium acetate was crushed and sieved to < 200 mesh, and then thermally treated in air at 1023 K for 8 h (ramp rate of 5 K min^{-1}) to form CaO (denoted as CaO-D-acetate). Additionally, calcium nitrate was crushed and sieved to <200 mesh, and then thermally treated in air at 923 K for 8 h (ramp rate of 5 K min^{-1}) to form CaO (denoted as CaO-D-nitrate).

A porous CaO sample was synthesized according to the method of surfactant-assisted hydrothermal interaction (denoted as CaO-H-nitrate).[142,143] First, calcium nitrate was heat treated under air at 1023 K for 8 h (ramp rate of 5 K min^{-1}) to decompose the nitrate group and form calcium oxide. Subsequently, 0.8 g of CaO was mixed in a beaker containing 150 cm^3 of DI water and 5 cm^3 of ethanol, and stirred for 2 h. The CaO solution was then ultrasonically treated for 2 h. The surfactant solution was prepared by dissolving 2.8 g of P123 in 100 cm^3 of water while stirring for 2 h. After stirring, the CaO-containing solution was added to the surfactant solution, left stirring for 72 h, and then ultrasonically treated for 4 h. The solution was then transferred to a 1000 cm^3 Teflon-lined stainless-steel autoclave for hydrothermal treatment at 473 K for 60 h. The solid substance was filtered out and washed with 480 cm^3 of DI water and 20 cm^3 of ethanol for the removal of the majority of the P123 surfactant. The solid was then dried overnight in a drying oven at 353 K. The as-obtained material was calcium hydroxide ($Ca(OH)_2$), which was subsequently thermally treated in air from room temperature to 923 K at ramping rate of 5 K min^{-1} for the generation of CaO.

5.2.2 Characterization

The synthesized CaO-based sorbents prepared via thermal decomposition, hydrothermal treatment and electrospinning were characterized using a variety of techniques. Powder X-ray diffraction patterns were obtained on an X-ray diffractometer (JEOL JDX-3530 and Philips X-Pert) using Cu Kα radiation of 1.54 Å to identify the CaO and $Ca_{12}Al_{14}O_{33}$ phases. The average crystallite sizes were found using Scherrer's formula. Nitrogen adsorption-desorption isotherms were measured at 77 K with a Micrometrics ASAP 2020 Plus system. The Brunauer-Emmett-Teller (BET) surface areas were calculated from the isotherms. The pore size distribution was derived from the adsorption branches of the isotherms using the Barrett-Joyner-Halenda (BJH)

model. Scanning electron microscopy with energy dispersive X-ray spectroscopy (NOVA 230 Nano SEM/EDS) was used to determine the morphology and chemical composition of the sorbents. The mean diameter and size distribution of the electrospun nanofibers were calculated from the SEM micrographs using ImageJ software (n = 250; where, n is the number of fibers that were measured and averaged). The FEI Titan 80-300 kV S/TEM was used to carry out the transmission electron microscopy (TEM) analysis. The TEM samples were prepared by drop casting an ethanolic dispersion of CaO onto a carbon-coated Cu grid.

5.2.3 Carbonation and Methane Reforming Testing

Reaction kinetics and capacities for CaO carbonation were collected via thermogravimetric analysis using a Perkin Elmer TGA. Alumina crucibles were used to hold the samples. Gas flowrates were set to 200 standard cm^3 min^{-1} to minimize external diffusion from the bulk gas to the sample interface. Heating/reaction occurred in house air (dry, CO_2-free), CO_2 (Wright Bros, Inc., 99.5%) and/or argon (Matheson UHP Argon, 99.999% purity) at a ramping rate of 5-20 K min^{-1}. Prior to carbonation reaction testing, CaO-marble samples were crushed and sieved to < 200 mesh. Prior to all reactions (carbonation or methane reforming) all samples were calcined in air at 923 K with a ramp rate of 5 K min^{-1} for 8 h in a Thermolyne F6028C-80 muffle furnace. In the TGA, prior to reaction with CO_2, the CaO-based sorbents were treated at 1073 K for 10 minutes at a ramp rate of 10 K min^{-1} in air to ensure the decomposition of any residual $Ca(OH)_2$ or $CaCO_3$ that formed during exposure to the atmosphere.[136] After the *in-situ* calcination, the samples were cooled at a rate of 20 K min^{-1} to their reaction temperatures and held for 20 min to equilibrate. All samples were carbonated for 1 h at 101 kPa in 200 sccm of pure CO_2.

The first cycle for each of the cycling studies were carried out according to the methods described in the previous paragraph. For subsequent cycles, following 1 h of carbonation, the gas

was switched from CO_2 to air, and the temperature was ramped from 873 K to 1073 K at a rate of 10 K min^{-1}. Samples were held at 1073 K for 10 min, then cooled to 873 K at a rate of 15 K min^{-1}. Samples were then held at 873 K for 15 min to equilibrate before the gas was switched from air to CO_2 to begin subsequent carbonation.

CaO-marble, CaO-nanofibers, and 1Al-20Ca-O-nanofibers were tested for sorption enhanced steam methane reforming (SE-SMR) in a stainless steel packed bed reactor (½" OD) containing physical mixtures of commercial NiO-based methane reforming catalyst (HiFUEL R110, Alfa Aesar, 40% nickel (II) oxide and 60% aluminum oxide) with CaO-marble (2.58 g of CaO-marble with 1.01 g of HiFUEL; 180-250 μm particles), CaO-nanofibers (0.247 g CaO-nanofibers with 0.384 g HiFUEL), or 1Al-20Ca-O-nanofibers (0.322 g 1Ca-20Al-O-nanofibers with 0.421 g HiFUEL) between two plugs of quartz wool. The CO_2 sorbents were pretreated ex-situ at 923 K for 8 h at a ramp rate of 5 K min^{-1} in air. Prior to reaction, the sorbent/catalyst mixture was pretreated in-situ under 50 sccm H_2 at 998 K (ramp rate of 2.3 K min^{-1}) for 10 hrs. After H_2 pretreatment, the temperature was reduced to 823 K (measured with a type-K thermocouple) in 50 sccm helium (Airgas UHP helium, 99.999% purity) before introduction of a 90% methane/10% argon reactant mixture (Praxair, ±2% methane). Reactant and product compositions were measured online using an Agilent 7890B GC system with a thermal conductivity detector. All gasses were introduced with electronic mass flow controllers (MKS, model GE50A). Water was introduced through a positive displacement pump into the gas line, which was heated to temperatures above 393 K from the gas inlet to the post reactor condenser, to ensure all water in the system is in vapor phase (temperatures along the gas line were measured using type-K thermocouples). The total flowrate at reaction conditions for the SE-SMR reaction containing CaO-marble was 300 cm^{-3} min^{-1}, and for the reaction containing CaO-nanofibers and 1Al-20Ca-

O-nanofibers, the total flowrate was 100 cm^{-3} min^{-1}. The ratio of sorbent to gas flow was 120 cm^{-3} min^{-1} g^{-1} for the reaction containing CaO-marble and 405 cm^{-3} min^{-1} g^{-1} and 310 cm^{-3} min^{-1} g^{-1} for the reactions containing CaO-nanofibers and 1Al-20Ca-O-nanofibers, respectively. The steam to carbon ratio is 3 for all reactions.

5.2.4 Random Pore Model

The random pore model (RPM), first proposed by Bhatia and Perlmutter[144,145] and simplified to two equations by Grasa et al.[146] for the kinetic (Equation 1) and diffusion reaction regimes (Equation 2), was used in this work to quantify carbonation reaction kinetics in terms of the reaction rate constant (k_{RPM}) and the effective diffusivity (D_{RPM}). The structural parameter, Ψ (Equation 3), was calculated using the initial surface area (S_0), initial length of pores (L_0), and initial porosity (ε_0), which were determined from the N_2 physisorption isotherms. The RPM was not applied to the cycling studies due to potential changes in Ψ during carbonation-calcination cycling. In Equations 1 and 2, C_b, C_e, t, M_{CaO}, ρ_{CaO}, and Z are the bulk concentration of CO_2, equilibrium concentration of CO_2, reaction time, molar mass of CaO, density of CaO, and ratio of molar volumes of $CaCO_3$ to CaO, respectively.

$$\frac{1}{\Psi}\left[\sqrt{1-\Psi\,ln(1-X)}-1\right]=\frac{k_{RPM}S_0(C_b-C_e)t}{2(1-\varepsilon_0)} \tag{1}$$

$$\frac{1}{\Psi}\left[\sqrt{1-\Psi\,ln(1-X)}-1\right]=\frac{S_0}{1-\varepsilon_0}\sqrt{\frac{D_{RPM}M_{CaO}C_bt}{2\rho_{CaO}Z}} \tag{2}$$

$$\Psi=\frac{4\pi L_0(1-\varepsilon_0)}{S_0^2} \tag{3}$$

5.3 Results and Discussion

5.3.1 Physiochemical Properties of CaO and Al-Ca-O Sorbents

TGA experiments were conducted on the PVP-Ca(NO$_3$)$_2$ nanofibers to quantify the extent of PVP removal during thermal treatment and provide evidence of the conversion to CaO. **Figure 25** shows the TGA curves of pure PVP and PVP-Ca(NO$_3$)$_2$ nanofibers. Pure PVP nanofibers were decomposed under argon at a heating rate of 10 K min^{-1} whereas PVP-Ca(NO$_3$)$_2$ nanofibers were decomposed under air at a heating rate of 5 K min^{-1}. The heating rate was reduced in the case of PVP-Ca(NO$_3$)$_2$ to mimic the post-thermal treatment conditions described in section 5.2.1. The nanofibers synthesized using pure PVP (MW=1,300,000) decomposed under argon in two steps, with a total weight loss of approximately 95%. The first step weight loss of 16% occurred between ambient temperature and 622 K. This weight loss step can be attributed to the evaporation of volatile solvents. The second step weight loss of 79% from 623 to 763 K can be attributed to the thermal degradation of the polymer chains. It is clear from the TGA curve that the majority of the PVP matrix is removed at temperatures higher than 923 K. Additionally, PVP-Ca(NO$_3$)$_2$ nanofibers decompose under air in multiple steps, with a total weight loss of approximately 80% (**Figure 25**). The first step weight loss of 12% occurred between ambient temperature and 360 K and can be attributed to the evaporation of volatile solvents. The second weight loss of 27% from 580 to 620 K can be attributed to the rapid combustion of PVP in the presence of oxygen. The third gradual weight loss of 14% from 620 to 770 K can be attributed to the oxidation of residual carbon remaining on the nanofibers. The final weight loss of 24% from 770 to 790 K can be attributed to the decomposition of calcium nitrate (Ca(NO$_3$)$_2$) to CaO, indicating that the thermal treatments of PVP-Ca(NO$_3$)$_2$ nanofibers in this study result in the formation of CaO nanofibers without residual carbon.
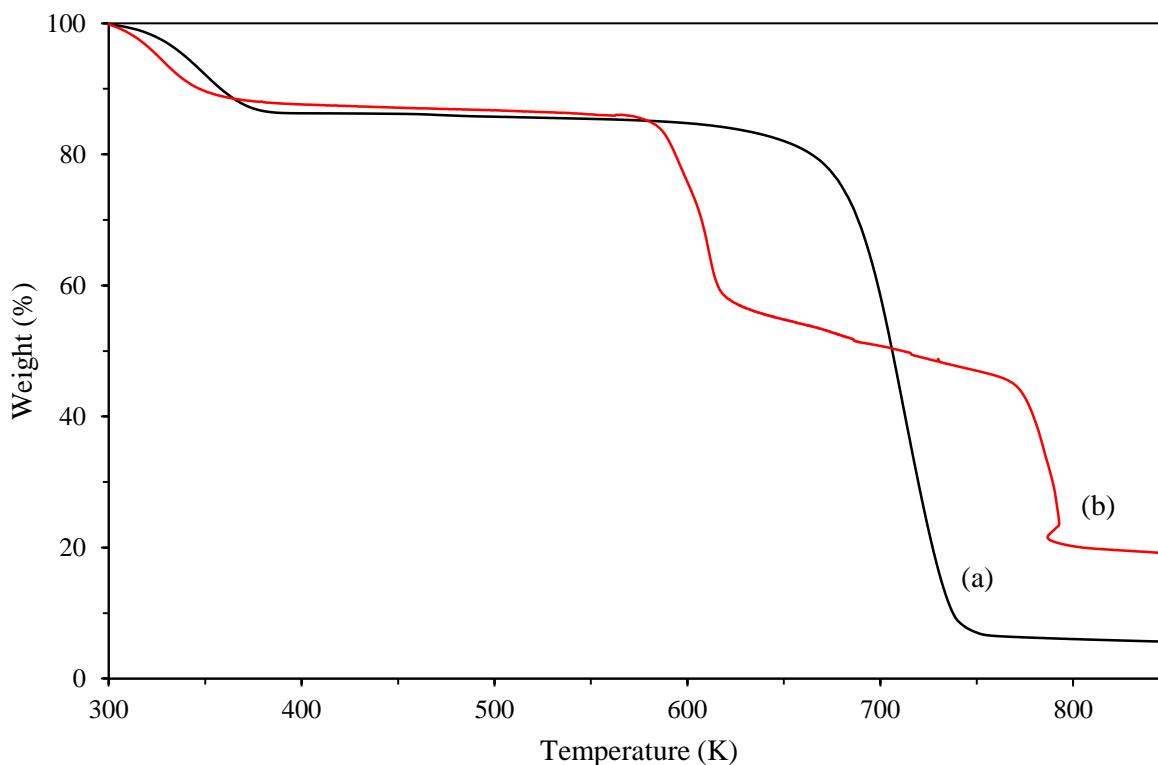
Figure 25. Weight loss profiles as a function of temperature from thermogravimetric analysis of (a) pure PVP nanofibers treated in argon (black) and (b) PVP-Ca(NO$_3$)$_2$ nanofibers treated in air (red).

XRD was used to identify the crystalline phases and average crystal sizes of the CaO and Al-Ca-O sorbents prepared using the synthesis techniques described in Section 5.2.1. **Figure 26 (a) (1)** shows the XRD patterns of the as-synthesized, non-doped PVP-Ca(NO$_3$)$_2$ nanofibers before thermal treatment at 923 K. Well defined diffraction peaks are absent from the XRD pattern, which indicates that the nanofibers consist of amorphous polymer phases and calcium species that are too small to diffract X-rays. **Figure 26 (a) (2-6)** shows the XRD patterns of CaO-nanofibers, CaO-D-acetate, CaO-D-nitrate, CaO-H-nitrate, and CaO-marble, respectively, after undergoing thermal treatment as described in section 5.2.1. Crystalline peaks of both CaO (■) and Ca(OH)$_2$ (●) were identified. Ca(OH)$_2$ was formed after the samples adsorbed moisture from the atmosphere because

of the hydroscopic nature of CaO.[147] The edge length of the unit cell of the five CaO sorbents was calculated using XRD. Each sample had a lattice parameter of 4.8 Å, confirming that the samples consist of cubic CaO. Average crystallite sizes were calculated from the peak at $2\theta = 37°$ using Scherrer's equation (**Table 13**). The average crystal domain sizes of CaO-nanofibers, CaO-D-acetate, CaO-D-nitrate, CaO-H-nitrate, and CaO-marble were 39 nm, 33 nm, 64 nm, 35 nm, and 84 nm, respectively, confirming that CaO derived from natural sources (in this case, marble) have significantly larger crystallite sizes than CaO derived from organometallic sources. The XRD patterns of the post-cycled CaO sorbents are shown in **Figure 26 (a) (7-9)**. Those results will be discussed in subsequent sections.
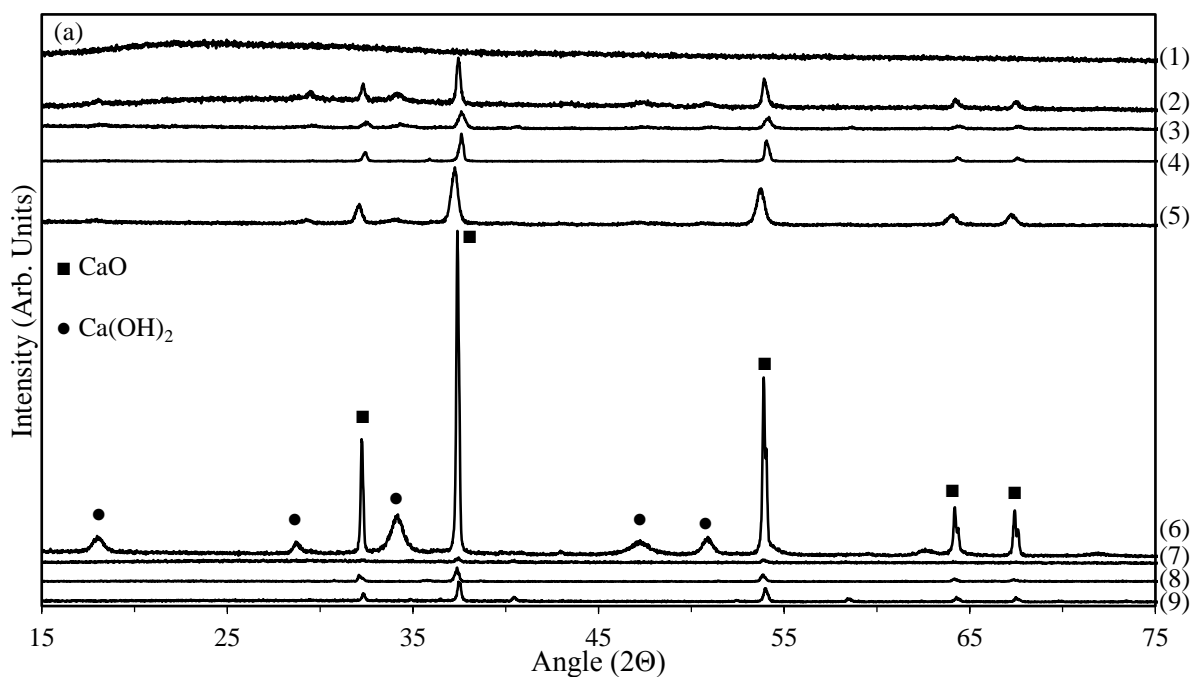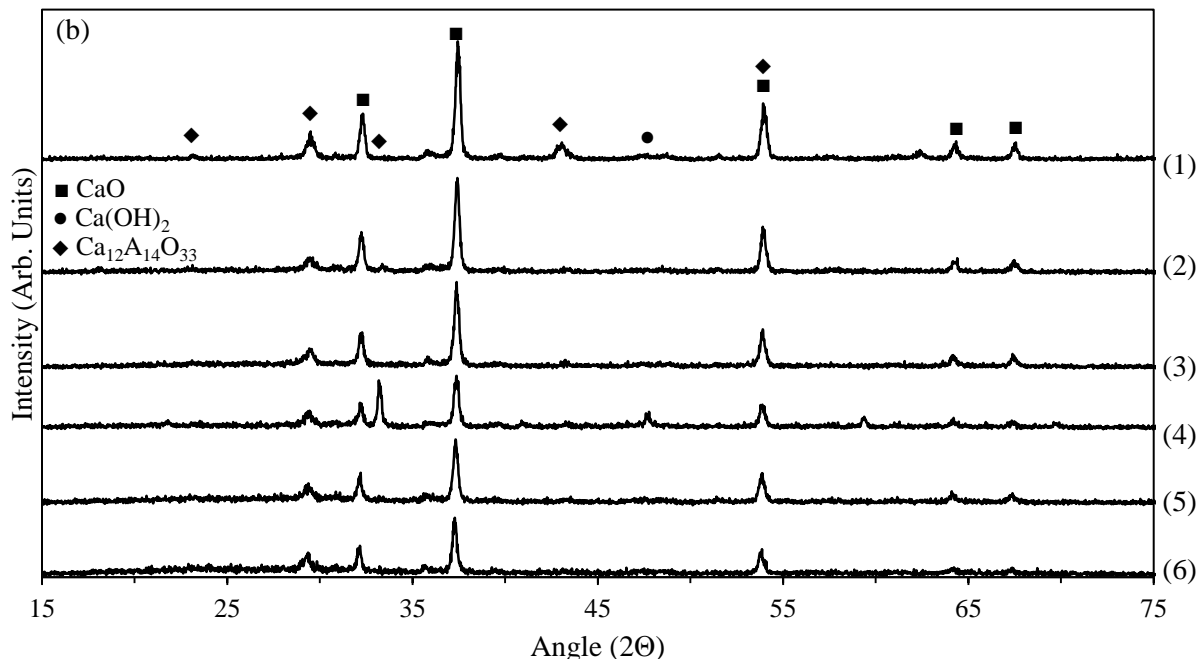
Figure 26. (a) XRD patterns of (1) PVP-Ca(NO$_3$)$_2$ nanofibers prepared via electrospinning prior to any thermal treatment, (2) CaO-nanofibers after thermal treatment (923 K, 101 kPa), (3) CaO-D-acetate (thermal decomposition), (4) CaO-D-nitrate (thermal decomposition), (5) CaO-H-nitrate (hydrothermal treatment), (6) CaO-marble (thermal treatment), (7) CaO-nanofibers after 10 cycles, (8) CaO-D-nitrate after 10 cycles, and (9) CaO-marble after 10 cycles. (b) XRD patterns of Al-doped electrospun materials: (1) 3Al-10Ca-O-nanofibers, (2) 1Al-10Ca-O-nanofibers, (3) 1Al-20Ca-O-nanofibers, (4) 3Al-10Ca-O-nanofibers after 17 cycles, (5) 1Al-10Ca-O-nanofibers after 16 cycles, and (6) 1Al-20Ca-O-nanofibers after 16 cycles. Characteristic peaks for CaO, Ca(OH)$_2$, Ca$_{12}$Al$_{14}$O$_{33}$ are indicated by squares, circles, and diamonds, respectively.

Figure 26 (b) shows the XRD patterns of the three Al-doped CaO-based nanofibers after undergoing thermal treatment at 1173 K as described in section 5.2.1. Crystalline peaks corresponding to mayenite,[148] Ca$_{12}$Al$_{14}$O$_{33}$, are evident in the XRD data as well as peaks corresponding to CaO. The XRD data confirms that Ca$_{12}$Al$_{14}$O$_{33}$, a stable composite metal, was integrated successfully into the CaO sorbent, to serve as a binder or a spacer. The average crystal domain sizes of the Al-doped electrospun materials were 53 nm (3Al-10Ca-O-nanofibers), 50 nm (1Al-10Ca-O-nanofibers), and 50 nm (1Al-20Ca-O-nanofibers). **Figure 26 (b)** also shows the

95

XRD patterns of the post-cycled Al-doped sorbents. Those results will be discussed in subsequent sections.

Table 13. Properties of CaO and Al-Ca-O sorbents. [a] Calculated by BET method. [b] Calculated by BJH method. [c] Based on XRD. [d] Obtained by EDS.

Sorbent	S_{BET} (m^2/g) [a]	V_{pore} (cm^3/g) [b]	Pore Diameter (nm) [b]	Crystallite Size (nm) [c]	Post-Cycled Crystallite Size (nm) [c]	Ca/Al [d]
CaO-marble	7.6	0.034	9.5	84	76 [10 cycles]	-
CaO-D-acetate	17	0.110	13.9	33	-	-
CaO-D-nitrate	4.8	0.003	2.7	64	73 [10 cycles]	-
CaO-H-nitrate	16	0.010	18.6	35	-	-
CaO-nanofibers	16	0.092	13.1	39	64 [10 cycles]	-
3Al-10Ca-O-nanofibers	-	-	-	53	50 [17 cycles]	3.5
1Al-10Ca-O-nanofibers	-	-	-	50	46 [16 cycles]	9.7
1Al-20Ca-O-nanofibers	-	-	-	50	48 [16 cycles]	22

N_2-physisorption was used to determine the surface area, pore volume, and average pore diameter of the CaO samples (**Table 13**). The CaO-nanofibers (16 m^2/g), CaO-D-acetate (17 m^2/g), and CaO-H-nitrate (16 m^2/g) samples exhibited more than twice the surface area of CaO-marble (7.6 m^2/g) and more than three times the surface area of CaO-D-nitrate (4.8 m^2/g). Similarly, the BJH pore volumes of the CaO-nanofibers (0.092 cm^3/g), CaO-D-acetate (0.110 cm^3/g), and CaO-H-nitrate (0.099 cm^3/g) samples were a factor of three higher than the CaO-marble sample (0.034 cm^3/g) and a factor of 30 higher than the CaO-D-nitrate sample (0.0032 cm^3/g). The chemically synthesized samples, with the exception of CaO-D-nitrate (2.7 nm), also had larger BJH average pore diameters (CaO-nanofibers: 13.1 nm, CaO-D-acetate: 13.9 nm, CaO-H-nitrate: 18.6 nm) compared to CaO-marble (9.5 nm). These data indicate that the techniques used to synthesize CaO

from organometallic precursors (i.e., hydrothermal treatment and electrospinning) lead to highly porous materials that retain their pore structure even after thermal treatments.

SEM was used to probe the effect of synthesis technique and calcium source on sorbent morphology at the micrometer scale. **Figure 28 (a, b)** shows the SEM image (5,000 and 20,000 times magnification) of the as-synthesized PVP-Ca(NO$_3$)$_2$ nanofibers before thermal treatment. The electrospun fibers consisted of uniform, continuous, and smooth nanofibers with circular cross sections. The fibers had a narrow distribution with a mean diameter of 180 $\pm$ 57 nm (**Figure 27**) and lengths of up to several hundred micrometers. As seen from **Figure 28 (a)**, a few spindle-like structural defects with an average diameter of 1.3 μm were present, and these defects were possibly formed from transient instabilities experienced by the travelling jet during the electrospinning process.[149,150] Upon thermal treatment at 923 K, CaO-nanofibers were obtained as indicated by the XRD analysis (discussed previously). The post thermally treated fibers (CaO-nanofibers) had a mean diameter of 208 $\pm$ 53 nm (**Figure 27 (b)**). By comparing the SEM images of the nanofibers before (**Figure 28 (a, b)**) and after thermal treatment (**Figure 28 (c)**), it becomes clear that the thermal treatment transforms the PVP-Ca(NO$_3$)$_2$ fibers from smooth and continuous nanofibers, which are cylindrical in shape, to a network of nanoparticles that are closely connected in a nanofibrous structure with considerable macro-porous (>300 nm diameter) intraparticle void volume. This change in morphology occurs, of course, because of the degradation of the polymer chains and the formation of CaO at these elevated temperatures.

Figure 28 (d-g) shows the SEM images of the remaining non-doped CaO sorbents (CaO-marble, CaO-D-acetate, CaO-D-nitrate, and CaO-H-nitrate) after undergoing thermal treatment. Both CaO-marble and CaO-D-nitrate had considerably large average agglomerate sizes, with the marble-derived sorbent having sizes of approximately 835 $\pm$ 262 nm (measured from the SEM

micrograph using ImageJ) and CaO-D-nitrate having agglomerates in the micron range. The agglomerate sizes of these two sorbents were a factor four or more larger than the other sorbents, with CaO-nanofibers having the smallest average agglomerate size of 184 ± 33 nm of the non-doped sorbents. Smaller agglomerate/particle sizes, in general, are believed to contribute to enhanced sorption performance due to their larger surface-to-volume ratios.[151] The SEM images in **Figure 28 (d-g)** also reveal that CaO samples prepared from the decomposition of calcium acetate and nitrate and from the hydrothermal treatment of CaO (using calcium nitrate as a precursor) have uneven surface textures with considerably rough and sharp edges. On the other hand, the marble-derived CaO and electrospun CaO nanofibers have well-defined, rounder, and smoother structures, with the nanofibers having a noticeably smaller domain size and visibly larger macro-sized void volumes.
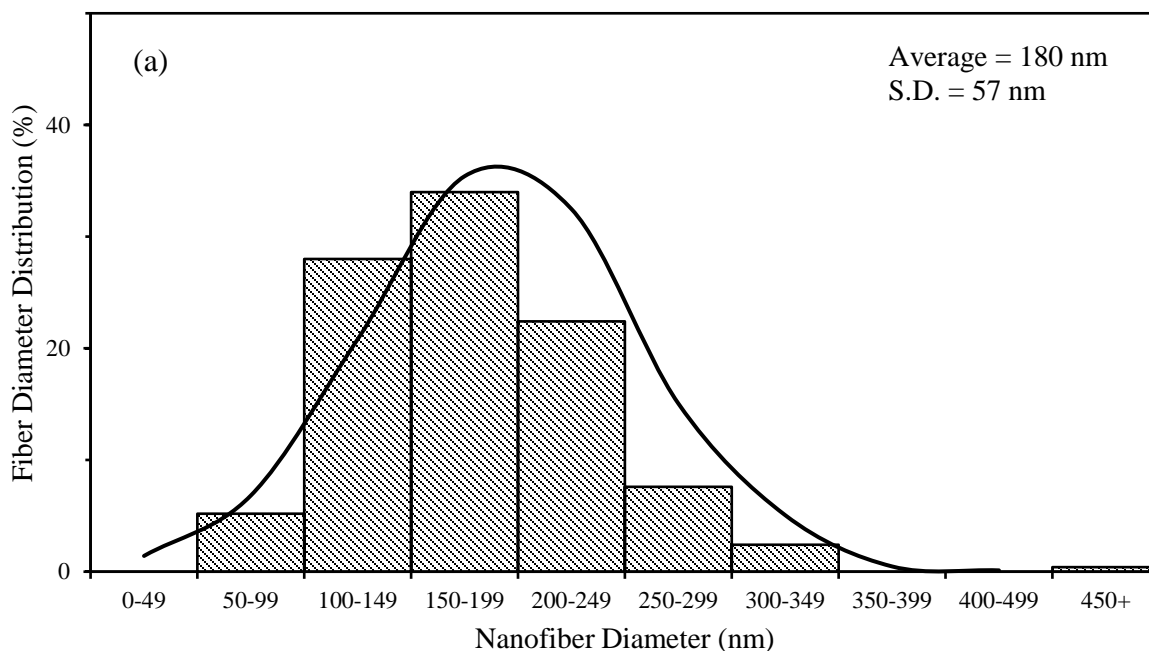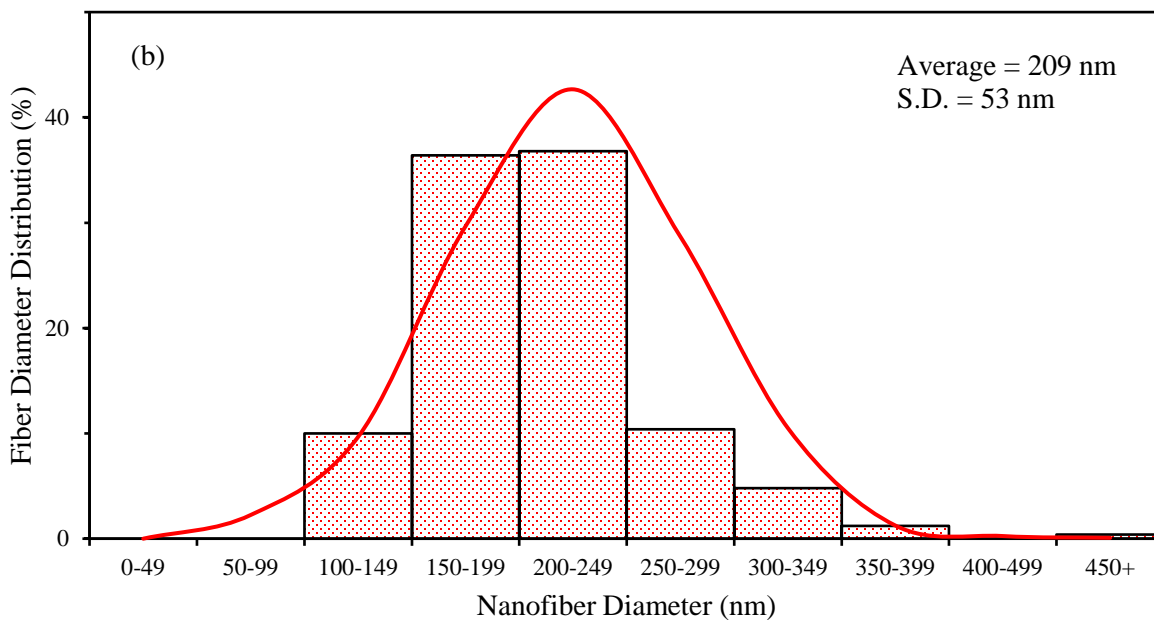
Figure 27. Diameter distribution and normal distribution of (a, black) PVP-Ca(NO$_3$)$_2$ nanofibers before thermal treatment and (b, red) CaO-nanofibers after thermal treatment at 923 K. The average diameter and standard deviation for the fibers were calculated using ImageJ (n=250) as described in section 5.2.2 in the main text.

Figure 28 (h-j) shows the SEM images of the Al-doped CaO sorbents (3Al-10Ca-O-nanofibers, 1Al-10Ca-O-nanofibers, and 1Al-20Ca-O-nanofibers). The SEM images reveal that all the Al-containing nanofibers have morphologically similar features as the non-doped CaO-nanofibers sorbent, albeit with slightly smaller domain sizes. The reduction in the domain size of the Al-Ca-O sorbents is believed to be due to the higher metal content present in the electrospinning solution (i.e., more aluminum nitrate ions), which increases the conductivity of the electrospinning solution, which in turn yields thinner fibers.[55,152] In addition to SEM, EDS analysis was performed on the Al-doped samples to confirm the atomic ratio of Al to Ca in the formed sorbents. **Table 13** shows the Al/Ca ratios obtained from the SEM/EDS analysis.

Figure 28 (k-o) shows the SEM images of the CaO-based sorbents following 10-17 cycles of carbonation and calcination. As seen from the SEM images, the non-doped CaO sorbents (CaO-

marble and CaO-nanofibers) suffered from severe morphological changes after 10 cycles of carbonation and calcination whereas the Al-doped samples were able to retain several morphological features (particularly, their macro-sized void volumes and fibrous structure) to higher degrees even after 16-17 cycles. The degree of resistance to sintering and change in morphology was, indeed, more pronounced in the samples that contained Al, especially those with higher Al to Ca ratios, as evidenced by the SEM images (**Figure 28 (k-o)**). The significance of these results and its impact on performance and sorbent stability is discussed in more depth in subsequent sections.
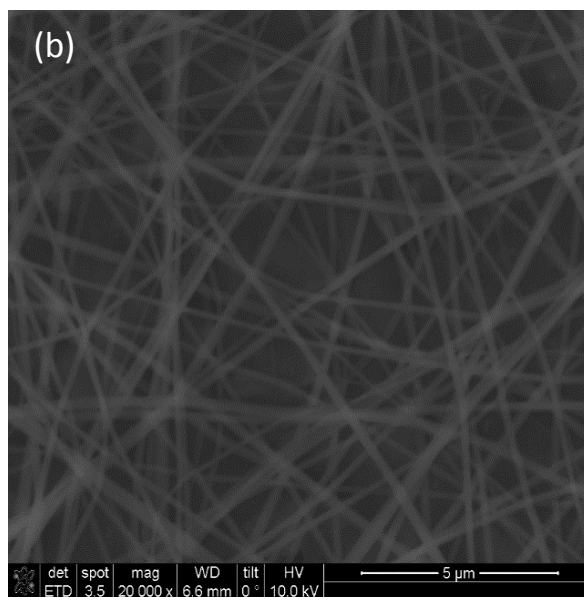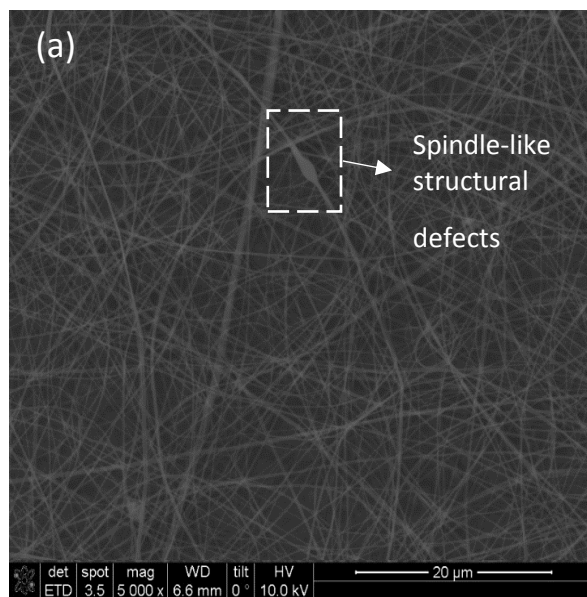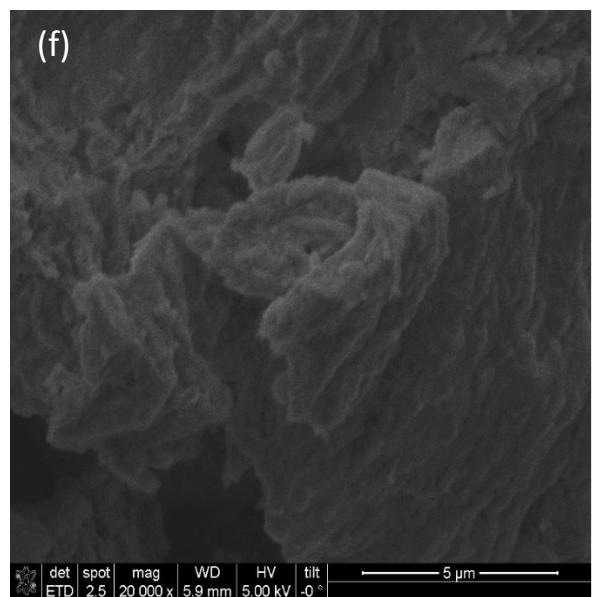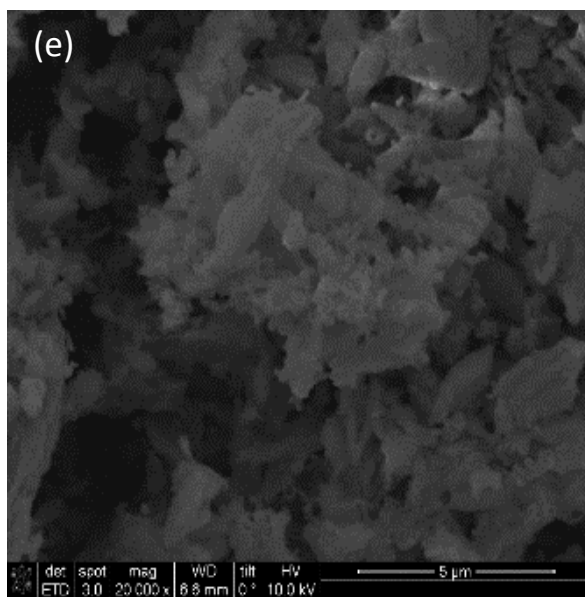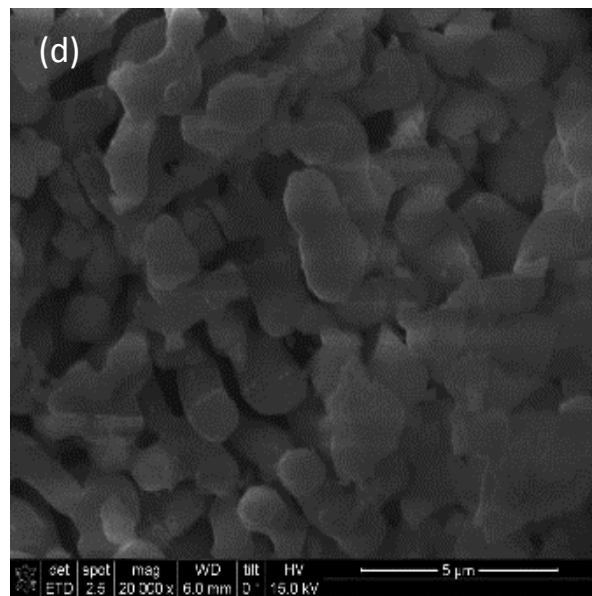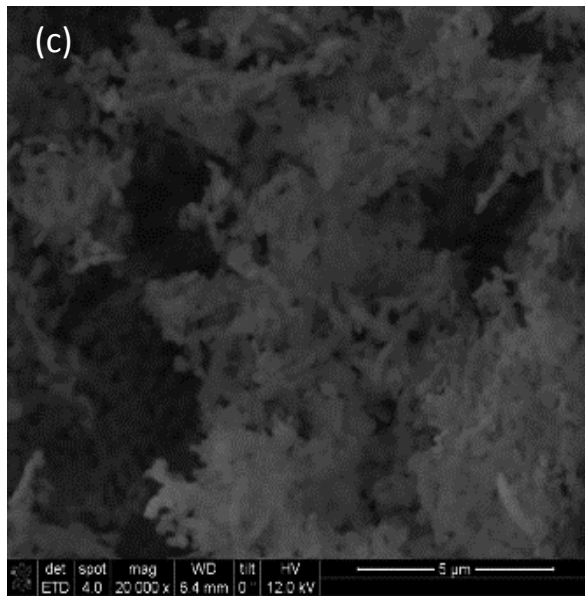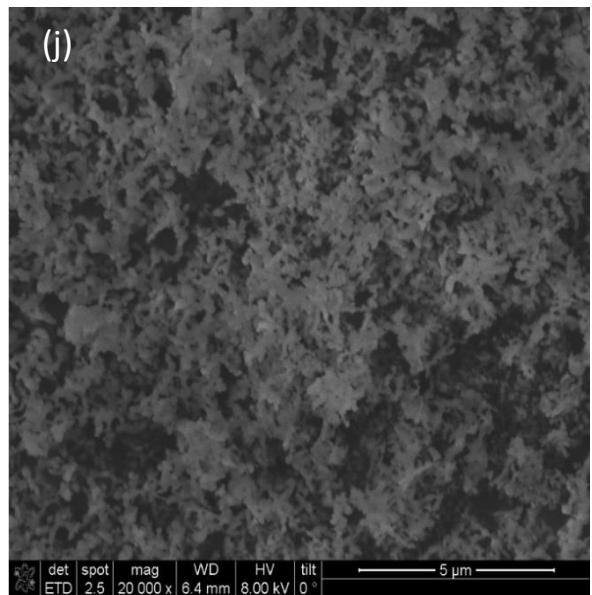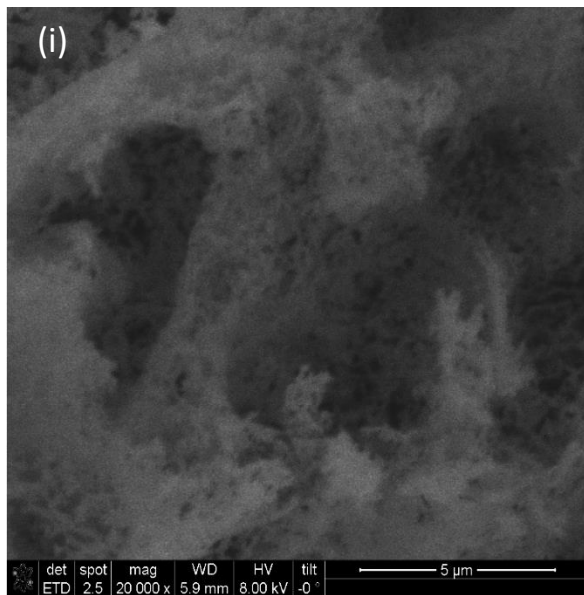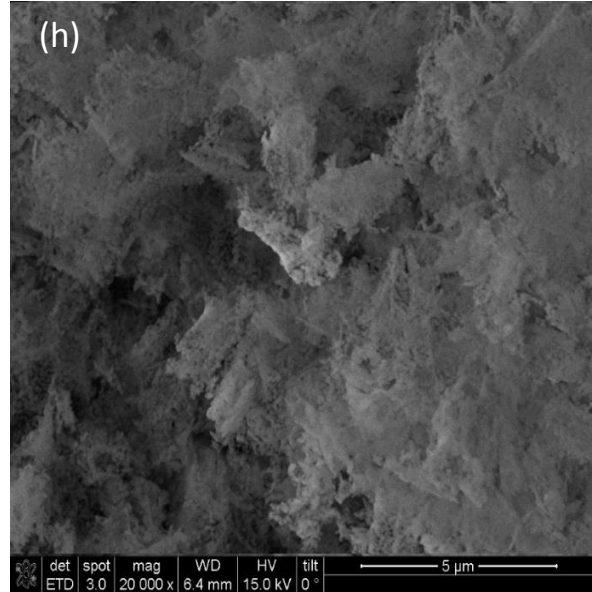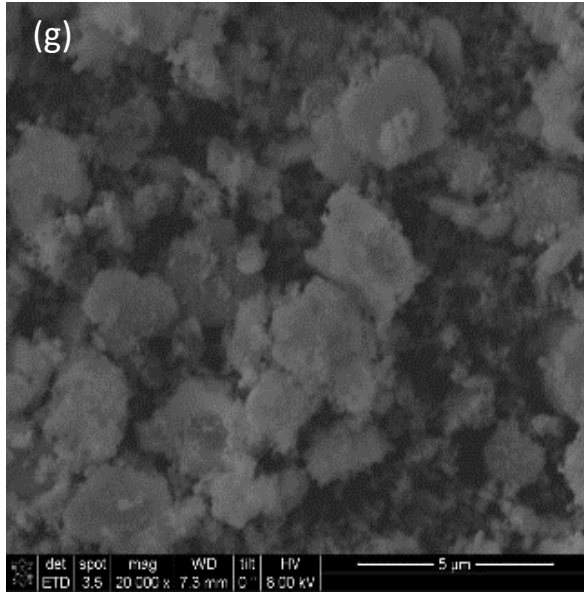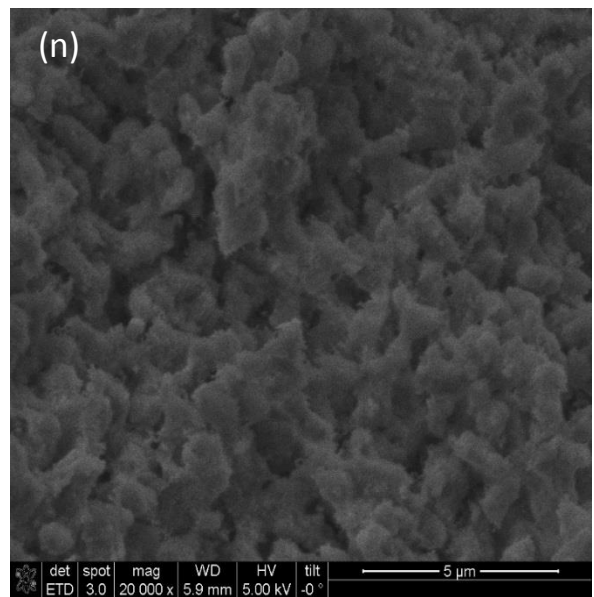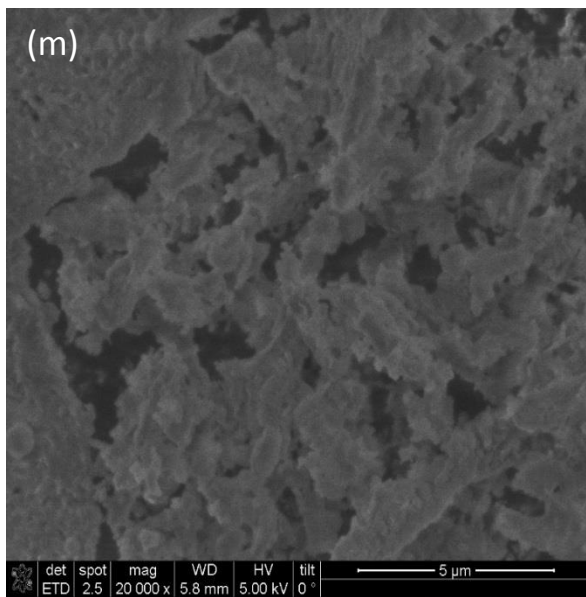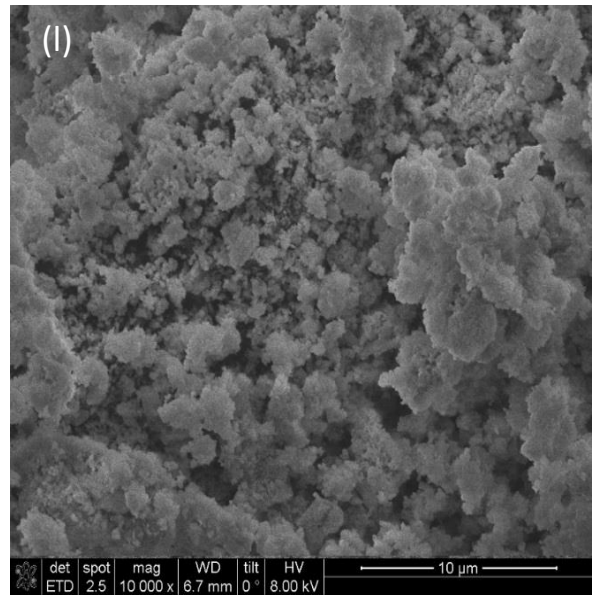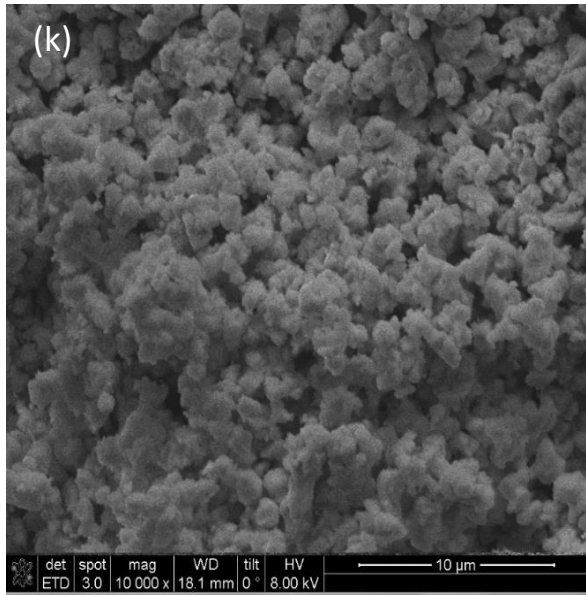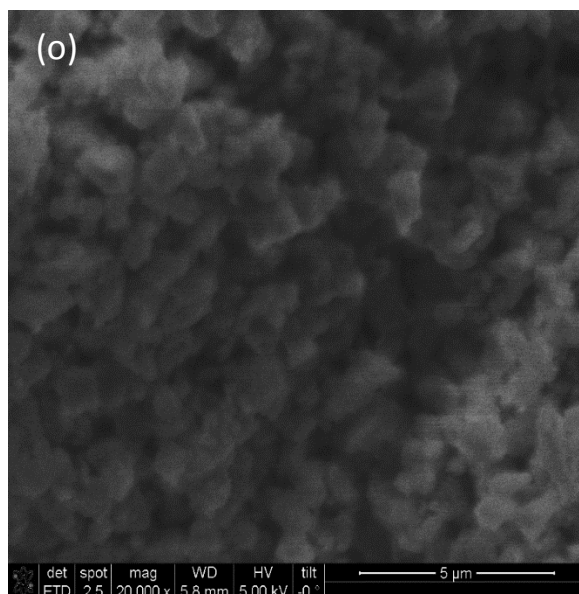
Figure 28. SEM images of as-synthesized PVP-Ca(NO$_3$)$_2$ nanofibers at (a) 5,000x and (b) 20,000x magnification, (c) CaO-nanofibers synthesized via electrospinning and thermally treated in air at 923 K (CaO-nanofibers), (d) CaO derived from marble (CaO-marble), (e) CaO synthesized from the thermal decomposition of calcium acetate in air at 1023 K (CaO-D-acetate), (f) CaO synthesized from the thermal decomposition of calcium nitrate in air at 923 K (CaO-D-nitrate), (g) CaO synthesized from thermal decomposition of calcium nitrate at 1023 K followed by treatment with an aqueous solution of P123 and thermal treatment in air at 923 K(CaO-H-nitrate), (h) 3Al-10Ca-O-nanofibers, (i) 1Al-10Ca-O-nanofibers, (j) 1Al-20Ca-O-nanofibers, (k) CaO-marble after 10 cycles, (l) CaO-nanofibers after 10 cycles, (m) 3Al-10Ca-O-nanofibers after 17 cycles, (n) 1Al-10Ca-O-nanofibers after 16 cycles, and (o) 1Al-20Ca-O-nanofibers after 16 cycle.

TEM analysis was performed on four non-doped CaO sorbents (CaO-marble, CaO-D-acetate, CaO-H-nitrate, and CaO-nanofibers) to supplement the SEM analysis and determine the impact of synthesis approach on morphology. **Figure 29** shows the TEM images of the four sorbents. It reveals that CaO derived from marble consists of large, closely-packed and multi-layered nanoparticles, with sizes ranging from roughly 50 to 180 nm. The CaO-H-nitrate and CaO-D-acetate samples, as seen in **Figure 29**, had comparatively smaller nanoparticles. Specifically, their particle sizes ranged from approximately 25 to 120 nm. The electrospun CaO-nanofibers had nanoparticles with diameters ranging from approximately 70 to 180 nm; however, they contained

significantly larger macro-porous intra-particle void volumes. These intra-particle spaces, as shown in **Figure 29 (c)**, appear as void channels and have diameters that are as small as 10 nm and as large as 0.45 µm. These larger pores (>300 nm) are undetectable using N_2 physisorption, however, they can be identified in the SEM and TEM images.
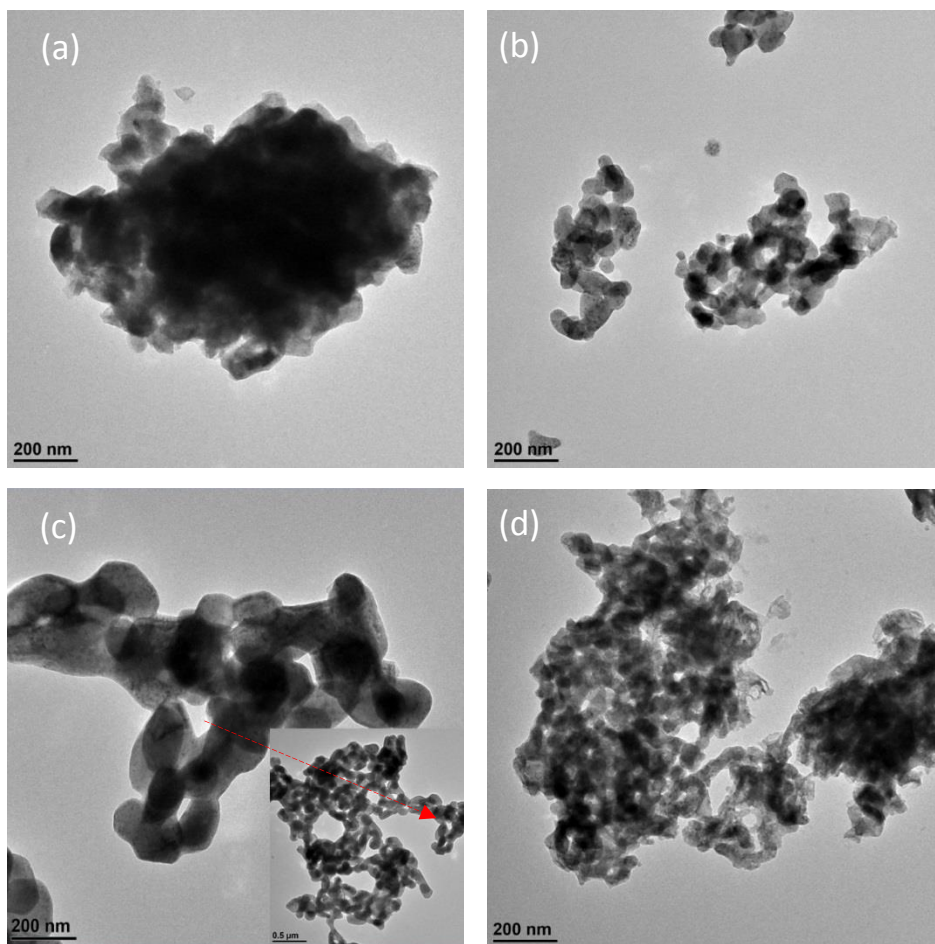
Figure 29. TEM images of (a) CaO derived from marble (CaO-marble), (b) CaO synthesized from the thermal decomposition of calcium nitrate at 1023 K followed by treatment with an aqueous solution of P123 (CaO-H-nitrate), (c) CaO-nanofibers synthesized via electrospinning and thermally treated in air at 923 K (CaO-nanofibers), and (d) CaO synthesized from thermal decomposition of calcium acetate in air 1023 K (CaO-D-acetate).

5.3.2 Carbonation of CaO-Based Sorbents

5.3.2.1 First Cycle

TGA experiments were conducted on the five non-doped CaO samples (CaO-marble, CaO-D-acetate, CaO-D-nitrate, CaO-H-nitrate, and CaO-nanofibers) to compare their CO_2 sorption capacity and reaction rates. **Figure 30** shows the first-cycle carbonation reaction curves (in terms of conversion of CaO to $CaCO_3$ and capacity (g_{CO2}/g_{CaO}) versus time on stream) at three temperatures (823, 873, and 923 K). From the experimental carbonation curves, the conversion appears to evolve with time in two stages: a fast chemical reaction-controlled stage followed by a slower increase that is controlled by diffusion of gaseous reactants through solid product layers.[153] TGA experiments were stopped after 60 minutes because at this time the conversion appears to approach a constant value with increasing time on stream.
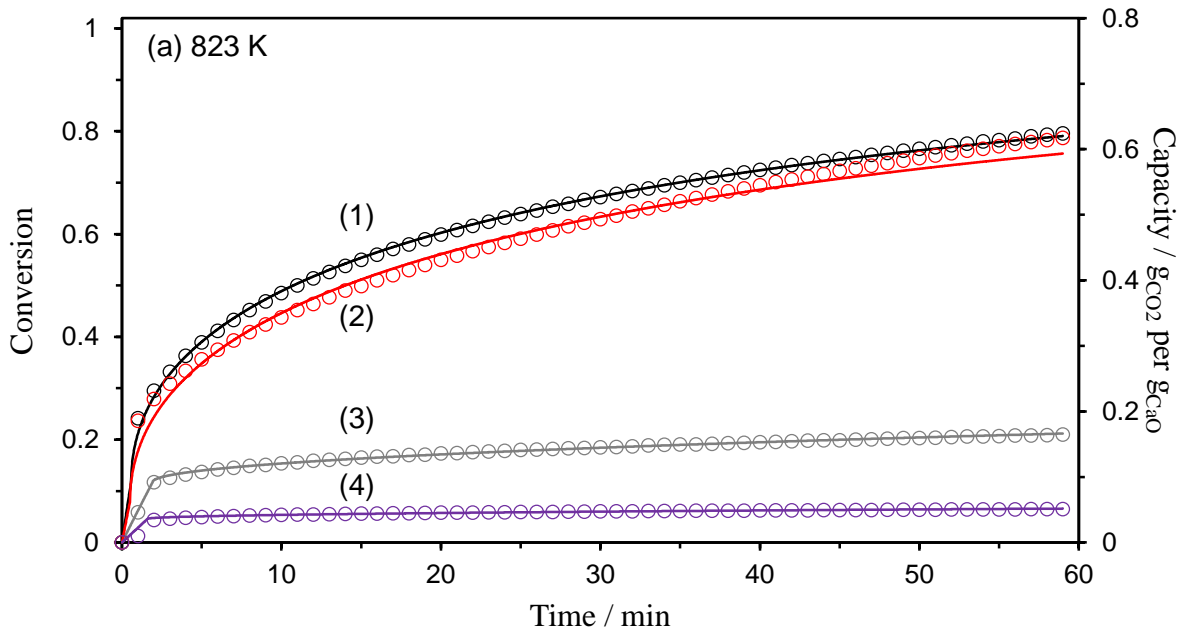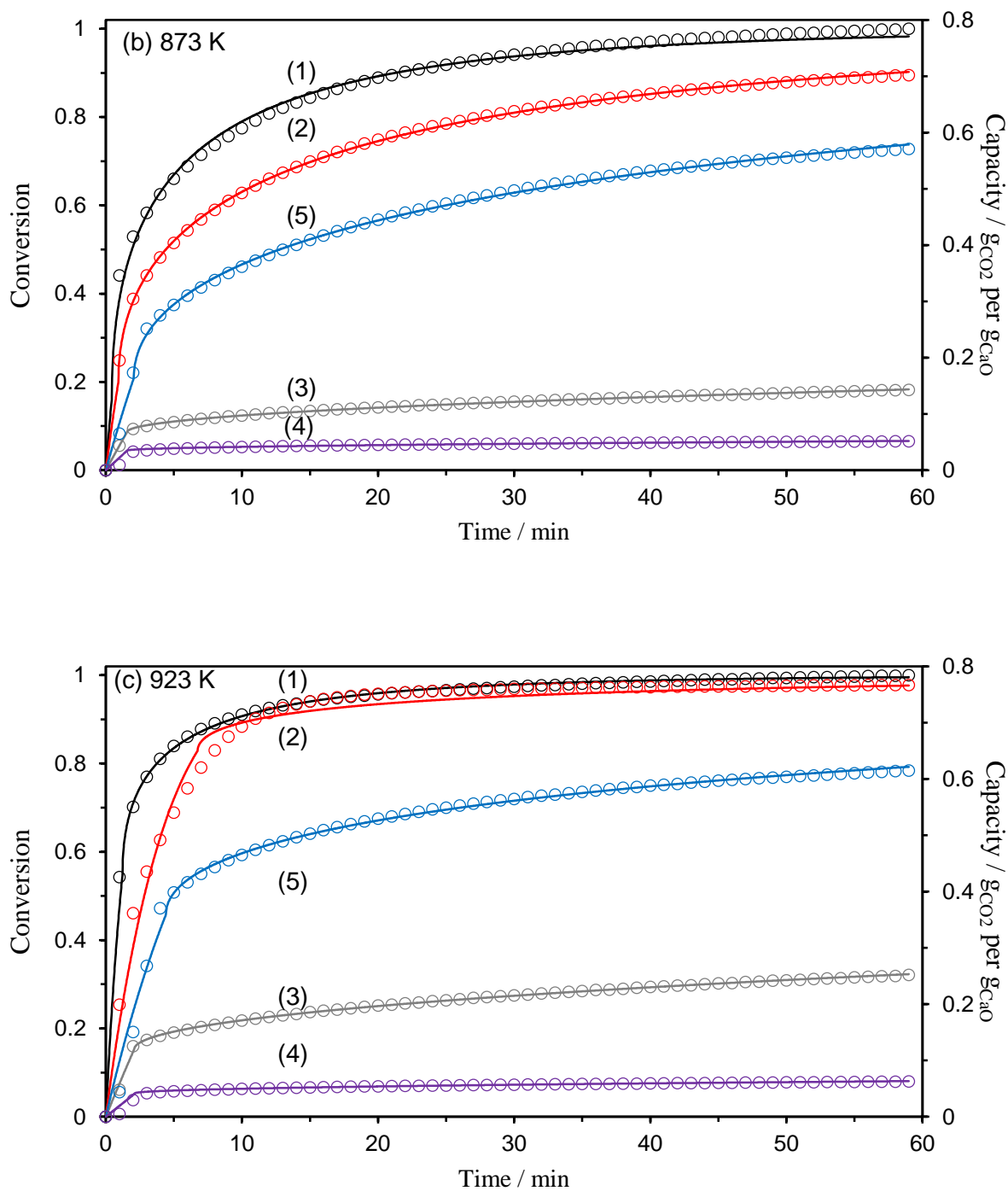
Figure 30. Experimental conversion, sorption capacities, and RPM prediction of conversion (lines) for (1) CaO-nanofibers, (2) CaO-D-acetate, (3) CaO-marble, (4) CaO-D-nitrate, and (5) CaO-H-nitrate measured by TGA at (a) 823 K, (b) 873 K, and (c) 923 K, 101 kPa, and with 200 sccm of CO_2.

The differences in conversion among the five samples (**Table 14**) indicates the effect of morphological features and physiochemical properties on CO_2 sorption. CaO-marble, a sample that has large agglomerate, particle and crystallite sizes as well as low surface area and intra-particle void volume (as discussed in section 5.3.1), exhibited conversions of 20% (0.17 g_{CO2}/g_{CaO}) at 823 K, 18% (0.14 g_{CO2}/g_{CaO}) at 873 K, and 32% (0.25 g_{CO2}/g_{CaO}) at 923 K, in agreement with previous studies.[131,154] Additionally, CaO-D-nitrate, another sample with a relatively large crystallite size and small surface area and pore volume (an order of magnitude smaller than CaO-marble), exhibited conversions of 6.5% (0.05 g_{CO2}/g_{CaO}) at 823 K, 6.5% (0.05 g_{CO2}/g_{CaO}) at 873 K, and 8% (0.06 g_{CO2}/g_{CaO}) at 923 K. The decrease in reactive surface area and pore volume for carbon dioxide diffusion resulted in approximately a four-fold decrease in conversion. On the other hand, the CaO samples synthesized from the decomposition of calcium acetate (CaO-D-acetate) and hydrothermal treatment of CaO (CaO-H-nitrate) exhibited more than threefold higher conversions than CaO-marble and CaO-D-nitrate at all temperatures (**Table 14**), with CaO-nanofibers achieving stoichiometric CO_2 capacity (0.79 g_{CO2}/g_{CaO}) in less than one hour of reaction at both 873 K and 923 K. The higher saturation conversion of the CaO-D-acetate, CaO-H-nitrate, and CaO-nanofibers provides evidence to support the conclusion that structures with small crystallites and high porosity (high surface area and intraparticle void volume) enhance the reactivity of CaO materials and reduce their susceptibility to transport limitations from the formation of product layers that cover surfaces and fill pores.

Table 14. TGA saturation conversion (in parenthesis) and sorption capacity (g_{CO2}/g_{CaO}) of CaO-marble, CaO-D-nitrate, CaO-H-nitrate, CaO-D-acetate, and CaO-nanofibers at different temperatures (823, 873 and 923 K) after 1 h of reaction with CO_2.

Temperature (K)	Sorbents Sorption Capacity (g_{CO2}/g_{CaO}) and Conversion (%)				
	CaO-marble	CaO-D-nitrate	CaO-H-nitrate	CaO-D-acetate	CaO-nanofibers
823	0.16 (21%)	0.05 (6.5%)	-	0.62 (79%)	0.63 (80%)
873	0.14 (18%)	0.05 (6.5%)	0.59 (73%)	0.70 (90%)	0.79 (100%)
923	0.25 (32%)	0.06 (8%)	0.62 (78%)	0.77 (98%)	0.79 (100%)

The CaO-nanofibers sample also exhibited higher capacity (0.79 g_{CO2}/g_{CaO} at 873 and 923 K) compared to CaO-D-acetate (0.70 and 0.77 g_{CO2}/g_{CaO} at 873 and 923 K, respectively) and CaO-H-nitrate (0.59 and 0.62 g_{CO2}/g_{CaO} at 873 and 923 K, respectively). These three samples all consisted of similar particle and crystallite sizes, surface areas, and meso-pore volumes (**Table 13**), therefore, the higher capacity of the nanofibers could potentially be attributed in part to the larger intra-macro-porosity within the nanofiber networks imparted by the electrospinning synthesis technique as shown via TEM in **Figure 29**. Furthermore, the CaO-H-nitrate sample synthesized by hydrothermal treatment in our studies exhibited a much higher conversion (73% at 873 K) compared to the thermally decomposed $Ca(NO_3)_2$ (CaO-D-nitrate) (6.5% at 873 K). As a matter of fact, the low conversion of CaO synthesized from the simple thermal decomposition of $Ca(NO_3)_2$ (CaO-D-nitrate) is consistent with the values reported by Le et al. (2.5%) for such materials.[136] Therefore, the studies reported herein indicate that synthesis technique plays a pivotal role in dictating the sorbent capacity of a CaO-based material by controlling morphology and properties such as, crystallite size, surface area, pore volume, pore diameter, and intraparticle void volumes. In this work, specifically, hydrothermal treatment and electrospinning were found to alter the macro-porosity of the sample; introduction of these macro-pores abates diffusional restrictions from pore filling and surface coverage effects, thus, leading to higher sorption capacities.

To quantify the observed differences in performance, the results from the TGA experiments were analyzed using the RPM. The RPM models the rate of change of pore radii at the initial stages of conversion using a reaction rate equation that is first order in the concentration of CO_2 and normalized by the surface area of the material. Thus, the reaction rate constant (k_{RPM}) in this equation is also normalized by surface area and reflects the rate of chemical reaction at the surface. The formation of non-reactive $CaCO_3$ surfaces serve as a diffusional barrier, and as the non-reactive product surfaces grow and intersect with each other, the system transitions into a more diffusion dominated regime. The effective diffusivity (D_{RPM}) quantitatively characterizes this regime and reflects the differences in product layer thickness and penetrability.

Values for k_{RPM} and D_{RPM} (**Table 15**) were determined using Athena Visual Studio. RPM model predictions (lines) are shown in **Figure 30** (overlaid with experimental conversion data points). The rate constants exhibit an exponential dependence on inverse temperature, and the activation energies for the reaction (E_a = 9, 20, 31, and 73 kJ/mol for CaO-D-nitrate, CaO-marble, CaO-D-acetate, and CaO-nanofibers, respectively) are within similar ranges as previous studies (E_a = 28.4 kJ mol^{-1} as reported by Zhou et al.[155]). Values for k_{RPM} for CaO-H-nitrate (2.5×10^{-4} ± 1.2×10^{-6} and 3.1×10^{-4} ± 1.7×10^{-6} cm^4 mol^{-1} s^{-1} at 873 and 923 K, respectively) are similar to those for CaO-D-nitrate (2.1×10^{-4} ± 1.1×10^{-6} and 2.3×10^{-4} ± 1.34×10^{-5} cm^4 mol^{-1} s^{-1} at 873 and 923 K, respectively) and CaO-marble (3.1×10^{-4} ± 1.2×10^{-6} and 3.8×10^{-4} ± 2.0×10^{-6} cm^4 mol^{-1} s^{-1} at 873 and 923 K, respectively), as expected for materials that are chemically the same (i.e., crystalline CaO). The D_{RPM} values for CaO-H-nitrate (4.7×10^{-12} ± 1.9×10^{-14} and 3.6×10^{-12} ± 5.1×10^{-14} cm^2 s^{-1} at 873 and 923 K, respectively), however, are 5 to 10 times larger than CaO-marble (2.0×10^{-13} ± 1.0×10^{-15} and 9.0×10^{-13} ± 5.0×10^{-15} cm^2 s^{-1} at 873 and 923 K, respectively). Additionally, the D_{RPM} values for CaO-D-nitrate (2.0×10^{-14} ± 1.0×10^{-15} and 4.0×10^{-14} ± 6.0×10^{-15} cm^2 s^{-1} at 873 and 923

110

K, respectively) are approximately one order of magnitude smaller than those for CaO-marble. This suggests that the differences in diffusivities are the primary reason for differences in conversion between the three samples. Thus, we conclude that the modification of CaO via hydrothermal treatment in the presence of P123 leads to CaO domains with similar reactivity as CaO-D-nitrate and CaO derived from marble, but the CaO-H-nitrate sample exhibits better conversion during carbonation because of smaller domain sizes and increased material porosity.

In contrast to CaO-H-nitrate, the higher k_{RPM} values (**Table 15**) for CaO-D-acetate ($3.2\times10^{-4} \pm 1.4\times10^{-5}$, $5.0\times10^{-4} \pm 2.5\times10^{-6}$, and $5.2\times10^{-4} \pm 4.8\times10^{-6}$ cm^4 mol^{-1} s^{-1} at 823, 873 and 923 K, respectively) and CaO-nanofibers ($4.6\times10^{-4} \pm 4.2\times10^{-6}$, $8.9\times10^{-4} \pm 1.8\times10^{-5}$, and $1.5\times10^{-3} \pm 9.5\times10^{-6}$ m^4 mol^{-1} s^{-1} at 823, 873 and 923 K, respectively) compared to CaO-marble indicate a difference in the surface chemistry of the reaction, beyond the effects of expanded pore structure that ameliorates diffusion restrictions because all three samples are chemically similar (i.e., consist of CaO). This enhanced reactivity with decreasing particle size, similar to that observed in catalysis by metal particles,[156,157] may result from the preferential exposure of high index planes that comprise smaller crystallites[158] or from CaO structures that are inherently imparted by the synthesis technique with lesser extents of long range order. Values of D_{RPM} were also larger for CaO-D-acetate ($4.2\times10^{-12} \pm 5.6\times10^{-14}$, $1.4\times10^{-11} \pm 3.7\times10^{-14}$, and $7.8\times10^{-12} \pm 2.1\times10^{-13}$ cm^2 s^{-1} at 823, 873 and 923 K, respectively) and CaO-nanofibers ($7.2\times10^{-12} \pm 1.9\times10^{-14}$, $4.3\times10^{-11} \pm 3.0\times10^{-13}$, and $5.5\times10^{-11} \pm 8.2\times10^{-13}$ cm^2 s^{-1} at 823, 873 and 923 K, respectively) compared to CaO-marble (**Table 15**) indicating the effect of smaller reactive domains and possibly the formation of thinner CaCO$_3$ layers with structures that are more easily penetrable by gaseous CO$_2$.[159–161]

Table 15. RPM parameters and 95% confidence intervals derived from the carbonation data in **Figure 30**.

Sample	823 K		873 K		923 K	
	k_{RPM} (x10^4) (cm^4 mol^{-1} s^{-1})	D_{RPM} (x10^{12}) (cm^2 s^{-1})	k_{RPM} (x10^4) (cm^4 mol^{-1} s^{-1})	D_{RPM} (x10^{12}) (cm^{2}s^{-1})	k_{RPM} (x10^4) (cm^4 mol^{-1} s^{-1})	D_{RPM} (x10^{12}) (cm^{2}s^{-1})
CaO-marble	2.8 ± 0.007	0.2 ± 0.002	3.1 ± 0.012	0.20 ± 0.001	3.8 ± 0.020	0.9 ± 0.005
CaO-D-acetate	3.2 ± 0.135	4.2 ± 0.056	5.0 ± 0.025	13.6 ± 0.037	5.2 ± 0.048	7.8 ± 0.206
CaO-D-nitrate	2.0 ± 0.010	0.02 ± 0.001	2.1 ± 0.011	0.02 ± 0.001	2.3 ± 0.134	0.04 ± 0.006
CaO-H-nitrate	-	-	2.5 ± 0.012	4.70 ± 0.019	3.1 ± 0.017	3.6 ± 0.051
CaO-nanofibers	4.6 ± 0.042	7.2 ± 0.019	8.9 ± 0.177	42.9 ± 0.298	14.5 ± 0.095	55.0 ± 0.822
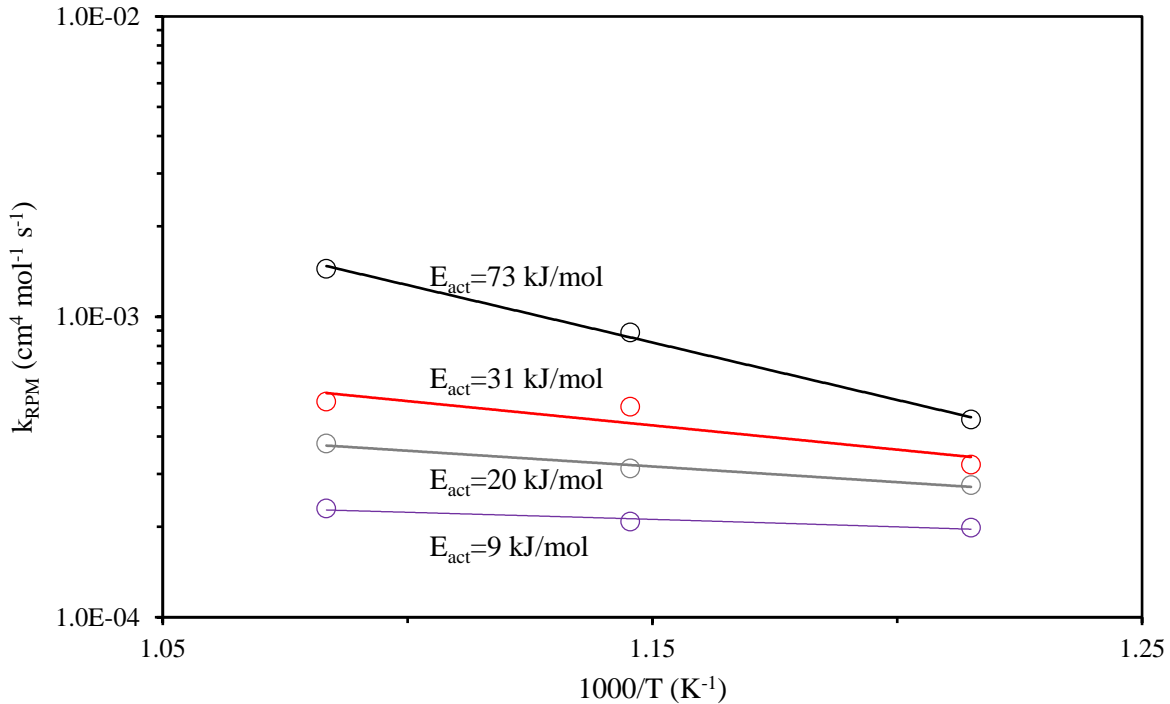
Figure 31. Arrhenius plots for reaction of CaO-nanofibers (black), CaO-D-acetate (red), CaO-marble (gray), and CaO-D-nitrate (purple). Circles represent experimentally determined reaction rate parameters for the random pore model determined from regression of conversion versus time data. Activation energies were determined by least squares regression of the experimentally determined parameters (lines).

5.3.2.2 Multi-Cycle Carbonation-Calcination of CaO

Ten cycles of carbonation and calcination were performed to study the stability of the CaO sorbents (CaO-marble, CaO-D-nitrate, and CaO-nanofibers) and the reversibility of the carbonation reaction. CaO-marble lost 1% (0.2 mg) of its initial sorption capacity after the first carbonation-oxidation cycle. **Figure 32** shows the sorption capacity of CaO-marble, CaO-D-nitrate, and CaO-nanofibers over ten carbonation and calcination cycles. The CaO-marble reached 12% (0.10 g_{CO2}/g_{CaO}) conversion on its tenth carbonation cycle, losing approximately 34% of its initial capacity. The CaO-D-nitrate reached 4.5% (0.036 g_{CO2}/g_{CaO}) on its on its tenth carbonation cycle losing approximately 30% of its initial capacity. The electrospun CaO sorbent reached 69%

($0.54 \ g_{CO2}/g_{CaO}$) conversion on its tenth carbonation, losing 31% of its initial capacity. The CaO-nanofibers sorbent retains a relatively high capacity even after 10 cycles of carbonation-calcination, although its loss of initial capacity is proportionally similar to CaO-marble and CaO-D-nitrate.
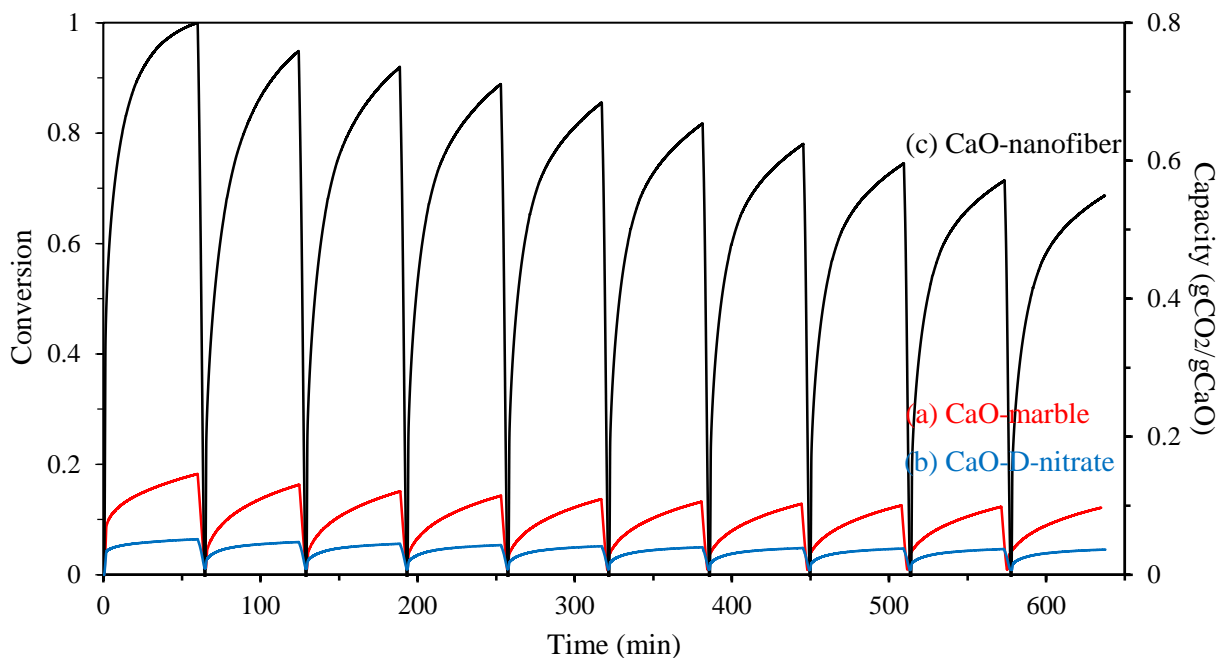
Figure 32. Conversion and capacity for (a, red) CaO-marble, (b, blue) CaO-D-nitrate, and (c, black) CaO-nanofiber over 10 carbonation-calcination cycles at 873 K, 101 kPa, and 200 sccm of CO_2 via thermogravimetric analysis.

Post-cycled CaO samples (CaO-marble, CaO-D-nitrate and CaO-nanofibers) were also calcined at 923 K for 8 h at 5 K min^{-1} to minimize the impact of hydroxide formation via exposure to ambient air and immediately analyzed by XRD, as seen in **Figure 26 (a) (7-9)**. The crystallite sizes of the post-cycled sorbents (**Table 13**) were calculated based on the peak at $2\theta = 37°$. The calculated crystallite size of CaO-marble, CaO-D-nitrate, and CaO-nanofibers were 76 nm, 73 nm, and 64 nm, respectively. The crystallite size of CaO-marble and CaO-D-nitrate remained relatively

unchanged after cycling because the formation of this sample likely occurred at conditions that led to sintering and agglomeration. In contrast, the crystallite size of CaO-nanofibers increased from 39 nm to 64 nm. The sintering and aggregation of the crystallites in the CaO-nanofibers is likely the reason for the loss in activity of the sorbent over repeated cycles in addition to possible loss of pore structure and volume.[127,133,162]

SEM analysis was also performed on the post-cycled CaO-marble and CaO-nanofibers samples to investigate the cycling effect on morphology. The SEM images of the thermally treated CaO-marble and CaO-nanofibers after 10 cycles of carbonation-calcination are shown in **Figure 28 (k, l)**. Both SEM images reveal that cycling detrimentally affected the morphology of the oxide fibers, especially the CaO-nanofibers sample which underwent drastic structural and morphological changes. Specifically, the SEM image shows that upon cycling, the CaO-nanofibers sample lost its porous, fibrous structure, which was initially responsible for mitigating pore plugging. This loss of nanoscale structure results in the reduction seen in the sorption capacity of CaO-nanofibers upon multiple cycling. **Figure 28 (k, l)** also reveals that both samples (after ten cycles) consisted of agglomerated and sintered nanoparticles that were irregular in shape. Therefore, although electrospinning results in the formation of CaO nanostructures that are highly active, repeated calcinations collapses the fibrous structure, and strategies such as metal doping may be required to maintain the morphology, and thus, the initial high sorption capacity of the active materials prepared via electrospinning.

5.3.2.3 Multi-Cycle Carbonation-Calcination of Al-Ca-O Sorbents

Carbonation-calcination cycles were also ran on three levels of Al-doped CaO nanofibers (Ca:Al=3.33, 10, 20) to study the balance between improved stability and decreased sorption capacity due to the introduction of aluminum. As seen in **Figure 33**, the initial sorption capacity

of 3Al-10Ca-O-nanofibers, 1Al-10Ca-O-nanofibers, and 1Al-20Ca-O-nanofibers at 873 K were

0.35, 0.58, and 0.74 $g_{CO2}/g_{sorbent}$, respectively. By comparing those values to the initial sorption

capacity of CaO-nanofibers (0.79 $g_{CO2}/g_{sorbent}$ at 873 K), it becomes evident that doping CaO with

aluminum decreases the capacity of the sorbent proportional to the quantity of aluminum added.

Figure 33 also shows an interesting behavior, as the initial sorption capacity obtained for a doped

material was not the maximum capacity attained. Instead, the maximum CO_2 sorption capacity

was attained in the second cycle where the sorption capacity was 0.36, 0.62, 0.76 $g_{CO2}\ g_{sorbent}^{-1}$ for

3Al-10Ca-O-nanofibers, 1Al-10Ca-O-nanofibers, and 1Al-20Ca-O-nanofibers, respectively. After

16 cycles, the sorption capacity of 3Al-10Ca-O-nanofibers, 1Al-10Ca-O-nanofibers, and 1Al-

20Ca-O-nanofibers were 0.35, 0.58, and 0.70 $g_{CO2}/g_{sorbent}$, respectively. As evident from **Figure

33**, all the Al-doped nanofibers retained >95% of their initial capacity throughout cycling, with the

sample containing 3:10 Al:Ca (3Al-10Ca-O-nanofibers) retaining approximately 98% of its initial

capacity, even after 17 cycles.

After completing the cycling tests, all three post-cycled samples were thermally treated at

923 K for 8 h at 5 K min^{-1} to minimize the impact of hydroxide formation via exposure to ambient

air and immediately analyzed by XRD and SEM. **Figure 26 (b) (4-6)** shows the XRD patterns of

the Al-Ca-O sorbents and **Table 13** shows the crystallite sizes calculated using Scherrer's formula

based on the crystallite peak at $2\theta = 37°$. As shown in **Table 13**, the crystallite sizes of the three

Al-doped materials remained roughly unchanged, as the calculated crystallite sizes of 3Al-10Ca-

O-nanofibers, 1Al-10Ca-O-nanofibers, and 1Al-20Ca-O-nanofibers were 53 nm, 50 nm, and 50

nm, respectively before cycling and 50 nm, 46 nm, and 48 nm, respectively, after cycling. Indeed,

the dispersed $Ca_{12}Al_{14}O_{33}$ phases among the CaO particles served as a stable matrix as it abated

the sorbent's crystallite size from significantly changing. This is particularly true when comparing

116

the crystallite size of the aluminum-doped materials to the undoped, CaO-nanofibers, which saw

its crystallite size change, in similar reaction conditions, from 39 nm initially to 64 nm after only

10 cycles.
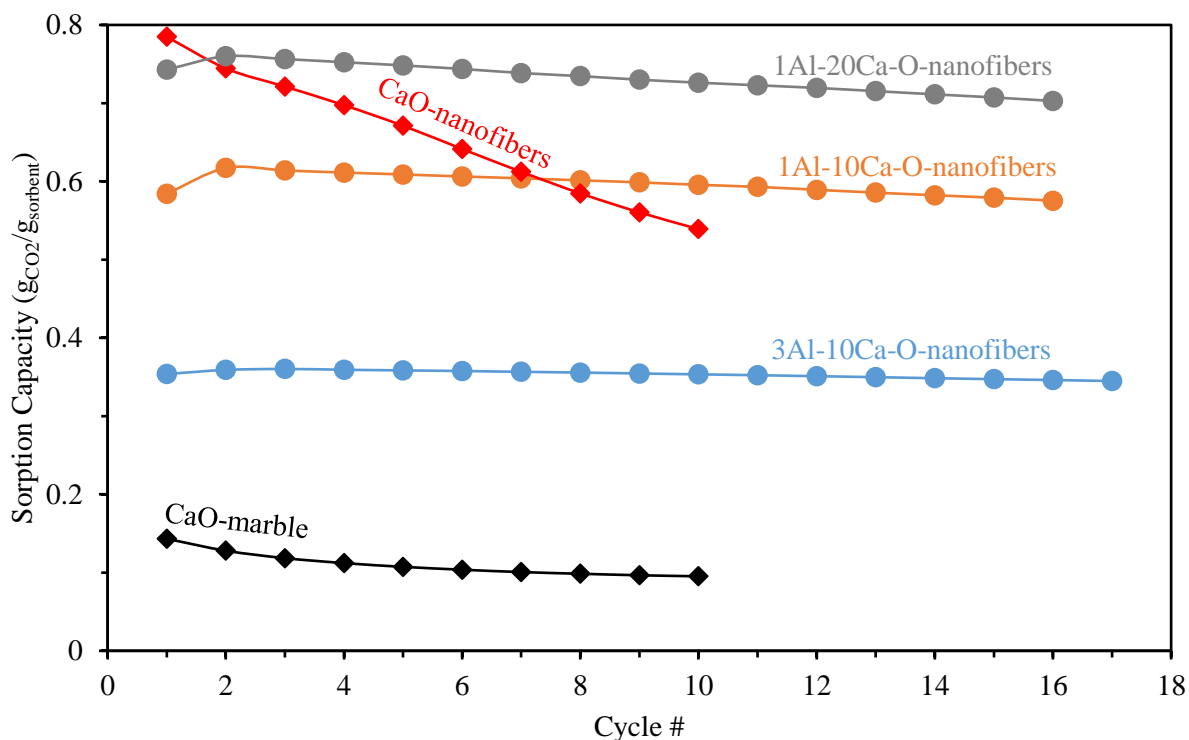
Figure 33. Sorption capacity of CaO-marble (black, diamonds), CaO-nanofibers (red, diamonds), 3Al-10Ca-O-nanofibers (blue, circles), 1Al-10Ca-O-nanofibers (orange, circles), and 1Al-20Ca-O-nanofibers (grey, circles) across multiple carbonation-calcination cycles at 873 K, 101 kPa, and 200 sccm of CO_2 via thermogravimetric analysis.

SEM analysis was also performed on the post-cycled Al-doped sorbents to investigate the

cycling effect on morphology. **Figure 28 (m-o)** shows the SEM images of the post-cycled Al-Ca-

O sorbents. As **Figure 28 (m-o)** shows, the 3Al-10Ca-O-nanofibers sorbent, which had a 3:10

atomic ratio of Al:Ca, had considerably smaller domain sizes, less agglomerated particles, and a

more intact porous, fibrous structure than the 1Al-20Ca-O-nanofibers sorbent. The SEM images

demonstrate that the amount of aluminum present in the sorbent affects the degree and speed of collapse of the fibrous structure (particularly, the macro-pores) upon cycling. The results in this section are in agreement with previous studies on doped or modified sorbents,[132,163–165] as it shows that certain inert materials such as $Ca_{12}Al_{14}O_{33}$ can be introduced into the CaO structure to act as a spacer or physical barrier (thus, preventing small $CaCO_3$ grains from sintering and aggregating) and preserve morphology. Certainly, the combination of metal doping with electrospinning in this work yields a promising avenue and a powerful tool for synthesizing sorbent materials with enhanced sorption capacity for CO_2 removal at elevated temperatures and improved lifespan and stability (i.e., slower decay in the initial sorption capacity).

5.3.3 Sorption Enhanced Steam Methane Reforming

5.3.3.1 First Cycle of Reforming

1Al-20Ca-O-nanofibers, CaO-nanofibers, and CaO-marble were tested as sorbents in SE-SMR and the results are shown in **Figure 34**. SE-SMR was operated under the following reaction conditions: 823 K, 101kPa, 91 kPa of steam, 28 kPa of methane, and 3 kPa of argon, in a fixed bed reactor with a commercial NiO-based catalyst. The methane conversion and H_2 product selectivity are shown as a function of time on stream in **Figure 34 (b)**. At early times on stream, undetectable amounts of CO_2 appear in the effluent from the reactor, indicating high rates of sorption (i.e., CO_2 produced from methane reforming is being removed). During this stage of reaction, each reactor (containing 1Al-20Ca-O-nanofibers, CaO-nanofibers, and CaO-marble) exhibited 100% selectivity to H_2. As shown in **Figure 34 (a)**, the reactors loaded with the electrospun materials had considerably higher methane conversion (83% and 84% for CaO-nanofibers and 1Al-20Ca-O-nanofibers, respectively) compared to 71% for CaO-marble. It's important to note here that each of these systems would approach the same conversion by increasing or decreasing the

loading/length (sorbents and catalysts) inside the reactor so that the reactor will always have a low concentration of CO_2 and CO to shift the SMR reaction right. **Figure 34 (a)** shows the CO_2 breakthrough time of the three sorbents, which was 1648, 7472, and 6375 mL gaseous flow/g_{CaO} for CaO-marble, CaO-nanofibers, and 1Al-20Ca-O-nanofifibers, respectively. After breakthrough, the concentration of CO_2 in the effluent, the selectivity to H_2, and the conversion of methane approach SMR equilibrium values. Interestingly, though, for the reactors that contained electrospun materials (specifically, CaO-nanofibers and 1Al-20Ca-O-nanofibers), as shown in **Figure 34 (b)**, these values approached SMR equilibrium at a much slower rate than CaO-marble. This behavior occurs because these sorbents continue to absorb CO_2, even after breakthrough, albeit in a slower sorption regime.

Furthermore, the longer duration of SE-SMR for the electrospun sorbents results primarily from the higher CO_2 capacity of these materials, which is imparted by their smaller CaO crystallite size and larger extent of macro-porosity. Their superior performance, as evident in **Figure 34**, would impact the entire SE-SMR process by allowing for a factor of three or more decrease in contact time compared to CaO-marble, to produce similar quality hydrogen streams under the same operating conditions (i.e., temperature, pressure, feed composition, and time between regeneration). Alternatively, the nanofibers could allow for three or more times longer reaction periods (before regeneration) compared to CaO-marble while producing the same hydrogen stream at the same conditions. Finally, the nanofibers could allow for the same quality hydrogen stream to be produced compared to CaO-marble but at milder conditions (i.e., lower temperature and pressures and shorter reactor contact time). Operation at milder conditions could decrease capital and operational costs for SE-SMR by allowing for the use of less expensive materials for construction.[123]
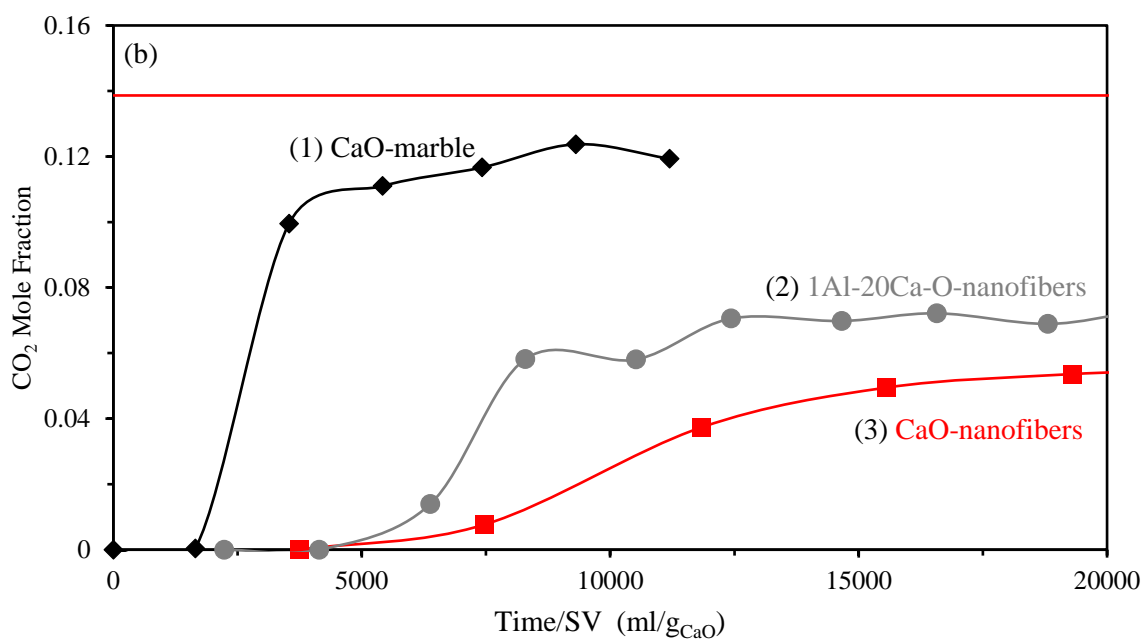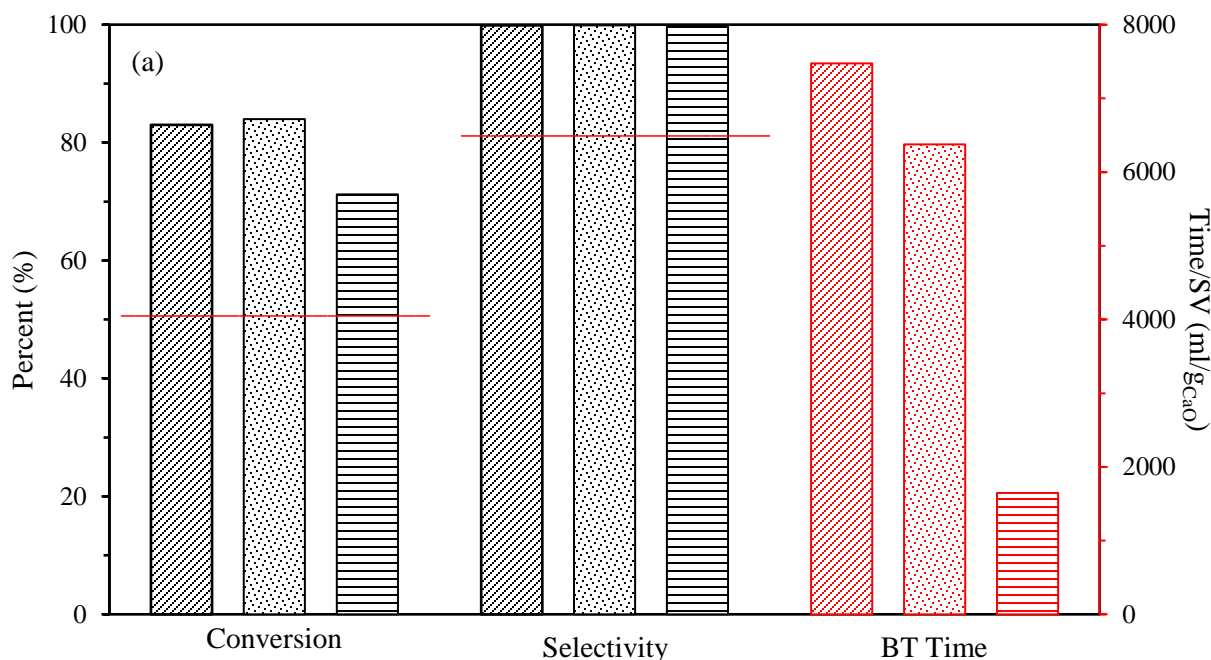
Figure 34. (a) Hydrogen selectivity, conversion, and CO_2 breakthrough time (in red) for SE-SMR processes using CaO-marble (horizontal lines), CaO-nanofibers (diagonal lines), and 1Al-10Ca-O-nanofibers (dotted lines). (b) CO_2 mole fraction as a function of time (normalized by space velocity) for SE-SMR experiments using (1) CaO-marble, (2) 1Al-20Ca-O-nanofibers, and (3) CaO-nanofibers, SMR equilibrium conversion and selectivity (red horizontal lines in a and) and equilibrium CO_2 mole fractions (red line in b) are for 823 K. SE-SMR reactions were carried out at 823 K, 91 kPa of steam, 28 kPa of methane, and 3 kPa of argon (total pressure of 101 kPa).

5.3.3.2 Cyclic Sorption Enhanced Steam Methane Reforming

CaO-nanofibers and 1Al-20Ca-O-nanofibers were tested in cyclic SE-SMR/calcination experiments under the same conditions described in the previous section. After each SE-SMR run, the sorbent was regenerated by flowing 50 sccm of UHP hydrogen gas at 998 K with a ramping rate of 2 K min^{-1} and held overnight. The results of these experiments are shown in **Figure 35**. After ten cycles of SE-SMR and calcination, the CaO-nanofibers sorbent performance was reduced by 45% (i.e., 45% decrease in its initial breakthrough time) whereas the 1Al-20Ca-O-nanofibers sorbent was reduced by only 6% of its initial breakthrough time, thus, showing far more stability. Both of the nanofibers lost more time on stream (i.e., breakthrough time) in the reforming experiments after ten cycles than they did in the TGA studies, which is due to the fact that the breakthrough time in the reforming experiments relies on the fast-kinetic regime and the reaction conditions are also different in the reforming than those in the TGA (e.g., the temperature is reduced in the SE-SMR experiment and the mole fraction of CO_2 is nearly an order of magnitude lower). Furthermore, the calcination temperature and calcination duration in the reforming experiments were harsher and longer, which in turn affected the fibers more severely.
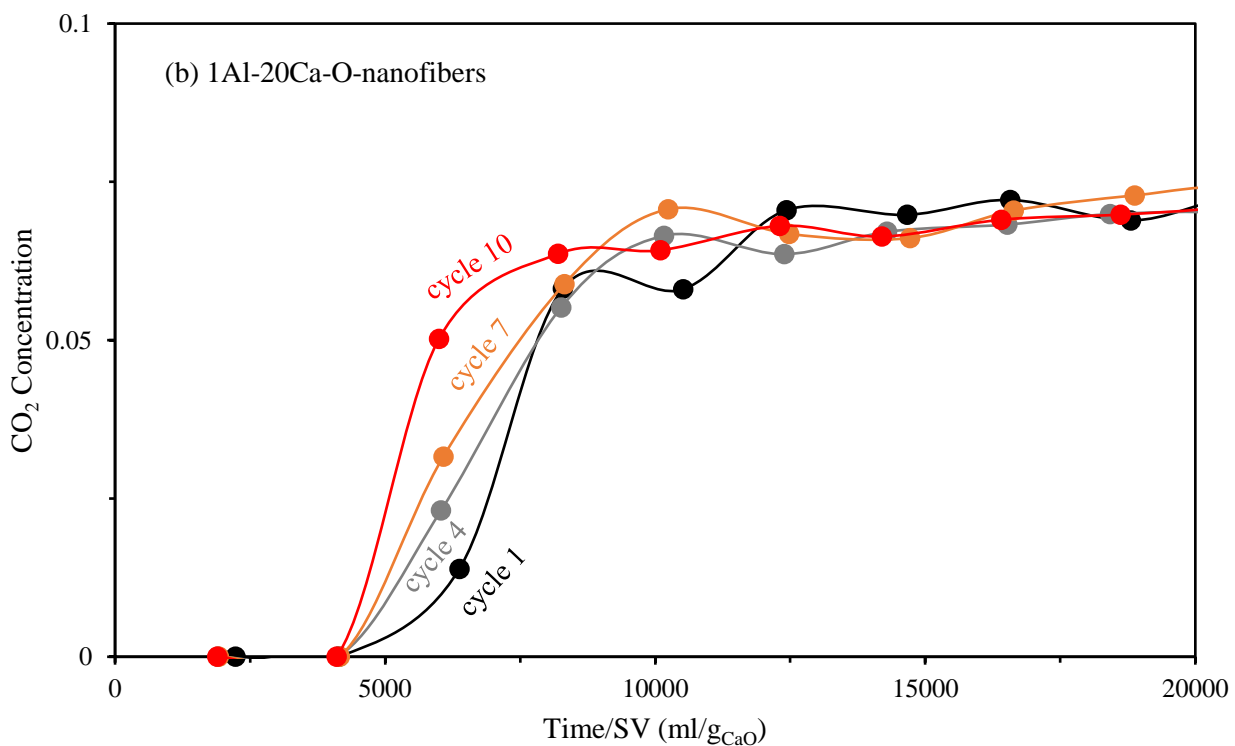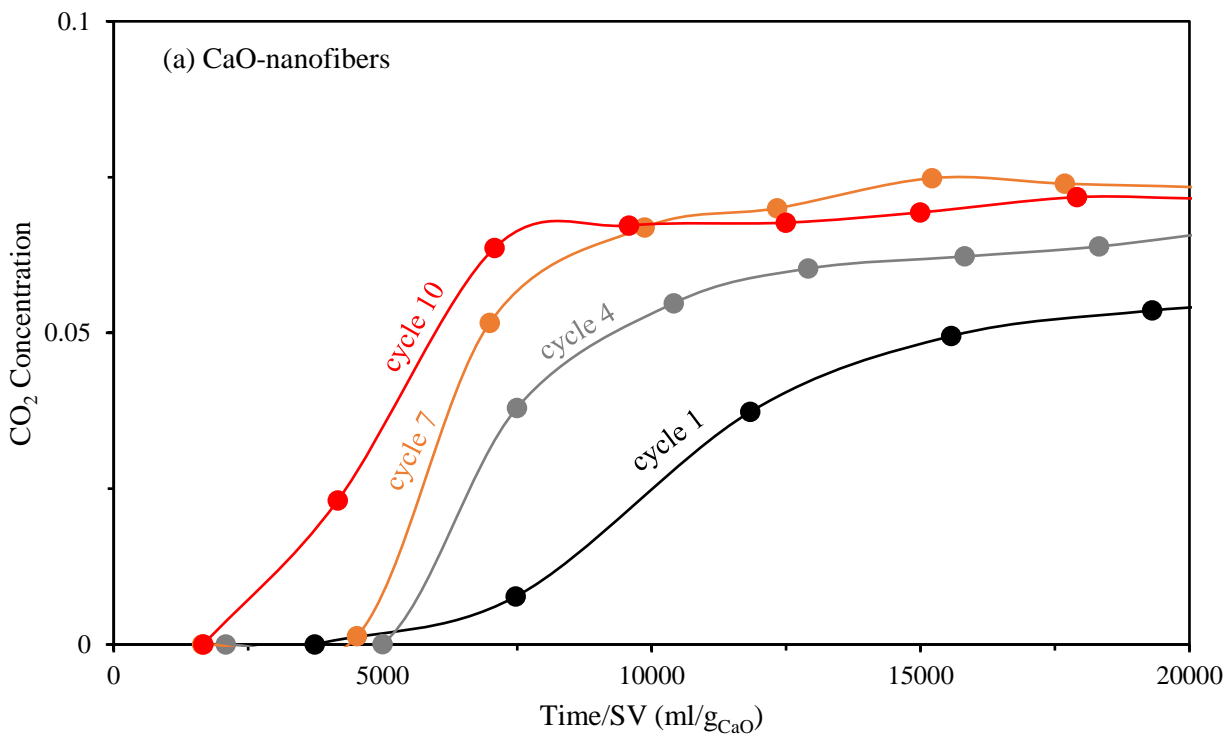
Figure 35. CO_2 mole fraction as a function of time (normalized by space velocity) over ten cycles of SE-SMR/calcination for (a) CaO-nanofibers and (b) 1Al-20Ca-O-nanofibers. The data is simplified to show the first run (black), fourth run (grey), seventh run (orange), and tenth run (red).

5.4 Summary

CaO-based nanofibers (pure CaO and Al-doped) were successfully synthesized via electrospinning and tested for their ability to react with CO_2 at elevated temperatures. Electrospinning, as a synthesis technique, resulted in the fabrication of a connected network of CaO (or Al-Ca-O) nanoparticles, which had a unique, highly porous fibrous structure. The synthesized metal oxide nanofibers were small in size and had large pore volumes, high surface areas and large intraparticle void spaces. In this work, specifically, it was shown that combining electrospinning with metal oxide synthesis resulted in the production of nanostructures that possessed optimal morphologies and appropriate physio-chemical properties for CaO carbonation.

When reacted with CO_2, electrospun CaO-nanofibers exhibited the highest conversion of all the materials tested in this work, reaching 100% conversion to $CaCO_3$, and achieving the highest rate of carbonation of all the materials studied (0.79 g_{CO2}/g_{CaO}), which included CaO-marble, CaO-D-acetate, CaO-D-nitrate, CaO-H-nitrate, 3Al-10Ca-O-nanofibers, 1Al-10Ca-O-nanofibers, and 1Al-20Ca-O-nanofibers. In this work, the saturation capacity of CaO-based sorbents was found to be strongly influenced by properties such as, surface area, pore volume, porosity, intraparticle void volume, crystallite size, grain size, and chemical composition. Significant differences in sorption capacities were also observed in CaO-nanofibers, CaO-D-acetate, and CaO-H-nitrate despite similarities in surface area, pore volume, and crystallite size. The differences in the sorption capacities of these materials was attributed to chemical differences at the reaction interface as well as properties such as pore volume/area and intra-particle void volume.

In this work, aluminum was used as a structural spacer for electrospinning stable CaO-based sorbents, as aluminum oxide and calcium oxide react at elevated temperatures to form

thermodynamically stable binary mixtures of CaO and $Ca_{12}Al_{14}O_{33}$. Three Al-doped samples (3Al-10Ca-O-nanofibers, 1Al-10Ca-O-nanofibers, and 1Al-20Ca-O-naofibers) were tested in the TGA and were found to have high sorption capacities (0.35-0.74 $g_{CO2}/g_{sorbent}$). These doped sorbents also demonstrated improved stability (i.e., losing less than 5% of their initial capacity after more than 15 cycles of carbonation-calcination) over CaO-nanofibers, which lost 31% of its initial capacity after 10 cycles, and CaO-marble, which lost 34% of its initial capacity after 10 cycles. This improved performance was due to the presence of stable Al-Ca mixed phases in the sorbent's matrix which were responsible for retaining the porous, fibrous structure imparted by electrospinning while also preventing the sorbent's crystallite size from increasing upon cycling. Indeed, the incorporation of aluminum into the CaO matrix is necessary for retaining and/or mitigating loss in activity.

The improvements observed in the TGA experiments for the electrospun materials were also observed in SE-SMR experiments where CaO-nanofibers and 1Al-20Ca-O-nanofibers exhibited three or more times the CO_2 capacity of CaO-marble and had three or more times longer breakthrough times in SE-SMR than traditional sorbents (e.g., CaO-marble). Upon multiple SE-SMR/calcination cycling, the 1Al-20Ca-O-nanofibers showed superiority in performance over CaO-nanofibers, as it retained its performance, losing merely 6% of its breakthrough time after 10 cycles whereas CaO-nanofibers' breakthrough time reduced by 45%. The results in this paper demonstrate the advantage of using electrospinning as a synthesis approach to making fibrous structures, with considerable macro-porosity, to enable CaO to reach full conversion to $CaCO_3$ upon reaction with CO_2. The doping of electrospun CaO-based sorbents with Al and thermally treating the fibers appropriately led to the formation high performing and durable sorbents, which

combined the high sorption capacity of electrospun materials and the stability of Al-doped structures.

Chapter 6 | Application II: High Temperature CO₂ Capture

6.1 Introduction

The increase in anthropogenic CO_2 emissions to the atmosphere is one of the most vital climate issues facing our society today. Due to our reliance on the combustion of fossil fuels for over a century now, CO_2 levels in the atmosphere have reached unprecedented levels and have already disrupted and adversely impacted several physical, ecological and biological systems.[166–169] The continued growth in the global population coupled with the rising standards of living in many countries are responsible for the continued increase in global use of fossil fuels and thus greenhouse gas emissions. Since its widely expected that humans will continue to rely on coal, oil, and natural gas for at least the next couple of decades,[170] it becomes vital to develop efficacious processes and materials that would adsorb CO_2 and reduce its emissions to mitigate climate change.

Recently, there has been considerable interest in identifying and developing efficient and low cost solid sorbents (e.g., activated carbonaceous materials, MOFs, zeolites, polymeric resins, carbonates, oxides, etc.) that could capture or separate CO_2 from CO_2-containing streams (e.g., flue gas).[171–178] Materials that could be applied to or combined with existing technologies, processes, and systems (e.g., geological storage sites, Integrated Gasification and Combined Cycle (IGCC), etc.) have received particular attention in the literature and industry. The Calcium Looping Process (CLP), which was proposed by Shimizu et al.[179] in the late 20th century, has positioned itself as a promising candidate for removing CO_2 from flue gas streams due to the many advantages associated with using CaO as a sorbent, which include (as discussed in chapter 5): abundance in nature, high theoretical adsorption capacity (0.79 g_{CO2}/g_{CaO}), fast carbonation-

calcination kinetics ($E_{carbonation}$ = 20 kJ mol^{-1}; $E_{calcination}$ = 104 kJ mol^{-1}),[127] low material cost, and adequate theoretical reversibility ($CaO + CO_2 \leftrightarrow CaCO_3$; K_{eq} = 87 at 923 K).[128–130].

Unfortunately, all previous studies investigating the reversibility of the carbonation-calcination reaction of $CaO/CaCO_3$ revealed that this reaction is far from reversible in practice and that maintaining the initial sorption capacity of CaO upon repeated cycling is rather difficult (experimentally confirmed in chapter 5).[132,161,180–183] Furthermore, the kinetics dictating how fast a CaO-based sorbent switches from the fast, chemically-controlled regime to the slow, diffusion-controlled regime and the level of conversion CaO achieves upon reaction with CO_2 differs vastly from one material to another.[153] Indeed, it's been shown that kinetics and conversion of CaO are strongly dependent on the sorbent's properties (e.g., porosity, pore volume, surface area, crystallite size, and composition).[184–187] In this reaction, the formation of a thick product layer of $CaCO_3$ (~50 nm in thickness)[188] around the free surfaces of CaO is what forces the kinetics to transition from the fast regime (could take 1-3 minutes at temperatures around 923 K) to the slow regime and what limits CaO from reaching full conversion to $CaCO_3$. This product layer effectively acts as a diffusion resistance layer, inhibiting CO_2 from reacting with a large fraction (~60%+ for naturally derived CaO such as limestone) of the interior CaO particles.[133,189–191] Therefore, to achieve a high initial conversion, porous materials are required.

It was demonstrated in chapter 5 that electrospinning, an electrostatic synthesis technique, was capable of synthesizing highly porous CaO nanofibers, which achieved complete conversion to $CaCO_3$ (0.79 g_{CO2}/g_{CaO}) upon reaction with CO_2 at 873 and 923 K. Despite their initial high capacity, it was found that electrospun materials lost a large portion of their sorption capacity (~30% after 10 cycles) upon repeated carbonation-calcination in a manner that was consistent with other CaO materials reported in the literature.[133,154,192] Issues such as, sintering and aggregation of

particles, simultaneous loss in surface area and pore volume, and increase in crystallite size were responsible for the observed loss in activity for pure, undoped CaO sorbents.[193–196] Indeed, it's inevitable to avoid sintering in such materials because the operating temperature for CaO sorbents is typically in the range of 873-973 K for carbonation and 1123-1223 K for calcination, which is significantly above the Tammann temperature of $CaCO_3$ (~806 K).[137,197]

A variety of techniques have been researched and investigated in the literature to augment the performance of CaO-based sorbents (i.e., increase conversion, prevent sintering/aggregation and improve stability), including (i) reactivating the sorbents via hydration,[198–202] (ii) modifying the structure of the calcium-based sorbents using organic acids (e.g., acetic acid, propionic acid, lactic acid, citric acid, and oxalic acid),[203–207] and (iv) introducing inert solid supports to the CaO structure to act as spacers to reduce or prevent sintering and particle agglomeration.[208–213] Of these methods, metal doping has been shown to be an effective method to produce CaO-based sorbents that are highly reactive and durable upon cycling. Aluminum-doped CaO sorbents have attracted the most attention in the literature. Li et al.,[214] in 2005, synthesized a $CaO/Ca_{12}Al_{14}O_{33}$ sorbent (mass ratio of CaO to $Ca_{12}Al_{14}O_{33}$ was 3 to 1) via a mixing method. The sorbent possessed a considerably high CO_2 sorption capacity (0.41-0.45 $g_{CO2}/g_{sorbent}$) and was stable for up to 13 cycles. Other aluminum-doped materials (e.g., Al_2O_3, $Ca_3Al_2O_6$, and $Ca_9Al_6O_{18}$) have also been reported by other authors, albeit they showed varying degrees of success.[215–219] Zr-doped sorbents have also received attention, showing great promise in improving the mechanical durability of CaO by forming a stable mixed oxide ($CaZrO_3$) phase, which acted as an effective spacer and barrier against sintering, thus, preventing growth in the CaO grains upon cycling.[138,210,213] Lu et al.,[137] for example, synthesized a zirconium-doped nano-sorbent with a Zr:Ca atomic ratio of 3:10 via flame spray pyrolysis. The Zr-doped sample exhibited excellent sorption capacity and stability for up to

100 cycles, owing to the high Tammann temperature of ZrO_2 (1491 K). MgO likewise has been shown to improve stability, especially when the CaO to MgO ratio is acceptable (e.g., 20 wt% MgO,[220] or a CaO to MgO molar ratio of 2 to 1[163]). MgO also offers another advantage: unlike Al_2O_3 and ZrO_2, it does not chemically interact with CaO (i.e., form a solid solution during thermal treatment), thus, when mixed with CaO, it does not reduce its CO_2 uptake capacity on a gram of sorbent basis.[221] Therefore, Mg-doped CaO sorbents tend to generally have relatively high initial sorption capacities. Other supports that have been reported to be effective in enhancing the CO_2 sorption capacity of CaO-based sorbents include: CeO_2,[137,187] $TiO_2/CaTiO_3$,[137,222,223] Nd_2O_3,[213,224] Y_2O_3,[209,225,226] La_2O_3,[164,225,227,228] $CaMnO_4$,[227] SiO_2,[229–231] Yb_2O_3,[213] and Pr_6O_{11}.[213]

Despite these numerous reports on doped CaO materials, the results are difficult to compare in a parallel manner, as only a few studies have comprehensively compared the effects of different support materials on CO_2 sorption capacity in repeated cycling by using the same synthesis method (e.g., flame spray pyrolysis, hydration-impregnation, combustion synthesis, etc.) and testing conditions (e.g., temperature, CO_2 concentration, duration, etc.). Furthermore, it's still unclear whether there are other metals that could function as stabilizers or performance enhancers for CaO-based sorbents. For these reasons, the current work reports on the synthesis of several CaO-based sorbents (e.g., Al-Ca-O, La-Ca-O, Mg-Ca-O, Er-Ca-O, Ga-Ca-O, Y-Ca-O, Li-Ca-O, Nd-Ca-O, In-Ca-O, Zn-Ca-O, and Co-Ca-O) (including four new supports) via electrospinning and compares their cyclic behavior in a thermogravimetric analysis (TGA) via reaction with CO_2. Electrospinning was used to synthesize these sorbents because it produces highly porous materials, which are optimal for solid-gas reactions (as shown in chapter 5). The metal supports tested in this work had a wide range of melting points and Tammann temperatures as well as oxidization states

and crystal structures, thus, providing insight into the basis and guidelines for selecting efficient refractories for high temperature CO_2 capture.

6.2 Experimental

6.2.1 Materials

Polyvinylpyrrolidone (PVP) (M.W. 1,300,000, Sigma-Aldrich), calcium nitrate tetrahydrate (Sigma Aldrich, ≥99.0%), aluminum nitrate nanohydrate (Sigma Aldrich, 99.997%), cobalt (II) nitrate hexahydrate (Alfa Aesar, 98%), zinc nitrate hexahydrate (Alfa Aesar, 99%), lanthanum (III) nitrate hexahydrate (99.9%), yttrium (III) nitrate hexahydrate (Alfa Aesar, 99.9%), erbium (III) nitrate hydrate (Alfa Aesar, 99.9%), indium (III) nitrate hydrate (Aldrich, 99.99%), neodymium (III) nitrate hexahydrate (Alfa Aesar, 99.9%), lithium nitrate anhydrous (Alfa Aesar, 99%), gallium (III) nitrate hydrate (Aldrich, 99.9%), magnesium nitrate hexahydrate (Aldrich, 99.999%), and ethyl alcohol (Sigma-Aldrich, 100%) were purchased and used without subsequent purification.

6.2.2 Synthesis of Electrospun CaO-Based Nanofibers

A polymer solution was prepared by dissolving 1.3 g of PVP in 23 cm^3 of ethanol. The solution was then vortexed (Fisher Scientific Digital Vortex Mixer) at 2900 rpm for 1 h until the PVP was completely dissolved. The polymer solution was left to settle for 5-10 mins, transferred to a beaker, and stirred for 15 mins. The metal containing solution was prepared by dissolving 0.98 g of calcium nitrate and an appropriate amount of metal nitrate (Mg, Al, Y, La, Zn, Er, Ga, Li, Nd, In, and Co) in 10 cm^3 of DI water and stirring the solution for 0.5 h. The metal to Ca atomic ratio was 3 to 10, for all sorbents. Since its been reported in the literature that Mg-doped CaO materials perform better when the Mg to Ca ratio is 1 to 2, an additional Mg sample was prepared to

correspond to this Ca to Mg ratio. The calcium- and metal-containing solution was then added dropwise to the polymer-containing solution. The solution was stirred for 0.25 h, and then vortexed for 0.5 h at 2900 rpm.

The electrospinning solution was placed in a 10 mL syringe (BD 10 mL syringe with Luer Lok^{TM} tip) with a hypodermic needle (Monoject^{TM} Standard 30G x ¾"). The distance between the tip of the needle and a stainless-steel collecting plate, which was covered with aluminum foil, was 16 inches. A Gamma High Voltage Research ES75 power supply was used to apply 30 kV on the polymer jet while the polymer solution was extruded through the needle at a rate controlled by a syringe pump (1.0 cm^3 h^{-1}; Kent Scientific Genie Plus). Dry air was circulated inside a 3 m^3 chamber at 6 cm^3 min^{-1} to control the relative humidity at $19.5 \pm 2\%$. All electrospinning was carried out at ambient conditions: temperature (294 ± 3 K) and pressure (101 kPa). The collected fibers were thermally treated in air at 773 K for 2 h at a ramping rate of 2 K min^{-1} to remove the majority of PVP and form calcium oxide. A second thermal treatment in air was performed at 923 K for 5 h at ramping rate of 5 K min^{-1} and then at 1173 K for 2 h at ramping rate of 2 K min^{-1}. The second thermal treatment was required to form a stable metal-calcium framework (e.g., $Ca_{12}Al_{14}O_{33}$)[140,141] for repeated carbonation and calcination. In this work, the non-doped electrospun CaO sorbent is denoted as CaO-nanofibers whereas the metal-doped CaO sorbents are denoted as xM-yCa-O-nanofibers, where "x" and "y" correspond to the atomic ratio of the metal (M) to Ca in the synthesis procedure.

6.2.3 Characterization

The synthesized CaO-based sorbents prepared via electrospinning were characterized using a variety of techniques. Powder X-ray diffraction patterns were obtained on an X-ray diffractometer (JEOL JDX-3530 and Philips X-Pert) using Cu Kα radiation of 1.54 Å. The average

crystallite sizes were found using Scherrer's formula. Scanning electron microscopy with energy dispersive X-ray spectroscopy (NOVA 230 Nano SEM/EDS) was used to determine the chemical composition of the sorbents.

6.2.4 Carbonation-Calcination Testing

Reaction kinetics and capacities for CaO carbonation were collected via thermogravimetric analysis using a Perkin Elmer TGA. Alumina crucibles were used to hold the samples. Gas flowrates were set to 200 standard cm^3 min^{-1} to minimize external diffusion from the bulk gas to the sample interface. Heating/reaction occurred in house air (dry, CO_2-free), CO_2 (Wright Bros, Inc., 99.5%) and/or argon (Matheson UHP Argon, 99.999% purity) at a ramping rate of 5-20 K min^{-1}. Prior to all reactions, all samples were calcined in air at 923 K with a ramp rate of 5 K min^{-1} for 8 h in a Thermolyne F6028C-80 muffle furnace. In the TGA, prior to reaction with CO_2, the CaO-based sorbents were treated at 1073 K for 10 minutes at a ramp rate of 10 K min^{-1} in air to ensure the decomposition of any residual $Ca(OH)_2$ or $CaCO_3$ that formed during exposure to the atmosphere.[136] After the *in-situ* calcination, the samples were cooled at a rate of 15 K min^{-1} to their reaction temperature (873 K) and held for 15 min to equilibrate. All samples were carbonated for 1 h at 101 kPa in 200 sccm of pure CO_2.

The first cycle for each of the cycling studies were carried out according to the methods described in the previous paragraph. For subsequent cycles, following 1 h of carbonation, the gas was switched from CO_2 to air, and the temperature was ramped from 873 K to 1073 K at a rate of 10 K min^{-1}. Samples were held at 1073 K for 10 min, then cooled to 873 K at a rate of 15 K min^{-1}. Samples were then held at 873 K for 15 min to equilibrate before the gas was switched from air to CO_2 to begin subsequent carbonation.

6.3 Results and Discussion

6.3.1 Physio-chemical properties of CaO-Based Sorbents

As indicated earlier, the sorbents were synthesized via electrospinning, using PVP as the polymer source. The electrospun nanofibers were then thermally treated in air to remove the PVP and convert $Ca(NO_3)_2$ to CaO and the metal-nitrate to either a metal oxide or a composite (e.g., $Ca_{12}Al_{14}O_{33}$). XRD was used to identify the crystalline phases and average crystal sizes of the CaO-nanofibers and M-Ca-O nanofibers, where M is metal (Mg, Al, Y, La, Zn, Er, Ga, Li, Nd, In or Co). **Figure 36** shows the XRD patterns of the doped CaO-based nanofibers. Crystalline peaks corresponding to CaO (■) were labeled. The unlabeled peaks in **Figure 36** corresponded to the oxide phase of the doped-metal (e.g., MgO, Y_2O_3, La_2O_3, ZnO, Er_2O_3, Ga_2O_3, Li_2O, Nd_2O_3, In_2O_3, CoO), except in the case of 3Al-10Ca-O, as the unlabeled peaks corresponded to mayenite ($Ca_{12}Al_{14}O_{33}$), a stable composite. The average crystal domain sizes of the metal-doped nanofibers as well as the Ca/M ratio obtained from EDS are shown in **Table 16**. The majority of sorbents, as shown, had an initial crystallite size of 25-60 nm.

Table 16. Properties of the metal (M)-doped CaO sorbents. [a] Obtained by EDS. [b] Based on XRD.

Sorbent	Ca/M[a]	Crystallite Size[b] (nm)	Post Cycled Crystallite Size[b] (nm)
1Mg-2Ca-O	2.12	26.5	53.5
3Mg-10Ca-O	3.11	28.1	-
3Al-10Ca-O	3.52	53.0	50.0
3Y-10Ca-O	-	35.3	50.5
3La-10Ca-O	3.36	47.7	-
3Zn-10Ca-O	3.60	27.6	-
3Er-10Ca-O	-	48.2	-
3Ga-10Ca-O	3.43	46.9	-
3Li-10Ca-O	-	58.6	77.0
3Nd-10Ca-O	-	63.6	59.4
3In-10Ca-O	-	53.9	58.7
3Co-10Ca-O	3.09	58.2	-
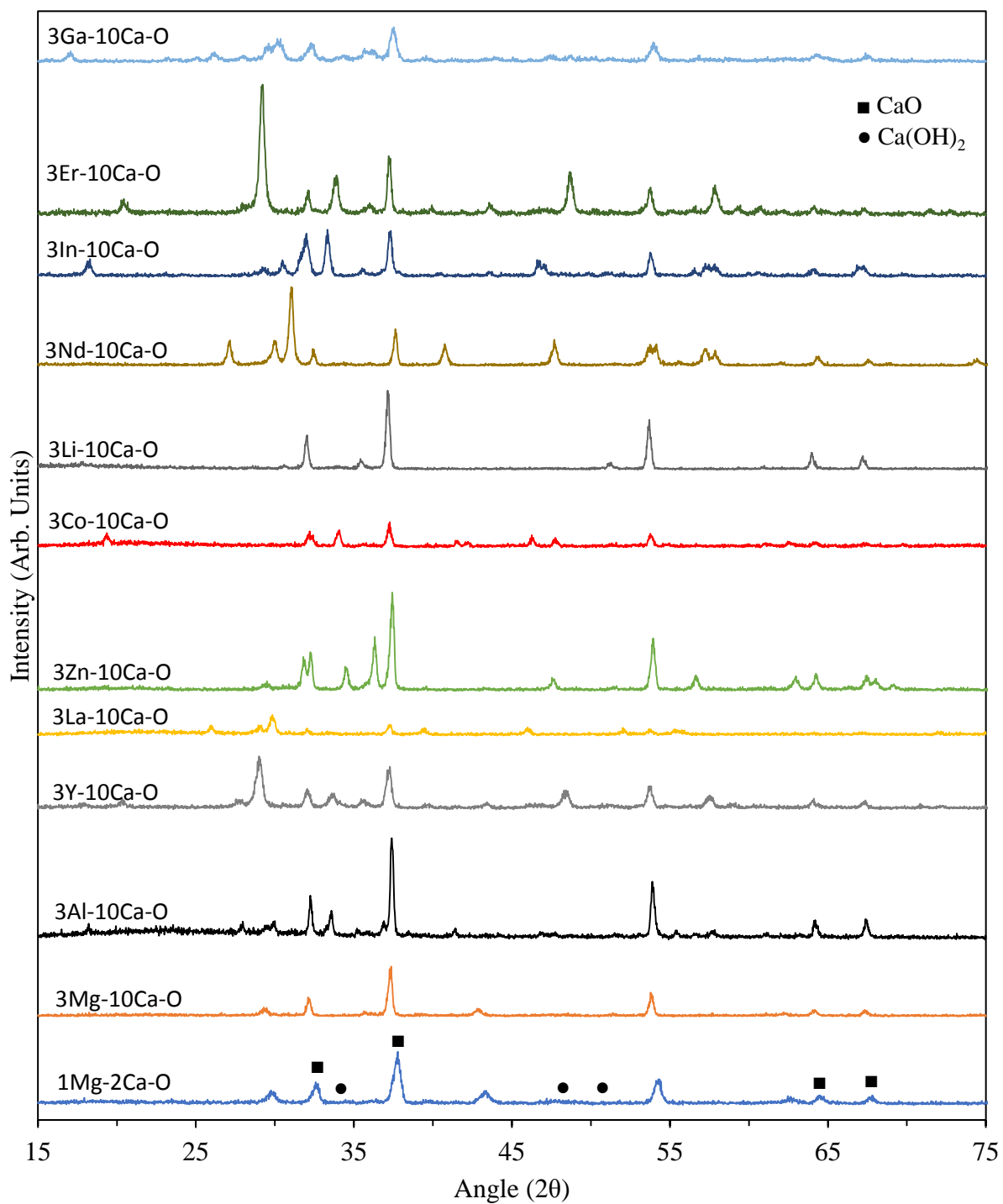
Figure 36. XRD patterns of metal-doped CaO nanofibers prepared via electrospinning after thermal treatment in air at 1173 K.

6.3.2 Multi-Cycle Carbonation-Calcination of Electrospun Metal-Doped CaO Nanofibers

Carbonation-calcination cycles were collected for the metal-doped nanofibers to study the effect of metal addition on the performance of the CaO-based sorbents. **Figure 37** shows the reaction-calcination results of the metal-doped CaO nanofibers. The results indicate that the choice of metal significantly impacts sorption capacity and durability. Specifically, two metal parameters (Tammann temperature and oxidation state) seem to correlate well with data. **Figure 37** shows that metal oxides that had high melting points and high Tammann temperatures had generally higher sorption capacities and demonstrated better stabilities after repeated cycling. For example, the three worst performing sorbents in this work in terms of sorption capacity and durability were 3Li-10Ca-O (0.04 $g_{CO2}/g_{sorbent}$), 3Co-10Ca-O (0.1 $g_{CO2}/g_{sorbent}$), and 3Zn-10Ca-O (0.3 $g_{CO2}/g_{sorbent}$). All three of these sorbents included a metal oxide within their framework that had a Tammann temperature that was lower than 1073 K (calcination temperature). On the other hand, the sorbents that worked well were the ones that generally had high melting points and high Tammann temperatures (e.g., Mg-,Y-, Er-, Nd-, La-, Al-, In-, and Ga-doped CaO).

The results in this section certainly indicate that the melting point and Tammann temperature of a refractory oxide are two important parameters to consider when selecting a dopant. Because temperature influences the transmission and diffusion of ions or atoms in a solid material, the melting temperature is a parameter that indirectly influences the sintering of an oxide. Generally, sintering occurs far below the melting point of a solid compound. When a compound reaches 50% to 75% of its melting point temperature (Tammann temperature), migration of ions and cavities within the oxide become significant.[225] At this temperature, the grain boundaries tend to integrate and overlap, leading to particle agglomeration. Indeed, it is for this reason that refractory dopants improve performance (i.e., durability) of CaO-based sorbents: they essentially

enhance the sintering resistance of a sorbent by effectively introducing a phase that has a high

Tammann temperature and melting point to the CaO structure. As mentioned in the introduction,

without a dopant, pure CaO sorbents (e.g., CaO-nanofibers in chapter 5) are bound to sinter and

agglomerate irrespective of how they were synthesized (e.g., electrospinning, thermal

decomposition, etc.) because the Tammann temperature of calcium carbonate is 806 K whereas

the carbonation and calcination operation temperatures in this work are much higher (873 K and

1073 K, respectively). Therefore, as shown in **Figure 37**, the sorbents that had a Tammann

temperature lower than 1073 K (e.g., Li_2O, CoO, and ZnO) did not possess optimal durability or

acceptable sorption capacity whereas the ones that did performed better.

Table 17. Melting-point and Tammann temperature of the metal oxides used in this work. Compounds that don't have a Tammann temperature in the literature were reported as a range, corresponding to 50% to 75% of the melting point.

Compound	Melting Point (K)	Tammann Temperature (K)
CaO	3171	1586 [225,232,233]
MgO	3125	1461 [225,232,233]
Y_2O_3	2683	1473 [225]
Er_2O_3	2617	1309 - 1963
Nd_2O_3	2506	1253 - 1879
La_2O_3	2490	1286 [225]
Al_2O_3	2273	1263 [225,232,233]
ZnO	2248	983 [225,234]
In_2O_3	2183	1092 - 1637
Ga_2O_3	2173	1087 - 1630
CoO	2103	1052 [225,233]
Li_2O	1711	856 - 1284
$CaCO_3$	1612	806 [225,233]

In addition to the influence of Tammann temperature on performance, the results in this

section further show that supports that were doped with metals that have a +3 oxidation state had

136

better durability than the supports that were doped with metals that have other oxidation states. This might be due to CaO forming more stable mixed oxide phases with metals that have a +3 oxidation state. Additionally, it's been shown that supports that partially carbonate (e.g., 3Mg-10Ca-O) exhibited higher initial sorption capacities than the supports that did not (e.g., 3Zn-10Ca-O), albeit they had reduced stabilities.
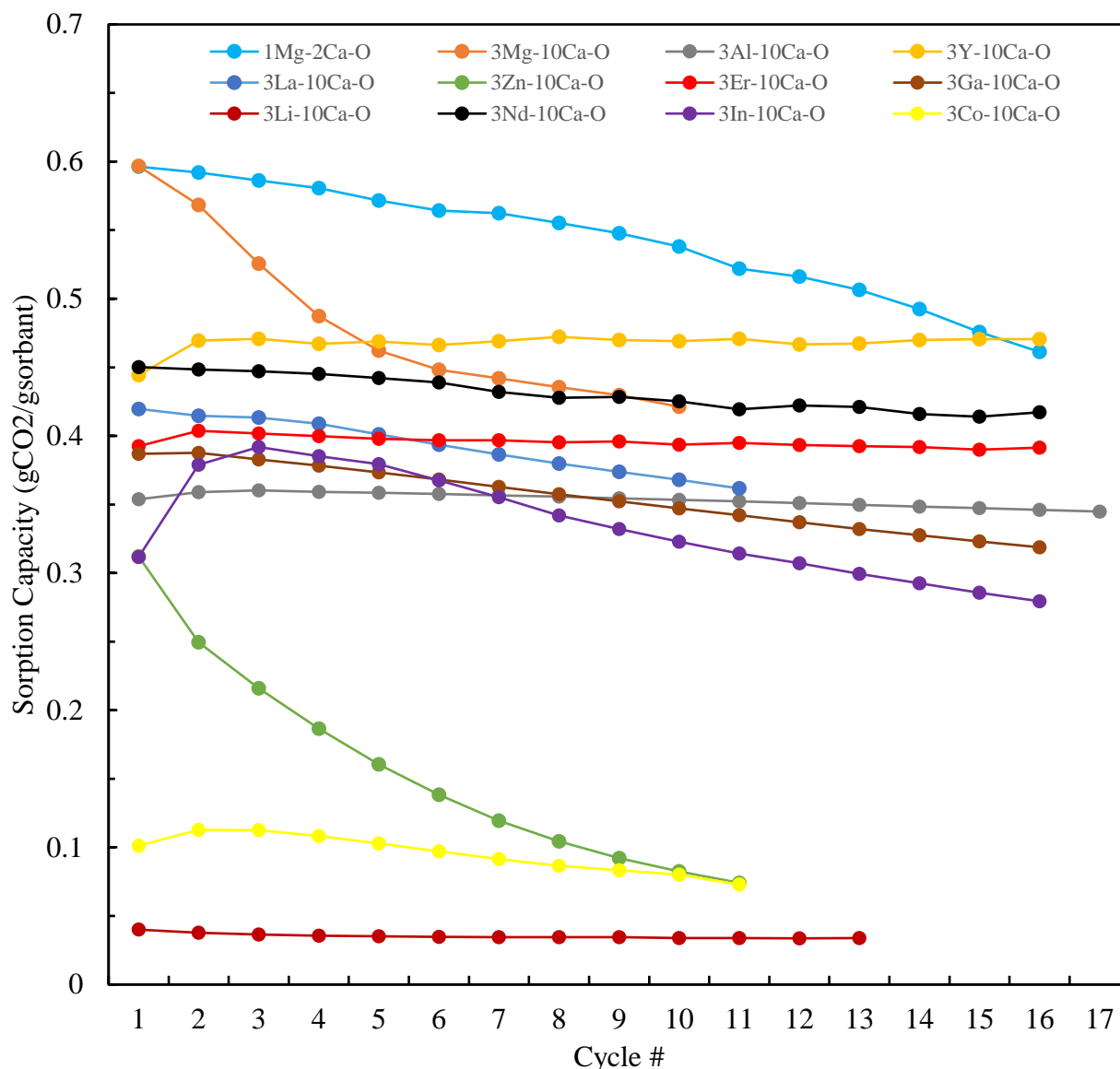
Figure 37. Sorption capacity of metal-doped (Mg, Al, Y, La, Zn, Er, Ga, Li, Nd, In, and Co) nanofibers across multiple carbonation-calcination cycles at 873 K, 101 kPa, and 200 sccm of CO_2 via thermogravimetric analysis.

6.4 Summary

In this chapter, various metal-doped CaO-based nanofibers were synthesized via electrospinning and tested in a cyclic carbonation-calcination operation in TGA at 873 K. After 10 cycles, the performance of the sorbents were in the following order: 1Mg-2Ca-O (0.54 $g_{CO2}/g_{sorbent}$) > 3Y-10Ca-O (0.47 $g_{CO2}/g_{sorbent}$) > 3Nd-10Ca-O (0.43 $g_{CO2}/g_{sorbent}$) > 3Mg-10Ca-O (0.42 $g_{CO2}/g_{sorbent}$) > 3Er-10Ca-O (0.39 $g_{CO2}/g_{sorbent}$) > 3La-10Ca-O (0.37 $g_{CO2}/g_{sorbent}$) > 3Al-10Ca-O (0.36 $g_{CO2}/g_{sorbent}$) > 3Ga-10Ca-O (0.34 $g_{CO2}/g_{sorbent}$) > 3In-10Ca-O (0.32 $g_{CO2}/g_{sorbent}$) > 3Zn-10Ca-O (0.08 $g_{CO2}/g_{sorbent}$) > 3Co-10Ca-O (0.08 $g_{CO2}/g_{sorbent}$) > 3Li-10Ca-O (0.03 $g_{CO2}/g_{sorbent}$). The first nine supports which included Mg-, Y-, Nd-, Er-, La-, Al-, Ga-, and In-phases mixed in with CaO exhibited melting temperatures and Tammann temperatures that were higher than the calcination temperature (1073 K) used in this work. As such, the dopants acted as stable inert metal phases thus, prevented CaO from sintering and agglomerating. Indeed, incorporating these metals into the CaO-framework resulted in improved CO_2 uptake capacities upon repeated cycling. On the other hand, metals that had relatively low melting points and Tammann temperatures (lower than the calcination temperature) (e.g., Li, Co, and Zn) demonstrated poor durability and had considerably lower sorption capacities.

Aside from the effect of melting point and Tammann temperature, oxidation state was also shown to influence the performance of the doped sorbents. Specifically, sorbents that included metals that had a +3 oxidation state seemed to perform better than those that had other oxidation states. Furthermore, metals that formed oxides that partially carbonated (e.g., Mg) had higher initial capacities than those that didn't. The results certainly demonstrate the effectiveness of incorporating inert metals into the CaO framework to yield active, stable and durable sorbents for high temperature CO_2 capture.

Chapter 7 | Application III: Removal of Hydrogen Sulfide at Low Temperatures

7.1 Introduction

Stringent environmental regulations in recent years have required several industries to seek effective and efficient techniques to sequester pollutants present in various chemical conversion processes. Hydrocarbon streams derived from oil, coal, and natural gas processing units are often contaminated by inorganic sulfur-containing compounds such as thiols (mercaptans), sulfides, thiophenes, and H_2S.[235,236] These sulfur compounds not only adversely affect the quality and specifications of the product streams but also conflict with health and environmental regulations.[237] Because sour oil and gas reservoirs, which contain high levels of acid gases, are playing a larger role in current energy production technologies due to rising demands for energy and depletion of cleaner petroleum reservoirs,[238] meeting these environmental regulations becomes increasingly challenging with existing processes and technologies.

H_2S, in particular, is a malodorous and toxic gaseous sulfur compound, which is generated in significant quantities in petrochemical plants across the globe. It causes a wide range of adverse health effects upon inhalation ranging from respiratory irritation to loss of consciousness to death, and its oxidized products (e.g., sulfur dioxide and sulfur trioxide) when released into the atmosphere may have serious, long-term environmental ramifications (e.g., acid rain).[239,240] Additionally, H_2S poses a corrosion hazard on transfer pipelines[238] and downstream equipment, and results in catalyst poisoning (particularly, catalysts containing precious metals, such as, platinum, palladium and rhodium)[241] even when present at low concentrations (1-3 ppmv).[242,243]

Because of the chemical affinity of H_2S for metallic cations, a frequently used technique to purify natural gas from these trace levels of sulfide constituents that often remain even after amine scrubbing is via chemical reaction over a solid surface. Such reactive sorption processes are advantageous because they are thermodynamically more favorable than physisorption leading to higher purity streams and higher solid phase contaminant capacities. Zn, Fe, Ca, Mn, and V metal oxides, carbonates, and hydroxides have been studied rather extensively in the literature as adsorbents for H_2S removal at elevated temperatures (>573 K).[242,244–250] However, the application of these materials and formation of metal sulfide according to the reaction given by (H_2S + MO → MS + H_2O, where M is the metal) is generally limited to T>523 K because at low temperatures, most of these materials suffer from low utilization factors as a result of kinetic limitations.[242,246,247,251–254]

Due to economic reasons and the emergence of new processes (e.g., fuel cell systems) as well as new energy sources (e.g., shale gas), there is an industrial push and a need to remove H_2S to sub-ppm levels at low temperatures (298-373 K). Unfortunately, commercially available sulfur-removal sorbents suffer from low removal efficiencies at these conditions.[255] As such, current research efforts have gravitated towards developing sorbents that are able to remove H_2S down to room temperature.

Some transition metal oxides (particularly, CuO, ZnO, Fe_2O_3, and NiO) are interesting in this respect because of the their thermodynamics for H_2S removal at room temperature ($\Delta G_{T=298K}=$ -126 kJ mol^{-1}, -76 kJ mol^{-1}, -74 kJ mol^{-1} and -136 kJ mol^{-1}, for CuO, ZnO, Fe_2O_3, and NiO respectively).[256] However, unlike high-temperature desulfurization studies there is limited work done on the removal of H_2S by metal oxides at low temperature.[257–259] Xue et al. investigated a series of pure metal oxides and mixed metal oxides (e.g., CuO, ZnO, NiO, CaO, SnO, Mn_3O_4, Zn-

Mn-O, Zn-Co.O, Zn-Al-O, and Zn-Ti-Zr), which were prepared from various hydrous oxides and hydroxycarbonates precursors, and found that several of these oxides had high H_2S adsorptivity values (10.0-28.0 mg H_2S g^{-1} sorbent) at room temperature.[259] Remarkably, despite possessing optimal $\Delta G_{T=298}$ values, these oxides when reacted with H_2S at room temperature suffer from low removal capacities due to (1) ion migrations to and from the lattice structure, (2) sintering,[260] (3) mechanical disintegration,[260] (4) diffusional resistance,[255,261] and/or (4) limitations in the number of adsorption sites.

Of the previously reported oxides that are capable of removing H_2S at low temperatures, CuO has garnered particular interest because of the highly-favored sulfidation thermodynamics of Cu^{2+} and Cu^{+1}. That, coupled with the high equilibrium constant of CuO for H_2S removal at room temperature ($K_s = 6.8 \times 10^{20}$ at 298 K),[262] enables CuO to reduce H_2S from several thousand ppm down to sub-ppm levels. Realizing these advantages, current research efforts have focused on (1) synthesizing small CuO nanoparticles and supporting them on mesoporous materials (e.g., activated carbon, SiO_2, Al_2O_3, clay, and modified zeolites),[254,260,263,264] or (2) combining other metal oxides (e.g., Zn, Fe, Al, V, and Mo-based) with CuO, [160,255,265] to create materials with improved thermodynamic stability and/or kinetics. However, because most of the literature deals with such supported or mixed oxide materials as well as high-temperature H_2S removal processes to avoid kinetic limitations imposed by ambient conditions, little work has been done on unsupported, pure CuO at these milder conditions. Knowledge about several parameters such as the influence synthesis procedures and crystallite size at low temperatures on reactivity is therefore critical to the use of reactive sorbents in purification processes.

In this work, pure CuO sorbents with varying properties (crystallite sizes, surfaces areas, pore volumes, and purities) and morphologies were synthesized via sol-gel, co-precipitation,

hydrothermal treatment, hydrolysis, and electrospinning, and reacted with 1000 ppmv H_2S/N_2 in a fixed bed reactor at room temperature and pressure. The sulfur removal capacity, q_s, and overall rate parameter, k, were evaluated by analysis of the collected breakthrough curves using a linear driving force model (described in depth in the SI section of the following reference).[266] Sol-gel, co-precipitation, hydrothermal treatment in the presence of a polymer, and hydrolysis were used to fabricate CuO nanoparticles with appropriate properties (i.e., small crystallite sizes) for this reaction as the literature indicates that high surface areas, porous structures, and nano-sized particles with small cluster sizes are advantageous for metal oxide desulfurization.[267] Electrospinning, which is a simple, easy-to-use electrostatic fabrication technique, was used to generate one-dimensional Cu-containing nanofibers with varying fiber diameters, which were later thermally treated to remove the polymer matrix and form CuO nanofibers. The CuO fibers were carefully designed to have high surface area-to-volume ratios, interconnected porous networks, and tunable porosities. In this work, polyvinylpyrrolidone (PVP; M.W.=1,300,000 and M.W.=40,000) and polyethylene glycol (PEO; M.W.=300,000) were used as sacrificial templates in the electrospinning synthesis process, and both PVP (M.W.=1,300,000) and P123 were used for the surfactant-templated hydrothermal dissolution-recrystallization method, to increase surface area and pore size and probe the effect of purity (i.e., residual carbon remaining on the surface of the sorbent) on CuO activity. To elucidate information regarding structure-function relationships, the sorbents were characterized using X-ray diffraction (XRD), thermogravimetric analysis (TGA), N_2-physiosorption measurements (BET), scanning electron microscopy (SEM), and X-ray photoelectron spectroscopy (XPS).

7.2 Experimental

7.2.1 Materials

Polyvinylpyrrolidone (PVP) (M.W. 1,300,000, Sigma-Aldrich), PVP (M.W. 40,000, Sigma Aldrich), polyethylene oxide (PEO) (M.W. 300,000, Alfa Aesar), copper (II) nitrate trihydrate (Sigma Aldrich, 99%), copper (II) acetate monohydrate (Sigma Aldrich, 99%), poly(ethylene glycol)-*block*-poly(propylene glycol)-*block*-poly(ethylene glycol) (P123; Sigma Aldrich, M_n ~ 5,800), methyl alcohol anhydrous (Sigma-Aldrich, 99.8%), sodium hydroxide (BDH, 97%), glacial acetic acid (VWR, ACS grade) and ethyl alcohol (Sigma-Aldrich, 100%) were purchased and used without subsequent purification.

7.2.2 Synthesis Methods

7.2.2.1 Sol-gel Synthesis of CuO Nanoparticles

CuO nanoparticles were prepared using an acid-catalyzed sol-gel process.[268] 1.0 cm^3 of glacial acetic acid was added to 300 cm^3 of 0.02 M copper (II) nitrate or copper (II) acetate solution under vigorous stirring and heating. At boiling point, 0.8 g of sodium hydroxide was added to the solution with continuous stirring. The solution was then allowed to cool to room temperature while a black precipitate continued to form and settle in the bottom of the beaker. The precipitate was then vacuum filtered or centrifuged for 10 minutes (JA-14 rotor) at 293 K and 6000 RPM. The supernatant was then poured off and the precipitate was washed with deionized water and ethanol. The washed precipitate was dried in a furnace for 8 h at 313 K and then samples were either collected or thermally treated a second time at higher temperatures to achieve particles of various crystallite sizes. Thermal treatment was performed by heating samples at a ramping rate of 1 K h^{-1} and holding the furnace temperature at 623 K, 823 K or 1023 K for 4 h. The samples prepared via this technique are denoted as NP-X, where X is the sample number (NP-1 to NP-6). **Table 18** shows the specific synthesis conditions for making the sorbents prepared in this work.

Table 18. Synthesis procedures of CuO sorbents, including, precursors used, processing/synthesis conditions, and thermal treatment conditions.

Sample ID	Synthesis Method	Precursors	Processing Conditions	Thermal Treatment
NP-1	sol-gel	$Cu(Ac)_2.3(H_2O)$, NaOH, CH_3COOH	vacuum filtration	dried at 313 K for 8 h
NP-2	sol-gel	$Cu(Ac)_2.3(H_2O)$, NaOH, CH_3COOH	vacuum filtration	dried at 313 K for 8 h, then treated at 623 K for 4 h
NP-3	sol-gel	$Cu(Ac)_2.3(H_2O)$, NaOH, CH_3COOH	vacuum filtration	dried at 313 K for 8 h, then treated at 823 K for 4 h
NP-4	sol-gel	$Cu(Ac)_2.3(H_2O)$, NaOH, CH_3COOH	vacuum filtration	dried at 313 K for 8 h, then treated at 1023 K for 4 h
NP-5	sol-gel	$Cu(NO_3)_2.3(H_2O)$, NaOH, CH_3COOH	centrifuging	dried at 313 K for 8 h
NP-6	sol-gel	$Cu(Ac)_2.3(H_2O)$, NaOH, CH_3COOH	centrifuging	dried at 313 K for 8 h
NP-7	co-precipitation	$Cu(NO_3)_2 \cdot 3(H_2O)$, NaOH	vacuum filtration	dried at 353 K for 14 h, then treated at 773 K for 4 h
NPC-1	hydrothermal	CuO (NP-7), P123	hydrothermal at 383 K (24 h)	dried at 353 K for 12 h, then treated at 823 K for 4 h
NPC-2	hydrothermal	CuO (NP-7), PVP (MW=1,300,000)	hydrothermal at 383 K (24 h)	dried at 353 K for 12 h, then treated at 823 K for 4 h
NB-1	co-precipitation	$Cu(NO_3)_2 \cdot 3(H_2O)$, NaOH	aged for 72 h, vacuum filtration	dried at 333 K for 12 h, then treated at 623 for 4 h
FP-1	hydrolysis	$Cu(Ac)2 \cdot 3(H_2O)$	synthesized at 373 for 45 minutes	dried at 353 K for 12 h
FP-2	co-precipitation	0.5 g of $Cu(NO_3)_2.3(H_2O)$, 50 cm^3 of DI H_2O	synthesized at 353 for 8 h	dried at 353 K for 12 h
FP-3	co-precipitation	2.0 g of $Cu(NO_3)_2.3(H_2O)$, 30 cm^3 of DI H_2O	synthesized at 376 for 24 h	dried at 353 K for 12 h
NF-1	electrospinning	2.7 g of PEO (MW=300,000), 22 cm^3 of EtOH, 1.0 g of $Cu(NO3)2 \cdot 3(H_2O)$, and 8 cm^3 DI H_2O	14 inches, 30 kV, 1.0 cm^3 h^{-1}	treated at 823 K for 4 h at a ramping rate of 1 Kmin^{-1}
NF-2	electrospinning	1.4 g of PVP (1,300,000), 22.5 cm^3 of EtOH, 0.15 g of $Cu(NO3)2 \cdot 3(H_2O)$, and 10 cm^3 of DI H_2O	15 inches, 35 kV, 5.0 cm^3 h^{-1}	treated at 898 K for 10 h at a ramping rate of 0.4 K min^{-1}
NF-3	electrospinning	10.5 g of PVP (40,000), 23 cm^3 of EtOH, 4.0 g of $Cu(NO3)2 \cdot 3(H_2O)$, and 23 cm^3 of DI H_2O	18 inches, 30 kV, 1.0 cm^3 h^{-1}	treated at 823 K for 4 h at a ramping rate of 1 K min^{-1}
NF-4	electrospinning	1.75 g of PVP (1,300,000), 25 cm^3 of EtOH, 1.75 g of $Cu(NO3)2 \cdot 3(H_2O)$, and 5 cm^3 of DI H_2O	6 inches, 20 kV, 1.0 cm^3 h^{-1}	treated at 773 K for 2 h at a ramping rate of 2 K min^{-1}
NF-5	electrospinning	1.3 g of PVP (1,300,000), 23 cm^3 of MeOH, 1.3 g of $Cu(NO3)2 \cdot 3(H_2O)$, and 10 cm^3 of DI H_2O	18 inches, 30 kV, 1.0 cm^3 h^{-1}	treated at 823 K for 4 h at a ramping rate of 2 K min^{-1}
NF-6	electrospinning	1.3 g of PVP (1,300,000), 23 cm^3 of EtOH, 1.3 g of $Cu(NO3)2 \cdot 3(H2O)$, and 10 cm^3 of DI H_2O	22 inches, 30 kV, 1.0 cm^3 h^{-1}	treated at 823 K for 4 h at a ramping rate of 2 K min^{-1}

7.2.2.2 Co-precipitation of CuO Nanoparticles

CuO nanoparticles were prepared by a drop-wise addition of aqueous 0.1 M sodium hydroxide solution to aqueous 0.1 M copper (II) nitrate trihydrate solution under continuous

mixing. The obtained material, copper (II) hydroxide, was then vacuum filtered with distilled water and ethanol, dried in air at 353 K for 14 h, and then thermally treated in air at 773 K for 4 h at a ramping rate of 1 K h^{-1}. The sample prepared via this technique is denoted as NP-7.

7.2.2.3 Hydrothermal Synthesis of CuO Nanoparticles

A porous CuO sample was synthesized according to the method of surfactant-assisted hydrothermal interaction using CuO powder as starting material.[142,143] The polymer-containing solution was prepared by dissolving 0.65 g of either P123 or PVP (M.W.=1,300,000) in 15 cm^3 of water while stirring for 2 h. After that, appropriate amounts of CuO (NP-7) was added to the beaker, so that the Cu to polymer weight ratio is 1:1, and the solution was left to stir at 800 rpm for 48 hours. The solution was then ultrasonically treated for 1 h and transferred to a glass tube reactor (cylindrical pressure vessel) for hydrothermal treatment at 383 K for 24 h. The black solid substance was centrifuged and washed with DI water and ethanol for the removal of the majority of the P123 surfactant or PVP polymer. The solid was then dried overnight in a drying oven at 353 K. The as-obtained material was subsequently thermally treated in air from room temperature to 823 K for 4 h at ramping rate of 2 K min^{-1} for the generation of CuO. These materials are denoted as NPC-1 (P123) and NPC-2 (PVP).

7.2.2.4 Co-precipitation of CuO Nanobelts

CuO particles with belt-like shapes were prepared by dropwise adding 5 M sodium hydroxide solution to aqueous 0.6 M copper (II) nitrate trihydrate solution under continuous mixing. The solution was then aged for 3 days and precipitates were then vacuum filtered and washed using ethanol and deionized water. The washed precipitates were dried overnight at 333 K and then thermally treated in air at 623 K for 4 hours. This material is denoted as NB-1.

7.2.2.5 Hydrolysis and Precipitation of CuO Flowerlike Nanostructures

CuO flowerlike nanostructures were synthesized using a facile route by hydrolyzing a copper acetate solution.[269] In a typical synthesis, 100 cm^3 of 0.02 M copper acetate solution was dissolved in deionized water in a beaker, and heated from room temperature to 373 K for 45 minutes. After hydrolysis and crystallization, the black precipitate formed in the solution was centrifuged and washed with DI water and ethanol and dried overnight in air at 353 K. The nanostructures prepared via this technique are denoted as FP-1.

7.2.2.6 Co-precipitation of CuO Nanoflake-Based Flowerlike Hierarchical Nanostructures

Nanoflake-based flowerlike CuO nanostructures were synthesized via thermally decomposing a $[Cu(NH_3)_4]^+$ solution, without the aid of any surfactants.[270] In a typical synthesis, 0.5 or 2.0 g of copper nitrate was dissolved in 50 or 30 cm^3 of deionized water in a sealed bottle. Ammonia (~ 1-3 cm^3) is then added dropwise until a change of color is observed (darker blue). The bottle is then sealed tightly and heated to 353 K for 8 h or 376 K for 24 h, while stirring. After that, the black precipitate that formed in the bottle was washed with distilled water and ethanol to remove impurities and then centrifuged. The centrifuged solid was dried in a drying oven (353 K) overnight. The solids collected from this synthesis technique are denoted as FP-2 (353 K) and FP-3 (376 K).

7.2.2.7 Electrospinning and Thermal Treatment of PVP-Cu(NO₃)₂ / PEO-Cu(NO₃)₂ to CuO Nanofibers

Polymer solutions were prepared by dissolving PVP M.W.=1,300,000 (1.30-1.75 g), PVP M.W.=40,000 (10.5 g) or PEO M.W.=300,000 (2.7 g) in solvent (methanol or ethanol; 22-25 cm^3). The polymer solution was then vortexed (Fisher Scientific Digital Vortex Mixer) at 3000 rpm for 1 h until the polymer was completely dissolved. The solution was left to settle for 10 minutes,

transferred to a beaker, and stirred for 0.5 h. The metal containing solution was prepared by dissolving copper (II) nitrate (0.15-4.0 g) in 5-10 cm^3 of DI water and stirring the solution for 0.5 h. The copper containing solution was then added dropwise to the polymer containing solution. The solution was stirred for 0.25 h, and then vortexed for 0.5 h at 3000 rpm.

The electrospinning solution was placed in a 10 mL syringe (BD 10 mL syringe with Luer Lok^{TM} tip) with a hypodermic needle (Monoject^{TM} Standard 30G x ¾"). The distance between the tip of the needle and a stainless-steel collecting plate, which was covered with aluminum foil, was 6-22 inches. A Gamma High Voltage Research ES75 power supply was used to apply 20-35 kV on the polymer jet while the polymer solution was extruded through the needle at a rate controlled by a syringe pump (1.0-5.0 cm^3 h^{-1}; Kent Scientific Genie Plus). Dry air was circulated inside a 3 m^3 chamber at 6 cm^3 min^{-1} to control the relative humidity at 19.5 ± 2%. All electrospinning was carried out at ambient conditions, temperature (294 ± 3 K) and pressure (101 kPa). The collected fibers were thermally treated in air at 773-898 K for 2-10 h at a ramping rate of 0.4-2.0 K min^{-1} to remove the majority of PVP/PEO and form CuO. The CuO nanofibers are denoted as NF-X (NF-1 to NF-6).

7.2.3 Characterization and Sulfidation Tests

7.2.3.1 Characterization

The synthesized CuO sorbents prepared via sol-gel, co-precipitation, hydrothermal treatment, hydrolysis, and electrospinning, as described in section 7.2.2 were characterized using a variety of techniques. Powder X-ray diffraction patterns were obtained on an X-ray diffractometer (JEOL JDX-3530 and Philips X-Pert) using Cu Kα radiation of 1.5410 Å to identify the CuO phases. The average crystallite sizes were found using Scherrer's formula. Nitrogen adsorption-desorption isotherms were measured at 77 K with a Micrometrics ASAP 2020 Plus

system. Before measurements, the samples were degassed at 1×10^{-3} Torr and 573 K. The Brunauer-Emmett-Teller (BET) surface areas were calculated from the isotherms by using the BET equation. The pore size distribution was derived from the adsorption branches of the isotherms using the Barrett-Joyner-Halenda (BJH) model. Scanning electron microscopy (NOVA 230 Nano SEM) was used to determine the morphology of the sorbents. The mean diameter and size distribution (standard deviation) of the electrospun nanofibers were calculated from the SEM micrographs using ImageJ software (n = 250; where, n is the number of fibers that were measured and averaged). Thermogravimetric analysis was conducted in a Perkin Elmer TGA. Alumina crucibles were used to hold the samples. Gas flowrates were set to 200 standard cm^3 min^{-1} to minimize external diffusion from the bulk gas to the sample interface. Heating/reaction occurred in air (Matheson UHP Argon, 99.999% purity) at a ramping rate of 10 K min^{-1}. XPS was conducted with PHI 3057 spectrometer using Mg Kα X-rays source at 1286.6 eV. The XPS experiments were carried out in an ultra-high vacuum system with a base pressure of about 6×10^{-10} Pa. The XPS spectra were recorded in normal emission. For the XPS analyses, the Casa XPS 2.3.14 software was used. All binding energy values presented in this paper were charge corrected to C 1s at 284.8 eV. For the interpretation of the spectra, the literature positions were applied.[271]

7.2.3.2 Fixed Bed Sulfidation Experiments

Reactive adsorption of H_2S was studied in an apparatus with plug-flow hydrodynamics shown schematically in **Figure 38**. Copper (II) oxide samples (120-200 mg) were sieved to 75-155 µm agglomerate diameter and packed between plugs of quartz wool in a 0.25-inch outer diameter tubular, stainless steel reactor. Flow rates of gaseous H_2S and N_2 (65 sccm) were introduced to the packed reactor via mass flow controllers (MKS GE50A and GM50A). Feeds to the reactors consisted of 1000 ppmv H_2S in N_2 and were produced by diluting a 1.0% H_2S (Praxair

UHP) in N_2 mixture with UHP N_2. All the sulfidation tests were carried at ambient temperature and pressure. The compositions of feed and effluents were monitored using online gas chromatography (Agilent 7890B) with a sulfur chemiluminescence detector (SCD; Agilent 755) and continuous gas phase FTIR spectroscopy (MKS Multigas). All gas transfer lines and the interior of the reactor were treated with an inert coating (SilcoNert 2000) to mitigate H_2S adsorption onto tubing walls.

1	Mass flow controller
2	Two way valve
3	Three way valve
4	Pressure gauge
5	Pressure relief valve
6	Tubular reactor
7	Heating jacket
8	Temperature control box
9	Back pressure regulator
10	To GC/FTIR
11	From GC/FTIR
12	Scrubber
13	Bubble flowmeter
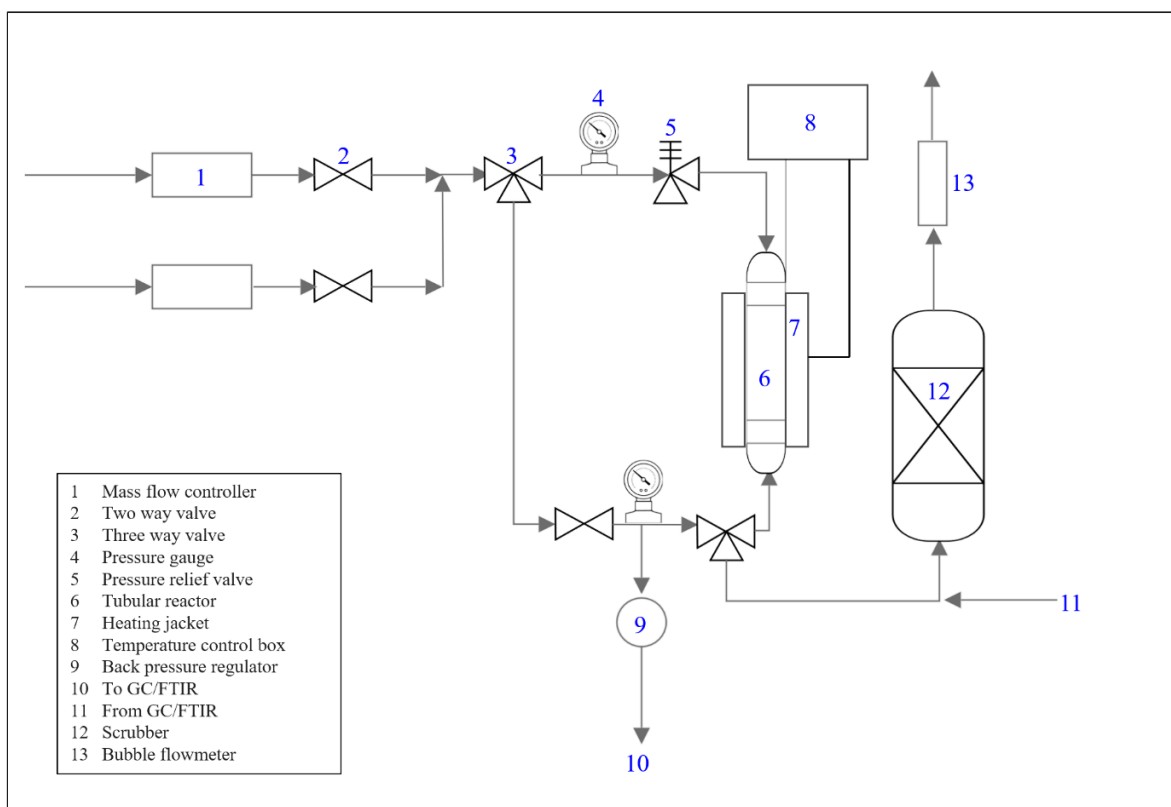
Figure 38. Experimental set-up of the packed-bed reactor used for the desulfurization runs.

7.3 Results and Discussion

7.3.1 Physio-chemical Properties of CuO Materials

XRD was used to identify the crystalline phases and average crystal sizes of the nineteen CuO sorbents prepared in this work using the synthesis techniques described in Section 7.2.2. As shown in **Figure 39**, all the XRD patterns collected show diffraction peaks which are characteristic of the planes of a single-phase monoclinic CuO. The average crystal domain size of the CuO sorbents calculated using Scherrer's formula based on the 38.8° peak were in the range of 5 to 74 nm, with the majority of the sorbents having crystallite sizes less than 25 nm (**Table 19**). The XRD results show that, in general, sorbents that did not undergo thermal treatment in air at elevated temperatures (T > 773 K) as part of their preparation technique had significantly smaller crystallite sizes (< 20 nm). This effect is important to highlight because it was observed in this work that crystallite size strongly influenced the H_2S removal capacity of pure CuO sorbents, irrespective of other properties (such as, surface area, pore size, and pore volume) generated by the synthesis technique (discussed in detail in Section 7.3.2). Furthermore, the d-spacing obtained from the XRD data for all sorbents was in the range of 2.29-2.30 Å for the (200) plane, which is consistent with the literature,[272] and indicative of copper (II) oxide.

Figure 39 also shows the XRD patterns of the as-synthesized NF-1 (PEO-$Cu(NO_3)_2$) and NF-4 (PVP-$Cu(NO_3)_2$) prior to any thermal treatment. Well defined diffraction peaks are absent from the XRD pattern of the pre-thermally treated NF-4 fibers, which indicates that these materials consist of amorphous PVP phases and copper species that are too small to diffract X-rays. Moreover, the XRD patterns of NF-1 (prior to thermal treatment) contains several small peaks consistent with PEO as well as copper nitrate peaks reported previously in the literature.[273,274] These results indicate that thermal treatment in air is required for the formation of CuO from the copper-species that exist in PEO or PVP nanofibers after electrospinning.
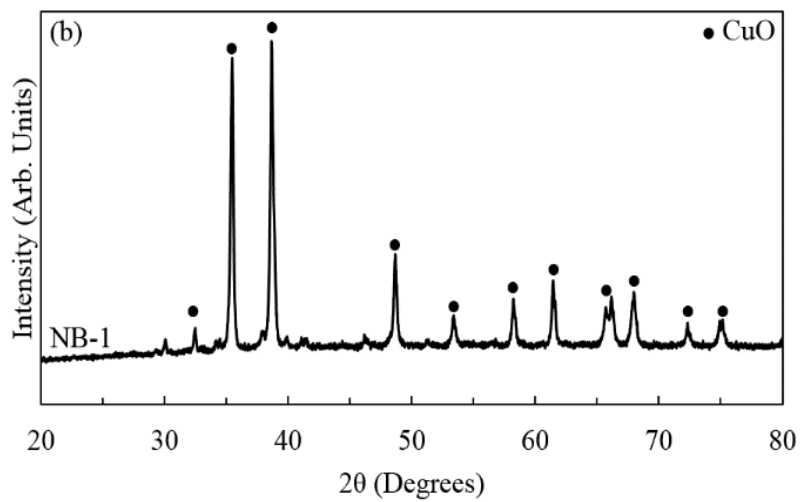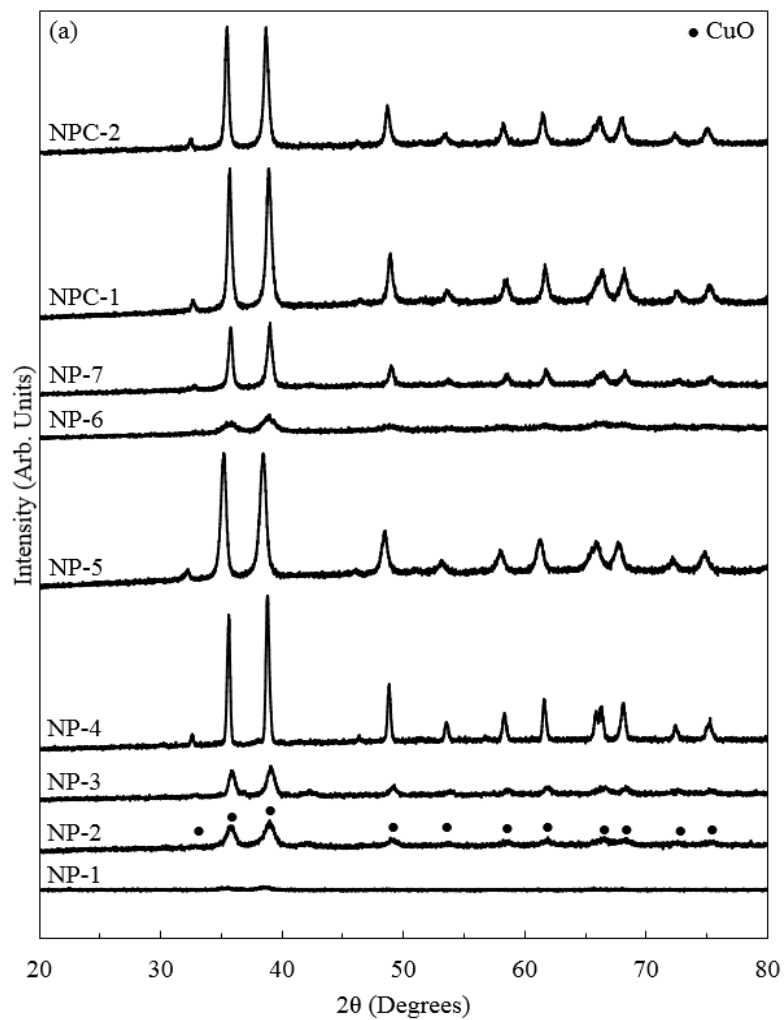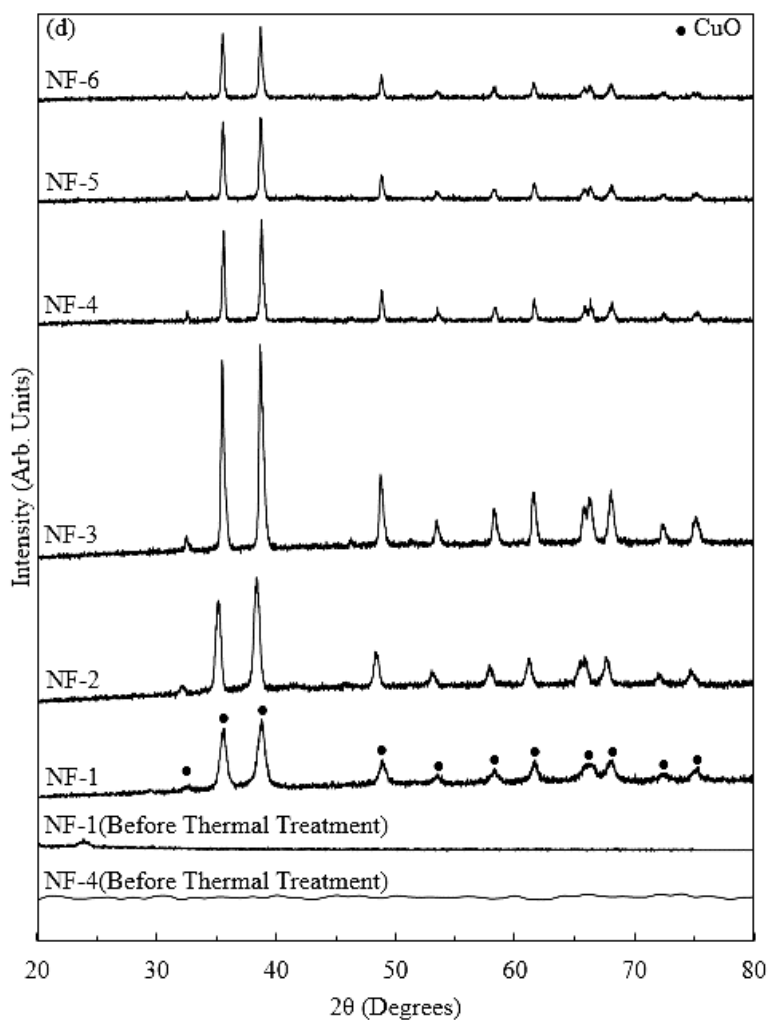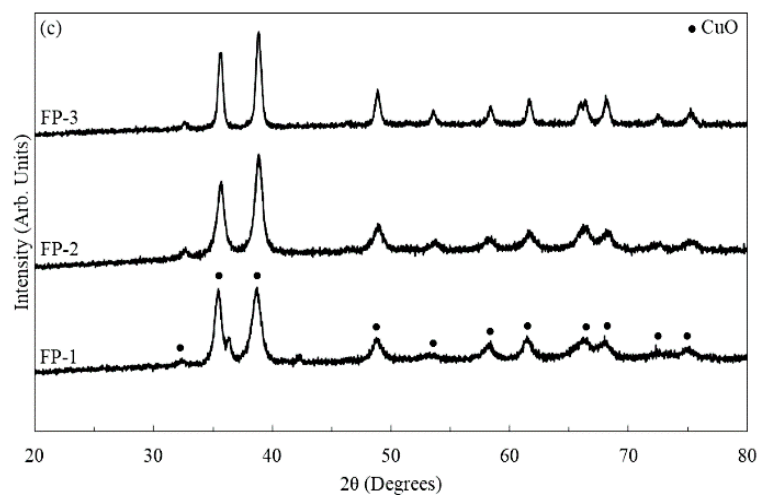
Figure 39. X-ray diffraction patterns of CuO sorbents. (a) nanoparticles via sol-gel, co-precipitation, and hydrothermal treatment (NP and NPC), (b) nanobelts via co-precipitation (NB), (c) flowerlike nanostructures via co-precipitation and hydrolysis (FP), and (d) nanofibers via electrospinning (NF).

152

Table 19. Physio-chemical properties of CuO sorbents prepared via sol-gel, co-precipitation, hydrothermal treatment, hydrolysis, and electrospinning, and their performance in the reaction with H$_2$S at 1000 ppmv H$_2$S/N$_2$, 294 K and 1 atm, in terms of sulfur removal capacity, q$_s$, and overall rate constant, k. [a] Based on XRD. [b] Based on BET. [c] Based on BJH method.

Sample ID	Synthesis method	Crystallite size (nm)[a]	q$_s$ (wt%)	$k \cdot 10^4$ (s^{-1})	S$_{BET}$ (m^{2}g^{-1})[b]	V$_{pore}$ (cm^{3}g^{-1})[c]
NP-1	sol-gel	5	12.0 ± 0.38	1.00 ± 0.0	-	-
NP-2	sol-gel	18	5.48 ± 0.70	2.10 ± 0.2	-	-
NP-3	sol-gel	26	0.54 ± 0.06	39.3 ± 3.9	-	-
NP-4	sol-gel	53	0.47 ± 0.06	27.9 ± 3.2	14.5	0.040
NP-5	sol-gel	9	10.4 ± 0.37	1.40 ± 0.0	-	-
NP-6	sol-gel	11	10.2 ± 0.38	1.90 ± 0.1	-	-
NP-7	co-precipitation	18	5.80 ± 0.23	4.50 ± 0.2	58.8	0.181
NPC-1	hydrothermal	21	1.90 ± 0.18	10.0 ± 0.8	-	-
NPC-2	hydrothermal	24	1.90 ± 0.12	7.50 ± 0.4	17.4	0.080
NB-1	co-precipitation	33	0.37 ± 0.03	31.8 ± 2.0	6.18	0.020
FP-1	hydrolysis	10	8.30 ± 0.91	10.0 ± 0.1	-	-
FP-2	co-precipitation	13	7.20 ± 0.50	3.20 ± 0.2	-	-
FP-3	co-precipitation	19	3.03 ± 1.57	8.40 ± 4.1	59.1	0.079
NF-1	electrospinning	14	2.20 ± 0.10	7.00 ± 0.3	-	-
NF-2	electrospinning	24	1.80 ± 0.10	30.0 ± 1.6	-	-
NF-3	electrospinning	25	1.10 ± 0.10	42.0 ± 1.9	-	-
NF-4	electrospinning	40	0.50 ± 0.02	70.0 ± 2.0	-	-
NF-5	electrospinning	74	0.50 ± 0.03	80.0 ± 3.5	-	-
NF-6	electrospinning	66	0.50 ± 0.04	60.0 ± 4.6	2.79	0.002

N$_2$-physiosorption was performed on a selected group of sorbents (NP-4, NP-7, FP-3 and NF-6) to determine the effect of synthesis on surface area and pore volume. These samples were selected to represent at least one sample per synthesis technique (i.e. morphology). **Table 19** shows the structural parameters calculated from nitrogen adsorption. Analysis of structural parameters along with the degree of micro- and meso-porosity reveals differences in surface area and porosity among the sorbents. Specifically, sorbents that were prepared via co-precipitation (NP-7 = 58.8 m^2 g^{-1} and FP-3 = 59.1 m^2 g^{-1}) possessed larger BET surface areas than those prepared from sol-gel (NP-4 = 14.5 m^2 g^{-1}) and electrospinning (NF-7 = 2.79 m^2 g^{-1}). Additionally, NP-7 (co-

precipitation) (0.181 cm^3 g^{-1}) had pore volumes that were two to three times larger than NP-4 (sol-gel) (0.040 cm^3 g^{-1}) and forty to ninety times larger than NF-6 (electrospinning) (0.002 cm^3 g^{-1}). The low surface area and low meso-porosity of the electrospun materials result from the formation of single CuO fibers with large intra-fiber interstices that are in the macro-range, as determined by SEM (**Figure 40 (h)**).

SEM was used to investigate the effect of preparation technique on the morphology of the synthesized materials. **Figure 40** shows the SEM images (20,000 times magnification) of the representative CuO materials synthesized in this work—nanoparticle samples: NP-1, NP-5, NP-7; nanoparticles synthesized with polymer: NPC-1; nanobelts: NB-1; flower-shaped particles: FP-2, FP-3; and electrospun nanofibers: NF-4. These SEM images reveal that various CuO morphologies and dimensionalities can be obtained by simply varying the preparation technique. **Figure 40 (a-b)** shows that nanostructures prepared via sol-gel (NP-1, NP-5) were found to have irregular particle shapes with varying domain sizes depending on the copper precursor (~5-25 µm for copper(II) acetate (NP-1) in **Figure 40 (a)** and 0.5-4 µm for copper(II) nitrate (NP-5)). Unlike sol-gel, which yielded materials that were irregular in shape, co-precipitation, hydrothermal treatment and electrospinning, yielded materials with regular, defined shapes and structures. For instance, by hydrothermally treating NP-7 (**Figure 40 (c)**) in the presence of P123 (NPC-1), closely aggregated and distinctly spherical CuO particles were formed, with sizes ranging from 4 to 9 µm as seen in **Figure 40 (d).** Properly aging precipitated CuO led the formation of nanobelt-like materials (NB-1) as shown in **Figure 40 (e)**. The effect of reaction time and metal concentration can also be observed in **Figure 40 (f-g)** for flowerlike-structures prepared via co-precipitation. As the reaction time and copper precursor concentration were increased, flowerlike structures formed (**Figure 40 (g)**), with an average size of 2.7 ± 0.9 µm. At low concentrations and temperatures,

154

however, instead of forming these micron-sized flowerlike structures, petal-like structures are formed (0.5-2 µm) (**Figure 40 (f)**).[275] Lastly, **Figure 40 (h)** shows how electrospinning can result in the fabrication of a highly porous, fibrous structure, with significant macro-porosity (NF-4). The fibers formed via electrospinning (NF-4), after undergoing thermal treatment, had an average diameter size of 629 ± 194 nm (measured using ImageJ, n=250). The SEM images, indeed, confirm that different synthesis techniques yield nanomaterials with markedly different morphological features while also shedding light on the growth mechanism of CuO nanostructures as a function of synthesis condition.

(c) NP-7

(d) NPC-1

(e) NB-1

(f) FP-2

156
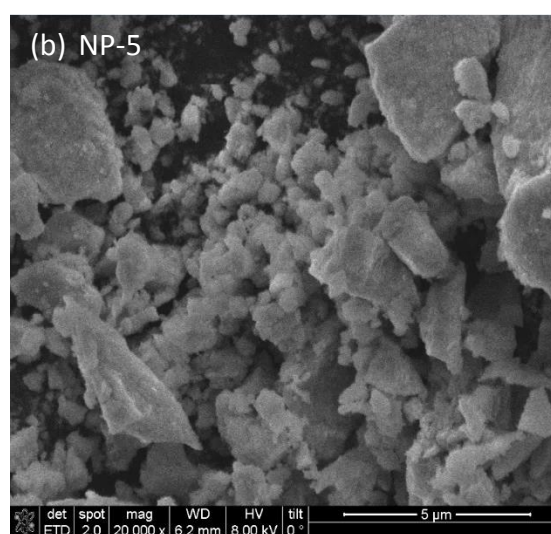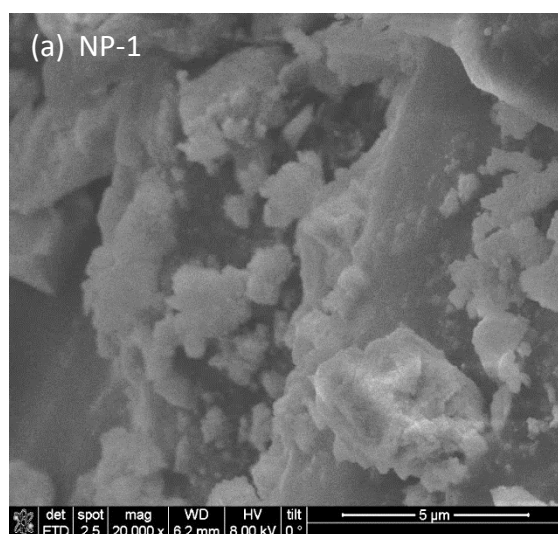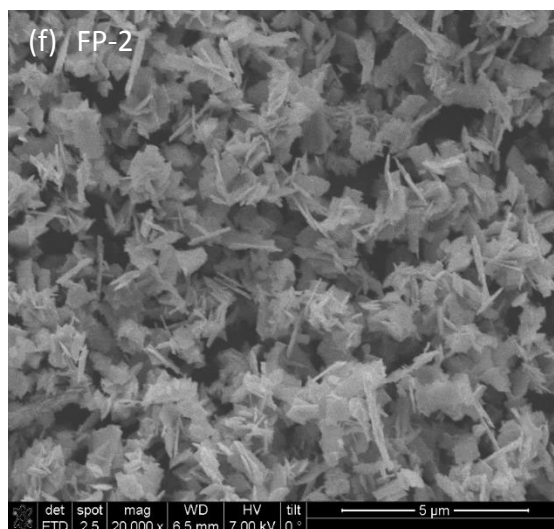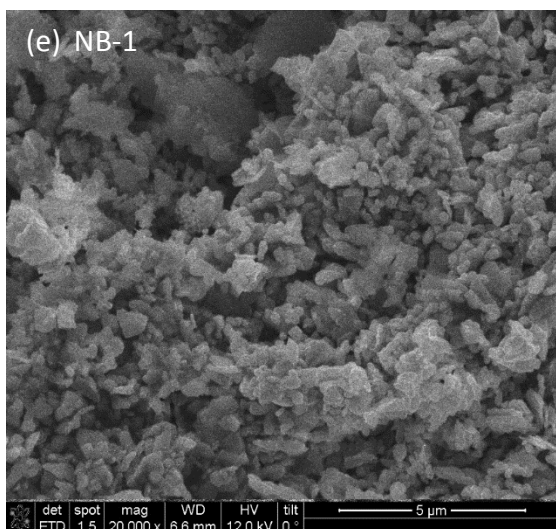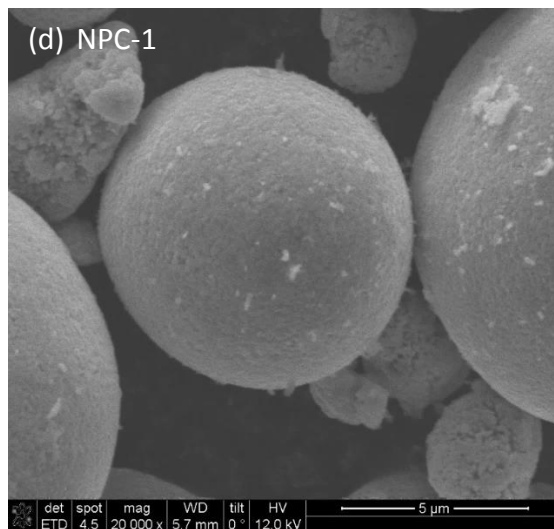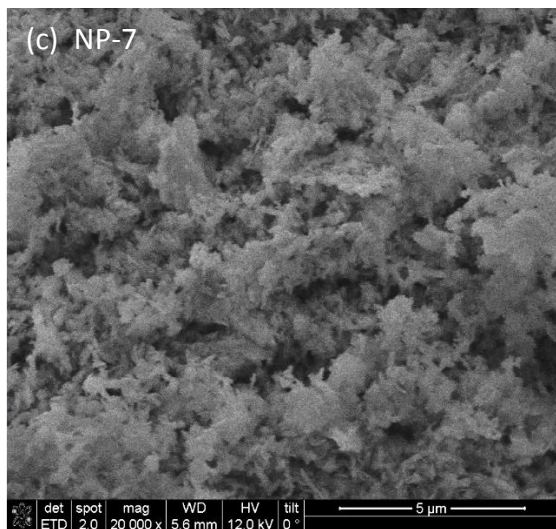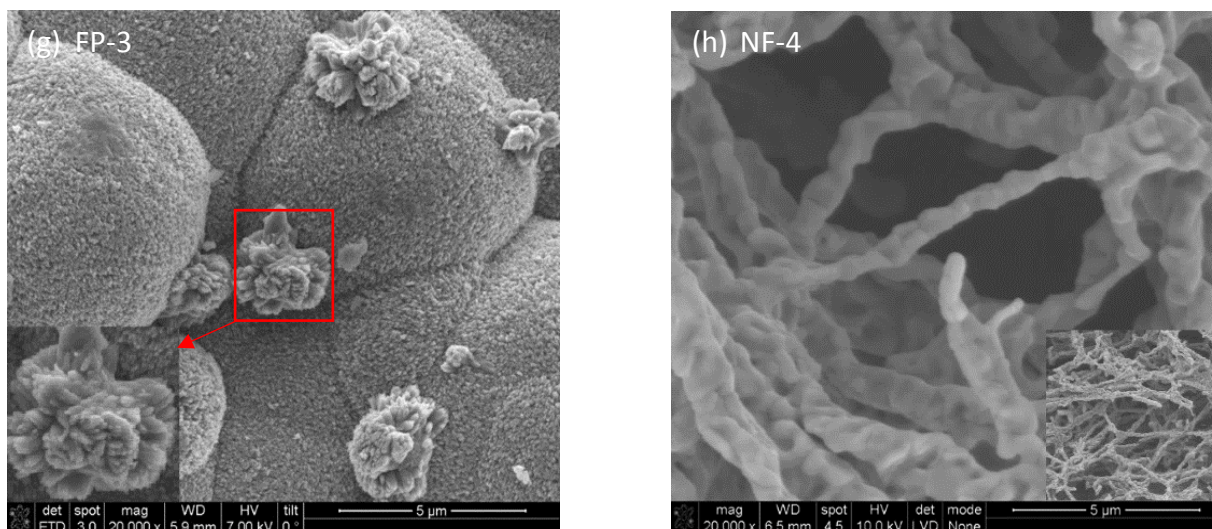
Figure 40. SEM images at 20,000 times magnification of a select group of CuO sorbents with different morphological features prepared via various synthesis techniques (e.g., sol-gel, co-precipitation, hydrothermal treatment with the aid of a polymer, hydrolysis, and electrospinning), as described in Section 7.2.2.

TGA experiments were conducted on pure PEO (M.W.=300,000), pure PVP (M.W.=1,300,000), and NF-4 (prior to thermal treatment; PVP-Cu(NO$_3$)$_2$) to quantify the extent of polymer removal during thermal treatment (i.e., quantity of residual carbon left after treatment, if any) and provide evidence of the conversion of copper nitrate to CuO. **Figure 41** shows the TGA curves of pure PEO, pure PVP, and NF-4. All three samples were decomposed under air at a heating rate of 10 K min^{-1}. The nanofibers synthesized using pure PEO (M.W.=300,000) decomposed under air in a single step, with a total weight loss of approximately 99%. The TGA results prove that at the 823 K, the majority of the PEO polymer is removed. The nanofibers synthesized using pure PVP (M.W.=1,300,000), on the other hand, decomposed under air in two steps, with a total weight loss of approximately 93.7% at 773 K, 94.2% at 823 K, and 94.7% at 897 K, which is a slightly lower weight loss percentage than PEO (**Figure 41**). In the case of PVP, the first step weight loss of 16% occurred between ambient temperature and 622 K and was

157

attributed to the evaporation of volatile solvents. The second step weight loss of 78% from 623 K to 773 K was attributed to the thermal degradation of the PVP chains. It is clear from the TGA curve that the majority of the PVP matrix (much like in the case PEO) is removed at temperatures higher than 773 K. The amount of carbon residue is probably higher in the case of PVP due to the presence of more carbon atoms in the PVP monomer (compared to PEO). The work of Borodko et al.[276] further supports the presence of residual carbon after the thermal treatment of PVP at elevated temperatures. Using spectroscopic techniques, the authors studied the degradation of PVP and showed that in an oxygen atmosphere the PVP forms a polyamide-polyene-like material at temperatures above 523 K, and at temperature above 573 K, these materials transform into amorphous carbon.

Lastly, NF-4, an electrospun nanofiber sample consisting of PVP (M.W.=1,300,000) and $Cu(NO_3)_2$, decomposed under air in two steps, with a total weight loss of approximately 84% (**Figure 41**). These total weight losses in air are consistent with the complete conversion of copper nitrate to CuO. Thus, the first step weight loss can be attributed to the evaporation of volatile solvents, and the second can be attributed to the decomposition of the PVP chains and the conversion of copper nitrate to CuO. **Figure 41** also reveals that the decomposition of NF-4 (475 K) occurs at a much lower temperature than pure PVP (640 K) indicating the effect of copper nitrate, which (as mentioned previously) weakens the bonds within the PVP chains, and of the nitrate anions, which act as an oxidant to combust the polymer. These TGA results are in agreement with the results from the other characterization techniques described in this section, as they provide quantitative evidence of the removal of the majority of the polymer (PEO or PVP), decomposition of the copper nitrate, and formation of CuO during the thermal treatment of electrospun nanofibers

(e.g., NF-4) in air while also hinting at the presence of small amounts of amorphous carbon remaining in the sorbent after thermal treatment of the as-synthesized fibers.
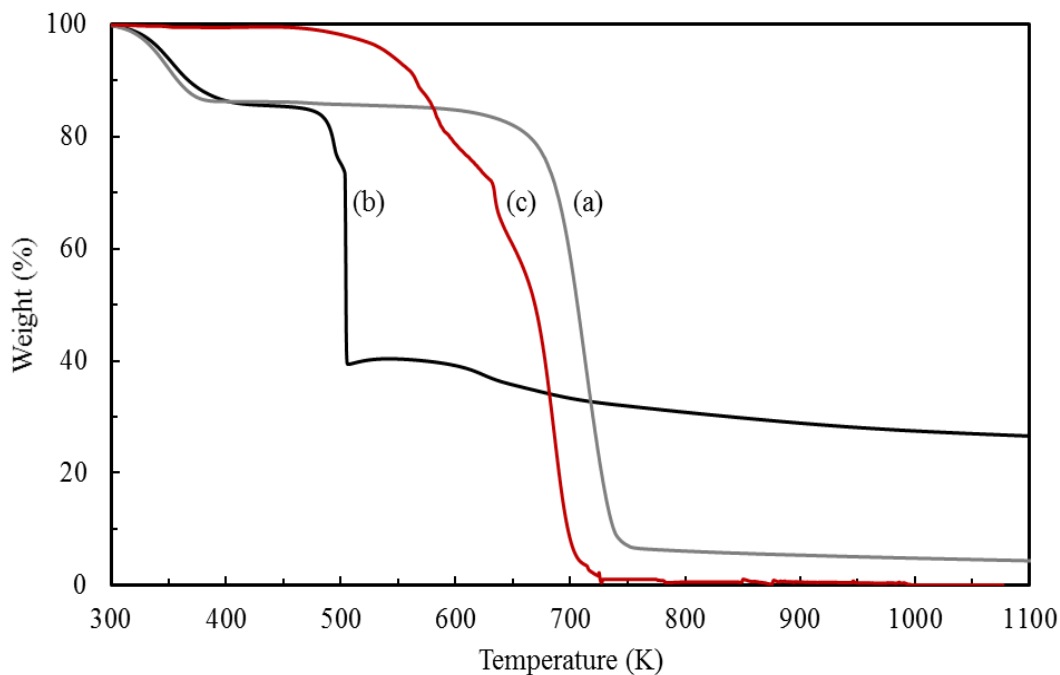
Figure 41. Weight loss profiles as a function of temperature from thermogravimetric analysis (TGA) of (a) pure PVP (M.W.=1,300,000), (b) NF-4 prior to thermal treatment (PVP-Cu(NO$_3$)$_2$), and (c) pure PEO (M.W.=300,000) nanofibers.

To further probe the presence of carbon and quantify its amount on the surface of the oxide sorbents, X-ray photoelectron spectroscopy (XPS) experiments were performed. **Figure 42** shows the overall XPS spectra as well as the spectra of the C 1s core level for a select group of sorbents (NP-7, NPC-2, and NF-4). As mentioned in Section 7.2.2, NP-7 was a CuO sorbent that was prepared via co-precipitation, NPC-2 was a CuO sorbent that was prepared by hydrothermally treating NP-7 in the presence of PVP (M.W.=1,300,000), and NF-4 was a CuO nanofibrous sample that was synthesized using electrospinning from a copper nitrate precursor in the presence of PVP.

159

In the case of both NPC-2 and NF-4, the weight ratio of PVP to Cu added during synthesis was 1:1 whereas no polymer was added in the case of NP-7. The XPS results reveal the presence of CuO nanocrystals, as shown by the Cu $2p_{3/2}$ peaks in **Figure 42**, for all three sorbents. The binding energy of the Cu $2p_{3/2}$ peak was found to be 933.6 eV, which is in agreement with the literature.[277,278] Additionally, the intensities of the Cu 2p shake-up peaks obtained from the CuO sorbents is close to the ratio characteristics of reference CuO.[271]

Figure 42 (b) shows the C 1s spectra for the three CuO sorbents. In **Figure 42 (b)**, the C 1s peak has the highest intensity, demonstrating the presence of carbon. The main carbon peak at 284.8 eV corresponds to the C-C bonding (all three sorbents contain this C-C bond) while the shoulder at 283.3 eV corresponds to the C-Cu bonding energy, which is believed to be mainly due to the carbon residue remaining on the surface of the sorbent after thermal treatment. Fitting results of the C 1s high-resolution XPS spectra were used to quantify the amount of C-Cu present in each sorbent. The fittings reveal that NPC-2 and NF-4 contained 22% and 19% C-Cu, respectively, whereas NP-7 contained less than 2% C-Cu. The XPS results discussed in this section signifies the impact of synthesis (i.e., the utilization of a polymer or a surfactant) on the amount of residual carbon (C-Cu) remaining on the surface of the sorbent after thermal treatment.
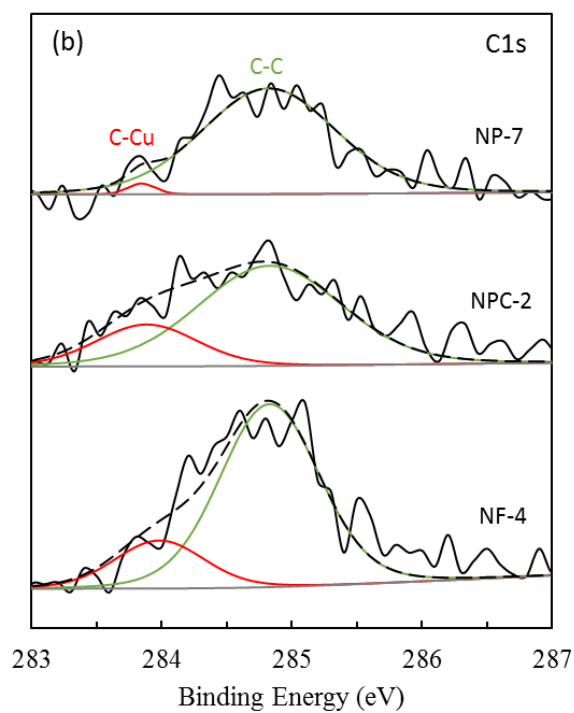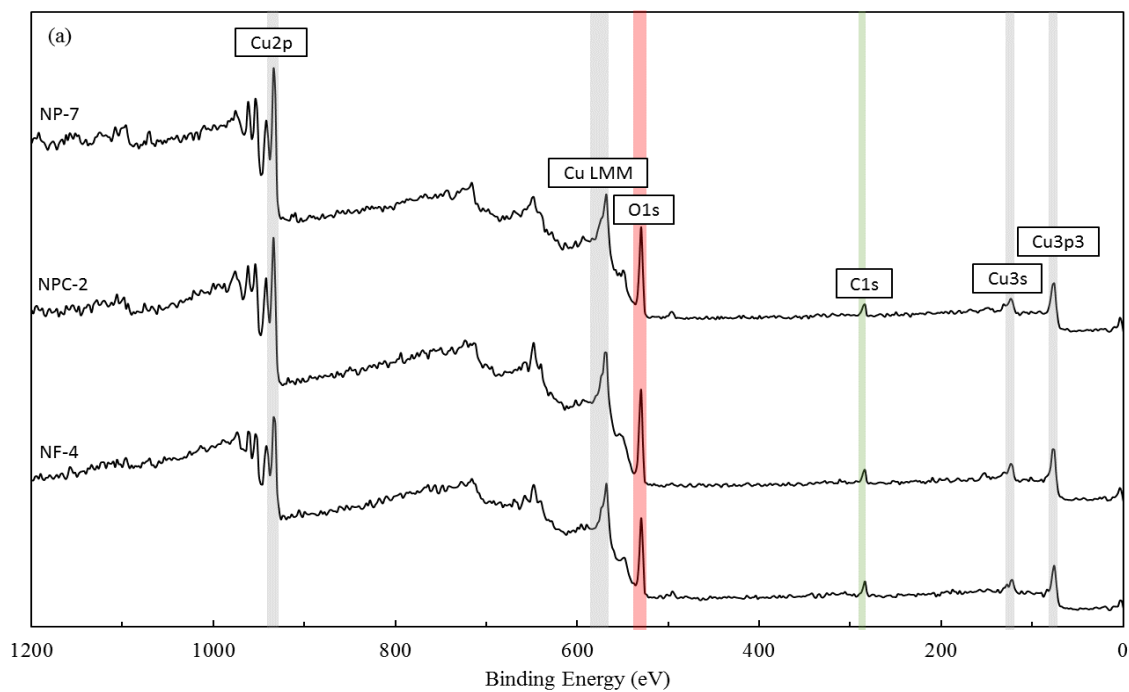
Figure 42. XPS spectrum of CuO nanomaterials (NP-7, NPC-2, and NF-4) prepared via co-precipitation (no polymer), hydrothermal treatment in the presence of PVP (M.W.=1,3000,000), and electrospinning, using PVP (M.W.=1,300,000) as a template, respectively. (a) Wide spectra of the copper oxide sorbents, (b) high-resolution spectra of C 1s, with peak fittings corresponding to C-C and C-Cu.

7.3.2 Effect of Crystallite Size on H₂S Removal

To probe the effect of morphology and crystallite size on H_2S removal performance, the H_2S removal capacities (defined as q_s in wt%) and sorption rate parameters of the sorbents synthesized in this work were measured in fixed bed experiments. Capacities were determined by introducing a feed with a nominal concentration of 1000 ppmv H_2S in N_2 to the reactor inlet and monitoring the H_2S concentration in the reactor effluent. Experiments were terminated after the concentration of the effluent was equal to the inlet concentration, and H_2S capacities were calculated from the difference between the total mass of H_2S that was fed to the reactor and that exited the reactor over the course of the experiment.

The capacities and rate parameters were plotted as a function of surface area, total pore volume and microscopic domain size (not shown), but no apparent correlations were observed with these properties. In contrast, **Figure 43 (a)** shows that H_2S capacity is inversely proportional to crystallite size (from a range of 5-26 nm) regardless of synthesis procedure and thus, regardless of morphology, surface area, and pore structure. Samples with crystallites >26 nm exhibited similarly low capacities (0.4-0.5 wt%) across a broad range of crystallite sizes (26-75 nm). These results indicate that CuO crystallite size is the most significant parameter that influences H_2S removal performance (compared to the other physical properties) and that a critical crystallite size exists at ~26 nm, above which H_2S removal is low. **Figure 43 (b)** also shows that sorption rate parameters (k) increase with increasing crystallite size, regardless of other properties of the material.

This effect of decreasing conversion/capacity with increasing crystallite size on conversion may be the result of decreasing effective diffusivities that are inversely proportional to the square of the diffusion length (in this case, the crystallite size) and those continuously decrease as dense onion-like sulfide layers form and grow during the sulfidation reaction.[160] However, the sorption

162

rate parameter (which contains this effective diffusivity) actually increases with increasing crystallite size, suggesting an additional effect of changing crystallite size beyond increasing diffusion length.

The apparently much stronger influence of crystallite size on sorption capacity (compared to morphology, surface area, and pore structure) may be the result of enhanced constraints for the solid diffusion of atoms across the bulk of the material as a function of crystallite size. Previous studies on the sulfidation of ZnO[279] proposed a reaction mechanism consisting of the following general steps: (1) the dissociative adsorption of H_2S on the particle surface, (2) nucleation of ZnS on the ZnO surface, (3) outward diffusion steps of Zn and O vacancies and of O atoms, and (4) vacancy annihilation and water desorption. A similar mechanism for CuO sulfidation in which oxygen atoms from the bulk CuO phase diffuse to the reaction interface (step 3 above) after reaction of H_2S molecules with the surface oxygen atoms (step 2 above) may be proposed here. It is probably that O atoms in smaller crystallites are more reactive with H_2S compared to those in larger crystallites. Thus, in addition to hindering diffusion phenomenon by increasing diffusion length, increasing crystallite size may also lower the reactivity of O atoms with H_2S, both of which are necessary for CuO to fully transform into copper sulfide (CuS) and achieve high conversions/capacities.
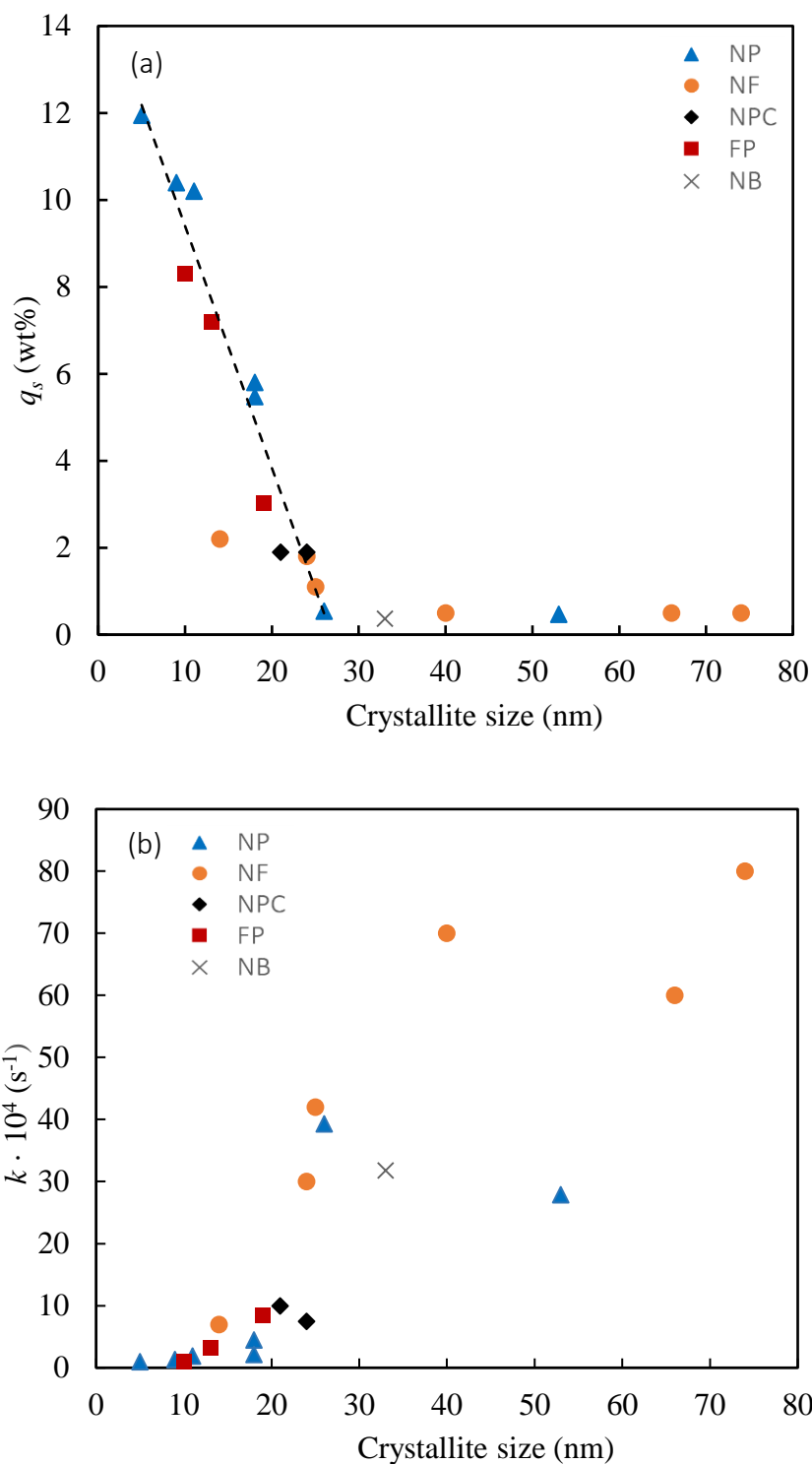
Figure 43. Effect of crystallite size of CuO sorbents prepared via various synthesis techniques as described in the experimental section of this chapter on (1) H_2S removal capacity and (b) overall rate constant, at 1000 ppmv H_2S/N_2, 294 K and 1 atm.

7.3.3 Influence of Carbon-Based Residues on H$_2$S Removal

Figure 43 (a) also shows that nanofibrous samples (orange circles) deviate from the linear trend of increasing capacity with decreasing crystallite size in the range from 5-26 nm. Specifically, sample NF-1, a nanofiber sample with a crystallite size of 14 nm, exhibited a removal capacity of 2.2 ± 0.1 wt% (compared to 7 wt% for the other samples with similar crystallite sizes). As explained in section 7.2.2, the synthesis of electrospun nanofibers requires the use of a polymer (PVP or PEO), which upon thermal treatment leaves carbon-based residues on the surface of the material, as discussed in section 7.3.1 and confirmed by XPS. Thus, this residual carbon, which is apparent on the surface from XPS, influences the reaction in such a manner as to decrease capacity when the crystallite size is less than 26 nm. To further probe the effect of residual C, a polymer with fewer carbon atoms per monomer (PEO in NF-1 with M.W.=300,000) was used during electrospinning for comparison with PVP (M.W.=1,300,000 used in NF-2). In fact, the slight improvement observed when PEO was used as a polymer as opposed to PVP was the result of PEO containing less carbon atoms per monomer than PVP, which essentially translated to less carbon remaining on the surface of the sorbent after thermal treatment. Furthermore, PEO was found to be a good stabilizing agent for CuO. When it was used instead of PVP, it produced CuO fibers with crystallites that were relatively smaller in size.

Moreover, changes in the molecular weight of the polymer, corresponding to NF-2 (PVP M.W.=1,300,000) and NF-3 (PVP, M.W.=40,000), had no significant effect on sorption capacity, although crystallites formed from PVP (M.W.=40,000) were relatively smaller in size. This observation further confirms that the amount of carbon present on the surface of the sorbent (i.e., the polymer's relative carbon content) is what truly affects the sorption capacity of CuO, not the polymer's molecular weight.

To further investigate the effect of carbon-based residues on the performance of CuO sorbents, CuO (NP-7) was hydrothermally treated in the presence of PVP (1,300,000) and P123, as described in section 7.2.2. Interestingly, the addition of these polymers/surfactants to CuO were found to compromise the sulfur uptake capacity of these sorbents. As mentioned previously, NP-4 had a crystallite size of 18 nm, which corresponded to a sulfur uptake capacity of 5.80 ± 0.23 wt% (prior to any polymer/surfactant addition) (**Table 19**). After P123 and PVP (M.W.=1,300,000) were added, corresponding to NPC-1 and NPC-2, respectively, the crystallite size of NP-4 increased slightly from 18 nm to 21 and 24 nm, respectively, and that together with the effect of carbon residue, reduced the sulfur uptake capacity of NP-4 to 1.9 wt% for both NPC-1 and NPC-2, which is well off the trend line for pure CuO materials with such crystallite sizes. These results indicate the strong inhibiting effect of carbon-based residues on the sulfur removal performance of CuO-based sorbents, and that the low removal capacity observed for electrospun nanofibers is likely due to these carbon-based residues, rather than to surface morphology or crystallite size alone. Carbon present on the surface of CuO sorbents might be blocking the active sites of the reaction, namely the surface oxygen atoms acting as Brønsted basic centers that react with the hydrogen atoms of H_2S molecules and/or the surface copper atoms acting as Lewis acid centers that bond to sulfur atoms.

7.4 Summary

Several CuO-based nanomaterials were prepared and tested for their performance as low-temperature desulfurizing sorbents by performing fixed-bed sulfidation experiments at ambient temperature and pressure. These materials were prepared via various synthesis techniques, including sol-gel, co-precipitation, hydrothermal treatment in the presence of a polymer (PVP or PEO) or surfactant (P123), hydrolysis, and electrospinning. A linear driving force model was used

to analyze the collected breakthrough curves, to evaluate the removal capacity, qs, and overall rate parameter, k, for the nineteen sorbents synthesized in this work and glean information about the properties that affect the sorption capacity of unsupported CuO-based sorbents.

Despite differences between the various properties of the tested CuO sorbents as well as their morphologies, a strong linear relationship was recognized between the sorbents' sulfur removal capacity and crystallite size, particularly when the crystallite size of CuO was below 26 nm. It was also observed that CuO materials with crystallite sizes larger than 26 nm had low sulfur uptake capacities (~0.5 wt%). The effect of residual carbon was also investigated, and it was found that carbon residues resulting from the use of a polymer (PVP or PEO) or a surfactant (P123) in the synthesis procedure remained on the surface of the sorbent after thermal treatment and detrimentally impacted its H_2S uptake capacity. The results in this paper demonstrate the strong influence of crystallite size of unsupported CuO sorbents and their purity on H_2S removal capacity at ambient conditions, irrespective of morphology and other physiochemical properties, such as surface area, pore size, and pore volume.

Chapter 8 | Conclusion

Electrospinning is a useful and a powerful process for synthesizing highly porous nanostructures. Compared to traditional synthesis techniques, electrospinning allows for the synthesis of materials with smaller domain sizes. In this work, in chapter 3, electrospinning was used to synthesize continuous, smooth, and defect-controlled PVP-Cu(NO$_3$)$_2$ nanofibers. Thermal treatment of the as-synthesized nanofibers was shown to alter the morphology of the electrospun materials, converting them to CuO nanoparticles. Parameters that affect the electrospinning process, both solution properties (polymer concentration, polymer molecular weight, metal concentration, and solvent properties) and processing conditions (applied voltage, extrusion rate, distance between the tip of the needle and collecting plate, and humidity) were thoroughly investigated on a metal-polymer system. Specifically, PVP was used as a model polymer and copper nitrate was used as a model metal precursor. The results in chapter 3 demonstrated that the morphology and bulk properties of PVP-Cu(NO$_3$)$_2$ nanofibers (e.g., diameter and morphology) were strongly influenced by these parameters—specifically, the solution properties, which indirectly affected viscosity, conductivity, dielectric constant, and surface tension. Of the processing conditions, only humidity was found to have a strong influence on fiber diameter and morphology. Furthermore, it's been demonstrated that by optimizing these parameters ultrathin nanofibers can be formed (<100 nm) whereas when these properties were not in the optimal range, structural defects (e.g., spindle-like fibers or spherical beads) were present.

In chapter 4, it was demonstrated that changing the metal precursor from copper nitrate to magnesium, nickel and calcium nitrate did not have a strong influence on the morphology and properties of the formed fibers. However, the effect of metal became apparent after thermal

treatment as each metal yielded an oxide (CuO, MgO, NiO, and MgO) with different structural and morphological features.

In chapter 5, CaO-based nanofibers (CaO-nanofibers and Al-doped CaO-nanofibers) were electrospun and tested for their ability to react with CO_2 as possible sorbents in SE-SMR. The CaO-based sorbents that were electrospun were shown to have unique, highly porous fibrous structures, which made them ideal candidates for this process. When reacted with CO_2, the electrospun materials achieved complete conversion to $CaCO_3$ (0.79 $g_{CO2}/g_{sorbent}$), which was considerably higher than the other sorbents which were prepared using traditional synthesis routes such as, thermal decomposition and hydrothermal treatment. Despite their initially high performance, CaO-nanofibers (much like the other CaO sorbents) lost approximately a third of their sorption capacity upon repeated cycling (reaction-calcination). As such, to preserve their high initial sorption capacity, aluminum was added into the CaO structure. The mixed Al-Ca phases resulted in the formation of a binary mixture of CaO and $Ca_{12}Al_{14}O_{33}$. The presence of the latter composite in the fibrous structure (particularly when the Al to Ca atomic ratio was 3 to 10) improved the stability of the sorbents by means of retaining the morphology of the electrospun material and combating the sintering of CaO particles. The improvements observed in the TGA experiments for the electrospun materials were also observed in SE-SMR experiments. Upon repeated SE-SMR and calcination cycling, the Al-doped CaO sorbent (1Al-20Ca-O-nanofibers) had an improved breakthrough time over traditional materials (3-4 times longer) and it retained that breakthrough time for up to 10 cycles, losing only 6% of its breakthrough as opposed to non-doped CaO-nanofibers which lost 45% of its breakthrough time at similar conditions.

In chapter 6, the effect of CaO doping was extended to other metals (other than Al). Specifically, CaO was doped with the following metals: Mg, Al, Y, La, Zn, Er, Ga, Li, Nd, In, and

Co. The results in this section showed that the melting point and Tammann temperature of the oxide form of the metal (dopant) were good indicators of whether a certain refractory would improve the stability and durability of CaO upon repeated carbonation and calcination or not. Since the Tammann temperature of calcium carbonate was 806 K, supports that had a Tammann temperature higher than $CaCO_3$ (and higher than the calcination temperature) generally prevented CaO from agglomerating and sintering upon repeated reaction and calcination. Of the metals tested, only Li, Zn, and Co performed poorly and this was due to their low melting point and Tammann temperature. Also, it was observed that metals that have a +3 oxidation state, generally, had higher capacities and improved stabilities over metals that have a +1 or a +2 oxidation state.

In chapter 7, electrospun CuO nanofibers were prepared and tested as low-temperature desulfurizing sorbents. For comparison, materials via different synthesis techniques such as, sol-gel, co-precipitation, hydrothermal treatment, and hydrolysis were also prepared. A linear driving force model was used to analyze the collected data and breakthrough curves and compare the performance (i.e., removal capacity) of the various sorbents. Despite differences between the various properties of the tested CuO sorbents as well as their morphologies, a strong linear relationship was recognized between the sorbents' sulfur removal capacity and crystallite size. It was observed that CuO materials with crystallites larger than 26 nm had low sulfur uptake capacities (~0.5 wt%) whereas CuO materials with smaller crystallites had considerably improved capacities that trended linearly. The effect of residual carbon was also probed. It was found that carbon residues resulting from the use a polymer (PEO and PVP) or a surfactant (P123) in the synthesis procedure remained on the surface of the sorbent even after thermal treatment. The residual carbon determinately impacted the H_2S uptake capacity of CuO.

It was shown in this work that electrospinning can be used to synthesize highly active and highly stable sorbents/materials for high temperature CO_2 removal (SE-SMR) and low temperature H_2S removal. Indeed, this work has demonstrated that the performance of electrospun nanofibers is superior to traditional powder-like materials, especially in applications that require or could benefit from porous materials with macro-pores. The results herein offer shrewd insight to the development of metal-polymer and metal oxide fibers, and the utilization of these material in sorption and catalysis applications.

References

1   K. Gajanan and S. N. Tijare, *Mater. Today Proc.*, 2018, **5**, 1093–1096.

2   N. Sharma, H. Ojha, A. Bharadwaj, D. P. Pathak and R. K. Sharma, *RSC Adv.*, 2015, **5**, 53381–53403.

3   D. G. and G. X. and J. Luo, *J. Phys. D. Appl. Phys.*, 2014, **47**, 13001.

4   S. K. Murthy, *Int. J. Nanomedicine*, 2007, **2**, 129–141.

5   L. L. Chng, N. Erathodiyil and J. Y. Ying, *Acc. Chem. Res.*, 2013, **46**, 1825–1837.

6   S. Nagpure and B. Bhushan, *Nanomaterials for Electrical Energy Storage Devices*, 2016.

7   S. E. Morgan, K. O. Havelka and R. Y. Lochhead, *Cosmetic Nanotechnology*, American Chemical Society, 2007, vol. 961.

8   J. A. Hubbell and A. Chilkoti, *Science (80-.).*, 2012, **337**, 303 LP-305.

9   Saloma, A. Nasution, I. Imran and M. Abdullah, *Procedia Eng.*, 2015, **125**, 608–612.

10   X.-Q. Liu and R.-Z. Tang, *Drug Deliv.*, 2017, **24**, 1–15.

11   G. Wang, R. Pandey and S. P. Karna, *Wiley Interdiscip. Rev. Comput. Mol. Sci.*, 2016, **7**, e1280.

12   X. He and H.-M. Hwang, *J. Food Drug Anal.*, 2016, **24**, 671–681.

13   F. R. Wurm and C. K. Weiss, *Front. Chem.*, 2014, **2**, 49.

14   T. Nagamune, *Nano Converg.*, 2017, **4**, 9.

15   T. O. and C. Joachim, *EPL (Europhysics Lett.*, 1998, **42**, 215.

16   L. Feng, S. Li, H. Li, J. Zhai, Y. Song, L. Jiang and D. Zhu, *Angew. Chemie Int. Ed.*, 2002, **41**, 1221–1223.

17   C. R. Martin, *Chem. Mater.*, 1996, **8**, 1739–1746.

18   P. X. Ma and R. Zhang, *J. Biomed. Mater. Res.*, 1999, **46**, 60–72.

19   J. M. Deitzel, J. D. Kleinmeyer, J. K. Hirvonen and N. C. Beck Tan, *Polymer (Guildf).*, 2001, **42**, 8163–8170.

20   S. Chand, *J. Mater. Sci.*, 2000, **35**, 1303–1313.

21   Z.-M. Huang, Y.-Z. Zhang, M. Kotaki and S. Ramakrishna, *Compos. Sci. Technol.*, 2003, **63**, 2223–2253.

22   W. Ma, Q. Zhang, D. Hua, R. Xiong, J. Zhao, W. Rao, S. Huang, X. Zhan, F. Chen and C. Huang, *RSC Adv.*, 2016, **6**, 12868–12884.

23   S. S. Mali, H. Kim, W. Y. Jang, H. S. Park, P. S. Patil and C. K. Hong, *ACS Sustain. Chem. Eng.*, 2013, **1**, 1207–1213.

24   C. J. Thompson, G. G. Chase, A. L. Yarin and D. H. Reneker, *Polymer (Guildf).*, 2007, **48**, 6913–6922.

25   A.   Khalil   E-mail: akhalil@masdar.ac.ae   and   R.   Hashaikeh   E-mail: rhashaikeh@masdar.ac.ae, , DOI:10.1016/J.MATCHAR.2014.06.005.

26   *Arab. J. Chem.*, , DOI:10.1016/J.ARABJC.2015.11.015.

27   N. Bhardwaj and S. C. Kundu, *Biotechnol. Adv.*, 2010, **28**, 325–347.

28   K. Garg and G. L. Bowlin, *Biomicrofluidics*, 2011, **5**, 13403.

29   S. Thenmozhi, N. Dharmaraj, K. Kadirvelu and H. Y. Kim, *Mater. Sci. Eng. B*, 2017, **217**, 36–48.

30   H. Li, K. Liu, Q. Sang, G. R. Williams, J. Wu, H. Wang, J. Wu and L.-M. Zhu, *Colloids Surfaces B Biointerfaces*, 2017, **159**, 277–283.

31   S. Wen, M. Liang, R. Zou, Z. Wang, D. Yue and L. Liu, *RSC Adv.*, 2015, **5**, 41513–41519.

32   H. Cho, S. Min and T. Lee, *Electrospun Organic Nanofiber Electronics and Photonics*, 2013, vol. 298.

33   S. T. Aruna, L. S. Balaji, S. S. Kumar and B. S. Prakash, *Renew. Sustain. Energy Rev.*, 2017, **67**, 673–682.

34   S. Ramakrishna, K. Fujihara, W.-E. Teo, T. Yong, Z. Ma and R. Ramaseshan, *Mater. Today*, 2006, **9**, 40–50.

35   M. Gorji, R. Bagherzadeh and H. Fashandi, in *Woodhead Publishing Series in Textiles*, ed. M. B. T.-E. N. Afshari, Woodhead Publishing, 2017, pp. 571–598.

36   M. M. Aldhahri, Y. Q. Almulaiky, R. M. El-Shishtawy, W. Al-Shawafi, A. Alngadh and R. Maghrabi, *ACS Omega*, 2018, **3**, 6346–6350.

37   L. N. Wang, C. Z. Xin, W. T. Liu, X. L. Xia, S. Q. He, H. Liu and C. S. Zhu, *Arab. J. Sci. Eng.*, 2015, **40**, 2889–2895.

38   S. Zhang, W. S. Shim and J. Kim, *Mater. Des.*, 2009, **30**, 3659–3666.

39   US patent 692,631, 1902.

40   US patent 1,975,504, 1934.

41   US patent 2,160,962, 1939.

42   US patent 2,187,306, 1940.

43   US patent 2,323,025, 1943.

44   V. Drozin, *J. Colloid Sci.*, 1957, **12**, 526–527.

45   W. E. T. and S. Ramakrishna, *Nanotechnology*, 2006, **17**, R89.

46   C. Burger, B. S. Hsiao and B. Chu, *Annu. Rev. Mater. Res.*, 2006, **36**, 333–368.

47   C. J. Angammana and S. H. Jayaram, *Part. Sci. Technol.*, 2016, **34**, 72–82.

48   A. L. Yarin and E. Zussman, *Polymer (Guildf).*, 2004, **45**, 2977–2980.

49   M. M. Demir, I. Yilgor, E. Yilgor and B. Erman, *Polymer (Guildf).*, 2002, **43**, 3303–3309.

50   D. H. Reneker and A. L. Yarin, *Polymer (Guildf).*, 2008, **49**, 2387–2425.

51   X. Zong, K. Kim, D. Fang, S. Ran, B. S. Hsiao and B. Chu, *Polymer (Guildf).*, 2002, **43**, 4403–4412.

52   S. De Vrieze, T. Van Camp, A. Nelvig, B. Hagström, P. Westbroek and K. De Clerck, *J. Mater. Sci.*, 2008, **44**, 1357.

53   A. H. Hekmati, A. Rashidi, R. Ghazisaeidi and J.-Y. Drean, *Text. Res. J.*, 2013, **83**, 1452–1466.

54   S. Zargham, S. Bazgir, A. Tavakoli, A. S. Rashidi and R. Damerchely, *The effect of flow rate on morphology and deposition area of electrospun nylon 6 nanofiber*, 2012, vol. 7.

55   V. Beachley and X. Wen, *Mater. Sci. Eng. C. Mater. Biol. Appl.*, 2009, **29**, 663–668.

56   T. Mazoochi, M. Hamadanian, M. Ahmadi and V. Jabbari, *Int. J. Ind. Chem.*, 2012, **3**, 2.

57   C. L. Casper, J. S. Stephens, N. G. Tassi, D. B. Chase and J. F. Rabolt, *Macromolecules*, 2004, **37**, 573–578.

58   S. Haider, Y. Al-Zeghayer, F. A. Ahmed Ali, A. Haider, A. Mahmood, W. A. Al-Masry, M. Imran and M. O. Aijaz, *J. Polym. Res.*, 2013, **20**, 105.

59   B. Tarus, N. Fadel, A. Al-Oufy and M. El-Messiry, *Alexandria Eng. J.*, 2016, **55**, 2975–2984.

60   Y. Liu, J.-H. He, J. Yu and H. Zeng, *Polym. Int.*, 2007, **57**, 632–636.

61   H. Fong, I. Chun and D. H. Reneker, *Polymer (Guildf).*, 1999, **40**, 4585–4592.

62   K. Acatay, E. Simsek, C. Ow-Yang and Y. Z. Menceloglu, *Angew. Chemie Int. Ed.*, 2004, **43**, 5210–5213.

63   A. V Stanishevsky, J. D. Wetuski and H. Yockell-Lelièvre, *Ceram. Int.*, 2016, **42**, 388–395.

64   C. Yao, X. Li and T. Song, *J. Appl. Polym. Sci.*, 2006, **103**, 380–385.

65   R. M. Nezarati, M. B. Eifert and E. Cosgriff-Hernandez, *Tissue Eng. Part C. Methods*, 2013, **19**, 810–819.

66   D. Li and Y. Xia, *Adv. Mater.*, 2004, **16**, 1151–1170.

67   M. Lauricella, G. Pontrelli, I. Coluzza, D. Pisignano and S. Succi, *Comput. Phys. Commun.*, 2015, **197**, 227–238.

68   J. Venugopal, Y. Z. Zhang and S. Ramakrishna, *Proc. Inst. Mech. Eng. Part N J. Nanoeng. Nanosyst.*, 2004, **218**, 35–45.

69   A. Greiner and J. H. Wendorff, *Angew. Chemie Int. Ed.*, 2007, **46**, 5670–5703.

70   J. Deitzel, J. D. Kleinmeyer, D. E. A. Harris and N. C. Beck Tan, *The Effect of Processing Variables on the Morphology of Electrospun Nanofibers and Textiles*, 2001, vol. 42.

71   J. Doshi and D. H. Reneker, *J. Electrostat.*, 1995, **35**, 151–160.

72   A. Haider, S. Haider and I.-K. Kang, *Arab. J. Chem.*, 2015.

73   W. K. Son, J. H. Youk, T. S. Lee and W. H. Park, *Polymer (Guildf).*, 2004, **45**, 2959–2966.

74   S. Chuangchote, T. Sagawa and S. Yoshikawa, *J. Appl. Polym. Sci.*, 2009, **114**, 2777–2791.

75   Y. Xu, L. Zou, H. Lu and T. Kang, *RSC Adv.*, 2017, **7**, 4000–4010.

76   P. Supaphol, C. Mit-uppatham and M. Nithitanakul, *Ultrafine Electrospun Polyamide‐6 Fibers: Effects of Solvent System and Emitting Electrode Polarity on Morphology and Average Fiber Diameter*, 2005, vol. 290.

77   C. J. Cooper, A. K. Mohanty and M. Misra, *ACS Omega*, 2018, **3**, 5547–5557.

78   T. Jarusuwannapoom, W. Hongrojjanawiwat, S. Jitjaicham, L. Wannatong, M. Nithitanakul, C. Pattamaprom, P. Koombhongse, R. Rangkupan and P. Supaphol, *Eur. Polym. J.*, 2005, **41**, 409–421.

79   C. Zhang, X. Yuan, L. Wu, Y. Han and J. Sheng, *Eur. Polym. J.*, 2005, **41**, 423–432.

80   C.-M. Wu, H.-G. Chiou, S.-L. Lin and J.-M. Lin, *J. Appl. Polym. Sci.*, 2012, **126**, E89–E97.

81   D. Fallahi, M. Rafizadeh, N. Mohammadi and B. Vahidi, *Polym. Int.*, 2008, **57**, 1363–1368.

82   S. Megelski, J. S. Stephens, D. Chase and J. Rabolt, *Micro- and Nanostructured Surface Morphology on Electrospun Polymer Fibers*, 2002, vol. 35.

83   R. Ghelich, M. Keyanpour Rad and A. Youzbashi, *Study on Morphology and Size Distribution of Electrospun NiO-GDC Composite Nanofibers*, 2015, vol. 10.

84   G. T. Kim, J. S. Lee, J. H. Shin, Y. C. Ahn, K. H. Jeong, C. M. Sung and J. K. Lee, *Microsc. Microanal.*, 2004, **10**, 554–555.

85   H. H. Htike, C. Long and S. Sukigara, *The Effect of Relative Humidity on Electrospinning ofPoly-(vinyl alcohol) with Soluble Eggshell Membrane*, 2012, vol. 58.

86   F. Zaera, *Chem. Soc. Rev.*, 2013, **42**, 2746–2762.

87   J. Xu, J. Niu and S. Zhang, *Procedia Environ. Sci.*, 2013, **18**, 472–477.

88   D. Li, Y. Wang and Y. Xia, *Nano Lett.*, 2003, **3**, 1167–1171.

89   N. Sangkhaprom, P. Supaphol and V. Pavarajarn, *Ceram. Int.*, 2010, **36**, 357–363.

90   S. Zhan, Y. Li and H. Yu, *J. Dispers. Sci. Technol.*, 2008, **29**, 823–826.

91   I. Keun Kwon, S. Kidoaki and T. Matsuda, *Biomaterials*, 2005, **26**, 3929–3939.

92   C. L. Casper, W. Yang, M. C. Farach-Carson and J. F. Rabolt, in *Polymeric Nanofibers*, American Chemical Society, 2006, vol. 918, pp. 15–205.

93   M. Teodorescu and M. Bercea, *Polym. Plast. Technol. Eng.*, 2015, **54**, 923–943.

94   J. Bai, Y. Li, M. Li, S. Wang, C. Zhang and Q. Yang, *Appl. Surf. Sci.*, 2008, **254**, 4520–4523.

95   G. F. and U. Cvelbar, *Nanotechnology*, 2012, **23**, 194001.

96   *Prog. Mater. Sci.*, 2014, **60**, 208.

97   S. Sharma, R. Rani, R. Rai and T. S. Natarajan, *Synthesis and characterization of CuO electrospum nanofiber using poly(vinyl acetate)/Cu(CH3COO)2 annealing method*, 2013, vol. 4.

98   Y. Cudennec and A. Lecerf, *Solid State Sci.*, 2003, **5**, 1471–1474.

99   V. Prakash, R. K. Diwan and U. K. Niyogi, *Characterization of synthesized copper oxide nanopowders and their use in nanofluids for enhancement of thermal conductivity*, 2015, vol. 53.

100 N. Wongpisutpaisan, P. Charoonsuk, N. Vittayakorn and W. Pecharapa, *Energy Procedia*, 2011, **9**, 404–409.

101 N. von Reitzenstein, X. Bi, Y. Yang, K. Hristovski and P. Westerhoff, *J. Appl. Polym. Sci.*, 2016, **133**, n/a--n/a.

102 Y. Y. Zhao, Q. B. Yang, X. F. Lu, C. Wang and Y. Wei, *J. Polym. Sci. Part B Polym. Phys.*, 2005, **43**, 2190–2195.

103 D. S. Gomes, A. N. R. da Silva, N. I. Morimoto, L. T. F. Mendes, R. Furlan and I. Ramos, *PolÃ\-meros*, 2007, **17**, 206–211.

104 S. L. Shenoy, W. D. Bates, H. L. Frisch and G. E. Wnek, *Polymer (Guildf).*, 2005, **46**, 3372–3384.

105   E.-R. Kenawy, J. M. Layman, J. R. Watkins, G. L. Bowlin, J. A. Matthews, D. G. Simpson and G. E. Wnek, *Biomaterials*, 2003, **24**, 907–913.

106   K. H. Lee, H. Y. Kim, H. J. Bang, Y. H. Jung and S. G. Lee, *Polymer (Guildf).*, 2003, **44**, 4029–4034.

107   C. Meechaisue, R. Dubin, P. Supaphol, V. Hoven and J. Kohn, *Electrospun mat of tyrosine-derived polycarbonate fibers for potential use as tissue scaffolding material*, 2006, vol. 17.

108   S. Hulsey, S. Absar and H. Choi, *Procedia Manuf.*, 2017, **10**, 652–661.

109   T. Uyar and F. Besenbacher, *Polymer (Guildf).*, 2008, **49**, 5336–5343.

110   *e-Polymers* , 2003, 3.

111   Y. Qiu, J. Yu, X. Zhou, C. Tan and J. Yin, *Nanoscale Res. Lett.*, 2008, **4**, 173.

112   T. Ha Tran and N. viet tuyen, *Copper Oxide Nanomaterials Prepared by Solution Methods, Some Properties, and Potential Applications: A Brief Review*, 2014, vol. 2014.

113   W. Liu, C. Huang and X. Jin, *Nanoscale Res. Lett.*, 2015, **10**, 237.

114   Y. Z. Zhang, J. Venugopal, Z.-M. Huang, C. T. Lim and S. Ramakrishna, *Polymer (Guildf).*, 2006, **47**, 2911–2917.

115   T. J. Sill and H. A. von Recum, *Biomaterials*, 2008, **29**, 1989–2006.

116   L. A. Bosworth and S. Downes, *J. Polym. Environ.*, 2012, **20**, 879–886.

117   A. Moheman, M. S. Alam and A. Mohammad, *Adv. Colloid Interface Sci.*, 2016, **229**, 1–24.

118   J. Pelipenko, J. Kristl, B. Janković, S. Baumgartner and P. Kocbek, *Int. J. Pharm.*, 2013, **456**, 125–134.

119   H. Lu, A. Khan and P. G. Smirniotis, *Ind. Eng. Chem. Res.*, 2008, **47**, 6216–6220.

120   J. Yu, L.-H. Xie, J.-R. Li, Y. Ma, J. M. Seminario and P. B. Balbuena, *Chem. Rev.*, 2017, **117**, 9674–9754.

121   G. T. Rochelle, *Science (80-.).*, 2009, **325**, 1652 LP-1654.

122   D. Y. C. Leung, G. Caramanna and M. M. Maroto-Valer, *Renew. Sustain. Energy Rev.*, 2014, **39**, 426–443.

123   D. P. Harrison, *Ind. Eng. Chem. Res.*, 2008, **47**, 6486–6501.

124   S.-Y. Lin, Y. Suzuki, H. Hatano and M. Harada, *Energy & Fuels*, 2001, **15**, 339–343.

125   A. Lopez Ortiz and D. P. Harrison, *Ind. Eng. Chem. Res.*, 2001, **40**, 5102–5109.

126   N. Chanburanasiri, A. M. Ribeiro, A. E. Rodrigues, A. Arpornwichanop, N. Laosiripojana, P. Praserthdam and S. Assabumrungrat, *Ind. Eng. Chem. Res.*, 2011, **50**, 13662–13671.

127   M. Ramezani, P. Tremain, E. Doroodchi and B. Moghtaderi, *Energy Procedia*, 2017, **114**, 259–270.

128   H. Guo, S. Wang, C. Li, Y. Zhao, Q. Sun and X. Ma, *Ind. Eng. Chem. Res.*, 2016, **55**, 7873–7879.

129   C. Luo, Y. Zheng, J. Guo and B. Feng, *Fuel*, 2014, **127**, 124–130.

130   J. Blamey, E. J. Anthony, J. Wang and P. S. Fennell, *Prog. Energy Combust. Sci.*, 2010, **36**, 260–279.

131   S. M. M. Nouri and H. A. Ebrahim, *Brazilian J. Chem. Eng.*, 2016, **33**, 383–389.

132   W. Liu, H. An, C. Qin, J. Yin, G. Wang, B. Feng and M. Xu, *Energy & Fuels*, 2012, **26**, 2751–2767.

133   G. S. Grasa and J. C. Abanades, *Ind. Eng. Chem. Res.*, 2006, **45**, 8846–8851.

134   B. R. Stanmore and P. Gilot, *Fuel Process. Technol.*, 2005, **86**, 1707–1743.

135   S. Kumar and S. K. Saxena, *Mater. Renew. Sustain. Energy*, 2014, **3**, 30.

136   H. Lu, E. P. Reddy and P. G. Smirniotis, *Ind. Eng. Chem. Res.*, 2006, **45**, 3944–3949.

137   H. Lu, A. Khan, S. E. Pratsinis and P. G. Smirniotis, *Energy & Fuels*, 2009, **23**, 1093–1100.

138   R. Koirala, K. R. Gunugunuri, S. E. Pratsinis and P. G. Smirniotis, *J. Phys. Chem. C*, 2011, **115**, 24804–24812.

139   L. Zhang, B. Zhang, Z. Yang and M. Guo, *Energy Technol.*, 2015, **3**, 10–19.

140   H. Boysen, M. Lerch, A. Stys and A. Senyshyn, *Acta Crystallogr. Sect. B*, 2007, **63**, 675–682.

141   S. S. Kazi, A. Aranda, J. Meyer and J. Mastin, *Energy Procedia*, 2014, **63**, 2207–2215.

142   C. Liu, L. Zhang, J. Deng, Q. Mu, H. Dai and H. He, *J. Phys. Chem. C*, 2008, **112**, 19248–19256.

143   J. C. Yu, A. Xu, L. Zhang, R. Song and L. Wu, *J. Phys. Chem. B*, 2004, **108**, 64–70.

144   S. K. Bhatia and D. D. Perlmutter, *AIChE J.*, 1980, **26**, 379–386.

145   S. K. Bhatia and D. D. Perlmutter, *AIChE J.*, 1981, **27**, 247–254.

146   G. Grasa, R. Murillo, M. Alonso and J. C. Abanades, *AIChE J.*, 2009, **55**, 1246–1255.

147   M. L. Granados, M. D. Z. Poves, D. M. Alonso, R. Mariscal, F. C. Galisteo, R. Moreno-Tost, J. Santamaría and J. L. G. Fierro, *Appl. Catal. B Environ.*, 2007, **73**, 317–326.

148   Z. Li, N. Cai and Y. Huang, *Ind. Eng. Chem. Res.*, 2006, **45**, 1911–1917.

149   M. M. Hohman, M. Shin, G. Rutledge and M. P. Brenner, *Phys. Fluids*, 2001, **13**, 2221–2236.

150   Y. M. Shin, M. M. Hohman, M. P. Brenner and G. C. Rutledge, *Polymer (Guildf).*, 2001, **42**, 9955–9967.

151   J. Piella, F. Merkoci, A. Genc, J. Arbiol, N. G. Bastus and V. Puntes, *J. Mater. Chem. A*, 2017, **5**, 11917–11929.

152   X.-H. Qin, E.-L. Yang, N. Li and S.-Y. Wang, *J. Appl. Polym. Sci.*, 2006, **103**, 3865–3870.

153   W. Liu, N. W. L. Low, B. Feng, G. Wang and J. C. Diniz da Costa, *Environ. Sci. Technol.*, 2010, **44**, 841–847.

154   H. Gupta and L.-S. Fan, *Ind. Eng. Chem. Res.*, 2002, **41**, 4035–4042.

155   Z. Zhou, P. Xu, M. Xie, Z. Cheng and W. Yuan, *Modeling of the carbonation kinetics of a synthetic CaO-based sorbent*, 2013, vol. 95.

156   M. Chen and D. W. Goodman, *Structure—Activity Relationships in Supported Au Catalysts*, 2006, vol. 37.

157   A. T. Bell, *Science (80-.).*, 2003, **299**, 1688–1691.

158   G. A. Somorjai, *Science (80-.).*, 1985, **227**, 902–908.

159   D. Mess, A. F. Sarofim and J. P. Longwell, *Product Layer Diffusion During the Reaction of Calcium Oxide with Carbon Dioxide*, 1999, vol. 13.

160   Z. Li and M. Flytzani-Stephanopoulos, *Ind. Eng. Chem. Res.*, 1997, **36**, 187–196.

161   R. Barker, *J. Appl. Chem. Biotechnol.*, 1974, **24**, 221–227.

162   M. V Iyer, H. Gupta, B. B. Sakadjian and L.-S. Fan, *Ind. Eng. Chem. Res.*, 2004, **43**, 3939–3947.

163   J. M. López, M. V Navarro, R. Murillo and G. S. Grasa, *Energy Procedia*, 2017, **114**, 230–241.

164   C. Luo, Y. Zheng, N. Ding, Q. Wu, G. Bian and C. Zheng, *Ind. Eng. Chem. Res.*, 2010, **49**, 11778–11784.

165   A. M. Kierzkowska, R. Pacciani and C. R. Müller, *ChemSusChem*, 2013, **6**, 1130–1148.

166   A. Malik, J. Lan and M. Lenzen, *Environ. Sci. Technol.*, 2016, **50**, 4722–4730.

167   C. Rosenzweig, D. Karoly, M. Vicarelli, P. Neofotis, Q. Wu, G. Casassa, A. Menzel, T. L. Root, N. Estrella, B. Seguin, P. Tryjanowski, C. Liu, S. Rawlins and A. Imeson, *Nature*, 2008, **453**, 353.

168   D. Coumou, A. Robinson and S. Rahmstorf, *Clim. Change*, 2013, **118**, 771–782.

169   G.-R. Walther, E. Post, P. Convey, A. Menzel, C. Parmesan, T. J. C. Beebee, J.-M. Fromentin, O. Hoegh-Guldberg and F. Bairlein, *Nature*, 2002, **416**, 389.

170   E. S. Sanz-Pérez, C. R. Murdock, S. A. Didas and C. W. Jones, *Chem. Rev.*, 2016, **116**, 11840–11876.

171   A. H. Berger and A. S. Bhown, *Energy Procedia*, 2013, **37**, 25–32.

172   J. C. Glier and E. S. Rubin, *Energy Procedia*, 2013, **37**, 65–72.

173   J. Wang, L. Huang, R. Yang, Z. Zhang, J. Wu, Y. Gao, Q. Wang, D. O'Hare and Z. Zhong, *Energy Environ. Sci.*, 2014, **7**, 3478–3518.

174   A. Samanta, A. Zhao, G. K. H. Shimizu, P. Sarkar and R. Gupta, *Ind. Eng. Chem. Res.*, 2012, **51**, 1438–1463.

175   S. C. Lee, H. J. Chae, S. J. Lee, B. Y. Choi, C. K. Yi, J. B. Lee, C. K. Ryu and J. C. Kim, *Environ. Sci. Technol.*, 2008, **42**, 2736–2741.

176   C.-M. Huang, H.-W. Hsu, W.-H. Liu, J.-Y. Cheng, W.-C. Chen, T.-W. Wen and W. Chen, *Energy Procedia*, 2011, **4**, 1268–1275.

177   T. D. Burchell and R. R. Judkins, *Energy Convers. Manag.*, 1996, **37**, 947–954.

178   K. A. Fayemiwo, G. T. Vladisavljević, S. A. Nabavi, B. Benyahia, D. P. Hanak, K. N. Loponov and V. Manović, *Chem. Eng. J.*, 2018, **334**, 2004–2013.

179   T. Shimizu, T. Hirama, H. Hosoda, K. Kitano, M. Inagaki and K. Tejima, *Chem. Eng. Res. Des.*, 1999, **77**, 62–68.

180 J. C. Abanades, *Chem. Eng. J.*, 2002, **90**, 303–306.

181 K. Chrissafis, *J. Therm. Anal. Calorim.*, 2007, **89**, 525–529.

182 B. Feng, H. An and E. Tan, *Energy & Fuels*, 2007, **21**, 426–434.

183 P. S. Fennell, R. Pacciani, J. S. Dennis, J. F. Davidson and A. N. Hayhurst, *Energy & Fuels*, 2007, **21**, 2072–2081.

184 M. Chen, N. Wang, J. Yu and A. Yamaguchi, *J. Eur. Ceram. Soc.*, 2007, **27**, 1953–1959.

185 F. D. M. Daud, K. Vignesh, S. Sreekantan and A. R. Mohamed, *New J. Chem.*, 2016, **40**, 231–237.

186 D. Alvarez and J. C. Abanades, *Energy & Fuels*, 2005, **19**, 270–278.

187 S. Wang, S. Fan, L. Fan, Y. Zhao and X. Ma, *Environ. Sci. Technol.*, 2015, **49**, 5021–5027.

188 D. Alvarez and J. C. Abanades, *Ind. Eng. Chem. Res.*, 2005, **44**, 5608–5615.

189 G. Grasa, I. Martínez, M. E. Diego and J. C. Abanades, *Energy & Fuels*, 2014, **28**, 4033–4042.

190 A. Biasin, C. U. Segre and M. Strumendo, *Cryst. Growth Des.*, 2015, **15**, 5188–5201.

191 Z. Li, F. Fang, X. Tang and N. Cai, *Energy & Fuels*, 2012, **26**, 2473–2482.

192 H. Pawlak-Kruczek and M. Baranowski, *Energy Procedia*, 2017, **105**, 4499–4512.

193 P. Sun, J. R. Grace, C. J. Lim and E. J. Anthony, *AIChE J.*, 2007, **53**, 2432–2442.

194 J. C. Abanades and D. Alvarez, *Energy & Fuels*, 2003, **17**, 308–315.

195 J. M. Valverde and S. Medina, *Phys. Chem. Chem. Phys.*, 2015, **17**, 21912–21926.

196 A. B. FUERTES, D. ALVAREZ, F. RUBIERA, J. J. PIS, G. MARBÁN and J. M. PALACOS, *Chem. Eng. Commun.*, 1991, **109**, 73–88.

197 M. A. Naeem, A. Armutlulu, A. Kierzkowska and C. R. Müller, *Energy Procedia*, 2017, **114**, 158–166.

198   B. V. Materić, C. Sheppard and S. I. Smedley, *Environ. Sci. Technol.*, 2010, **44**, 9496–9501.

199   L. Han, Q. Wang, Q. Ma, J. Guan, Z. Luo and K. Cen, eds. G. Yue, H. Zhang, C. Zhao and Z. Luo, Springer Berlin Heidelberg, Berlin, Heidelberg, 2010, pp. 726–731.

200   J. Blamey, V. Manovic, E. Anthony, D. Dugwell and P. Fennell, *On steam hydration of CaO-based sorbent cycled for CO2 capture*, 2015, vol. 150.

201   A. Wang, N. Deshpande and L.-S. Fan, *Energy & Fuels*, 2015, **29**, 321–330.

202   V. Manovic, D. Lu and E. J. Anthony, *Fuel*, 2008, **87**, 3344–3352.

203   Y. Hu, W. Liu, J. Sun, M. Li, X. Yang, Y. Zhang, X. Liu and M. Xu, *Fuel*, 2016, **167**, 17–24.

204   Y. Li, C. Zhao, L. Duan, C. Liang, Q. Li, W. Zhou and H. Chen, *Fuel Process. Technol.*, 2008, **89**, 1461–1469.

205   Y. Li, C. Zhao, H. Chen, C. Liang, L. Duan and W. Zhou, *Fuel*, 2009, **88**, 697–704.

206   F. N. Ridha, V. Manovic, A. Macchi, M. A. Anthony and E. J. Anthony, *Fuel Process. Technol.*, 2013, **116**, 284–291.

207   R. Sun, Y. Li, S. Wu, C. Liu, H. Liu and C. Lu, *Powder Technol.*, 2013, **233**, 8–14.

208   R. Koirala, G. K. Reddy and P. G. Smirniotis, *Energy & Fuels*, 2012, **26**, 3103–3109.

209   V. S. Derevschikov, A. I. Lysikov and A. G. Okunev, *Ind. Eng. Chem. Res.*, 2011, **50**, 12741–12749.

210   H. R. Radfarnia and M. C. Iliuta, *Ind. Eng. Chem. Res.*, 2012, **51**, 10390–10398.

211   A. Antzara, E. Heracleous and A. A. Lemonidou, *Energy Procedia*, 2014, **63**, 2160–2169.

212   P. Chang, W.-C. Huang, T.-J. Lee, Y.-P. Chang and S.-Y. Chen, *ACS Appl. Mater. Interfaces*, 2015, **7**, 6172–6179.

213   Y. Hu, W. Liu, H. Chen, Z. Zhou, W. Wang, J. Sun, X. Yang, X. Li and M. Xu, *Fuel*, 2016, **181**, 199–206.

214   Z. Li, N. Cai, Y. Huang and H. Han, *Energy & Fuels*, 2005, **19**, 1447–1452.

215   M. Sayyah, E. Abbasi, Y. Lu, J. Abbasian and K. S. Suslick, *Energy & Fuels*, 2015, **29**, 4447–4452.

216   J. Jing, X. Zhang, S. Wang, T. Li and W. Li, *Energy Procedia*, 2017, **142**, 3258–3263.

217   M. Guo, L. Zhang, Z. Yang and Q. Tang, *Energy & Fuels*, 2011, **25**, 5514–5520.

218   L. Barelli, G. Bidini, A. Di Michele, F. Gallorini, C. Petrillo and F. Sacchetti, *Appl. Energy*, 2014, **127**, 81–92.

219   B. Feng, W. Liu, X. Li and H. An, *Energy & Fuels*, 2006, **20**, 2417–2420.

220   K. O. Albrecht, K. S. Wagenbach, J. A. Satrio, B. H. Shanks and T. D. Wheelock, *Ind. Eng. Chem. Res.*, 2008, **47**, 7841–7848.

221   M. A. Naeem, A. Armutlulu, Q. Imtiaz, F. Donat, R. Schäublin, A. Kierzkowska and C. R. Müller, *Nat. Commun.*, 2018, **9**, 2408.

222   S. F. Wu and Y. Q. Zhu, *Ind. Eng. Chem. Res.*, 2010, **49**, 2701–2706.

223   C.-T. Yu and W.-C. Chen, *Powder Technol.*, 2013, **239**, 492–498.

224   Y. Hu, W. Liu, J. Sun, M. Li, X. Yang, Y. Zhang and M. Xu, *Chem. Eng. J.*, 2015, **273**, 333–343.

225   Y. Xu, C. Luo, Y. Zheng, H. Ding, Q. Wang, Q. Shen, X. Li and L. Zhang, *RSC Adv.*, 2016, **6**, 79285–79296.

226   X. Zhang, Z. Li, Y. Peng, W. Su, X. Sun and J. Li, *Chem. Eng. J.*, 2014, **243**, 297–304.

227   C. Luo, Y. Zheng, J. Yin, C. Qin, N. Ding, C. Zheng and B. Feng, *Energy & Fuels*, 2013, **27**, 4824–4831.

228   C. Luo, Y. Zheng, N. Ding and C. Zheng, *Korean J. Chem. Eng.*, 2011, **28**, 1042–1046.

229   J. M. Valverde, A. Perejon and L. A. Perez-Maqueda, *Environ. Sci. Technol.*, 2012, **46**, 6401–6408.

230   M. Zhao, X. Yang, T. L. Church and A. T. Harris, *Environ. Sci. Technol.*, 2012, **46**, 2976–2983.

231   M. H. Sedghkerdar, N. Mahinpey, Z. Sun and S. Kaliaguine, *Fuel*, 2014, **127**, 101–108.

232   S. Tian, J. Jiang, F. Yan, K. Li and X. Chen, *Environ. Sci. Technol.*, 2015, **49**, 7464–7472.

233   J. Phromprasit, J. Powell and S. Assabumrungrat, *Chem. Eng. J.*, 2016, **284**, 1212–1223.

234   C. Doornkamp, M. Clement and V. Ponec, *J. Catal.*, 1999, **182**, 390–399.

235   H. Cui, S. Q. Turn and M. A. Reese, *Catal. Today*, 2009, **139**, 274–279.

236   T. J. Bandosz, *J. Am. Chem. Soc.*, 2001, **123**, 516.

237   C. Song, *Catal. Today*, 2003, **86**, 211–263.

238   M. J. Goodwin, O. M. Musa and J. W. Steed, *Energy & Fuels*, 2015, **29**, 4667–4682.

239   R. O. Beauchamp, J. S. Bus, J. A. Popp, C. J. Boreiko, D. A. Andjelkovich and P. Leber, *CRC Crit. Rev. Toxicol.*, 1984, **13**, 25–97.

240   G. E. Likens, R. F. Wright, J. N. Galloway and T. J. Butler, *Sci. Am.*, 1979, **241**, 43–51.

241   N. S. Nasri, J. M. Jones, V. A. Dupont and A. Williams, *Energy & Fuels*, 1998, **12**, 1130–1134.

242   I. Rosso, C. Galletti, M. Bizzi, G. Saracco and V. Specchia, *Ind. Eng. Chem. Res.*, 2003, **42**, 1688–1697.

243   S. Rasi, J. Läntelä and J. Rintala, *Trace Compounds Affecting Biogas Energy Utilisation—A Review*, 2011, vol. 52.

244   K. Balichard, C. Nyikeine and I. Bezverkhyy, *J. Hazard. Mater.*, 2014, **264**, 79–83.

245   S.-H. Kang, J. W. Bae, S.-M. Kim and K.-W. Jun, *Effect of Phosphorus Modification on Cu−ZnO−Al 2O 3 for the Removal of H 2S*, 2008, vol. 22.

246   D. Montes, E. Tocuyo, E. González, D. Rodríguez, R. Solano, R. Atencio, M. A. Ramos and A. Moronta, *Microporous Mesoporous Mater.*, 2013, **168**, 111–120.

247   B. Elyassi, Y. Al Wahedi, N. Rajabbeigi, P. Kumar, J. S. Jeong, X. Zhang, P. Kumar, V. V Balasubramanian, M. S. Katsiotis, K. Andre Mkhoyan, N. Boukos, S. Al Hashimi and M. Tsapatsis, *Microporous Mesoporous Mater.*, 2014, **190**, 152–155.

248   M. Pineda, J. M. Palacios, L. Alonso, E. García and R. Moliner, *Fuel*, 2000, **79**, 885–895.

249   M. J. Bagajewicz, S. S. Tamhankar, M. F. Stephanopoulos and G. R. Gavalas, *Environ. Sci. Technol.*, 1988, **22**, 467–470.

250   S. S. Chauk, R. Agnihotri, R. A. Jadhav, S. K. Misro and L.-S. Fan, *AIChE J.*, 2000, **46**, 1157–1167.

251   H. Yang and B. Tatarchuk, *AIChE J.*, 2010, **56**, 2898–2904.

252   V. Girard, A. Baudot, D. Chiche, D. Bazer-Bachi, C. Bounie and C. Geantet, *Fuel*, 2014, **128**, 220–230.

253   H. F. Garces, H. M. Galindo, L. J. Garces, J. Hunt, A. Morey and S. L. Suib, *Microporous Mesoporous Mater.*, 2010, **127**, 190–197.

254   M. Balsamo, S. Cimino, G. de Falco, A. Erto and L. Lisi, *Chem. Eng. J.*, 2016, **304**, 399–407.

255   D. Jiang, L. Su, L. Ma, N. Yao, X. Xu, H. Tang and X. Li, *Appl. Surf. Sci.*, 2010, **256**, 3216–3223.

256   T. Baird, P. J. Denny, R. Hoyle, F. McMonagle, D. Stirling and J. Tweedy, *Modified zinc oxide absorbents for low-temperature gas desulfurisation*, 1992, vol. 88.

257   G. Huang, E. He, Z. Wang, H. Fan, J. Shangguan, E. Croiset and Z. Chen, *Ind. Eng. Chem. Res.*, 2015, **54**, 8469–8478.

258   T. Baird, K. C. Campbell, P. J. Holliman, R. Hoyle, D. Stirling and B. P. Williams, *J. Chem. Soc. Faraday Trans.*, 1995, **91**, 3219–3230.

259   M. Xue, R. Chitrakar, K. Sakane and K. Ooi, *Green Chem.*, 2003, **5**, 529–534.

260   O. Karvan and H. Atakül, *Fuel Process. Technol.*, 2008, **89**, 908–915.

261   J. M. Sánchez, E. Ruiz and J. Otero, *Ind. Eng. Chem. Res.*, 2005, **44**, 241–249.

262   I. Barin, O. Kubaschewski and O. Knacke, 1977, lxxxviii, 861 .

263   O. Karvan, A. Sirkecioğlu and H. Atakül, *Fuel Process. Technol.*, 2009, **90**, 1452–1458.

264   T.-H. Ko, H. Chu and L.-K. Chaung, *Chemosphere*, 2005, **58**, 467–474.

265   S. Yasyerli, G. Dogu, I. Ar and T. Dogu, *Ind. Eng. Chem. Res.*, 2001, **40**, 5206–5214.

266   A. S. Hoffman, S. Azzam, K. Zhang, Y. Xu, Y. Liu, S. R. Bare and D. A. Simonetti, *React. Chem. Eng.*, , DOI:10.1039/C8RE00020D.

267   C. L. Carnes and K. J. Klabunde, *Chem. Mater.*, 2002, **14**, 1806–1811.

268   Z. N. Kayani, M. Umer, S. Riaz and S. Naseem, *J. Electron. Mater.*, 2015, **44**, 3704–3709.

269   J. Zhu, H. Bi, Y. Wang, X. Wang, X. Yang and L. Lu, *Mater. Lett.*, 2007, **61**, 5236–5238.

270   J. Huang, F. Tang, C. Gu, C. Shi and M. Zhai, *Front. Optoelectron.*, 2012, **5**, 429–434.

271   M. C. Biesinger, L. W. M. Lau, A. R. Gerson and R. S. C. Smart, *Appl. Surf. Sci.*, 2010, **257**, 887–898.

272   D. Su, X. Xie, S. Dou and G. Wang, *Sci. Rep.*, 2014, **4**, 5753.

273   V. M. Mohan, V. Raja, A. K. Sharma and V. V. R. Narasimha Rao, *Ionics (Kiel).*, 2006, **12**, 219.

274   J. M. Aguirre, A. GutiÃ\copyrightrrez and O. Giraldo, *J. Braz. Chem. Soc.*, 2011, **22**, 546–551.

275   Q. Zhang, K. Zhang, D. Xu, G. Yang, H. Huang, N. Fude, C. Liu and S. Yang, *CuO nanostructures: Synthesis, characterization, growth mechanisms, fundamental properties, and applications*, 2014, vol. 60.

276   Y. Borodko, H. S. Lee, S. H. Joo, Y. Zhang and G. Somorjai, *J. Phys. Chem. C*, 2010, **114**, 1117–1126.

277   D. S. Kozak, R. A. Sergiienko, E. Shibata, A. Iizuka and T. Nakamura, *Sci. Rep.*, 2016, **6**, 21178.

278   Š. Biljana, B. C. E., C. Alison and C. R. G., *Electroanalysis*, **19**, 79–84.

279   L. Neveux, D. Chiche, J. Pérez-Pellitero, L. Favergeon, A.-S. Gay and M. Pijolat, *Phys. Chem. Chem. Phys.*, 2013, **15**, 1532–1545.